Optimization of low-speed rear crash structures for a Solar Electric Vehicle

S. Potkamp

Technische Universiteit Delft

TU Delft

Lightyear

Optimization of rear low-speed crash structures for a Solar Electric Vehicle

by

S. Potkamp

to obtain the degree of Master of Science
at the Delft University of Technology,
to be defended publicly on Wednesday March 4, 2020 at 13:30.

Student number:	4154304	
Project duration:	February 25, 2019 until March 4, 2020	
Thesis committee:	Prof. C.A. Dransfeld,	TU Delft, chair
	Ir. J. Sinke,	TU Delft, supervisor
	Dr. Ir. J.M.J.F. van Campen,	TU Delft, examiner
	R. Grooten,	Lightyear, supervisor

This thesis is confidential and cannot be made public until March 4, 2025.

TU Delft

Preface

This master thesis is an attempt to provide Lightyear with insights in how the design of the rear low-speed crash structures, but also trade-offs in structural engineering in general, should be different for their upcoming Solar Electric Vehicle compared to cars that are currently on the road. I have attempted to show that structural engineering does not always consist of finding the solution that leads to the lowest weight, but that it can be used in a systems engineering approach to unlock the potential of innovative technologies. This research is performed as a final step for obtaining my Master of Science at the Faculty of Aerospace Engineering at Delft University of Technology. Before this thesis was started, a literature study [57] has been carried out. The vital elements of the literature study are repeated in chapter 2 making this a stand-alone document.

I would like to express my gratitude to Ir. Jos Sinke for his support and supervision, keeping the research on track with critical and thoughtful questions. For my supervision at Lightyear I want to thank Roel Grooten for helping me shape the direction of the research and giving practical advice. I also want to thank two of my colleagues at Lightyear, Andrea Carpi and Mathijs Brands, for their support and helping me with reflecting on my own work.

S. Potkamp
Eindhoven, February 2020

Nomenclature

Acronyms

BB	Bumper Beam	
BEV	Battery Electric Vehicle	
CB	Crash Box	
CFRP	Carbon Fiber Reinforced Plastic	
CLE	Crush Load Efficiency	
DAF	Dynamic Amplification Factor	
EA	Energy Absorption	J
ECE	Economic Commission for Europe	
FEA	Finite Element Analysis	
GFRP	Glass Fiber Reinforced Plastic	
ICE	Internal Combustion Engine	
MSRP	Manufacturer Suggested Retail Price	
OEM	Original Equipment Manufacturer	
RCAR	Research Council for Automobile Repairs	
SEA	Specific Energy Absorption	kJ/kg
SEV	Solar Electric Vehicle	
SKM	Annual Solar Kilometers	
TCO	Total Cost of Ownership	
UD	Uni-Directional	
WLTP	Worldwide harmonised Light Vehicle Test Procedure	

Greek symbols

δ	Intrusion distance	mm
ϵ	Coefficient of restitution	-
ϵ_D	Densification strain of foam filler	kg/m^3
η	Efficiency	-
η_L	Effective crush length ratio	-
ϕ	Hinge rotation	rad
ϕ	Incidence angle	deg
ρ	Density	kg/m^3

σ_0	Flow stress	MPa
σ_f	Foam plateau stress	MPa
σ_u	Ultimate stress	MPa
σ_y	Yield stress	MPa
θ	Angle	rad

Roman symbols

A	Area	m^2
a	Acceleration	m/s^2
A_{Ef}	Foam core crush force efficiency	-
b	Width	mm
b_i	Width of foam section	mm
C	Cost	€
C_d	Drag coefficient	-
C_{avg}	Average value of interaction coefficient	-
C_{ine}	Constant	-
C_{max}	Maxmimum value of interaction coefficient	-
c_{rr}	Rolling resistance coefficient	-
D	Diameter	mm
d	Deformation	mm
d	Section depth	mm
E	Energy	J
E	Young's modulus	MPa
e	Euler's number	-
E_{solar}	Annual solar irradiation	kWh/m^2
F	Force	N
f	Flange width	mm
F^D	Dynamic force	N
F^S	Static force	N
g	Gravitational constant	$9.81\ m/s^2$
H	Half natural lobe length	mm
I	Area moment of inertia	mm^4
I	Inertia	
k	Curvature	mm^-1
L	Length	mm

M	Applied moment	Nmm
m	Mass	kg
P	Power	W
R	Radius of curvature	mm
r	Correlation coefficient	-
r_{depr}	Yearly depreciation rate	-
r_{scrap}	Scrap rate	-
S_E	Stroke efficiency	-
v	Velocity	m/s
w	Width	mm
w_1	Weight factor for initial purchase price	-
w_2	Weight factor for Total Cost of Ownership	-
w_3	Value of weight saving	€/kg
w_4	Value of energy efficiency	-
w_5	Value of Annual Solar Kilometers	€/SKM
w_6	Value of trunk space	€/mm
w_7	Weight factor for environmental impact	-
y	Distance from neutral axis	mm

List of Figures

List of Tables

Abstract

This thesis investigates how the design of the rear low-speed crash structures should be different for a Solar Electric Vehicle (SEV) compared to a conventional vehicle. This new type of vehicle introduces the additional parameter annual solar kilometers (SKM) to the evaluation of the performance of the design. Next to this, a constraint is added due to the presence of the relatively expensive solar arrays that should not be damaged during the low-speed load cases.

This investigation is carried out through the creation of a general optimization tool for the conceptual design of the rear low-speed crash structures, to allow for a direct comparison between an SEV and conventional vehicles. This optimization tool consists of a performance evaluation model, which determines the 'total cost' of each design based on six performance evaluation parameters, derived from the designs weight, manufacturing cost and intrusion distance. The intrusion distance, along with whether a design can pass all relevant load cases, is calculated using an analytical structural performance model that is developed. This analyzes the structural behaviour during the Research Council for Automobile Repairs (RCAR) full width test, the RCAR structural test, and the RCAR corner test. The manufacturing cost of each design is estimated using a simple cost model that has been developed specifically for this thesis.

Validation of the structural response as predicted by the optimization tool is performed by running a Finite Element Analysis (FEA) on one of the designs for all three load cases. It was found that the accuracy is good enough for its predictions to be useful in the conceptual design of the rear low-speed crash structures. Validation of the full model is performed by predicting the actual situation of two benchmarked vehicles, with good results. The materials and manufacturing techniques are predicted correctly, as well as most of the geometry defining parameters and the intrusion distance. This shows that the results from the optimization model are useful for the structural design of the rear low-speed crash structures, and that it works for different vehicles.

It is shown that including the parameter SKM and the constraints due to the solar arrays increases the motivation for the optimization tool to minimize the intrusion distance, allowing for an increase in weight and manufacturing cost. The total intrusion distance is reduced by 26.2% while the total weight of the crash structures is increased by 13.5%. The manufacturing cost is increased by 7.3%. This provides an additional 44.5 SKM, corresponding to a value of €254.4. The optimal design for the Lightyear One consists of foam-filled aluminium crash boxes and an aluminium bumper beam with a high wall thickness to increase its energy absorption. Foam-filling the crash boxes improves the Crush Load Efficiency (CLE), reducing the peak force compared to the mean force. This allows for the absorption of the impact energy in a shorter distance while minimizing the crash rails weight penalty that is incurred by an increased peak force.

Using the optimization tool developed during this thesis is therefore shown to improve the conceptual design of the rear low-speed crash structures of the Lightyear One. Next to this, it can also be used for the conceptual design of different conventional vehicles in order to speed up the design process. The calculation of the structural performance that is done within the optimization tool will reduce the amount of finite element simulations that are needed, as it provides an improved starting point for the design.

Contents

1 Introduction

To accelerate the transition towards clean mobility, Lightyear is developing a Solar Electric Vehicle (SEV). Lightyear is a technology startup in Helmond, The Netherlands, founded in 2016 and aims to start production of its first car, the Lightyear One in 2021. The Lightyear One will be an SEV, an electric vehicle that is able to get a part of its energy directly from solar cells integrated in the roof, hood and tailgate. In the Dutch climate the Lightyear One will be able to drive 8750 km per year directly on solar energy. Based on data from 2015, the average Dutch car travels 13.022 km per year[1]. This means that over two-thirds of the distance travelled by the average car will be done on completely renewable and clean energy.

This new type of vehicle introduces additional constraints and parameters that should already be taken into account during the early design phases. An important design driver that is not present for already existing vehicles is the amount of yearly solar kilometers that can be driven (SKM), which is a combination of the amount of energy that can be harvested annually and how many kilometers can be driven per unit of energy. One apparent additional constraint is the presence of the relatively expensive solar arrays, which if not properly protected will have a large influence on the damage, repair and insurance cost during the vehicle's lifetime, which will result in an increased total cost of ownership. An overview of the main physical parts that are taken into account during this thesis, along with their names, can be seen in figure 1.1.

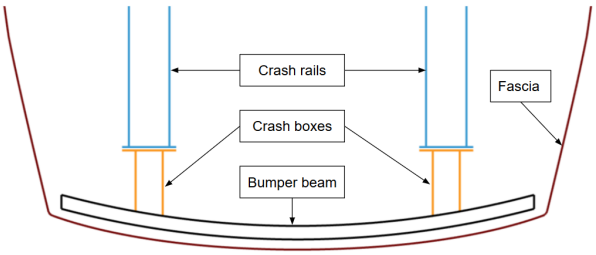

Figure 1.1: Overview of main physical parts considered during this thesis

1.1. Scope

The aim of this thesis is to create insight in how the trade-offs in structural engineering should be different when designing an SEV, compared to conventional vehicles. This is done through the creation of an optimization tool for the conceptual design of the rear low-speed crash structures. This formalizes both the design approach and the trade-offs, allowing for a fair and direct comparison.

It was decided to use the design of the rear low-speed crash structures because of the expectation that significant improvements could be made in this area, in terms of a higher amount of yearly solar kilometers and/or

[1] `http://www.odyssee-mure.eu/publications/efficiency-by-sector/transport/distance-travelled-by-car.html`, accessed on 14/04/2019

a lower Total Cost of Ownership (TCO), by deviating from the conventional design approach. It is also more favorable to quantify the effect of damage cost, compared to safety of the occupants. Next to this, pedestrian impact does not have to be considered for the rear of the vehicle. According the the Research Council for Automobile Repairs (RCAR) 30% of the low speed impacts occur at the rear of the vehicle, compared to 54% for the front and 16% for the side of the vehicle [2].

The markets that are considered during this thesis are the USA and the EU. This means that the insurance and homologation load cases that are considered are valid for when the vehicle will be sold in both the USA and the EU. It is also not attempted to provide a design that can directly be implemented in the final design of the vehicle and manufactured. Additional engineering efforts will be necessary to progress the conceptual design that the optimization tool provides towards a detailed design. For these steps, FEA will be necessary.

1.2. Research questions

Since an SEV is a new type of vehicle, and additional constraints and parameters that determine the performance of the design are added, it is not yet known what the optimal design of the rear low-speed crash structures should look like. Next to this it is desired to provide insight in what trade-offs will be encountered during the structural design of an SEV. Therefore the main research question to be answered during this thesis is:

> **"In what way should the design of the rear low-speed crash structures of an SEV be different compared to conventional vehicles?"**

In order to find the answer to this question, and provide a guideline for the different steps that need to be performed during this thesis, the following subquestions also need to be answered:

1. What parameters should be used to evaluate the performance of the design of the rear low-speed crash structures?
2. What materials and geometries can be used for the design of the rear low-speed crash structures?
3. What are the critical load cases and requirements for the rear low-speed crash structures?
4. How can the structural performance of the rear low-speed crash structures be evaluated analytically?

1.3. Structure of the report

In chapter 2 the literature review is shown, providing a brief overview of research that has already been performed concerning the structural analysis of crash structures, and which materials and geometries can be used for the design of low-weight crash structures. Chapter 3 determines what parameters need to be calculated for each candidate design and how they can be used to evaluate the performance of the design, using a formula for total cost. The types of candidate designs that the optimization model should be able to analyze are shown chapter 4, along with the material properties and manufacturing techniques. Chapter 5 discusses which load cases will be considered for the structural analysis, and builds on this to create a methodology for the analytical analysis of the structural performance. A simple manufacturing cost model is developed in chapter 6, in order to estimate the manufacturing cost of different designs and production volumes.

The verification and validation efforts are reported in chapter 7. The validation consists of both Finite Element Analysis (FEA) to check the accuracy of the prediction of the structural performance, and using the optimization tool to predict the actual situation of two benchmarked vehicles to show that the tool can successfully be used to generate a conceptual design of the rear low-speed crash structures for different vehicles. The optimal design for the Lightyear One is presented in chapter 8. This design is compared with the result when SKM is not included. Chapter 9 shows the results of the parameter sensitivity analysis, which is used to generate additional understanding of the robustness of the model and its solutions.

In chapter 10 the conclusions and answers to the main research question will be presented. This is followed by a discussion and recommendations for improvements in the optimization tool and future research in chapter 11, to conclude the report.

[2] `https://www.rcar.org/Papers/Procedures/CrashStandards_GermanRatingSystem.pdf`, accessed on 18/12/2019

2

Literature review

To provide background information on the design process of the rear low-speed crash structures a literature review is presented in this chapter. This will provide a starting point for some of the questions that should be answered during this thesis, as well as show the relevant literature on how the structural performance of the low-speed crash structures can be analyzed.

An overview of which material types can be used for the lightweight design of both the bumper beam and crash boxes is shown in section 2.1. The preferred geometries and cross-sectional shapes for both the bumper beam and crash boxes are investigated in section 2.2. In section 2.3 it is shown (based on the materials and geometries determined before) how the deformation mechanisms of the crash boxes work, and how trigger mechanisms are used to reduce the peak force. Section 2.4 shows how the elastic energy absorption and restitution of this portion of the impact energy can be estimated. The effect of the impact incidence angle on the structural behaviour is explained in section 2.5. Finally, in section 2.6, analytical equations for the structural analysis of metal crash boxes are presented.

2.1. Materials

In this section it is determined which material types are generally used for the design of both the bumper beam and the crash boxes. It will also be shown how these materials perform in terms of weight, with respect to each other. This is done for the bumper beam and the crash boxes separately, as the different loading conditions lead to potential differences in how the materials perform.

2.1.1. Bumper beam

There are different materials that can be used for the design of the bumper beam. The materials that are used most often are steel alloys, aluminium alloys, Carbon Fiber Reinforced Plastics (CFRP) and Glass Fiber Reinforced Plastics (GFRP) composites. Traditionally the bumper beam used to be made from steel, but in recent years more and more cost-effective lightweighting options have been found through the switch to aluminium alloys. In some rare cases the bumper beam is made from a composite material, either CFRP or GFRP, if low weight is of extreme importance and the budget for weight saving is large. An example of a vehicle with a CFRP pultruded bumper beam is the 2020 Corvette Stringray.

There are two material properties that influence the bumper beam's impact behaviour, namely Young's modulus and yield strength. The density of the material is important for the weight of the bumper beam, which is desired to be as low as possible. Next to this, it also matters if the material shows ductile or brittle behaviour [47].

Tie Wang has shown that large weight savings can be achieved by using CFRP instead of steel. He found that a bumper beam could achieve a similar performance with a weight reduction from 4.96 kg to 2.18 kg, which is 56%. Part of this weight saving is because in his research a variable thickness is used for the CFRP design but not for the steel design. This means a lower thickness can be used at locations where less strength and stiffness is needed. If this effect is not taken into account, the weight saving is still 53.2%. For this analysis a

steel alloy with a yield strength of 800 MPa was used, and the analysis was performed using FEA in LS-DYNA. Only the ECE-R42 pendulum test has been considered [73].

Tai found that redesigning a steel bumper beam in an aluminium alloy could lead to a 28% reduction in weight, as well as a 45.6% increase in energy absorption by crushing of the bumper beam. The steel alloy used in this comparison has a yield strength of 115 MPa and the 6061 aluminium alloy has a yield stress of 69 MPa, and strain-hardening effects are taken into account [68].

Belingardi redesigned a bumper beam-crash box combination, originally made from steel, using GFRP. Through this redesign it was found that the weight could be reduced from 7.67 kg for the steel design to 3.72 kg for the GFRP design, which is a weight decrease of 51.5%. When using uni-directional glass fibers, the weight could even be decreased by 58.3%. It should be noted that additional effects are in play here, as this weight saving also includes the crash boxes where energy is absorbed through axial crushing [8].

Foam-filling

It has been investigated by Hanssen whether foam-filling of the bumper beam could improve the structural performance and reduce the weight of the bumper beam. This investigation has been performed based on aluminium alloys along with three different densities of aluminium foam. It was found that the initial peak moment capacity of the beam under a three point bending test increased for foam-filled beams, the exact amount depending on the density of the foam that is used. The higher the density the higher the initial peak moment capacity of the beam. When the foam core fails, the total beam moment decreases towards the value expected for a non-filled beam. This increase in beam strength can be explained by the foam resisting local buckling of thin-walled beams. It was also found that the plastic hinge that develops becomes less dependent on the shape of the impactor when a foam filler is used. The increase in initial peak capacity was found to be up to 200%, depending on the temper and alloy of the extruded aluminium beam and the density of aluminium foam. A value normalized for the weight is not given [28]. It is important to note that energy absorption through crushing of the bumper beam section is not considered here.

Zhang has found that filling the bumper beam with foam does not increase the specific energy absorption, and even reduced the peak load of the beam under a three point bending test. This is shown in figure 2.1 and 2.2 respectively [80]. An explanation for the differences between these two researchers has not been found, but it is expected to be due to differences in the material properties of the metal and the foam.

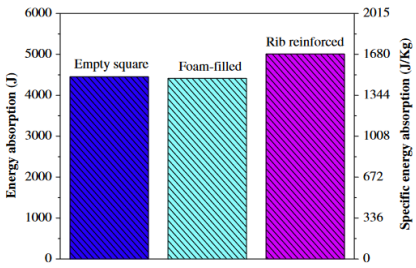

Figure 2.1: Specific energy absorption comparison of empty, foam-filled and rib-reinforced bumper beam [80]

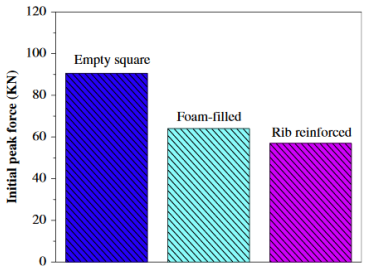

Figure 2.2: Peak force comparison of empty, foam-filled and rib-reinforced bumper beam [80]

Based on the data from the research that has been found, it is decided to not consider foam-filling of the bumper beam during this thesis. Results are contradictory on whether foam-filling a thin-walled beam in a three-point bending test improves its structural performance, and none of the papers investigated actually explicitly showed the potential of weight reduction.

2.1.2. Crash boxes

The structural performance is measured for the crash boxes by evaluating the weight and energy absorption, combined in the term Specific Energy Absorption (SEA). This term provides an easy basis to compare both different materials and geometries. Other important parameters for the crash boxes are peak force and average force, the ratio between these two called Crush Load Efficiency (CLE), as well as effective stroke. It should be noted that all these parameters do not only depend on the material but also on the geometry of the crash

box design. In this section literature is presented on crash boxes made from steel alloys, aluminium alloys, CFRP and GFRP, as well as foam-filled crash boxes.

Steel alloys

Tarigopula has performed both quasi-static and dynamic axial crushing tests on square tubes made from DP800 high-strength steel. Impact velocities of up to 15 m/s and an impactor mass of 600 kg were used in the dynamic tests. in the quasi-static test SEA values of up to 12.1 kJ/kg were found, while in the dynamic tests the SEA values turned out to be lower. When an impact speed of 5.0 m/s was used, the SEA was found to be 12.3 kJ/kg. With an impact speed of 10.0 m/s the SEA was lowered to 11.2 kJ/kg. With an impact speed of 15.0 m/s this was reduced even further to 8.1 kJ/kg. This reduction in SEA is due to a less predictable deformation pattern involving fewer folds and a smaller effective stroke. It is also stated that the SEA will increase by approximately 1.1 kJ/kg for a yield strength increase of 100 N/mm^2 in both the quasi-static and dynamic analysis [71].

Aluminium alloys

Farley has tested the SEA of two crash tubes from the aluminium 6061 alloy (no temper is specified). It was found that with a tube diameter of 25.4 mm and a wall thickness of 1.5 mm the SEA was 77.5 kJ/kg, while a tube with a diameter of 38.1 mm and a wall thickness of 2.4 mm had a SEA of 88.5 kJ/kg [21]. The diameter of these tubes is much smaller than normally found in vehicle's crash boxes, as a certain cross-sectional dimension is needed for global stability during both a straight impact and an impact with an incidence angle. This makes this result less usable, as the SEA values presented here are larger than can be achieved with a crash box design that will provide enough stability.

Bisagni has tested a crash tube made from an aluminium alloy, with an inside diameter of 70 mm and a wall thickness of 2.6 mm (representative for the dimensions used for crash boxes in vehicles). The SEA was found to be 39.7 kJ/kg. No specific alloy is mentioned but since this research is quite recent it is assumed that this value is reasonably accurate for what can be achieved with the current material standards. It was also found that the crush force efficiency is 1.43 for this specific sample [9].

CFRP

Farley has investigated the dependence of the SEA (called Specific Sustained Crushing Stress in his paper) on the ply orientation. Different carbon fiber/epoxy tubes were experimentally tested, with ply orientations of $[0/\pm\theta]$, where θ is varied from 15 to 90 degrees in discrete steps of 15 degrees. The results can be found in figure 2.3. From this figure it can be seen that the SEA is the highest, around 100 kJ/kg, when the ply orientation is [0/ ± 15deg], while for many other test specimens the SEA is only around 50 kJ/kg. It can also be seen from the figure that the values for SEA are lower in dynamic tests for low values of θ, while they are higher in dynamic tests for high values of θ [21].

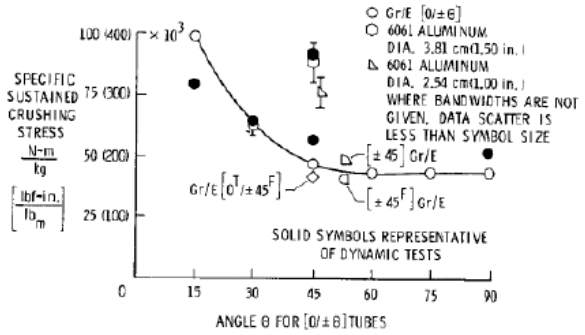

Figure 2.3: SEA vs θ. White circles show static tests, black circles show dynamic tests of CFRP tubes [21]

Bisagni has tested CFRP tubes using a drop test tower, with a maximum impact velocity of 10 m/s. In these tests different types of carbon fibers were used, namely M46J and T1000, as well as different types of matrix

material. The tubes have four plies and are oriented at 0 deg and 90 deg only. It was found that the SEA of the tubes varied between 46.14 kJ/kg and 74.87 kJ/kg. The reason this is lower than the values that were shown previously is that the ply orientations are not optimized. The crush load efficiency was found to be between 1.09 and 1.18, and the use ratio was found to be between 0.33 and 0.62 [9]. This use ratio is not the same as the crush stroke efficiency, as the impact energy was absorbed before the maximum crush stroke was reached.

GFRP

Farley [21] has investigated the effect of ply orientation on the SEA for GFRP. Different glass fiber/epoxy tubes were tested with ply orientations of $[0/\pm\theta]$, where θ is varied from 15 to 90 degrees in discrete steps of 15 degrees. The results can be found in figure 2.4. From this figure it can be seen that the SEA is the highest, around 50 kJ/kg, when the ply orientation is $[0/\pm 75\text{deg}]$ while for most other test specimens the SEA is only around 30 kJ/kg.

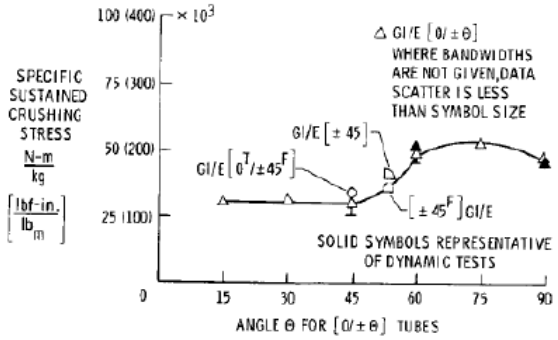

Figure 2.4: SEA vs θ. White circles show static tests, black circles show dynamic tests of GFRP tubes [21]

Bisagni [9] has experimentally tested glass fiber/epoxy tubes and found an SEA of 47.9 kJ/kg with a crush load efficiency of 1.13. This was tested on a drop test machine, with a speed of 10.0 m/s.

Foam-filling

Many researchers have focussed on improving the crash behaviour of aluminium and CFRP tubes with the addition of foams, mainly aluminium foam. Hanssen [30] has found an interaction effect between the aluminium tube and the foam that generated an energy absorption that is higher than the sum of both materials, as shown in figure 2.5. This can be attributed to the foam supporting the buckling of the walls, and increasing the amount of folds that are created during the impact. It was concluded that significant savings in mass (8.0%) and length (32.1%) can be achieved by using a foam-filler, with the side note that a smaller outer cross-section needs to be used. For this research an aluminium alloy with a strength of 239 MPa is used.

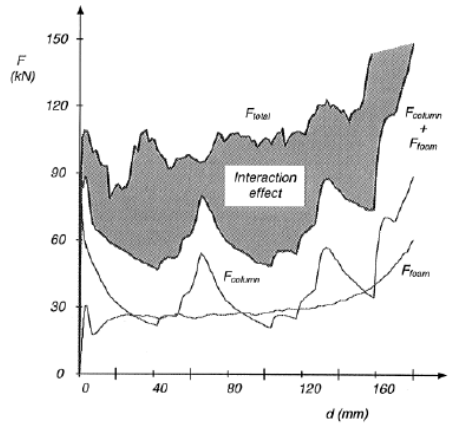

Figure 2.5: Force-deformation graph showing interaction effect between column and foam [30]

In contract to this, no weight savings/improvements in SEA were found due to the addition of the foam-filler in the research of Li [42]. For the square tubes it was found that both the empty and foam-filled specimens

had an SEA of 12.5 kJ/kg, but the crush load efficiency improved from 2.63 to 1.66 due to the addition of the foam. For the circular sections it was found that adding the foam actually reduced the SEA from 27.5 kJ/kg to 17.5 kJ/kg, but improved the crush load efficiency from 1.43 to 1.25.

Sun has investigated the influence of filling CFRP tubes with aluminium foam and aluminium honeycomb. It was found that the SEA of filled (both foam and honeycomb) CFRP tubes decreased a lot, leading to a heavier design. This is explained by the more comparable density of the foam and the CFRP, while the structural properties of the CFRP are much higher. CFRP tubes filled with honeycomb did show a more stable collapse pattern.

Based on the research that was found, it is decided to consider foam-filling for metal crash boxes as it shows potential for weight reduction and an improvement in CLE. No apparent advantages are found for foam-filling composite crash boxes as their structural properties are already too good for the foam to improve them.

2.2. Geometries

This section presents findings from literature on geometries that are used for the bumper beam and crash boxes, as well as their relative performance. This is done for the bumper beam and the crash boxes separately, as the different loading conditions lead to potential differences in what geometries are desired. A split is also made between ductile materials (steel and aluminium alloys) and brittle materials (composites) as they have different energy absorption mechanisms which will be elaborated on in section 2.3.

2.2.1. Bumper beam

For the design of the bumper beam different cross-sectional geometries can be chosen. In general closed cross-sections are chosen due to their improved torsional resistance, but open cross-sections are also an option. Possible variations in the bumper beam geometry are found in the cross-sectional shape, and graded wall thickness. This section is valid for both metal and composite bumper beams.

Sudin has investigated the optimal cross-sectional geometry of the bumper beam under cantilever boundary conditions, in terms of deflection and weight. Four types of beams were tested, namely an I-profile, a rectangular closed profile, a C-profile and a T-profile. The results of this investigation are shown in table 2.1, where the deflection ratio is the maximum deflection that is found multiplied by the weight of the profile, and then normalized for the comparison. From these results it can be seen that the rectangular profile has the best performance for bending resistance per weight, as expected [64]. To keep the complexity of the optimization tool reasonable only single-cell closed rectangular profiles will be evaluated for the bumper beam, as multi-cell cross-sections can be introduced in the design phases after the conceptual design.

Table 2.1: Comparison of maximum deflection ratio for different cross-sections, adapted from Sudin [64]

Cross-section	**Deflection ratio**
I-profile	1.00
Rectangular profile	0.89
C-profile	1.39
T-profile	2.5

The curvature of the bumper beam is for a large part dictated by the styling and packaging of the vehicle, as it must fit inside the bumper fascia with preferably a constant spacing between the two. However, an increased curvature increases the energy absorption of the bumper beam, as well as the stability of the beam. It also extends the space available for barrier intrusion. A beam with a higher curvature should also be able to more effectively transfer the impact loads towards the crash boxes [16, 73].

Another method to improve the structural performance and/or reduce the weight of the bumper beam is thickness variations. These can be incorporated in two different ways, either in the cross-section or along the length of the bumper beam. Different parts of the cross-section perform different functions while providing bending resistance or energy absorption. This means that it is efficient to not have all parts of the cross-section with the same thickness. This was done by Farkas to achieve a 7.8% reduction in weight while keeping the performance of the bumper beam roughly the same [20]. This type of thickness variation is easy

to incorporate in extruded bumper beams. Thickness variations along the length of the bumper beam can be used when using for example composite materials with a lay-up process. Tie Wang used thickness variations along the length of the bumper beam to reduce the weight by 6.0% while keeping the structural performance similar. This was done by reducing the thickness from 5.4 mm to 4.2 mm starting from the connection to the crash boxes and outwards [73]. However, it is chosen to not include these thickness variations in this thesis as this would make the development of the optimization tool more complicated. Thickness variations should be incorporated in later phases of the design process, when FEA is used.

2.2.2. Crash boxes

The optimal geometry to be used for the crash boxes is different for ductile materials and brittle materials, as they exhibit different energy absorbing mechanisms. For this reason this section is split in geometries for metal crash boxes and geometries for composite crash boxes.

Metal crash boxes

The effect of the cross-sectional shape on the SEA has been researched by Liu [43]. For this a numerical LS-DYNA model was used, in which the cross-sectional shape of steel (σ_y = 200 MPa) crash boxes was varied. The cross-sections that were studied are rectangular, square, circular, hexagonal and octagonal. The load case the crash boxes were subjected to was a 40% offset collision with an impact velocity of 16 km/h. When normalizing the SEA and peak force of all crash boxes considered, setting the best performing cross-section (the square crash box) to 100, this leads to the results as can be seen in table 2.2. For the normalized SEA a higher value is better, while for the normalized peak force a lower value is better.

Table 2.2: Comparison of normalized SEA and peak force, adapted from Liu [43]

Cross-section	**Normalized SEA** [-]	**Normalized peak force** [-]
Square	100	100
Rectangular	96.9	136.1
Circular	97.9	99.0
Hexagonal	98.2	123.0
Octagonal	95.9	141.3

This result of a square cross-section being optimal for metal crash boxes in terms of SEA is confirmed by the research by Hanssen. His paper on square crash boxes shows improvements in terms of SEA compared to circular crash boxes [29, 30]. The favorability of square cross-sections can be explained by a larger amount of energy being absorbed by deformation in corners. This is also confirmed by initial benchmarking of vehicles that are currently on the road, where square or rectangular crash boxes are standard. This is also because square or rectangular crash boxes are easier to handle during the process of assembling the crash boxes to the bumper beam.

It was determined by Kim that improvements in SEA can be made for metal crash boxes by increasing the complexity of the cross-section. Improvements can already be made when using the same outer cross-section, but using partitions to increase the amount of closed cells that are present. This type of geometry is relatively easy to manufacture using extrusion. Even more improvements in SEA can be realized when a more complex multi-cell design is used. An overview of the results for different multi-cell cross-sections is shown in figure 2.6. A graphical representation of the complex multi-cell design is shown in figure 2.7. Crash boxes with a multi-cell cross-section show a shorter buckling wavelength, therefore improving the stability of the progressive collapse.

Even though multi-cell sections show promise of a reduced crash box weight, there is not yet enough knowledge about its effects on the CLE and stroke efficiency. This means that this concept is not yet mature enough to include during this thesis, but that this is instead something that should be considered an improvement to investigate in later phases of the design when using FEA.

Composite crash boxes

For composite crash boxes the most promising cross-sectional shape is circular. This is explained by the energy absorption mechanisms, that benefit from a constant situation all along the cross-section. This allows for a smooth and stable progressive crushing behaviour. This argument is supported by research from both

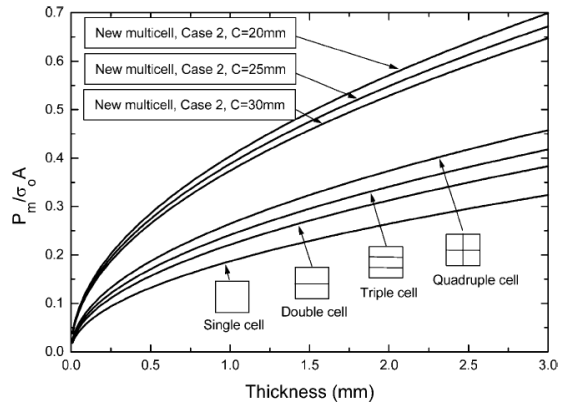

Figure 2.6: Overview of results for multi-cell cross-sections [39]

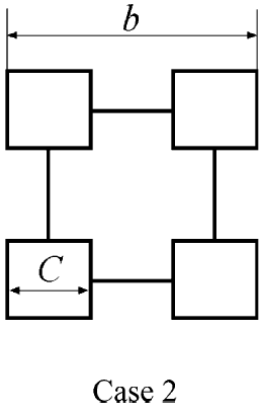

Figure 2.7: Cross-sectional shape of new multi-cell design [39]

Farley and Bisagni [9, 21, 22]. Lu also explicity confirms that axially loaded circular composite columns absorb more specific energy than similar square ones [44].

2.3. Deformation mechanisms crash boxes

The materials used for the crash boxes can be classified as metals and composites in terms of their deformation mechanisms. A column loaded in axial compression can fail through three different modes: Euler buckling, shell buckling leading to progressive folding, and brittle fracture. Euler buckling is not desired due to the small amount of energy it can absorb. Choosing the geometry of the crash can correctly can ensure that Euler buckling will not occur and this failure mode is therefore not considered any further. Due to plasticity of the material the energy absorption mechanism for metals is called progressive folding and is explained in more detail in section 2.3.1. The brittle nature of composite materials means that the energy absorption mechanism for composites is progressive crushing and is elaborated on in section 2.3.2.

2.3.1. Progressive folding

When a metal, e.g. an aluminium alloy, is used for the crash boxes the desired energy absorption mechanism is progressive folding. This mechanism can absorb a lot of energy due to the high percentage of the material that will plastically deform compared to Euler buckling. Plastic hinges are formed and the material can fold onto itself. Depending on the cross-sectional shape of the crash box the collapse modes are different, but only the collapse mode for square columns is shown here as only square columns are considered for metal crash boxes during this thesis.

During the collapse of square metal tubes both extensional and inextensional deformations are present at both stationary and moving plastic hinge lines. Roughly one-third of the energy is absorbed by the extensional deformations that are existing in a small fraction of the total shell area. The other two-thirds of the impact energy is absorbed by the inextensional deformations. In figure 2.8 it can be seen what happens to the geometry of the crash box when it is fully crushed [1, 44]. A typical example of the force-deflection diagram for progressive folding is shown in figure 2.9.

In figure 2.9 it can be seen that at the start of the impact the force increases linearly until the peak force is reached. From this point the progressive folding starts, and the force starts undulating around the mean force. Each peak in the graph corresponds to the initiation of a new fold. This continues until the maximum deformation is reached, after which the applied force increases again (not shown in figure).

Trigger mechanism

The peak force, as can be identified in figure 2.9, is also an important attribute of the structural behaviour of the crash box. This peak force needs to achieve a certain minimum level to ensure that the crash boxes are not damaged in a very low-speed impact, and on the other hand the peak force needs to be limited as this determines the maximum deceleration of the vehicle and the load the high-speed crash structures need to be able to handle without getting damaged. This peak force is normally too high when no trigger mechanism is used,

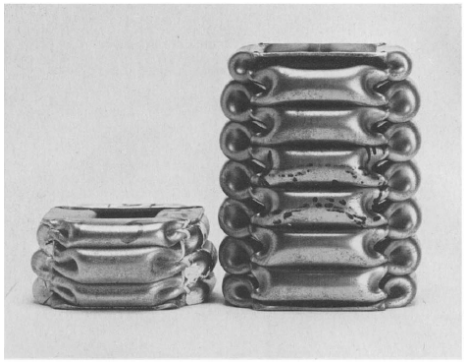

Figure 2.8: Two examples of progressively crushed square aluminium columns [1]

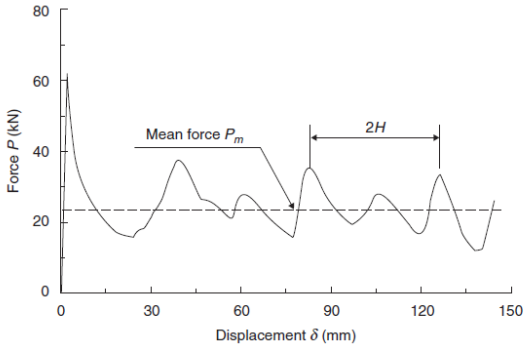

Figure 2.9: Example of force-deflection diagram typical for progressive folding [75]

and it is preferred to have the peak force as close to the mean force as possible. It was found that the trigger mechanism has no significant influence on the mean force, effective stroke length or SEA of the crash box [44].

Examples of methods that can be used to reduce the peak force, i.e. trigger mechanisms, are:

- Chamfering one end of the tube
- Pre-buckling of the faces on one end of the tube
- Creating weak spots with holes or indentations on one end of the tube

It was found by Hanssen that, while trigger mechanisms play an important role in the reduction of the peak force when crash boxes are tested as individual components, the Heat Affected Zone (HAZ) that is created after welding the crash boxes and bumper beam together can take over the role of the trigger mechanism. This weakened area also reduces the peak force on the crash boxes and can eliminate the need for a mechanical triggering mechanism [31].

It is difficult to take into account the exact trigger mechanism that is used when analysing the peak force and the structural performance of the crash boxes as part of the rear low-speed crash structures. For this reason it will be assumed that a proper trigger mechanism will be designed in later phases of the design when FEA can be used to add these details in the design.

2.3.2. Progressive crushing

Due to the brittle nature of composites the colums will fail, if properly designed, through progressive crushing. This means that a stable zone of microfractures propagates through the tube. The difference between the peak load and sustained crushing load is determined by the design of the crushing trigger, often a chamfered edge on one side of the tube.

There are four different crushing modes that can be distinguished, namely transverse shearing, brittle fracturing, lamina bending, and local buckling. A large percentage of composite columns fail in the brittle fracturing mode which is a combination of transverse shearing and lamina bending. It should be noted that these crushing mechanisms can be strain-rate dependent, influencing the level of energy absorption. A schematic representation of the crushing process of a composite crash tube is shown in figure 2.10. A typical force-deflection diagram for progressive crushing is shown in figure 2.11. These figure do not show any specific crushing mode [35].

It can be seen from figure 2.11 that the force increases linearly until the peak force is reached and the process of progressive crushing is started. From this point the load quickly drops to roughly the mean force. The force will stay close to the mean force (less variation than for progressive folding of metal columns) until a fully crushed state is reached and the force increases again.

Trigger mechanism

Identical to the desire for metal crash boxes to reduce the peak force, a trigger mechanism is also needed for composite crash boxes. The main method that is used for reducing the peak force of composite crash boxes

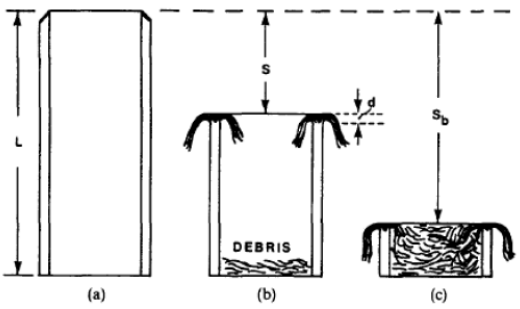

Figure 2.10: Representation of composite tube crushing process: (a) with chamfered end, (b) partially crushed, (c) fully crushed with compacted debris inside [35]

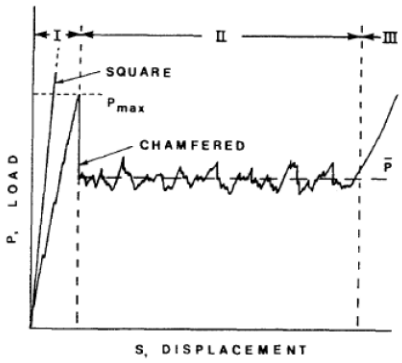

Figure 2.11: Typical force-deflection diagram for progressive crushing [35]

is chamfering one end of the tube. This can be seen in figure 2.10 (a). The chamfer provides a smaller surface area that is in contact with the impactor and therefore leads to higher compressive stresses at the same load. This means that the crushing will start at lower force levels. It does also reduce the stiffness of the elastic portion of the force-displacement curve, as can be seen in figure 2.11. No research has been found on how to implement this trigger mechanism when the crash boxes are combined with a bumper beam.

Also for composite crash boxes it is difficult to include the exact trigger mechanism and its effect on the peak force when the crash box is part of the rear low-speed crash structures. Because of this it is assumed that a proper trigger mechanism will be added in later phases of the design when FEA is available to work out these detailed parts of the design.

2.4. Elastic energy and restitution

During an impact event a part of the kinetic energy is absorbed through permanent deformation but another part is stored in the structure as elastic energy. Once the difference in velocity between the vehicle and the impactor becomes zero, the elastic energy will start to be restituted as kinetic energy of the vehicle. This effect can be easily identified in online videos of vehicles performing the RCAR rear full width test for example. The coefficient of restitution is defined in equation 2.1, where v_1 is the velocity of the first body prior to impact, v_1' is the velocity of the first body after impact, v_2 is the velocity of the second body prior to impact and V_2' is the velocity of the second body after impact. That means $v_2' - v_1'$ is the relative separating velocity after impact, and $v_1 - v_2$ is the relative closing velocity before impact.

$$\epsilon = \frac{v_2' - v_1'}{v_1 - v_2} \tag{2.1}$$

The elastic energy is stored in the complete vehicle by elastic deformation, not just in the crash structures. In fact only a small portion of the elastic energy is stored in the crash structures as these have a high stiffness in the loading direction, leading to very small elastic deformations and therefore a negligible amount of absorbed energy. Since only the design of the crash structures is taken into account during this optimization, it becomes impossible to analyze the total elastic energy absorption and include it in the structural analysis.

As can be seen from figures 2.12 and 2.13 the coefficient of restitution is dependent on the impact speed and too large to neglect during the analysis. For vehicle-to-vehicle impacts a trendline with $r = 0.904$ has been developed by Antonetti [7] to calculate the coefficient of restitution depending on the impact velocity. This trendline can be found in equation 2.2, where V is the closing velocity in m/s. For vehicle-to-barrier impacts no trendline has been developed by Antonetti, but based on the data shown in figure 2.13 it seems like the same trendline can be used, although with a lower accuracy.

$$\epsilon = 0.5992^{(-0.2508V + 0.01934V^2 - 0.001279V^3)} \tag{2.2}$$

When the impact occurs with a stationary rigid barrier (RCAR full width test, RCAR corner test), equations 2.1 and 2.2 can be combined to directly find the kinetic energy of the vehicle post-impact, and therefore also

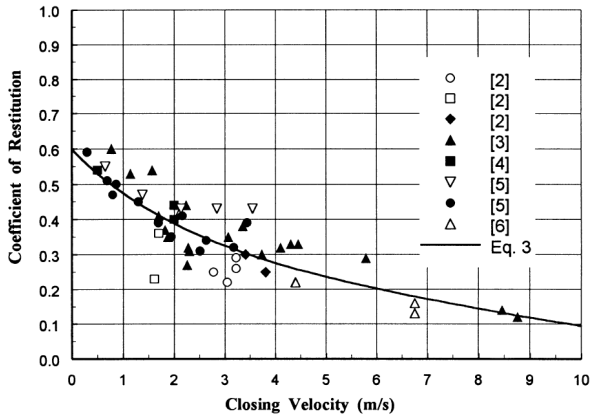

Figure 2.12: Trendline (R=0.904) for Coefficient of Restitution for vehicle-vehicle impact at different impact speeds [7]

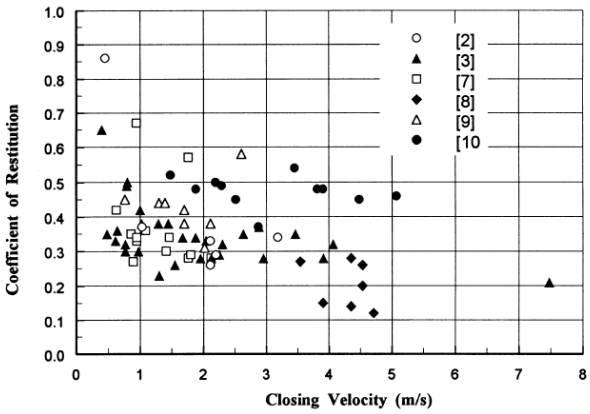

Figure 2.13: Data points for Coefficient of Restitution for vehicle-barrier impact at different impact speeds [7]

the amount of impact energy that is absorbed by the crash structures. However, when the impact occurs with a moving barrier (RCAR structural test, ECE-R42 pendulum tests), additional steps are needed as only the relative separating velocity of the two bodies is found using equations 2.1 and 2.2. The additional equation is found in conservation of momentum, where the momentum before the impact needs to be equal to the momentum after the impact, as show in equation 2.3.

$$m_{car} * V_{car} + m_{barrier} * V_{barrier} = m_{car} * V'_{car} + m_{barrier} * V'_{barrier} \tag{2.3}$$

Solving these equations simultaneously will yield the vehicle and barrier velocities after impact. This means that the kinetic energy post-impact can now be calculated, and subtracted from the kinetic energy pre-impact to find the amount of impact energy that is absorbed during the collision. This is shown in equation 2.4. It should be noted that due to the use of the statistical trendline provided in equation 2.2 the amount of energy absorbed during the load cases with the moving barriers is not dependent on the actual design of the rear low-speed crash structures, but only on the impact speed, barrier mass and vehicle mass. This is a simplification of reality.

$$E_{absorbed} = \frac{m_{barrier}}{2} V_{barrier}^2 - \left[\frac{m_{car}}{2} V_{car}'^2 + \frac{m_{barrier}}{2} V_{barrier}'^2 \right] \tag{2.4}$$

Since the coefficient of restitution is only dependent on the impact speed, this value does not depend on the design of the vehicle. The values for the coefficient of resitution for the different load cases are shown in table 2.3.

Table 2.3: Values for coefficient of restitution used for the different load cases

Loadcase	**Impact speed (km/h)**	**Impact speed (m/s)**	ϵ
RCAR structural test	16	4.4444	0.2574
RCAR full width test	10.5	2.9167	0.3293
RCAR corner test	5.5	1.5278	0.4254
ECE-R42 pendulum test	4.25	1.1806	0.4569
ECE-R42 pendulum corner test	2.6	0.7222	0.5048

2.5. Effect of impact angle on structural behaviour of crash boxes

During the RCAR structural test the impact has an incidence angle of 10 degrees, representing that in reality the impact is not always perfectly aligned with the longitudinal axis of the vehicle. Han and Park [27] have investigated the collapse behaviour of square thin-walled columns under oblique loads, and have found certain results that can be used to take the effect of the incidence angle into account. When the load angle is small the collapse behaviour is dominated by axial collapse, but at a certain load angle, called the critical load angle ϕ_c, the bending collapse starts to dominate the behaviour. Both the axially-dominated behaviour and

the bending-dominated behaviour are shown with their corresponding mean crush load levels in figure 2.14, as well as the transition zone between them.

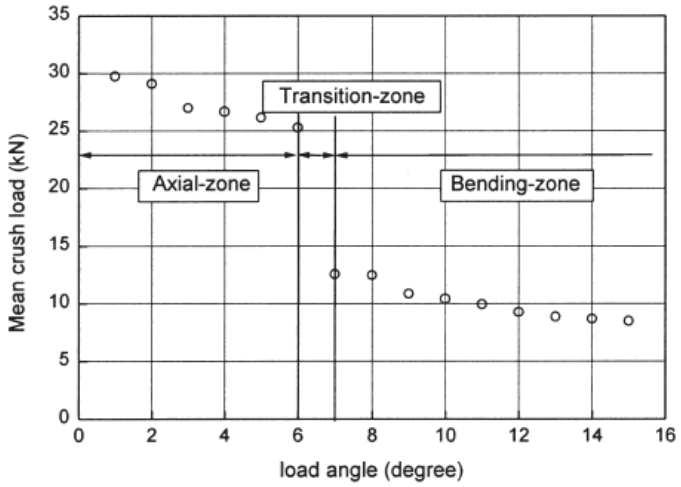

Figure 2.14: Effect of load angle on mean crush load for axial-zone, transition-zone and bending-zone [27]

From figure 2.14 it can be seen that the mean crush load is slowly reduced by increasing the load angle, up until the critical load angle, where a sharp drop of the mean crush load can be seen. It was found that the wall thickness of the section has almost no influence on the critical load angle, but there was a high dependence on the width and length of the section. This can be explained by the width of the section increasing the area moment of inertia, and thus the bending resistance, and the length of the section having a negative effect on the stability of the column. The relation between the critical load angle and the L/b ratio has been captured by Han [27] with the development of a trendline, as can be seen in figure 2.15 and equation 2.5.

$$\phi_c = 4.81 + 1564e^{-1.12(L/b)} \tag{2.5}$$

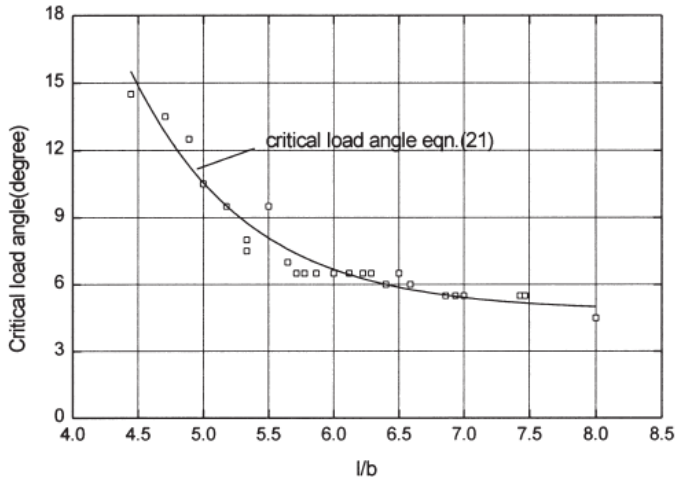

Figure 2.15: Trendline for the relationship between the critical load angle and L/b ratio (Han 1999)

Where ϕ_c is the critical load angle in degrees, L is the length of the column, and b is the width of the column. It is highly beneficial to use an L/b ratio small enough to ensure that the bending collapse does not dominate the behaviour. This switch in behaviour happens in a small transition zone, and when the bending collapse dominates the behaviour as much as 60% of the energy absorption capability is lost [27].

To estimate the decrease in the mean crush force while still in the axial-zone, a curve-fitted equation has been developed by Han [27]. It can be found in equation 2.6, where ϕ is the incidence angle of the loading

condition and F_{mean} is the mean crush force as calculated for the crash box under an incidence angle of zero degrees.

$$F_{mean,\phi} = \left[\frac{1.06 + 0.41e^{-0.24\phi}}{1.47}\right] F_{mean} \tag{2.6}$$

2.6. Analytical equations for structural behaviour of metal crash boxes

In this section it is shown what has been found in literature on the analysis of the structural behaviour of crash boxes using analytical equations. Verified equations for the static structural behaviour of empty and foam-filled square extrusions are presented in section 2.6.1. Analytical equations for the static structural analysis of double-hat folded geometries are shown in section 2.6.2. A method to estimate the dynamic amplification factor is explained in section 2.6.3.

2.6.1. Square extrusions

As part of research into the energy absorption efficiency of filling square aluminium extrusions with aluminium foam, Hanssen [30] has developed analytical equations to predict the mean and peak forces of both empty and foam-filled square extrusions. For square extrusions non-filled equations 2.7 can be used to calculate the static mean crush force. If the extrusion is foam-filled, equation 2.8 should be used. [30].

$$F^S_{mean} = 13.06\sigma_0 b^{1/3} t^{5/3} \tag{2.7}$$

$$F^S_{mean} = 13.06\sigma_0 b^{1/3} t^{5/3} + \sigma_f b_i^2 + C_{avg}\sqrt{\sigma_f \sigma_0} bt \tag{2.8}$$

Where σ_0 is the flow stress of the material, defined as $\sigma_0 = \frac{\sigma_y + \sigma_u}{2}$, b is the sectional width, t is the wall thickness, σ_f is the plateau stress of the foam, b_i is the width of the foam section and C_{avg} is equal to 5.5 as it is a statistically determined parameter representing the interaction effect.

When the mean crush force is known, the peak force of non-filled extrusions can be estimated using equation 2.9. The value 0.48 comes from the statistical relationship between the mean and peak force for square aluminium extrusions. A specific value for steel extrusions has not been found, but experimental results in literature seem to be very similar to aluminium extrusions [30] It should be noted that the peak force is highly dependent on the trigger mechanism that is used. For this equation it is assumed that the trigger mechanism is implemented correctly, resulting in the lowest peak force and therefore the maximum crush load efficiency.

$$F_{peak} = \frac{F_{mean}}{0.48} \tag{2.9}$$

The peak force of foam-filled extrusions can be estimated using equation 2.10.

$$F_{peak,foam} = F^0_{peak} + \frac{1}{A_{Ef}}\sigma_f b_i^2 + C_{max}\sqrt{\sigma_f \sigma_0} bt \tag{2.10}$$

Where F^0_{peak} is the peak force of a non-filled extrusion as calculated using equation 2.9, A_{Ef} is the foam core crush force efficiency, assumed to be 0.85. C_{max} is statistically determined to be 2.

The accuracy of the mean crush force prediction using equation 2.8 has been verified by Hanssen [30] using a large amount of experimental tests. Experiments have been performed on both empty and foam-filled square aluminium extrusions, and the accuracy turns out to be very high, as can be seen in figure 2.16.
The correlation between the predicted peak force of foam-filled columns and the experimental results is shown in figure 2.17. It can be seen that the scatter is larger than for the mean crush force prediction, but the predictive power is still strong enough.

Stroke efficiency

To fully understand the structural behaviour and calculate the energy absorption of extruded square crash boxes it is also necessary to have equations to calculate percentage of the original length that can be crushed. The stroke efficiency is estimated using a statistical constant that is different for aluminium and steel alloys.

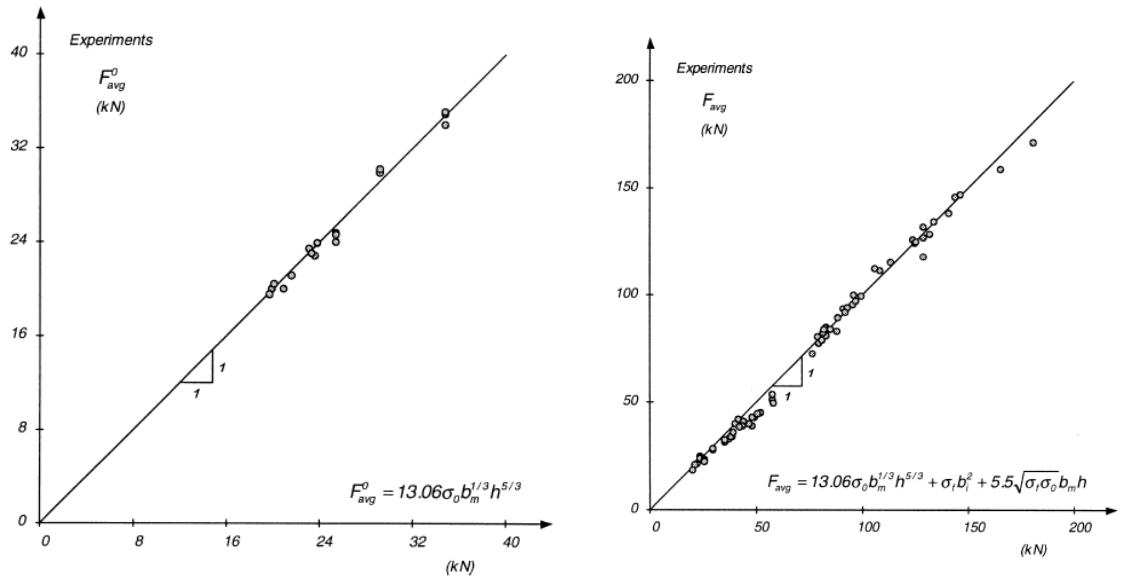

a) b)

Figure 2.16: Correlation between experimental and analytical results for a) empty square aluminium columns and b) foam-filled square aluminium columns [30]

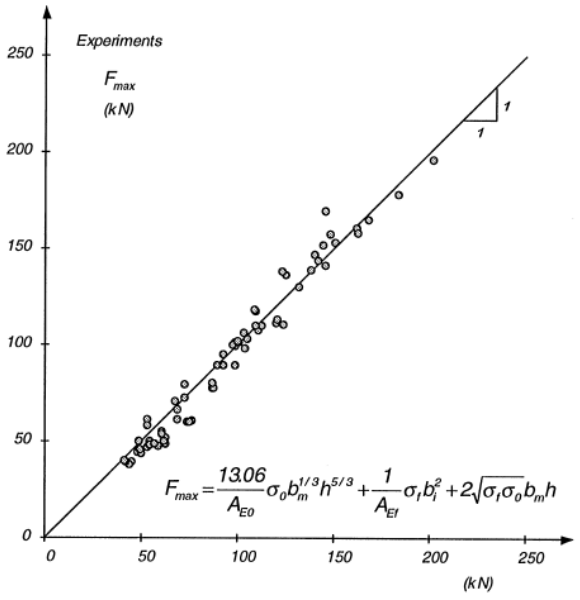

Figure 2.17: Correlation between predicted peak force of foam-filled columns and experimental results [30]

The stroke efficiency for steel alloys is estimated to be on average 64%, and the maximum deformation is calculated using equation 2.11 [71]. The stroke efficiency for aluminium alloys is estimated to be on average 76%, and the maximum deformation is calculated using equation 2.12 [30].

$$d_{max,steel} = 0.64 \times L_{cb} \tag{2.11}$$

$$d_{max,alu} = 0.76 \times L_{cb} \tag{2.12}$$

Where L_{cb} is the undeformed length of the crash box. If the crash boxes are filled with foam, the effective crushing length that can be achieved changes due to the interaction effect between the foam and metal. In order to calculate the effective crushing length of foam-filled crash boxes equation 2.13 can be used. This equation is a force-weighted average of the foam influenced stroke efficiency and the densification strain of the foam filler [30].

$$S_E = \frac{\left(F^0_{mean} + C_{avg}\sqrt{\sigma_f \sigma_0}bt\right) S^F_E + \left(\sigma_f b_i^2\right)\epsilon_D}{F_{mean}} \tag{2.13}$$

Where F^0_{mean} is the mean crushing force for the non-foam-filled extrusion as calculated using equation 2.8 without the second and third terms, C_{avg} is the interaction coefficient and is statistically estimated to be 2.5 in this equation. The foam-influenced stroke efficiency S^F_E can be calculated using equation 2.14 for steel alloy extrusions and equation 2.15 for aluminium alloy extrusions [30].

$$S^F_E = 0.64\left(1 - 1.7\left(\frac{\rho_f}{\rho_{f0}}\right)^{0.8}\right) \quad \text{for steel alloy extrusions} \tag{2.14}$$

$$S^F_E = 0.76\left(1 - 1.7\left(\frac{\rho_f}{\rho_{f0}}\right)^{0.8}\right) \quad \text{for aluminium alloy extrusions} \tag{2.15}$$

Where ρ_f is the density of the foam and ρ_{f0} is the full-solid density of the foam material, e.g. the density of the solid aluminium alloy the aluminium foam is made of. The densification strain of the foam filler can be calculated using equation 2.16.

$$\epsilon_D = 1 - 1.5\left[\frac{\rho_f}{\rho_{f0}}\right] \tag{2.16}$$

2.6.2. Folded double-hat section

When, instead of extrusion, metal folding is used as the manufacturing process, the final geometry of the crash boxes is also different. It is chosen to only consider a double-hat section for the closed cross-section crash boxes made by metal folding, as they perform relatively well with respect to energy absorption and analytical equations have been developed in literature that can be used to analyze the structural behaviour and energy absorption. Based on the super folding element method, the static mean crush force of the double-hat section can be calculated using equation 2.17 [71].

$$F_{mean} = 8.22\sigma_0 t^2 \left(\frac{B}{t}\right)^{1/3} \tag{2.17}$$

Where σ_0 is the flow stress as defined in section 2.6.1, t is the wall thickness, $B = 4(b+f)$ where b is the section width and f is the flange width.

2.6.3. Dynamic amplification factor

According to the research by Hanssen [30] a Dynamic Amplification Factor (DAF) should be applied to the equations for the crash box mean force as shown before to include the inertia effects and increase the accuracy when trying to predict dynamic tests. The dynamic amplification factor of the crash box can be calculated using equation 2.18.

$$\text{DAF} = C_{ine}\left(\frac{b_m}{t}\frac{\rho_0}{\sigma_0}v_0^2\right)^{1/2} \tag{2.18}$$

Where ρ_0 is the density of the crash box wall's material and v_0 is the impact velocity. C_{ine} is a constant that influences how much effect the dynamic amplification factor has, dependent on the ratio between the total deformation length of the crash box and the half natural lobe length H. This means that it is first necessary to calculate the static mean force and deformation, in order to iterate with these values to achieve the dynamic mean force and deformation. The development of C_{ine} as a function of d/H can be seen in figure 2.18.

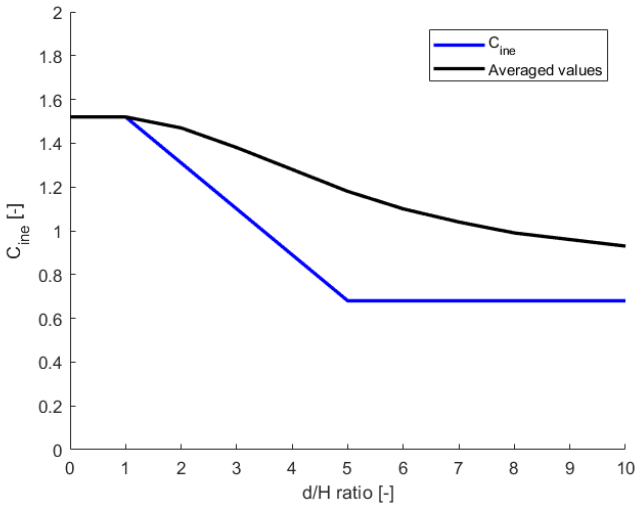

Figure 2.18: Influence of d/H on C_{ine}, adapted from [30]

This blue graph in figure 2.18 are the values for C_{ine} as determined by Hanssen, and can be used to calculate the ratio between the static and dynamic force at specific d/H value. In order to use this for the mean force, the values should be averaged over the deformation up to the total deformation. This is shown in the black graph. For easy implementation in the optimization model a trendline with $r = 0.9253$ is created and shown in equation 2.19.

$$C_{ine} = 0.0013\left(\frac{d}{H}\right)^3 - 0.017\left(\frac{d}{H}\right)^2 - 0.012\left(\frac{d}{H}\right) + 1.5 \tag{2.19}$$

The half natural lobe length H can be calculated using equation 2.20.

$$H = 0.99 b^{2/3} t^{1/3} \tag{2.20}$$

When the deformation d and the natural half lobe length H are known it is possible to calculate the constant C_{ine}. From equation 2.19 and 2.18, as well as figure 2.18, it can be seen that the dynamic amplification factor has a larger contribution to the applied force if the deformation of the crash box is small, decreasing approximately linearly until a d/H value of 5 is reached. From there on it stays constant. This is due to decreasing accelerations as a function of deformation, leading to reduced inertia effects [30].

The dynamic mean force on non-filled crash boxes can then be calculated using equation 2.21. It was found by Hanssen that the contribution of the foam to the mean force is not influenced by the dynamic impact, and therefore the dynamic mean force of foam-filled crash boxes can be calculated using equation 2.22.

$$F^D_{mean} = 13.06\sigma_0 b^{1/3} t^{5/3} [1 + \text{DAF}] \tag{2.21}$$

$$F^D_{mean} = 13.06\sigma_0 b^{1/3} t^{5/3} [1 + \text{DAF}] + \sigma_f b_i^2 + C_{avg}\sqrt{\sigma_f \sigma_0} bt \tag{2.22}$$

It should be noted that this dynamic amplification factor is only applicable for the calculation of the mean force. From the experimental test results presented in his paper it does seem like the peak force is also increased under dynamic impact conditions, but a methodology to estimate this effect has not been developed. This dynamic amplification factor is also not applicable to composite crash boxes, as it specifically includes the inertia effects of accelerating the sidewalls from the original shape into the lobes during progressive folding. Since composites display progressive crushing, this effect is not present.

3

Performance evaluation parameters

In this chapter the parameters that will be used to evaluate the performance of the rear low-speed crash structures candidate designs are presented. It will be shown how these parameters can be influenced by the design of the rear low-speed crash structures, and why they are important to take into account. There are two categories of parameters, the first one being the parameters that are derived directly from the design. These direct parameters are the weight, the initial cost, and the intrusion distance, as discussed in sections 3.1, 3.2 and 3.3 respectively. The second category of parameters is derived from the set of direct parameters and can therefore be seen as indirect parameters. These are necessary as they show the effect of the direct parameters on aspects of the vehicle that are important for either the manufacturer or the customer. These indirect parameters are energy efficiency, the amount of annual solar kilometers, trunk space, and total cost of ownership, as shown in sections 3.4, 3.5, 3.6, and 3.7 respectively. The method of integrating these different parameters into a performance evaluation function is explained in section 3.8.

3.1. Weight

The main vehicle parameter that can be influenced by the design of the rear low-speed crash structures is the weight. The weight of the candidate design is of high importance as it influences secondary parameters like energy efficiency, annual solar kilometers, total cost of ownership and sustainability. For example, reducing the vehicle weight with 1 kg will save 12.5 g CO_2 per 100 km driven for an average car [4]. It should also not be forgotten that an important aspect of lightweighting is the secondary weight reduction. This means that weight savings in a certain subsystem can decrease the amount of energy the vehicle needs to drive a certain distance, which results in a smaller battery capacity and thus a lower battery weight for the same range. The engine power can also be decreased while keeping the same acceleration, improving the energy efficiency (reducing the necessary battery capacity) and decreasing the weight even more (although a second iteration of the lightweight cycle is not performed in this optimization model).

Saving weight on a structural design often means either using more expensive materials or more expensive processes. The amount of money that can be spent per kilogram of weight saved depends mainly on the type of vehicle (Internal Combustion Engine (ICE), Battery Electric Vehicle (BEV)) but also on the segment (small car to luxury vehicle) that is intended. For an ICE vehicle the accepted cost per kg saved per vehicle that is manufactured is between 3 €/kg for a small car to 10 €/kg for a luxury vehicle. This can for example be spent on more expensive materials with improved structural properties, or on more expensive manufacturing processes that can be used to realize weight savings.

For a BEV this cost ranges from between 5 and 8 €/kg for a small car to between 10 and 20 €/kg for a luxury vehicle, depending on the price of batteries per kWh [1]. This additional cost is justified by both the energy efficiency effect and the secondary weight savings, as cost is saved compared to the heavier design, because for example a smaller and therefore cheaper battery can be used. This influence of weight savings on energy efficiency is incorporated in the value of energy efficiency as outlined in section 3.4, so for the value of weight

[1] `https://www.mckinsey.com/~/media/mckinsey/dotcom/client_service/automotive%20and%20assembly/pdfs/lightweight_heavy_impact.ashx`, accessed on 14-06-2019

saving no distinction needs to be made between ICE and BEV.

The weight of the rear low-speed crash structures is highly dependent on both the material that is chosen, through its density and material properties, and on the geometry through the amount of material that is used. Due to the direct effect of the design of the low-speed crash structures on the weight of the crash rails, the weight of the crash rails is also estimated and included in the weight of the design. This methodology is shown in section 5.5.2. In the evaluation of the performance of the candidate design the additional value of weight saving for BEVs is calculated through the secondary effects of energy efficiency, annual solar kilometers and total cost of ownership. This indirect value of weight saving comes on top of the direct value of weigh saving as outlined in this section.

The desired direct value for weight savings w_3 should be multiplied with the difference between a baseline weight and the weight of the candidate design. The baseline weight of the low-speed crash structures and crash rails are inputs of the model, as they do not influence which candidate design is preferred but rather shifts the performance evaluation towards this baseline. The baseline weight of the low-speed crash structures as well as the crash rails can be estimated by using for example the current situation or the weight budget that is assigned to them during the design phase.

3.2. Purchase price

The purchase price of the vehicle is one of the first aspects that is considered by potential customers. In a study by Deloitte 84% of respondents mentioned the purchase price of the vehicle having a high importance in their decision which vehicle to buy [2]. This makes sense, as the purchase price determines if the customer is able to buy it, or, if a loan is necessary, how high the monthly payments will be. The purchase price is a combination of the cost for the OEM (Original Equipment Manufacturer) to manufacture and sell the vehicle, plus a profit margin. This means that a reduced manufacturing cost could lead to increased profit margins, if the purchase price of the vehicle is fixed.

The design of the rear low-speed crash structures has only a small influence on the total manufacturing cost of the complete vehicle, as it is only one of the many subsystems in the car. Setting the absolute upper limit of the manufacturing cost of the rear low-speed crash structures for high-volume cars to €50 would be very conservative. This would correspond to a maximum of 0.25% of the total cost for a €20,000 vehicle. The cost of the rear low-speed crash structures consists of material cost, manufacturing cost and assembly cost. In order to estimate this for the different candidate designs, a simple cost model is developed in section 6.

Instead of using the target purchase price of the vehicle to represent the complete picture in the performance evaluation, only the cost of the low-speed crash structures is used and compared to a baseline cost. This baseline cost is an input for the model, as it does not influence which candidate design is preferred but only shifts the performance evaluation towards the baseline. The standard value for baseline manufacturing cost of the low-speed rear crash structures can be determined in such a way that it reflects for example the cost budget during the design phase or the actual situation in case of a redesign.

3.3. Intrusion distance

The intrusion distance is defined as the maximum distance that an impactor enters the vehicle during the most critical low-speed load case. This distance should be seen as defining for the area at the rear of the vehicle where damage is expected to occur during low-speed rear impact. Based on the requirements given by the RCAR guidelines, as shown in section 5.1, this means that only parts that are easy and cheap to replace should be present in this area.

When assuming the outer dimensions of the vehicle are fixed, the intrusion distance defines how far backwards the interior trunk space can extend. In the case of an SEV it also defines how far backwards the solar cells can be placed without being damaged during a rear low-speed impact. In fact, this has a rather large effect as can be seen from the following calculations, when taking the Lightyear One as example. The width

[2] `https://www2.deloitte.com/content/dam/Deloitte/in/Documents/manufacturing/in-mfg-dtcm-steps-in-the-buying-process-noexp.pdf`, accessed on 12-6-2019

of the rearmost point of the tailgate is 1.2 meters, so being able to extend the solar array with another 5 centimeters would lead to an additional 0.06 m^2 of solar area. Assuming a baseline area of 5 m^2, this means that decreasing the intrusion distance by 5 cm increases the available area for solar cells by 1.2% while the outer dimensions of the vehicle stay the same. If 5 m^2 of solar area results in 8,750 annual solar kilometers in Amsterdam, adding 0.06 m^2 of solar area provides an additional 105 annual solar kilometers. As a comparison, it is found that a weight saving of around 45 kg is necessary to provide the same amount of annual solar kilometers through improved energy efficiency. The influence of the intrusion distance on the size of the solar array, which is used to calculate the annual solar kilometers can be seen in equation 3.13.

It is possible to influence the intrusion distance with the design of the rear low-speed crash structures. On the one hand this can be done by positioning the subsystem as far backwards as possible, but this is a matter of packaging and considered out of scope of this thesis. However, it is attempted to show the importance of the location of the rear low-speed crash structures with respect to the outer dimensions of the vehicle. A second method to limit the intrusion distance is to use a higher average sustained load on the energy-absorbing elements, leading to higher accelerations of the vehicle in order to absorb the impact energy in a smaller distance. This has a negative effect on the weight of the crash rails, as their strength needs to increase to ensure that they do not get damaged by the increased force during a low-speed crash. The methodology to calculate the weight penalty of the crash rails is explained in section 5.5.2. This also shows the importance of having the peak force during low-speed impact as low as possible w.r.t. the mean force.

The intrusion distance is an output from the structural analysis of the load cases, and is used to calculate the deviation from the baseline of the amount of annual solar kilometers. The baseline annual solar kilometers is calculated using the baseline intrusion distance, which is an input to the model.

3.4. Energy efficiency

The energy efficiency of a vehicle can be defined as the amount of Wh it needs to drive a single kilometer. This value is determined by a standard drivecycle. Since September 2017 the Worldwide Harmonised Light Vehicle Test Procedure (WLTP) is used. A graphical representation of this drivecycle is shown in figure 3.1. Energy efficiency is important to take into account during this thesis as it influences the following factors:

- Environmental impact of driving the vehicle
- Energy cost portion of Total Cost of Ownership
- Battery capacity of the vehicle, assuming fixed range (BEV & SEV only)
- Amount of charging infrastructure needed (BEV & SEV only)
- Charging rate in km/h, assuming a fixed power (BEV & SEV only)
- Amount of annual solar kilometers (for SEV only)

From the factors mentioned here the amount of charging infrastructure needed and the charging rate in km/h assuming a fixed power are not taken into account in the performance evaluation. These are seen as external to the engineering of the vehicle and therefore considered outside the scope of this thesis. It can be seen that the energy efficiency of the vehicle has a large importance, even more so for an SEV due to the addition of the annual solar kilometers parameter. The design of the rear low-speed crash structures can influence the energy efficiency of the complete vehicle through the weight of the design. Weight influences the energy efficiency in two different ways, as explained in the following paragraphs.

Rolling resistance

The first way how the vehicle weight can influence the energy efficiency is through rolling resistance. The rolling resistance of the vehicle's tires is expressed through the dimensionless constant c_{rr}. This value depends on the tire, and a large difference between them is found. According to the Transportation Research Board the measured values for the coefficient of rolling resistance in 2002 were found to be between 0.0062 and 0.0133, with an average of 0.0102 [3]. When this coefficient is known, the rolling resistance of the vehicle

[3] `http://onlinepubs.trb.org/onlinepubs/sr/sr286.pdf`, accessed on 17/07/2019

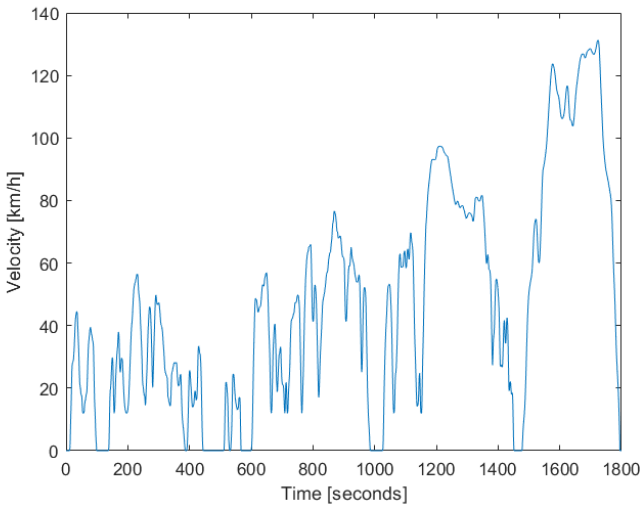

Figure 3.1: WLTP drivecycle class 3b

can be calculated using equation 3.1.

$$F_{roll} = m \times g \times c_{rr} \tag{3.1}$$

Where $m = m_{vehicle}+25kg+0.15m_{payload}$ (in which $m_{payload}$ is the maximum payload weight that is allowed in the vehicle) and g is the gravitational constant. From equation 3.1 it can be seen that the frictional force due to rolling resistance is directly related to the weight of the vehicle.

Braking energy

When driving a car it is also often necessary to decelerate the vehicle using the brakes, as can be seen from the WLTP drivecycle in figure 3.1. This will transform the kinetic energy of the vehicle into heat in order to slow down, meaning this energy is wasted. For an average vehicle around 27% of the total energy supplied to the wheels is lost (turned into heat) due to slowing down the vehicle using the brakes. This is different for BEVs, as they are able to recuperate energy through regenerative braking. The efficiency of regenerative braking is 63% on average, meaning that 63% of the energy that normally would be lost by braking can be recovered [10].

MatLab model to calculate energy efficiency

The energy efficiency depends on many different variables, and is not linear further away from the design point. With the goal of making the optimization model as general as possible, it is chosen to create a simple MatLab model to calculate the energy efficiency of candidate designs compared to the baseline. This model takes the following inputs:

- $A_{frontal}$, the frontal area of the vehicle
- C_d, the drag coefficient of the vehicle
- c_{rr}, the rolling resistance coefficient of the tires
- η_{pt}, the powertrain efficiency
- η_{regen}, the regenerative braking efficiency
- P_{aux}, the auxiliary power
- $I_{vehicle}$, the inertia of the vehicle
- $m_{vehicle}$, the mass of the vehicle
- $m_{payload}$, the mass of the payload
- ρ, the density of air at 17C, 1.22323 kg/m^3
- g, the gravitional constant 9.81 m/s^2

With these inputs and the WLTP drivecycle with one datapoint every second, and the velocity in m/s, the acceleration, forces due to acceleration, aerodynamic forces, rolling resistance forces and total forces can be calculated using equations 3.2 to 3.6. These are calculated for every timestep i.

$$a(i) = v(i+1) - v(i) \tag{3.2}$$

$$F_a(i) = m \times a(i) \times (1 + I_{vehicle}) \tag{3.3}$$

$$F_{aero}(i) = 0.5 \times \rho \times C_d \times A_{frontal} \times v(i)^2 \tag{3.4}$$

$$F_{roll}(i) = m \times g \times c_{rr} \tag{3.5}$$

$$F_{total}(i) = F_a(i) + F_{aero}(i) + F_{roll}(i) \tag{3.6}$$

Now that all the forces have been calculated for each timestep, the motor power at each timestep can be calculated using equation 3.7.

$$P_{motor}(i) = F_{total}(i) \times v(i) \tag{3.7}$$

The power at the motor should now be used to calculate the power at the battery for a BEV, as this is where the energy comes from. If the power at the motor is positive the powertrain efficiency should be used, but when the power at the motor is negative the regenerative braking efficiency should be used. For an ICE vehicle, the powertrain efficiency creating propulsion from the fuel should be used (there is no regenerative braking for most ICE vehicles). The auxilary power draw should also be included. All of this can be seen in equations 3.8 and 3.9.

$$P_{battery}(i) = \frac{P_{motor}(i)}{\eta_{pt}} + P_{aux} \quad \text{(if motor power is} \geq 0) \tag{3.8}$$

$$P_{battery}(i) = P_{motor} \times \eta_{regen} + P_{aux} \quad \text{(if motor power is} < 0) \tag{3.9}$$

Now that the power at the energy storage is known at every timestep, the total energy in Joules that is used can be calculated by taking the sum of the battery power at each timestep, as each timestep is one second. This is in this case equal to integrating the total power over the total time of the drivecycle. In order to get the total energy in Wh, the value in Joules should be divided by 3600. The energy efficiency in Wh/km can now be calculated using equation 3.10.

$$\text{Energy Efficiency [Wh/km]} = \frac{\int_0^{1800} P_{battery}\, dt \,/3600}{\text{total distance}} \tag{3.10}$$

Where the total distance of the WLTP drivecycle is 23.26 km.

Value of energy efficiency

The main value of energy efficiency is from the increased performance in other aspects that are derived from it. These other aspects are different for different types of cars. When considering an ICE, the main value of energy efficiency can be seen in a reduced amount of fuel used during the lifetime of the vehicle, which is represented in TCO through fuel cost reduction and pollution cost reduction.

When considering a BEV the value of using a reduced amount of kWh of electricity is less than for an ICE vehicle, as electricity is cheaper and has lower pollution cost per kilometer driven. The main value of energy efficiency for a BEV comes from increased range with a fixed battery capacity, or less battery capacity needed with a fixed range. When making the assumption that the range of the vehicle should stay equal, it can be calculated how much the capacity in kWh of the battery can be reduced. Multiplying this reduction with the estimated cost per kWh of battery capacity (157 EUR/kWh[4]) gives the first part of the value. A reduction of the battery capacity also means that the weight will go down, having a value through the lightweighting cost as explained in section 3.1. The specific energy of the battery is estimated to be 0.2 kWh/kg. A second iteration of the lightweighting cycle will not be performed. For a BEV the value of increased (or decreased) energy efficiency can be calculated using equation 3.11.

$$C_{eff} = -\left[E_{batt} - \left(\frac{\text{Energy Efficiency Design}}{\text{Energy Efficiency Baseline}}\right) E_{batt}\right] \times \left(€157 + \frac{1}{0.2 kWh/kg}\, w_3\right) \tag{3.11}$$

[4] https://about.bnef.com/blog/behind-scenes-take-lithium-ion-battery-prices/, accessed on 17/07/2019

Where w_3 is the lightweighting value as defined in section 3.1. For an SEV both factors that are taken into account for BEVs should also be taken into account. The baseline energy efficiency is found by using model input vehicle weight, while the energy efficiency of the candidate design is calculated using the input vehicle weight, minus the baseline weight of the low-speed crash structures and crash rails, plus the weight of the candidate design (including the crash rails). Additionally there is the increase of annual solar kilometers. This is valued according to section 3.5, and as part of the TCO in section 3.7 due to reduced charging and pollution cost.

3.5. Annual Solar Kilometers

The amount of annual solar kilometers that the vehicle can drive is specific to SEVs only, and this parameter should not be used to assess the performance of conventional vehicles. This parameter is defined as the amount of kilometers that can be driven by the vehicle, based on the energy efficiency from the WLTP cycle as defined earlier, purely on the energy harvested by the vehicle's solar cells in one calendar year. This value will be different for every location on earth, due to differences in the annual solar irradiation, but Amsterdam is taken as the baseline. Amsterdam does not have a very sunny climate, but the calculation of the additional value of SKM (on top of the reduction of charging costs, considered in TCO) is later in this section shown to be independent of the location that is chosen as a baseline. As a comparison between different climates, the annual solar irradiation and target SKM for the Lightyear One is shown in table 3.1 for a few different cities [5].

Table 3.1: Overview of annual solar irradiation and target SKM for Lightyear One for different climates

Location	**Annual Solar Irradiation [kWh/m2]**	**Target SKM Lightyear One [km]**
Amsterdam	1,040	8,750
Rome	1,686	14,185
Madrid	2,028	17,063
Los Angeles	2,329	19,595

It is of high importance to get the amount of annual solar kilometers as high as possible, because this means the highest amount of kilometers driven on clean energy is provided. It also means that the vehicle has less dependence on the existing energy grid as it does not have to be charged as often resulting in more convenience for the driver, but also in less strain on the charging infrastructure. It is also important for Lightyear as a company to provide proof that the concept of putting solar cells on top of a car actually works and is useful in practice.

In order to calculate the amount of annual solar kilometers first a baseline of the current situation is needed. This baseline consists of the area of solar cells, efficiency of the solar cells, annual solar irradiance and shadow correction factor of the target vehicle. On the other side, the energy efficiency of the target vehicle is needed to calculate the amount of annual solar kilometers from the amount of energy that is generated yearly. This can be calculated using equation 3.12. From this baseline situation, the area of solar cells can be influenced by the design of the rear low-speed crash structures through the intrusion distance and the energy efficiency through the weight of the vehicle.

$$SKM = \frac{kWh \text{ generated per year}}{kWh \text{ needed per km}} = \frac{A \times E_{solar} \times \eta_{cell} \times \eta_{conversion} \times \eta_{shadow}}{\text{Energy Efficiency}} \tag{3.12}$$

Where A is the area of solar cells in m^2, E_{solar} is the annual solar irradiation in kWh/m^2, η_{cell} is the dimensionless solar cell efficiency, $\eta_{conversion}$ is the conversion efficiency of energy harvested by the solar cell to energy stored in the battery, η_{shadow} is the dimensionless shadow correction factor, and Energy Efficiency is the amount of kWh needed per km driven according to the WLTP cycle. The only parameters that can be influenced by the design of the rear low-speed crash structures are the area of the solar cells and the energy efficiency. The area of solar cells corresponding to a candidate design will be calculated based on the intrusion distance, and the energy efficiency based on the weight. The fixed values that are used for the other parameters can be found in table 3.2.

[5] `globalsolaratlas.info`, accessed on 29/01/2020

Table 3.2: Values used for fixed parameters in the calculation in the amount of annual solar kilometers

Parameter	Value
E_{solar}	1040 $[kWh/m^2]$
η_{cell}	[redacted] [-]
η_{shadow}	[redacted] [-]

The value for annual solar radiation is chosen to be 1040 kWh/m^2 as this is the average value for Amsterdam, the value for solar cell efficiency is [redacted] as the actual solar cells that will be used on the Lightyear One have an efficiency of [redacted]%, and the shadow correction factor is estimated by Lightyear to be [redacted] which would mean that [redacted]% of the available energy is not harvested due to the curvature of the roof and shadows on the car because of trees and buildings.

The change in area of the solar array due to the intrusion distance corresponding to the candidate design can be calculated using equation 3.13.

$$A_{solar} = A_{solar,baseline} - (\delta - \delta_{baseline})\, w_{array} \tag{3.13}$$

Where $A_{solar,baseline}$ is an input parameter, $\delta_{baseline}$ is the intrusion distance corresponding to the baseline design of the rear low-speed crash structures, and w_{array} is the width of the solar array at the rearmost point of the vehicle (also an input). From here, the difference in annual solar kilometers with respect to the baseline can be calculated using equation 3.14.

$$\delta_{SKM} = \frac{A_{solar} \times E_{solar} \times \eta_{cell} \times \eta_{conversion} \times \eta_{shadow}}{\text{Energy Efficiency Design}} - \frac{A_{baseline} \times E_{solar} \times \eta_{cell} \times \eta_{conversion} \times \eta_{shadow}}{\text{Energy Efficiency Baseline}} \tag{3.14}$$

How to value annual solar kilometers

Two distinct methods have been developed for putting a value on the amount of annual solar kilometers, both having their strong points and specific situations in which they can be used. They can also be used simultaneously, and their weights can be adapted using the weight factors defined in section 3.8. The first method is using a value based on the design point of the car and can be found in equation 3.15.

$$\text{Value of SKM} = \frac{\text{MSRP}}{SKM} = \frac{€50,000}{8,750} = €5.71 \tag{3.15}$$

Where MSRP stands for Manufacturer Suggested Retail Price. The annual amount of solar kilometers is used in this calculation instead of the amount over the entire expected lifetime of the vehicle, as this provides a better frame of reference for the customer. This does not have an influence on the results. It is understood that this value is an overestimation of the actual real-world value, but this can be explained by Lightyear having to prove the concept of an SEV first. However, this value is useful for design trade-offs across the entire vehicle as it is desired to maximize the amount of annual solar kilometers to prove the SEV concept.

The second method consists of including the annual SKM in the calculation of the TCO. By doing this the charging cost are reduced, but also the cost of the pollution caused by generating the electricity is reduced to zero. This is shown, along with additional explanation, in equation 3.21.

3.6. Trunk space

The amount of trunk space that is available in the vehicle can be directly influenced by the design of the rear low-speed crash structures. The outer edge of the trunk space, generally bounded by the rear closing panel of the body-in-white, should not be damaged during any of the RCAR load cases. This means that if the intrusion distance is reduced by for example 50 mm, the longitudinal dimension of the trunk can be extended by 50 mm. This is valid for all types of vehicles that are considered during this thesis.

It is important to include the value of trunk space in the performance evaluation of the candidate design for multiple reasons. Firstly, an increase of trunk space provides actual value to the customer that buys the vehicle as it increases the utility. Secondly, it is one of the main reasons why car manufacturers do not use very long low-speed crash structures. The other reasons being more length available for the crash rails, leading to improved safety in high-speed impact, and less damage to surrounding parts such as the tailgate and lighting modules. These last two reasons are however very difficult to capture in numbers and will probably be very different between vehicles.

The value of the amount of trunk space can be calculated using equation 3.16. This equation uses the difference in intrusion distance in mm between the baseline design and the current design, and multiplies that difference with the weight factor w_8. The value of this weight factor should represent the value in euros for one additional mm of longitudinal trunk space. A minus is placed in front of the weight factor to ensure that an increased trunk space leads to a lower cost, and thus a higher value. It is explicitly kept variable to allow the model to work for different importance of trunk space, but an estimation needs to be made for this value in order to compare the output of this model with benchmarked vehicles, or to generate the results for the design of the LY01.

$$C_{trunk} = -w_8 \times (\delta_{baseline} - \delta) \tag{3.16}$$

The value of w_8 will vary between different vehicles. Similarly to the value for weight saving, that is dependent on the 'class' of the vehicle, a cheap vehicle should have a lower value of trunk space than a luxury vehicle. It can also change depending on the opinion of the OEM on how important this trunk space is exactly. To estimate the value of trunk space for different vehicles during this thesis, the value for w_8 is estimated using equation 3.17.

$$w_8 = 0.003\sqrt{\text{MSRP}} \tag{3.17}$$

Where MSRP is the Manufacturer Suggested Retail Price. The MSRP of the base version of the vehicle is taken, for the USA. This is done to eliminate the influence of BPM (Belasting van Personenauto's en Motorrijwielen) that is present in The Netherlands and is not representative for the retail price in European or global markets. It is chosen to scale the value of trunk space with the square root of MSRP to ensure that the increase of the value of w_8 levels off with increasing MSRP. This is also similar to the value for weight saving. When considering a vehicle with an MSRP of €20,000, this leads to a value for w_8 of €0.4472/kg. For a vehicle with an MSRP of €60,000, this leads to w_8 = €0.7746/kg.

This means that increasing the longitudinal trunk space with 50 mm results in an increased value of trunk space of €22.36 for a vehicle with an MSRP of €20,000. For a vehicle with an MSPR of €60,000 the increase in value of trunk space is €37.73. When comparing this to the influence of the intrusion distance on the value due to annual solar kilometers (assuming the width of the solar array to be 1200 mm), it is found that the value of trunk space is similar (10% difference) for the €60,000 vehicle if only the energy cost and sustainability cost is taken into account. When including the additional value of solar kilometers as is done for the Lightyear One, the value due to annual solar kilometers is ~20 times higher than the value of trunk space for the €60,000 vehicle, and ~35 times higher for the €20,000 vehicle.

It should be noted that it is possible that there are additional reasons for a car manufacturer to value trunk space higher than expected. One of these reasons could be that spending additional effort and/or weight budget on reducing the intrusion distance can allow for the spare wheel to fit inside the trunk. Other reasons could be that with just a few centimeters extra a standard sized bike or skis can fit inside. Based on this it can be concluded that the value of trunk space does not increase linearly with the longitudinal length of the trunk, but rather has large increases at distinct locations corresponding to certain specific items that can fit, with a slower increase in between these locations. However, since these things are very specific and dependent on the exact packaging of the vehicle as well as the wishes of the OEM, it is not possible to include this behaviour in such a general optimization model. It is therefore decided to approximate this using the linear approach as shown above.

3.7. Total Cost of Ownership

Total Cost of Ownership is an estimation of both the direct and indirect cost related to the ownership of a product. In the case of a car this means that instead of looking at the initial purchase price of the vehicle, the expected depreciation cost, fuel cost, insurance cost, maintenance cost and fees and taxes are taken into account. To make the concept of TCO even more complete, instead of only the cost for the consumer, also social- and environmental costs such as pollution can be included.

The concept of TCO is becoming more important due to the rise in popularity of electric vehicles, as their initial purchase price is higher than similar conventional vehicles but due to their lower energy consumption and expected maintenance cost, this initial cost difference can be offset over the long run. For an SEV this is even more important, as here an additional investment is made in the solar arrays, increasing the initial purchase price, that will only pay off over time. This means that manufacturers of electric vehicles are switching the narrative towards TCO. Including the environmental cost in TCO during this thesis is also important, as Lightyear aims to provide clean mobility. This will be done in such a way that it can also be chosen to not include these environmental costs, making sure the model can also represent the decision-making framework used by OEMs for conventional vehicles where less (or no) emphasis is placed on sustainability.

As TCO is heavily dependent on the vehicle owner's behaviour it is necessary to define some assumptions that roughly represent an average vehicle owner. These assumptions are listed below:

- 12,009 km driven per year (2015 EU average [6])
- 10 years ownership of vehicle (Close to the Italian average, [61])

Depreciation cost

Depreciation of the vehicle means the amount of value that is lost over the lifetime or ownership duration of the vehicle. A car holds residual value after using it for a few years, and this value should be subtracted from TCO. It is assumed that the depreciation of the vehicle can be described with an exponential function, effectively reducing the value of the vehicle with the same percentage each year. It has been found that the depreciation rate is different for different types of vehicles, as can be seen in table 3.3. It should be mentioned that the depreciation rate of BEVs is much less well-established as the market for second hand electric vehicles is still very limited [17].

Table 3.3: Depreciation rate pear year for different vehicle technologies [17]

Technology	Depreciation rate
Petrol	0.845
Diesel	0.827
BEV	0.786

The method to calculate the total depreciation over the assumed lifetime of the vehicle, according to the depreciation rates found in table 3.3, can be found in equation 3.18. It can be seen that the design of the rear low-speed crash structures only affects the initial purchase price part of this equation.

$$C_{depr} = (C_{design} - C_{baseline}) \times \left[1 - r_{depr}^{10}\right] \tag{3.18}$$

where C_{depr} is the total cost due to depreciation, C_{design} is the manufacturing cost of the candidate design, and r_{depr} is the yearly depreciation rate as shown in table 3.3.

Fuel cost

The fuel cost portion of TCO depends on the energy efficiency of the vehicle, but also the type of fuel that is used. The design of the rear low-speed crash structures can only affect the energy efficiency. How the fuel cost portion of TCO is calculated can be seen in equation 3.19.

$$C_{fuel} = \big(10 \text{ years} \times 12.009 \text{ km per year} \times (\text{Energy Efficiency Design - Energy Efficiency Baseline})\big) \times \frac{€}{MJ} \tag{3.19}$$

[6] https://www.odyssee-mure.eu/publications/efficiency-by-sector/transport/distance-travelled-by-car.html, accessedon26/08/2019

where the energy efficiency should be in MJ/km. The term €/MJ depends on whether an ICE or BEV is considered. Gasoline contains 33.7 MJ/liter, and the price per liter is €1,741 [7] in The Netherlands. This results in a gasoline price of €0.0517 per MJ. Diesel contains 36.9 MJ/liter, and the price per liter is €1,458 [6], resulting in a diesel price of €0.0395 per MJ. For electricity as fuel the assumption is made that charging is done at public charging stations (not fast chargers), which gives a price of roughly €0.35 per kWh in The Netherlands. This results in an electricity price of €0.097 per MJ. An overview of these values can be found in table 3.4.

Table 3.4: Fuel cost parameters

Fuel type	**Energy content**	**Cost**	**Cost [€/MJ]**
Electricity	3.6 MJ/kWh	0.35 €/kWh	0.097
Gasoline	33.7 MJ/L	1.741 €/L	0.0517
Diesel	36.9 MJ/L	1.458 €/L	0.0395

These values for the cost per MJ of energy are then implemented in equation 3.19, together with the energy efficiency of the vehicle as determined in section 3.4, to find the contribution of fuel cost in the total cost of ownership.

Environmental cost during operation

For vehicles the environmental effects can be split in three distinct phases. The first phase is the manufacturing of the vehicle through energy use for primary material production and manufacturing processes, the second phase is the operation of the vehicle where the amount of energy used depends on the energy efficiency of the vehicle, and the third phase is the end-of-life or disposal of the vehicle. For TCO only the operation of the vehicle is considered. Including environmental effects and sustainability in this thesis is important, as Lightyear's mission is to provide clean & affordable mobility. This means that pollution should be priced in, in order to effectively work towards the mission.

Even vehicles driving completely on electricity still have an effect on the environment through pollution, as not all electricity is generated in a fully sustainable way. In fact, the amount of CO_2 produced per kWh of electricity varies heavily in the European Union. A brief overview of the EU average and some selected countries is shown in table 3.5, data based on European Environment Agency [8].

Table 3.5: CO_2 emission intensity of public electricity production for selected European countries in 2016

Country	**Emission intensity [g CO_2/kWh]**
EU average	295.8
Netherlands	505.2
Germany	440.8
France	58.5
Spain	265.4
Italy	256.2

From table 3.5 it can be seen that there are large differences between countries, with France being far below average due to their widespread use of nuclear power generation, and The Netherlands being far above the average (as in 2016 only 6.0% of power generation was done using renewable sources, compared to 39.0% in Spain). For this thesis it is chosen to use the average EU emission intensity in 2016, as this is also the market for the Lightyear One.

Next to the pollution of greenhouse gasses like CO_2, NO_2 and CH_4, there are also local pollutants like NO_x, SO_x and Particulate Matter. Although an electric vehicle does not have any exhaust pollution, there is pollution where the electricity is generated. Rusich [61] has provided emission values for both greenhouse gasses and local pollutants based on the Italian situation in 2011. Assuming that the relative composition of the

[7] Gemiddelde Landelijke Adviesprijs, `www.nu.nl/brandstof`, accessed on 20/06/2019

[8] `https://www.eea.europa.eu/data-and-maps/indicators/overview-of-the-electricity-production-2/assessment-4`, accesed on 12-6-2019

pollutants stays the same, it is possible to scale the emissions (with a factor 0.93) to represent the EU average in 2016. The results of this are shown in table 3.6.

Table 3.6: Overview of environmental cost per MJ of electricity used for driving a BEV, adapted from Rusich [61]

Pollutant	**Emission Italy 2011 [g/MJ]**	**Emission EU 2016 [g/MJ]**	**Environmental cost [€/g]**	**Environmental cost per MJ [€/MJ]**
NO_x	0.0724	0.0674	0.01	0.000674
SO_x	0.0790	0.0735	0.01	0.000735
PM_{rural}	0.0022	0.0020	0.12	0.00020
PM_{urban}	0	0	0.21	0
GHG	34.6	32.2	0.000093	0.003
Total	-	-	-	0.0046

From table 3.6 it can be seen that there is no environmental cost associated with particulate matter in urban or metropolitan areas, as an electric vehicle has no local pollution. The values for the greenhouse gasses do not correspond completely to the data from table 3.5, because the greenhouse gasses NO_2 and CH_4 are also included in this as well as an estimation of energy losses from transferring the energy from the powerplant to the vehicle. Taking all of this into account, it can be seen that the environmental cost per MJ of electricity used in a BEV according to the European average in 2016 is €0.0046, or 0.46 eurocent. This value can be used for pricing in environmental effects due to differences in energy efficiency.

The environmental cost of using gasoline to power the vehicle can also be calculated. The environmental cost per MJ of energy used in an ICE vehicle is shown in table 3.7.

Table 3.7: Overview of environmental cost per MJ of gasoline used for driving an ICE, adapted from [61]

Pollutant	**Emission Italy 2011 [g/MJ]**	**Environmental cost [€/g]**	**Environmental cost per MJ [€/MJ]**
NO_x	0.0603	0.01	0.000603
SO_x	0.0551	0.01	0.000551
PM_{rural}	0.00071	0.12	0.0000852
PM_{urban}	0.00313	0.21	0.000657
GHG	77.73	0.000093	0.0072
Total	-	-	0.0091

Data has also been found to calculate the environmental cost of using diesel to power the vehicle. This data is shown in table 3.8.

Table 3.8: Overview of environmental cost per MJ of diesel used for driving an ICE, adapted from [61]

Pollutant	**Emission Italy 2011 [g/MJ]**	**Environmental cost [€/g]**	**Environmental cost per MJ [€/MJ]**
NO_x	0.1202	0.01	0.001202
SO_x	0.049	0.01	0.00049
PM_{rural}	0.0006	0.12	0.000072
PM_{urban}	0.0029	0.21	0.000609
GHG	73.32	0.000093	0.0068
Total	-	-	0.0092

It is interesting to note that the environmental cost per MJ of energy while driving a gasoline or diesel car is around 2 times higher than while driving a BEV, but the average BEV can drive 1.96 km per MJ while the average gasoline ICE can only drive 0.434 km per MJ and the average diesel ICE 0.505 km per MJ (Rusich 2015). When considering these average efficiencies, the environmental cost for a BEV is 0.0023 €/km and for a gasoline car the environmental cost is 0.021 €/km, which is 9.13 times higher. For a diesel vehicle the environmental cost is 0.0182 €/km, which is 7.91 times higher. The environmental cost portion of TCO can be calculated using equation 3.20.

$$C_{environmental} = (10 \text{ years} \times 12.009 \text{ km per year} \times (\text{ Energy Efficiency Design - Energy Efficiency Baseline})) \times \frac{€}{MJ} \tag{3.20}$$

where energy efficiency should be in MJ/km and the term $€/MJ$ depends on the type of fuel and can be found in either table 3.6, 3.7 or 3.8.

Including annual solar kilometers

When the optimization model is running for an SEV, the amount of annual solar kilometers should be included in the TCO. This can be done by calculating the total amount of solar kilometers over the expected lifetime of 10 years and multiplying that by the energy efficiency of the vehicle, resulting in the total amount of energy in MJ that is generated during the lifetime. It is then calculated what the cost would be when charging the vehicle for this amount of energy, as well as what the environmental costs are of generating this energy with the 2016 EU average. How this is calculated can be seen in equation 3.21.

$$C_{SKM} = -10 \times \delta_{SKM} \times \text{Energy Efficiency Design} \times (€ \text{ charging cost per MJ} + € \text{ environmental cost per MJ}) \tag{3.21}$$

Estimating the charging cost per MJ at €0.097 (calculated from the price of public charging in The Netherlands of €0.35 per kWh in 2016 [9]) and the environmental cost per MJ at €0.0046 (as found in table 3.6, it is found that the value of one annual solar kilometer is approximately equal to €0.37 when the energy efficiency of the vehicle is 100 Wh/km. If the assumption is made that charging will only be done at home, this reduces the price per kWh to €0.22, the value of one annual solar kilometer is approximately equal to €0.24 when the energy efficiency of the vehicle is 100 Wh/km. This would be a conservative lower limit of the value of one annual solar kilometer, as the lowest value in the cost range for electricity is used and The Netherlands is used as location to calculate the amount of energy harvested. This value also does not include the convenience of the car charging itself and the relative independence from the grid, as this is included in the additional value of SKM as determined in section 3.5.

Maintenance, repair and insurance cost

An additional factor in the TCO of owning a vehicle is the maintenance, and repair and insurance cost. However, these are not taken into account during this thesis, and this section will provide the explanation of why that is the case.

Maintenance cost is not taken into account as it is not influenced by the design of the rear low-speed crash structures. Maintenance consists of the repair of parts of the vehicle that break down due to normal use, such as filters, tyres or drivetrain components. The low-speed rear crash structures only need to be repaired (or changed for new ones) in case of a collision event, which means that this should not be considered maintenance. All parts of the maintenance cost are independent of the design of the rear low-speed crash structures, and as such it is not necessary to take this into account.

Repair and insurance cost can be influenced by the design of the rear low-speed crash structures. However, during this thesis the assumption is made that all designs must pass the three RCAR load cases which should lead to similar damage during a low-speed rear collision event. This ensures that the differences in repair and insurance cost are limited. Next to this, the repair and insurance cost if for the largest part determined by the parts surrounding the rear low-speed crash structures. These parts are for example the bumper fascia, but also lighting modules and sensors. For these reasons, insurance and maintenance cost are considered, but not directly taken into account during this thesis.

3.8. Performance evaluation function

In this section the parameters that influence the performance of the candidate design and the vehicle have been discussed. The only parameter that is not included here in the cost function is the intrusion distance, as no value has been assigned directly to minimizing the intrusion distance but instead the amount of annual solar kilometers and trunk space are derived from it. The other parameters do directly impact the performance of the design, and an overview of how these parameters influence the performance is provided here. It is interesting to note that it is possible for a cost to be negative, which would in fact mean that it instead has value.

To show the importance of the parameters with respect to each other, as well as absolute values weight factors have been used in all cost subfunctions. These weight factors are w_1, w_2, w_3, w_4, w_5 and w_6 and most

[9] http://www.changemagazine.nl/klimaatkennis/mobiliteit_en_energie/wat-kost-het-opladen-van-een-elektrische-auto, accessed on 03/12/2019

of them are dependent on the target vehicle that is provided as an input for the model. It should be noted that there are some limitations on the values these weight factors have. For example, $w_1 + w_2 = 1$ should always be true in order to not take the initial purchase price into account more or less than once. The value of lightweighting is represented through w_3 and means the €/kg value minimizing weight. w_4 should be set to 1 for electric vehicles, as this will give the actual value of efficiency, due to a reduction in battery size, as a result. The value of annual solar kilometers is represented through w_5, in terms of €/SKM. The value of trunk space is captured in the weight factor w_6 in terms of €/mm longitudinal trunk space. The importance of sustainability is shown by w_7, where a value of 1 should be used to take into account the real cost due to pollution.

If a parameter with the subscript 'baseline' needs to be known, it is explained in the sections before this one how this baseline is defined. The initial purchase price can be calculated using equation 3.22.

$$C_{IP} = w_1 \times \left(C_{target} - C_{baseline} + C_{design}\right) \tag{3.22}$$

where w_1 is the weight factor, C_{target} is the target cost in €as the vehicle (input for the model), $C_{baseline}$ is the cost in €of the rear low-speed crash structures baseline design, and C_{design} is the cost in €of the rear low-speed crash structures design that is being evaluated. These costs come from the cost model as presented in chapter 6.

In equation 3.23 the method to include the cost due to TCO is shown.

$$C_{TCO} = w_2 \times \left[C_{depr} + C_{fuel} + (w6 \times C_{environmental}) - w_7 \times C_{SKM1}\right] \tag{3.23}$$

where w_2 is the weight factor for TCO itself, and w_7 is a weight factor that could either be 0 or 1, depending on whether the considered vehicle is an SEV. C_{SKM1} is the cost, or rather value, of the amount of solar kilometers as calculated based on the charging and environmental cost. w_6 is the weight factor of sustainability, making it possible to choose whether or not it should be included in the total cost of ownership. It should be noted that some parameters that do have an influence on TCO are not taken into account in this calculation, as the design of the rear low-speed crash structures either has no effect or only a negligible effect on these parameters. These parameters are, among others, maintenance cost, annual technical control and registration tax.

Equation 3.24 shows the additional value due to weight savings. The mass of the baseline design and the design that is being evaluated is calculated according to section 3.1.

$$C_{mass} = w_3 \times \left(m_{design} - m_{baseline}\right) \tag{3.24}$$

where w_3 is the weight factor of the mass savings, and should in this situation be seen as the lightweighting value in $€/kg$. m_{design} and $m_{baseline}$ are the weight in kg of the candidate design plus the crash rails and the baseline of these structures respectively.

If the vehicle is a BEV the cost of the efficiency is calculated according to equation 3.25. It should be noted that there is a minus before w_4, the weight factor that should in this case be set to 1, to show that an improvement in efficiency results in a decrease of the cost and therefore to a more desirable solution. If the vehicle that is considered is not an electric vehicle, w_4 should be set to zero.

$$C_{eff} = -w_4 \times \left[E_{batt} - \left(\frac{\text{Energy Efficiency Design}}{\text{Energy Efficiency Baseline}}\right) E_{batt}\right] \times \left(157\frac{EUR}{kWh} + \frac{1}{0.2kWh/kg} \times w_3\right) \tag{3.25}$$

where w_4 is the weight factor, E_{batt} is the capacity of the battery in kWh, η_{design} is the energy efficiency of the evaluated design in Wh/km, $\eta_{baseline}$ is energy efficiency of the baseline design in Wh/km and w_3 is the lightweighting value in $€/kg$ as seen before. A cost of €157 per kWh of battery capacity and an energy density of 200 Wh/kg are assumed here [10].

[10] https://about.bnef.com/blog/behind-scenes-take-lithium-ion-battery-prices/, accessed on 26/08/2019

If the vehicle that is being considered is an SEV the cost, or rather value, of the annual solar kilometers can be calculated using equation 3.26. Here w_5 is the weight factor, showing the value of a single annual solar kilometer. This is calculated according to the method shown in section 3.5. SKM is the amount of annual solar kilometers corresponding to the design that is being evaluated.

$$C_{SKM2} = -w_5 \times [\delta_{SKM}] \tag{3.26}$$

Combining equations 3.22 up to 3.26 into a single performance evaluation function, equation 3.27 is found. This equation can be used to evaluate all the candidate designs, and determine which one is preferred under the current set of weights and criteria. The candidate design that has the lowest value for the total cost is the preferred design.

$$C_{total} = C_{IP} + C_{TCO} + C_{mass} + C_{eff} + C_{SKM} + C_{sustainability} \tag{3.27}$$

4

Generation of candidate designs

In this chapter the generation of the candidate designs is discussed. In section 4.1 the different materials that will be available are shown, along with their properties. Section 4.2 will elaborate on the bumper beam cross-sections that are considered, and section 4.3 does the same for the crash boxes. The chosen manufacturing processes along with the argumentation is found in section 4.4. In section 4.5 it is explained how from these materials and geometries the different designs are generated.

4.1. Available materials

Based on the literature study two material groups were found to be commonly used for the design of low-speed crash structures, being metals and (sometimes) fiber-reinforced plastics. Within the group of metals there is a distinction between steel alloys and aluminium alloys, and respectively three and four representative alloys per main alloying element are chosen to take into account during the optimization. Since the energy absorption mechanism for metal structures is based on ductility, a minimum elongation before break of 10% is imposed as a requirement [30]. With alloys that allow for less ductility the chance of tearing becomes large, reducing the effectiveness in absorbing the impact energy, as shown by Hanssen [30]. The parameters of the material that are used in the calculation of the energy absorption are the yield stress, σ_y, and the flow stress σ_0, where the flow stress is simplified as $\sigma_0 = 0.5(\sigma_y + \sigma_u)$. This flow stress is the average of the yield stress and ultimate stress, and is used to incorporate the strain hardening effect.This means that the materials with the desired properties have the highest value for either $\frac{\sigma_y}{\rho}$ or $\frac{\sigma_0}{\rho}$, depending on whether it is used for the bumper beam or the crash boxes.

For the fiber-reinforced plastics, the main differences can be found in the type of fiber that is used, but also the type of resin has an influence. During this optimization only continuous fibers are considered, and one type of carbon-fiber/epoxy and one type of fiberglass/epoxy are chosen.

4.1.1. Aluminium alloys

The first two aluminium alloys that are chosen are AL-6061 T6 and AL-2024 T4. Both of these are chosen based on their high yield stress and ultimate stress, as well as a maximum elongation of at least 10%. It was also set as a requirement that the chosen material is easy to extrude using hot extrusion.
The other two alloys are chosen because Novelis, one of the largest automotive aluminium suppliers in the world, offers them as the best in their portfolio for crash component applications. The difference between the two tempers is that additional cost is incurred when achieving the T61 temper, but also increasing the material properties.

4.1.2. Steel alloys

The first steel alloy that is chosen is AISI 1020 as it is used by Onsalung [54] in his research and therefore proven to work for rectangular empty and foam-filled tubes. AISI 1020 is a carbon steel and is not tempered,

[1] https://2gjjon1sdeu33dnmvp1qwsdx-wpengine.netdna-ssl.com/wp-content/uploads/2019/02/Advanz-6CM-s300-DataSheet-012119.pdf

Table 4.1: Typical properties of chosen aluminium alloys, values from (CES EduPack 2018)

Alloy	ρ **[kg/m3]**	σ_y **[MPa]**	σ_u **[MPa]**	σ_0 **[MPa]**	**E [GPa]**	ϵ_{max} **[%]**
Al-6061 T6	2710	260	314	287	68.3	12.2
Al-2024 T4	2760	289	402	345.5	74.5	13.0
Advanz 6CM-s300 T4 [1]	2700	100	160	130	70	22
Advanz 6CM-s300 T61 [1]	2700	230	275	252.5	70	14

resulting in mediocre material properties but also a low material cost. The material properties of the chosen alloys can be found in table 4.2.

Table 4.2: Typical properties of chosen steel alloys (CES EduPack 2018, [71])

Alloy	ρ **[kg/m3]**	σ_y **[MPa]**	σ_u **[MPa]**	σ_0 **[MPa]**	**E [GPa]**	ϵ_{max} **[%]**
AISI 1020	7850	295	395	347.5	210	35.5
DP800	7870	530	800	665	200	14
YS800, cold rolled	7850	800	1090	945	210.5	10

The second steel alloy that is chosen is DP800, a dual phase steel that is used in the research by Tarigopula [71] for rectangular hollow crash tubes. The material properties are reasonable and the material cost is as well.

The third and last steel alloy is the cold rolled YS800, a complex phase steel. According to CES EduPack 2018 automotive safety components belong to its typical uses. It has a high yield and ultimate stress, while still having a maximum elongation that is just high enough to not cause rupture of the crash boxes. The material cost is relatively high as shown in chapter 6.

4.1.3. CFRP

Based on a literature review in the book by Ahmed [3] typical energy absorption values for crash tubes with carbon fibers and an epoxy matrix of between 60 and 70 kJ/kg have been found. Due to the lack of quantitative design equations on the effect of e.g. fiber type, fiber volume fractions and resin type it has been decided to use only a single CFRP material, and to assume a Specific Energy Absorption (SEA) value of 60 kJ/kg. This should be a realistic and achievable value that should be definitely possible to realise during the later stages of the structural design, using Finite Element Analysis (FEA). When CFRP is chosen as the material of the crash boxes, only circular tubes will be considered as they show the highest SEA and no advantages have been found for other geometries.

The properties of the CFRP laminate depend on the thickness and layup of the laminate. These properties can be calculated using the ply properties that can be found in table 4.3. The laminate stiffnesses are derived from the layup using classical laminate theory.

Since only symmetric and balanced laminates will be considered, and during the bending of the bumper beam there are only axial stresses (tension, compression), the ply allowables can be transformed to laminate allowables by assuming equal strain in all plies. The average stress level at which the first ply reaches its local maximum stress can be calculated using equation 4.1.

$$X_{t,laminate} = \frac{C_{11}}{Q_{11}} X_{t,ply} \tag{4.1}$$

Where C_{11} is the first entry in the laminate's stiffness matrix, and Q_{11} is the first element in the stiffness matrix of the ply in the direction of the axial load. The method of equation 4.1 also works for the other allowables, X_c, Y_t, Y_c and S.

Farley [21] has shown that the optimum fiber orientation for maximum SEA of the crash boxes is $[0/\pm 15\,\text{deg}]$. This means that this lay-up will be chosen for the crash boxes. For the bumper beam the optimum layup

is dependent on both the geometry and the ply thickness., but the plies should mainly be orientated in the direction of the axial stresses, although some limits are imposed:

- The laminate must be symmetric
- The laminate must be balanced
- Maximum four plies with the same direction can be grouped
- Only 0 deg, -45/45 deg and -90/90 deg plies can be used
- A minimum of 25% of the plies should be in either -45/45 or -90/90 deg orientation

Table 4.3: Ply properties of chosen carbon fiber/epoxy and glass fiber/epoxy prepregs, from Mitsubishi datasheet

	4708 UD carbon/epoxy	**7781 E-glass fabric/epoxy**
t_{ply} [mm]	0.15	0.3
V_f [-]	0.6	0.6
ρ [kg/m3]	1600	2200
ν_{xy} [-]	0.3	0.3
E_x [MPa]	151000	32000
E_y [MPa]	7930	32000
G_{xy} [MPa]	5060	6500
X_t [MPa]	2870	696
X_c [MPa]	1570	793
Y_t [MPa]	43.1	696
Y_c [MPa]	164	793
S [MPa]	87.5	89.6

However, when the structural behaviour of the crash boxes is analyzed the material properties are not determined by using the method above. No verified analytical equations have been found for the estimation of the mean sustained load during progressive crushing. This is probably due to the highly complex behaviour of both the anisotropic material properties and the different physical effects that occur during crushing, e.g. transverse shearing and lamina bending. In order to still be able to estimate the structural performance of composite crash boxes it has been decided to use reasonable values from literature, making the assumption that in the preliminary and detailed design phase a good design is achieved using FEA and these literature values are achieved. This means that the only geometrical parameters influencing the structural response of the composite crash boxes are the cross-sectional area and the length of the crash boxes.

The values taken from literature are as follows:

- SEA_{CFRP} = 60 [kJ/kg], lower bound of range given by [3]
- CLE (Crush Load Efficiency) = 1.15 [-], average of values found in the range of 1.12 to 1.18 by [9]
- η_L (Effective length) = 0.9 [-], approximation; dependent on debris build-up inside the tube, but almost the complete length can be used [35]

To include the influence of which manufacturing process is used the value for Specific Energy Absorption (SEA) of CFRP of 60 kJ/kg is taken as corresponding to the prepreg process. If the braiding process is used an increase in SEA of 5% is taken into account, due to the high volume fraction that can be achieved and the braids having crack-stopping properties. However, if the vacuum-infusion is used a reduction in SEA of 5% is taken instead. This lower value can be explained by the lower fiber volume fraction and less control over fiber orientations.

4.1.4. GFRP

Typical energy absorption values for GFRP crash tubes with an epoxy matrix are between 40-50 kJ/kg [3]. For the same reasons as with CFRP it has been decided to use only a single GFRP material and to assume an SEA of 40 kJ/kg. When GFRP is chosen as the material of the crash boxes, only circular tubes will be considered as they show the highest SEA and no advantages have been found for other geometries.

For the GFRP laminate only a fabric based prepreg is considered, as Uni-Directional (UD) glass fiber is not used often due to cost considerations. The ply properties can be found in table 4.3. The laminate stiffnesses and allowables are derived in the same method as for the CFRP laminates.

When analyzing the crash boxes again the SEA is assumed as no analytical equations for the mean crush force and energy absorption have been found. The values taken from literature are as follows:

- SEA_{GFRP} = 40 [kJ/kg], lower bound of range given by [3]
- CLE = 1.15 [-], average of values found in the range of 1.12 to 1.18 by [9]
- η_L = 0.9 [-], approximation; dependent on debris build-up inside the tube, but almost the complete length can be used [35]

Also for GFRP the 40 kJ/kg is taken as value for crash boxes manufactured using prepreg, and the 5% increase in SEA when manufactured using the braiding technology, and the 5% reduction in SEA when manufactured using vacuum-infusion is also taken into account.

4.2. Bumper beam geometries

The simplified geometry of the bumper beam can be defined by only a few parameters. The only cross-sectional shape that is considered is a thin-walled rectangle, as this was shown during the literature review to give the most lightweight results and minimum deflection. It is also easy to manufacture, using the extrusion process. This also means that the cross-section is considered to be constant along the length. Limiting the cross-section to a rectangle means that the geometry can be defined using only the section height, section depth, wall thickness, beam length and radius of curvature. These parameters are discussed in the following subsections.

It should be noted that when the bumper beam has no curvature, it is also possible to manufacture it using the metal folding process, creating a slightly different geometry due to the flanges that are present. It has been chosen to still define the cross-section using the same parameters as for bumper beams without flanges, and to locate the split between the shells on the vertical axis of symmetry. In this way the presence of the flanges does not influence the centroid which could lead to increased localized stresses. These flanges can not be used to increase the vertical height of the bumper beam in order to more easily comply with the RCAR requirements, as the flanges need to be at least 5 mm thick for them to qualify. Technically it would be possible to generate a design that would creatively pass the RCAR requirements, but this is not attempted in this model. The flange length is defined as 16 mm, as that is the value commonly used in the automotive industry for minimum flange length for bonding or welding.

4.2.1. Section height

The section height is defined as the vertical distance between the lowest and highest points of the section. The lower limit on the section height is imposed by the RCAR requirements as shown in section 5.1, and is 100 mm. Increasing the height of the section is not a weight-efficient method for increasing the bending stiffness or the energy absorption of the bumper beam, but it is important to have a certain minimum height to allow for bumper beams of different vehicles to ensure a good contact during various impact situations.

4.2.2. Section depth

The depth of the section is defined as the horizontal distance between the frontmost and rearmost points of the cross-section. There are no requirements on this dimension following from the load cases , but this dimension is highly important for the bending stiffness due to its contribution to the area moment of inertia, and therefore energy absorption and intrusion distance of the bumper beam. When the section depth is large, the intrusion distance will increase. This means that is not possible to determine an optimum dimension, and this parameter should therefore be varied. The range of section depths that will be considered is from 20 mm to 60 mm.

4.2.3. Wall thickness

The wall thickness is considered constant all along the cross-section, as an optimization of the thickness distribution can be performed in later stages of the structural design using FEA. The range of wall thicknesses is

different for all the different materials, on the one hand due to the different material properties and limitations of manufacturing processes but also because the composites need to have specific wall thickness values due to their discrete ply thicknesses.

4.2.4. Beam length

The length of the beam is defined as the horizontal distance between the leftmost and rightmost point of the bumper beam. This means that the curvilinear length of the bumper beam is longer than the beam length. The minimum length is imposed by the requirements from the RCAR load cases, as shown in section 5.1, resulting in a minimum beam length that is equal to 70% of the vehicle width at the rear wheel wells. However, for the RCAR corner test and the ECE-R42 pendulum corner test it could be beneficial to slightly extend the bumper beam as this will allow for a contact patch (and therefore more deformation before losing contact) during impact.

4.2.5. Radius of curvature

The radius of curvature is defined as the inverse of the curvature of the beam. A bumper beam without curvature is the easiest to manufacture, but a curved bumper beam will increase its bending stiffness, will fit the packaging of the vehicle better, and will decrease the intrusion distance of the impact barrier as the impact point is located closer to the outer skin of the vehicle. For this thesis all the bumper beams have a constant radius of curvature along their length.

4.3. Crash box geometries

The simplified geometry of the crash boxes can also be defined with a limited number of parameters, although the definition is not exactly the same for the metal and composite crash boxes. In the literature review it was found that the most optimal cross-section for metal crash boxes is a thin-walled square, while for the composite crash boxes it is a thin-walled circular cross-section. This can be explained by the difference in energy absorption mechanisms between the two materials. The crash boxes are defined using the length of the crash box and the wall thickness, and the cross-sectional width for a metal crash box but the diameter for the composite crash box. For metal crash boxes foam-filling is also considered, as it has been shown in the literature review that this can increase the SEA. Composite crash boxes do not benefit from foam-filling since their material properties are too high, as shown in section 2.1.2.

Due to the limited level of detail that can be included in this conceptual design optimization, the triggering mechanisms of the crash boxes have been left out in the geometry generation. It is instead assumed that a properly working triggering mechanism is included in all crash boxes leading to the desirable lower peak force and predictable deformation behaviour. This triggering mechanism should be designed in the later phases of the design using FEA.

4.3.1. Metal crash boxes

In this subsection the geometry defining parameters of metal crash boxes are discussed. It should be noted that the actual geometry is different when extrusion is used as the manufacturing process compared to metal folding, due to the presence of flanges to close the cross-section in the folded crash box. The section is however still defined using the same parameters, as the double-hat cross-section can be defined using the same parameters if the flange length is constant. A flange length of 16 mm is used, as this value is often taken as a minimum length in the automotive industry to be able to properly connect the two flanges. Figure 4.1 shows the geometry of the double-hat section, and in figure 4.2 the geometry of an extruded metal crash box is shown on the left.

Length

The length of the crash box is defined as the horizontal distance between the attachment to the crash rails and the attachment to the bumper beam. In the case of a curved bumper beam the attachment to the bumper beam varies in longitudinal position, so the center point of the attachment is used. A small length of the crash boxes leads to a smaller intrusion distance, but higher mean- and peak-forces. Long crash boxes means that the mean- and peak-forces are lower, but at the price of a larger intrusion distance.

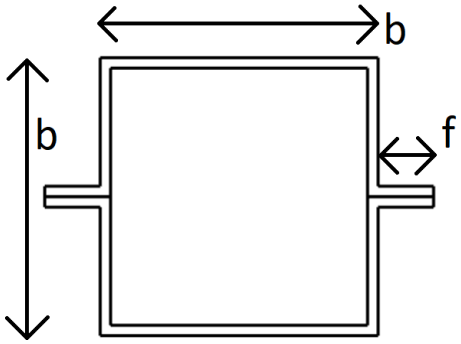

Figure 4.1: Geometry of double-hat crash box cross-section

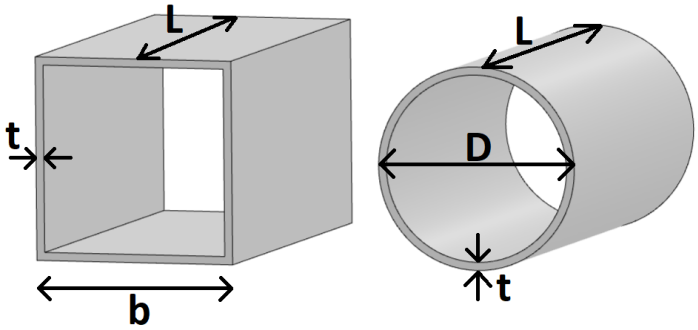

Figure 4.2: Graphical representation of crash box geometry defining parameters. Left: metal crash box. Right: composite crash box

Width

The width of the crash box is defined as either the horizontal distance between the leftmost and rightmost point, or the vertical distance between the lowest and highest point of the cross-section. This can be explained by the choice for only square cross-sections. The crash box width needs to have a minimum dimension, as a crash box that has a cross-section that is too small is prone to column buckling. This needs to be avoided. A larger width also improves the behaviour during impact with an incidence angle, e.g. the RCAR structural test. Increasing the width is also not favorable, as this is found to reduce the SEA, leading to a higher weight.

Wall thickness

Similarly to the wall thickness of the bumper beam, here it is also considered constant all along the cross-section. Optimization of the thickness distribution can be performed in later stages of the structural design. It has been found in literature that increasing the wall thickness in the corners and decreasing the wall thickness away from the corners can increase the SEA. When choosing the range of wall thicknesses for which to run the optimization model, it is important to keep in mind the minimum wall thicknesses that are defined based on the manufacturing processes.

Foam-filling

In the literature review it has been shown that the specific energy absorption of steel and aluminium crash boxes can be improved by filling the section with an aluminium foam. In order to investigate the effect of filling the crash boxes with aluminium foam, and to find which density type works best, there are three different densities of aluminium foam incorporated in the generation of the candidate designs. Their properties can be found in table 4.4. Designs without foam-filling are also generated, for these the density and plateau stress are both set to zero.

4.3.2. Composite crash boxes

In this subsection the geometry defining parameters of composite crash boxes are discussed. A graphical representation of the parameters can be found in figure 4.2 on the right.

Table 4.4: Structural properties of chosen aluminium foams [30]

	Density [kg/m3]	Plateau stress [MPa]
No foam	0	0
Low-density aluminium foam	170	1.5
Medium-density aluminium foam	340	5.5
High-density aluminium foam	510	13.5

Crash box length

The length of the crash box is defined as the horizontal distance between the attachment to the crash rails and the attachment to the bumper beam. In the case of a curved bumper beam the attachment to the bumper beam varies in longitudinal position, so the center point of the attachment is used. A small length of the crash boxes leads to a smaller intrusion distance, but higher mean- and peak-forces. Long crash boxes means that the mean- and peak-forces are lower, but at the price of a larger intrusion distance.

Crash box diameter

The crash box diameter needs to have a minimum dimension, as a crash box that has a cross-section that is too small is prone to column buckling. This needs to be avoided. A larger diameter also improves the behaviour during impact with an incidence angle, e.g. the RCAR structural test.

Wall thickness

The wall thickness is considered constant all along the circular cross-section for manufacturing reasons. Contrary to metal crash boxes, thickness variations along the cross-section are not expected to increase the SEA.

4.4. Manufacturing process

In this section it is determined which manufacturing processes will be considered for the candidate designs of both the crash boxes and the bumper beam. A split has been made between metals and composites, as they have distinct manufacturing processes. All mentioned processes for metals are able to be used with both steel and aluminium alloys, and the mentioned processes for composites are able to be used for both carbon fibers and glass fibers with a thermoset resin.

4.4.1. Metals

An overview of the initial review of available manufacturing processes for metal candidate designs is presented in table 4.5. Extrusion, folding of sheets, and stamping are analyzed on their energy absorption performance, cost of the equipment necessary for the process, the cost of tooling, labour cost and for what production volumes they are a good fit. It is also checked for the crash boxes and bumper beam separately if it possible to create the desired geometry with the process.

Table 4.5: Initial review of available manufacturing processes for metal crash boxes and bumper beam

Process	Performance	Equipment cost	Tooling cost	Labour cost	Volume	Crash boxes	Bumper beam
Extrusion	++	-	+	++	+	Y	Y
Folding	-	+	++	- -	- -	Y	N
Stamping	-	- -	- -	++	++	Y	Y

From table 4.5 it can be seen that extrusion should be the preferrable process for high-volume applications, while folding is preferred for low-volume production. Stamping could be beneficial to use as it can better integrate specific interface geometries and trigger mechanisms due to the increased design freedom, which is beneficial especially at high-volume production. It is also a more fitting process for when steel alloys are chosen, as they are more difficult to extrude. However, at this stage stamping is left out of the analysis due to the lower energy absorption performance and the expensive tooling.

It can also be seen that the metal folding process is not able to create all the desired bumper beam geometries, as it is not possible to manufacture a bumper beam with curvature. However, it is possible to use folding for the bumper beam if it has no curvature. It should be noted that when using the metal folding process flanges will be present to create closed cross-sections. This negatively affects the specific energy absorption of the

crash boxes as either a double-hat design should be used or there are overlapping flanges. For the bumper beam the weight is also increased for equal performance, as these flanges will have overlapping material.

When extrusion is used, additional steps are needed after the process to create either the triggering mechanism (with a CNC machine) in the crash boxes or adding the curvature to the bumper beam (using e.g. roll bending). These additional steps add to the manufacturing cost and should be considered in the cost model.

It is necessary to realize that the possible range of wall thicknesses is limited by the manufacturing process. When using the metal folding process it is dictated by the minimum plate thickness that is available, generally 1 mm. For extruded profiles the determination of the minimum wall thickness is a bit more complex, as it depends on factors such as the specific alloy, the cross-sectional shape and the desired tolerances. In the Nordisk Profil Design Manual [2] the minimum wall thickness for hollow sections with a simple and symmetric profile is said to be 1.2 mm.

4.4.2. Composites

An overview of the initial review of the available manufacturing processes for composite candidate designs can be found in table 4.6. The different processes are scored on the same attributes as for the metal manufacturing processes, and it is also checked if the process is able to manufacture both crash boxes and bumper beam. All processes need additional manufacturing steps to add the trigger mechanisms into the design.

Table 4.6: Initial review of available manufacturing processes for composite crash boxes and bumper beam

Process	Performance	Equipment cost	Tooling cost	Labour cost	Volume	Crash boxes	Bumper beam
Pultrusion	-	-	+	++	++	N	Y
Filament winding	- -	-	+	++	++	N	Y
Carbon braiding	++	- -	+	++	++	Y	Y
Prepreg	++	++	+	- -	- -	Y	Y
Vacuum-infusion	+	++	+	-	- -	Y	Y

From table 4.6 it can be seen that pultrusion and filament winding are unfavorable for the energy absorption performance of mainly the crash boxes. This is due to the limitations on fiber orientation. The optimum fiber orientation for the crash boxes was found to be [0/ $\pm$ 15] degrees [21], and for pultrusion it is possible to use 0 degree fibers, but fibers with different angles can only be included if they are added using a woven cloth. This means that the second orientation would either have to be $\pm$45 degrees or 0/90 degrees. If the ratio is kept at 50% 0 degree and 50% of the second orientation, this would lead to a reduction in SEA of around 50% [21]. The pultrusion process would be a good fit for the manufacturing of bumper beams, as it is possible to create curved beams (as showcased in the 2020 Corvette Stingray) and the limitations on fiber orientations are not having a large effect on the structural performance of the bumper beam. However, for now it is left out of the model.

For the filament winding process it can also be seen that there is a high reduction in energy absorption performance, mainly for the crash boxes but also for the bumper beam. Due to the nature of the filament winding process, it is not possible to use 0 degree fibers as the minimum angle is around 15 degrees. The 0 degree fibers contribute the most to both the energy absorption of the crash boxes and the bending stiffness of the bumper beam. Therefore the filament winding process will not be considered for this analysis.

Carbon braiding is able to manufacture both crash boxes and bumper beams with the desired fiber orientations, and actually has increased performance due to the braids creating a crack stopping barrier. The tooling and labour cost are low, but the equipment is expensive.

Prepreg and vacuum-infusion can both be used to successfully manufacture crash boxes and bumper beams with the desired performance, although when vacuum-infusion is used the structural properties will be lower due to the lower fiber volume fraction. The equipment cost and tooling cost are relatively low, but due to the high labour cost these processes are mainly suited for low-volume production.

[2] `https://www.nordisk-profil.dk/media/1124/purso_profile_design_manual_a5_36s_eng_web.pdf`, accessed on 09/12/2019

Based on the points mentioned above it has been decided to consider only carbon braiding, pre-preg and vacuum-infusion as manufacturing processes for composite crash boxes and bumper beams during this thesis.

The manufacturing process of composite parts also dictate a minimum wall thickness that is achievable. This does however not change much between the different processes considered here, and it can be assumed that a minimum wall thickness of 1 mm is realistic for all of them. The exact wall thicknesses that are possible are dependent on the discrete ply thicknesses that are used. This is not expected to be limiting, due to the low density of these materials, as well as the high forces both the bumper beam and the crash boxes need to withstand.

4.5. Design generation algorithm

The goal of the candidate design generation is to create the full set of designs, consisting of material and geometry for both the bumper beam and crash boxes, that should be considered during the structural analysis. This is done in an automated manner using MatLab, as the amount of candidates that is generated will be very large. There are four main combinations that are used as the basis of the generation of the candidate designs. These combinations can be seen in table 4.7.

Table 4.7: Main combinations of candidate design generation

1: metal BB - metal CB
2: metal BB - composite CB
3: composite BB - metal CB
4: composite BB - composite CB

Based on these four combinations, a script is used to make these combinations for all metal alloys as well as the different composite materials that are considered. This is done for all possible variations for the geometry, as shown earlier this chapter. Initially, no foam-filling of the metal crash boxes is considered. In the next step the candidate designs that include metal crash boxes are then recreated to include the different types of foam-filling. On overview of the parameters that are varied between the different designs that are generated can be seen in the following lists, split in parameters that belong to the crash boxes and parameters that determine the design of the bumper beam:

- Material CB
- Manufacturing process CB
- L_{cb}
- w_{cb}
- t_{cb}
- ρ_{foam}

- Material BB
- Manufacturing process BB
- L_{bb}
- h_{bb}
- d_{bb}
- t_{bb}
- R_{bb}

Due to the large amount of variables being varied to create the different candidate designs, a large set of data is generated. Certain design combinations that have been made are not possible in reality, or are not desired to be included as no methods to analyze them have been developed. These combinations are the following:

- Curved bumper beam manufactured with the metal folding process
- Foam-filled crash boxes manufactured with the metal folding process

Once all the designs have been generated all of the designs are checked on these undesired combinations. If a candidate design is found that should not exist, it is deleted.

4.6. Calculation of mass of design

In order to evaluate if the candidate design has the desired properties it is necessary to calculate the mass of the crash boxes and bumper beam combination. It should not be forgotten that each candidate design consists of one bumper beam and two identical crash boxes. In general the mass is calculated by simply multiplying the volume of material with the material density, but for some designs a few additional equations are needed. These are shown below.

Curved bumper beams

The length of the bumper beam is defined as the lateral length, which should be used for calculating the volume of the material if the bumper beam is straight. If the bumper beam is curved however, the curvilinear length of the beam is needed. This can be calculated using equation 4.2.

$$L_{curved} = 2\pi R_{bb} \frac{sin^{-1}\left(\frac{0.5L_{bb}}{R_{bb}}\right)}{360} \tag{4.2}$$

Where R_{bb} is the radius of curvature.

Folded metal parts

All the candidate designs made using the metal folding manufacturing process consist of two shells instead of a continuous cross-section. To join these two shells together flanges are present. The flange length is chosen to be equal to 16 mm, and the thickness equal to the wall thickness of the rest of the part. This means four of these flanges are present on each part. The additional surface area due to the presence of these flanges is calculated using equation 4.3.

$$A_{flanges} = 4 \times 16\ mm \times t \tag{4.3}$$

Where t is the wall thickness of the part.

Cross-sectional shape of crash boxes

As determined earlier this chapter the cross-sectional shape of metal crash boxes is square while for composite crash boxes it is circular. This influences how the cross-sectional area, which is used to calculate the volume, should be calculated. For metal crash boxes the cross-sectional area is calculated using equation 4.4 and for composite crash boxes using equation 4.5.

$$A_{cb,metal} = b^2 - (b-2t)^2 \tag{4.4}$$

Where b is the width of the cross-section and t is the wall thickness.

$$A_{cb,composite} = \pi\left(\frac{D}{2}\right)^2 - \pi\left(\frac{D-2t}{2}\right)^2 \tag{4.5}$$

Where D is the diameter of the cross-section and t is the wall thickness.

5

Structural performance

In this chapter the methods used to analyze the structural performance of the candidate designs are explained. The load cases that will be evaluated and the requirements that should be fulfilled in order to pass them are presented in section 5.1. For each candidate design it is necessary to understand what the expected structural performance is in terms of peak force, average crush force, specific energy absorption, and the maximum intrusion distance. The analytical methods to find values for these parameters are discussed in sections 5.2 to 5.4. Additional notes on the structural analysis can be found in section 5.5.

5.1. Load cases

The load cases that should be considered during the design of the rear low-speed crash structures are defined by both insurance companies (RCAR) and homologation (ECE-R42). Homologation means the granting of approval by an official authority, which in this case means approval that the vehicle meets the regulations. Both types have as main goal to reduce unnecessary damage cost during low-speed impact. These load cases have been chosen based on the literature study that has been carried out before this thesis. An overview of the load cases that are considered can be seen in table 5.1.

Table 5.1: Overview of applicable low-speed load cases

Load case	Impact speed [km/h]	Overlap [%]	Incident angle [deg]	Impactor description	Type
RCAR full width rear	10.0 +- 0.5	100	0	Stationary barrier	Insurance
RCAR corner test rear	5.0 +- 0.5	15	0	Stationary barrier	Insurance
RCAR structural test rear	15 + 1	40	10	Moving barrier 1400 kg	Insurance
ECE-R42 pendulum rear	4 + 0.25	x	x	Rigid pendulum, weight = car weight	EU homologation
ECE-R42 pendulum corner rear	2.5 + 0.1	x	x	Rigid pendulum, weight = car weight	EU homologation

These load cases will be explained in detail, so that they can be properly modelled using the different analytical methods. The requirements that need to be fulfilled in order to pass the load cases will also be shown.

High-speed load cases are seen as out-of-scope for this thesis, as they involve additional parts of the vehicle but also have a different objective; keeping the occupants safe instead of minimizing the damage cost. The influence of the design of the rear low-speed crash structures on the behaviour during rear high-speed load cases is also relatively small due to their limited length.

5.1.1. RCAR full width test rear

In the RCAR full width rear test[1] the vehicle impacts a rigid barrier with a speed of 10.0 ± 0.5 km/h. The test protocol is designed to encourage bumper systems with energy absorbing beams of sufficient vertical dimension and crash boxes, positioned at a standardized height, in order to effectively protect the vehicle from damage in low speed crashes. A vehicle performing the RCAR full width rear test is shown in figure 5.1 and the rigid barrier is shown in figure 5.2.

Figure 5.1: RCAR rear bumper test example[1]

Figure 5.2: RCAR bumper barrier[1]

The rigid bumper barrier is made from steel and has a radius of 3400 mm ± 25 mm. The width is 1500 mm ± 25 mm and the height of the vertical face is 100 mm ± 2 mm. The ground clearance of the bumper barrier is 405 mm ± 3 mm. A rigid backstop is included on the barrier, positioned 25 mm ± 1 mm behind the vertical face of the bumper barrier. However, this backstop is left out in the analysis as the low-speed crash structures will not make contact with it. On the vertical face of the bumper barrier an energy absorber is located. This energy absorber has a depth of 50 mm and covers the full height of the vertical face of the bumper barrier, and the cross-section has an external radius of 150 mm. The stiffness of this energy absorber is estimated to be between 160 and 300 N/mm when impacted quasi-statically with a rectangular piece of steel with a width of 160 mm and a height of 50 mm. This should be a representation of the contact patch between the vehicle bumper and the barrier[1]. The upper limit of the amount of impact energy that can be absorbed by this energy absorber is roughly 160J, assuming an average force of 4 kN over a distance of 40 mm. This is a very small amount, for a low-weight vehicle that weighs only 1000 kg it is only 4.1% of the total kinetic energy.

The centerline of the vehicle should correspond to the center of the bumper barrier during impact, with a maximum lateral deviation of ± 50 mm. The vehicle should be within 10 mm of its nominal ride height. The tire pressure should be similar to the recommended pressure for single occupancy and low-speed conditions. The fuel tank (if present) should be filled for at least 90% of the maximum capacity, and a 75 ± 5 kg test dummy shall be secured on the driver's seat. During impact no external propulsive forces shall act on the vehicle.

In order to pass the test, the following requirements need to be fulfilled [2]:

1. The bumper system has a height of at least 100 mm
2. The bumper system has a relevant vertical engagement of at least 75 mm
3. No damage to the vehicle structure is allowed (this mainly includes the crash rails and all parts and panels permanently fixed to the vehicle)
4. No damage to the tailgate, caused directly by the barrier, is allowed

It is expected that this load case is critical for the design of the bumper beam as a high amount of energy needs to be absorbed and the contact patch will be much smaller than the full width of the barrier. This means a high force needs to be transferred from the centerline of the bumper beam towards the crash boxes. The crash boxes are expected to also deform in order to be able to absorb the impact energy. It should be noted that not all the kinetic energy will be absorbed by the crash structures as the impact is not perfectly plastic. The elastic portion of the impact energy is returned to the vehicle as kinetic energy.

[1] `http://www.rcar.org/Papers/Procedures/BumperTestProcedure.pdf`, accessed on 02/08/2019
[2] `http://www.rcar.org/Papers/Procedures/German_Rating_System_02_2018_V1.pdf`, accessed on 16/08/2019

5.1.2. RCAR corner test rear

The RCAR corner test rear [3] is very similar to the full-width version, in the sense that the same barrier and the same vehicle conditions are used. The impact speed is 5.0 ± 0.5 km/h. The vehicle is positioned with an overlap of 15% with the barrier, measured at the wheel wells on the rear axle. The maximum lateral deviation is ± 25 mm. A schematic representation of the frontal version of this test and how the overlap is measured can be found in figure 5.3. The concept of the rear corner test is identical to the frontal version.

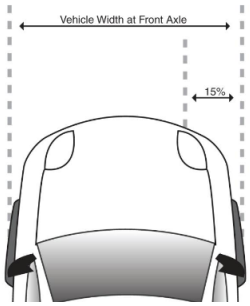

Figure 5.3: Schematic representation of RCAR front corner test, rear corner test is identical [3]

The description of the rigid bumper barrier and vehicle conditions can be found under the RCAR full-width load case. In order to pass the RCAR corner test rear, the following requirements have to be fulfilled:

1. Qualifying bumper beam width is at least 70% of the width of the vehicle as measured at the rear wheel wells
2. The bumper system has a relevant vertical engagement of at least 75 mm
3. No damage to the vehicle structure is allowed
4. No damage to the tailgate, caused directly by the barrier, is allowed

It is expected that this load case is critical for the design of the bumper beam, but not for the crash boxes. Here the width of the bumper beam is important to make sure that the barrier impact can be absorbed. The bumper beam cross-section needs to provide enough stiffness to keep the deflection acceptable.

[3] `http://www.rcar.org/Papers/Procedures/BumperTestProcedure.pdf`, accessed on 02/08/2019

5.1.3. RCAR structural test rear

The RCAR structural test [4] has been developed together with the Allianz Center for Technology, a subsidiary of one of the largest insurance companies in Germany. This test was developed to assess a vehicle's damageability and repairability during low-speed rear impacts. The objective of the test is to limit unnecessary damage to the structure of the vehicle. A rigid moving barrier of 1400 ± 5 kg is used with an impact speed of 15 +1 km/h. A schematic representation of the RCAR structural test is shown from top view in figure 5.4 and side view in figure 5.5.

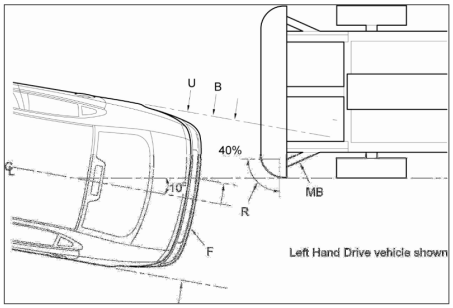

Figure 5.4: Schematic representation of RCAR structural test, top view [4]

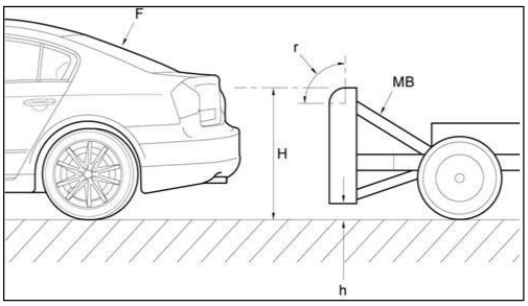

Figure 5.5: Schematic representation of RCAR structural test, side view [4]

The mobile barrier has a weight of 1400 ± 5 kg and shall be vertical to within ± 1 degree. The longitudinal axis of the barrier is oriented with 10 ± 1 degrees relative to the longitudinal axis of the test vehicle. An overlap of 40% ± 25 mm of the vehicle width is used. How this is measured can be seen in figure 5.4. The mobile barrier has a width of 1572 mm, of which the sides have a 150 mm radius. The ground clearance is 200 ± 10 mm and the height of the barrier itself is 500 mm with a 50 mm radius at the top. The barrier does not have any energy absorbing structures, and can therefore be considered rigid.

During the test the vehicle fuel tank (if present) shall be full to within 5% of the specification. This means that the vehicle test weight should be equal to the curb weight, plus a 75 ± 5 kg test dummy. The transmission shall be in neutral and the parking brake fully released.

For the RCAR structural test no requirements are specified in order to pass the test. The goal of the test is to minimize the cost of repairing the damage from the test. This can be done by making sure that the damage is contained to physical parts that are easily replaced. For the scope of this thesis, the following requirements are imposed to ensure a reasonable repair cost:

1. No damage to the vehicle structure is allowed (this mainly includes the crash rails and all parts and panels permanently fixed to the vehicle)
2. No damage to the tailgate, caused directly by the barrier, is allowed

It is expected that this is the critical load case for the crash boxes. The speed is the highest of all the load cases and only one crash box can be used to absorb the energy. Also the load is introduced under an angle, influencing the structural behaviour. Since the impact location is close to the connection of the bumper beam to the crash box, the bumper beam is not expected to absorb a high amount of energy. It should be noted that not the complete kinetic energy of the mobile barrier needs to be absorbed, as the impacted vehicle will start moving and after the impact both the mobile barrier and the vehicle will have a certain velocity and therefore kinetic energy.

[4] `https://azt-automotive.com/_Resources/Persistent/683b2c0557a7a308bc56e1705b31db983cce60fe/RCAR%20Structure%20Test%20procedure%20Version%202_3.pdf`, accessed on 14/08/2019

5.1.4. ECE-R42 pendulum rear

The ECE-R42 pendulum test [5] has been implemented to assure protection of the exterior during contact and small shocks, without causing any serious damage. For this a pendulum with a weight roughly equal to the vehicle weight impacts the vehicle with 4.0 ± 0.25 km/h. Two tests will be performed, one based on the unladen weight of the vehicle and one based on the laden weight. A schematic overview of the pendulum test can be seen in figure 5.6 and the geometry of the pendulum in figure 5.7.

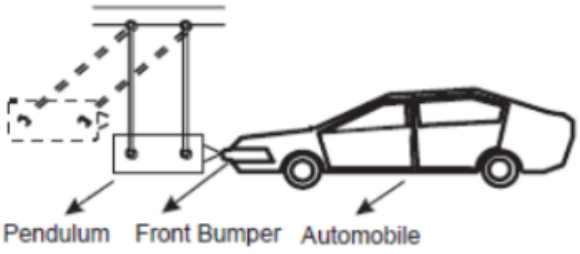

Figure 5.6: Schematic representation of ECE-R42 front pendulum test, rear is identical [47]

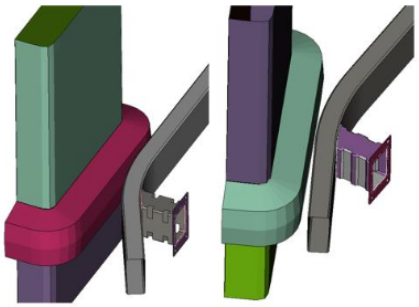

Figure 5.7: CAD model of ECE-R42 pendulum test [14]

The impactor is a rigid pendulum, made from hardened steel. The total width of the impactor is 810 mm with an 102 mm radius on both sides. The 'vertical face' of the impactor has a height of 114 mm with a 3 mm radius on both sides. The 'vertical face' has an 8 degree taper, focusing the impact in the center of the height of the 'vertical face', where a 13 mm radius is used to make sure there is no sharp corner. The reference height (center of the vertical impactor face) is 445 mm. During the test the pendulum weight should be equal to the unladen weight of the vehicle, which is equal to the curb weight.

The impact location of the impactor for the first impact can be chosen by the manufacturer, but the second impact location should be at least 300 mm away from the first. The extremities of the impactor are not allowed to fall outside the width of the vehicle. The vehicle needs to be positioned in such a way that when the pendulum is at rest, it touches the vehicle at the desired impact location but the force it exerts is not large enough to move the vehicle.

During the test the vehicle shall be at rest with the front wheels in neutral position. The tyres have to be inflated to the recommended pressure, the brakes shall be disengaged and the transmission shall be in neutral. The vehicle weight should be equal to the curb weight during the first test, but during the second test the weight is increased with three occupants of 75 kg each (assuming a 4- or 5-seater car).

In order to pass this load case, the following requirements need to be fulfilled after the test:

1. Lighting and signalling devices shall continue to work correctly and remain visible
2. Vehicle trunk and doors shall be operable in the normal manner
3. Fuel and cooling systems shall not have leaks or constrictions preventing normal functioning
4. Vehicle exhaust system shall not suffer damage preventing its normal function
5. Vehicle propulsion, suspension, steering and braking systems shall remain in adjustment and shall operate in a normal manner

This load case is not critical for the design of either the bumper beam or the crash boxes, as the impact speed during the RCAR full-width test is much higher. This means that this load case does not have to be implemented in the optimization model. This can be explained by the fact that this is a homologation load case and therefore mandatory, while the RCAR test is optional. The requirements should not be difficult to manage, although this is mostly out of scope for the design of the rear low-speed crash structures. The design of the physical parts around them have a much larger influence on whether the requirements will be fulfilled or

[5] `https://www.unece.org/fileadmin/DAM/trans/main/wp29/wp29regs/2009/r042e.pdf`, accessed on 21/08/2019

not. The actual test has to be performed twice, once with the unladen and once with the laden weight.

5.1.5. ECE-R42 pendulum corner rear

The ECE-R42 pendulum corner test [6] is a variation on the normal pendulum test as discussed before. The pendulum impactor that is used is identical, but the impact location is different and the impact speed is lowered to 2.5 + 0.1 km/h. The first corner test is performed with the vehicle at unladen weight on one corner, and the second test is performed with the vehicle at laden weight on the other corner. This test ensures that also the corners of the vehicle are able to withstand small contacts and shocks without significant damage or loss of function.

The impactor is identical to the one used for the normal pendulum test, with a weight equal to the unladen weight of the vehicle. The vehicle should be positioned in such a way that the impactor makes an angle of 60 ± 5 degrees with the longitudinal plane of the vehicle. The first point of contact shall be in the centerline of the impactor within a tolerance of ± 25 mm. The state of the vehicle is otherwise equal to the state during the normal pendulum test.

In order to pass this load case, the same requirements as for the ECE-R42 pendulum rear test need to be fulfilled.

This load case is also considered to be non-critical, as the RCAR corner test will impose restrictions on the design that make sure the pendulum corner test automatically should pass. When assuming a worst-case upper limit for the car width at the rear wheel wells of 2 meters, the 15% overlap from the RCAR corner test means only an overlap of 300 mm. The half-width of the pendulum is 405 mm, and 303 mm when excluding the radius on the end. Under an angle of 30 degrees this becomes an effective width of $cos(30^\circ) \times 303 = 262.4$ mm, which is less than 300 mm. However, the bumper beam needs to extend a certain distance past the 15% overlap location to ensure that the bumper barrier makes contact with the bumper beam. Also the exterior shape of a vehicle is not perfectly rectangular, but the width slightly decreases towards the rear end of the vehicle and there is also a corner radius. Both of these mean that the contact point of the corner pendulum moves further inside. These three points together guarantee that if the bumper beam width is large enough to pass the RCAR corner test, the bumper beam width is automatically sufficient for the ECE-R42 corner pendulum test. If the vertical height of the bumper beam is large enough and at the correct ground clearance to pass the RCAR corner test, the positioning will also be good for the ECE-R42 pendulum corner test. The cross-sectional properties will also automatically be sufficient, as the impact velocity during the RCAR corner test is two times the impact velocity and therefore four times the impact energy during the pendulum corner test.

This means that the ECE-R42 corner pendulum test does not have to be evaluated in the optimization model. Being able to eliminate the ECE-R42 corner pendulum test from the optimization is very positive, as detailed exterior dimensions of the vehicle need to be known in order to accurately assess the impact location. Reducing the amount of load cases also leads to less effort in creating the optimization model and less computational power needed for the model to run. Of course when the final design is known it should be checked using FEA if the ECE-R42 load case is indeed passed without problems.

[6] `https://www.unece.org/fileadmin/DAM/trans/main/wp29/wp29regs/2009/r042e.pdf`, accessed on 21/08/2019

5.2. Analytical analysis: RCAR full width bumper test

In this section the analysis method for the RCAR full width bumper test is developed. It is shown what equations are used to make an estimation of the amount of energy that is absorbed, the intrusion distance and the peak force. It is also checked if it is possible to absorb all the kinetic energy of the vehicle during the impact. Due to the setup of the model, with the desire to be able to handle multiple geometries and materials, not all parts of the analysis are applicable to each candidate design. A distinction is made between brittle (composites) and ductile (metals) materials.

The different steps of the analysis are visualized in figure 5.8. The first step, A, shows the situation where only elastic deformation of the bumper beam is taken into account. When the yield stress of the bumper beam material is reached, the bumper beam will start to deform elastoplastically until the bumper beam has the same curvature as the barrier. This can be seen in the second step, B. At this point, the load will no longer be introduced at the center of the beam but at the location of the crash boxes. This will lead to either progressive folding or progressive failure in the crash boxes, depending on their material. The final position is shown in the third step, C, where all the energy of the impact is absorbed. The force that is exerted by the barrier on the bumper beam is resisted by a reaction force through the inertia of the vehicle, in this figure represented as the center of gravity.

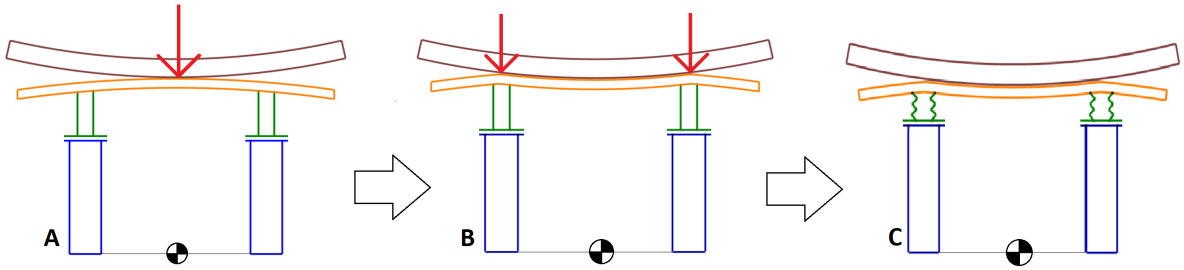

Figure 5.8: Different steps in analytical analysis: a) elastic deformation of bumper beam, b) maximum elastoplastic deformation of bumper beam plus crushed bumper beam section, c) maximum plastic deformation of crash boxes

For different candidate designs the analysis method will be different, due to the difference in material behaviour. The first step of elastic deformation is the same for both material types. The second step of elastoplastic deformation and collapse of the section is not present for composites because the bumper beam would fail in a brittle manner instead of yielding. The energy absorption mechanism, and therefore also the analysis method, of the crash boxes is also different for both materials. At each step the amount of absorbed energy and the intrusion distance is calculated. When these are all combined the total amount of energy absorption and total intrusion distance will be known. A flowchart of the steps taken for the different material types is shown in figure 5.9.

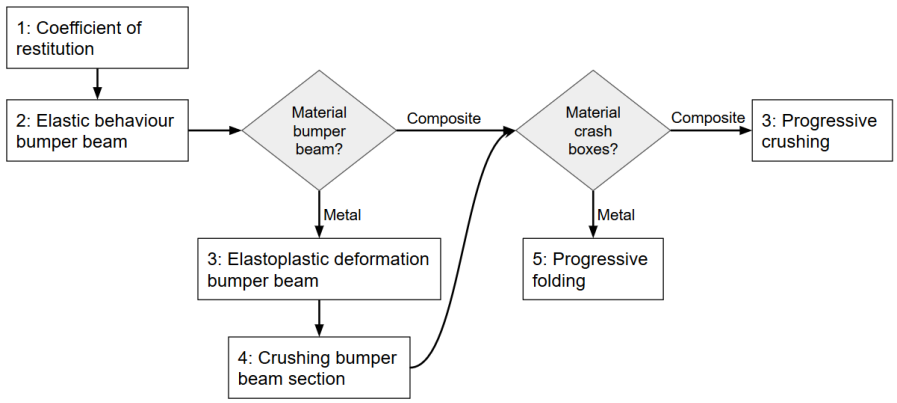

Figure 5.9: Flowchart of different steps in structural analysis RCAR full width test

5.2.1. Absorption of impact energy

The amount of energy that is absorbed by the rear low-speed crash structures during the RCAR full width test is not equal to the kinetic energy of the vehicle prior to impact, due to the elastic energy stored in the complete vehicle. This elastic energy is restituted as kinetic energy of the vehicle after the impact. To estimate the velocity of the vehicle after the impact the coefficient of restitution is calculated according to the trendline developed by Antonetti [7] as shown in section 2.4. With an impact speed of 10.5 km/h, or 2.92 m/s, it follows that $\epsilon = 0.3293$. This means that the velocity of the vehicle after the impact is $V = 2.92 \times 0.3293 = 0.96$ m/s = 3.46 km/h. The amount of energy that is absorbed by the low-speed rear crash structures can now be calculated using equation 5.1.

$$E_{absorbed} = \frac{m_{vehicle}}{2} 2.92^2 - \frac{m_{vehicle}}{2} 0.96^2 = 3.79 m_{vehicle} \tag{5.1}$$

Because the coefficient of restitution is in reality different for each vehicle and candidate design, using the statistical trend inherently introduces a margin of error in the analysis. As the scatter of test data at the impact velocity of the RCAR full width test is especially large, a sensitivity study has been carried out. The minimum and maximum values for the coefficient of restitution around a 3 m/s impact speed are roughly 0.2 and 0.45 respectively, so this range is used to analyze the sensitivity of the amount of energy that is absorbed to the coefficient of restitution. The results are plotted for different vehicle mass in figure 5.10.

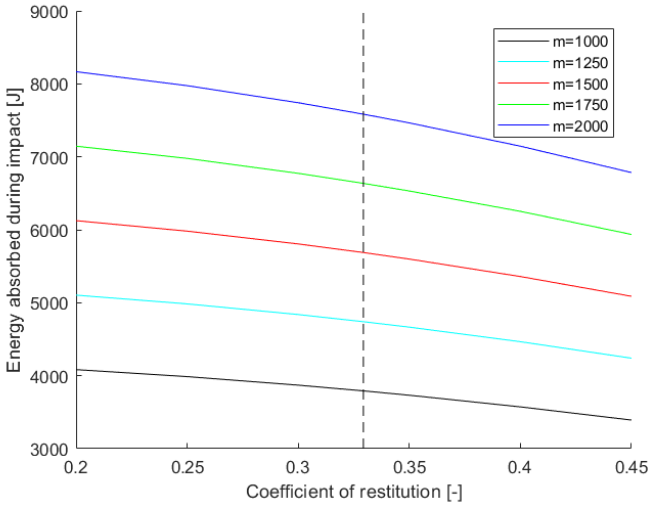

Figure 5.10: Sensitivity analysis of energy absorption during RCAR full width test, with respect to coefficient of restitution, for different values of vehicle mass

As expected the relative error is not dependent on vehicle mass, but a difference of 20.4% has been found between the energy absorption values for the highest and lowest values of the coefficient of restitution. When calculating the error around the assumed solution $\epsilon = 0.3293$, it was found that the absorbed energy could be underestimated by a maximum of 7.7% and overestimated by a maximum of 11.8%. From this it can be seen that even though there is scatter in the values for the coefficient of restitution, the error in the amount of energy absorbed is much smaller. The influence on the design of the low-speed crash structures will be even smaller than this, as the energy absorption during the RCAR structural test is more critical, and there this maximum error is lower as will be shown later.

5.2.2. Elastic deformation bumper beam

In order to analyze the elastic deformation and energy absorption of the bumper beam, the load case is simplified as a three-point bending test. Since only the elastic deformation is calculated, this method is applicable to both brittle and ductile materials. This means that the beam is assumed straight, the beam is simply supported and the load is applied as a point load in the center of the beam. Because of this, the applied moment at the center of the beam at the onset of yield can be found using equation 5.2.

$$M_y = \frac{\sigma_y I}{\overline{y}} \tag{5.2}$$

Where M_y is the applied moment at the center of the beam at the onset of yield, σ_y is the yield stress of the material, and $\overline{y}$ is the distance from the neutral axis. Now that the applied moment is known, the corresponding curvature at the onset of yielding can be found using equation 5.3.

$$k_y = \frac{M_y}{EI} \tag{5.3}$$

Where E is the Young's modulus of the material and I is the second moment of inertia of the cross section. For rectangular thin-walled cross-sections I can be calculated using equation 5.4.

$$I = \frac{ba^3}{12} - \frac{(b-2t)(a-2t)^3}{12} \tag{5.4}$$

Where b is the width of the cross-section, a is the height of the cross-section and t is the wall thickness. If the bumper beam is manufactured using the metal folding process, and therefore flanges are present, the second moment of inertia is calculated using equation 5.5.

$$I = \frac{ba^3}{12} - \frac{(b-2t)(a-2t)^3}{12} + 2\frac{16(2t)^3}{12} \tag{5.5}$$

From the applied moment at the onset of yield it is possible to find the equivalent applied force using equation 5.6.

$$F_y = \frac{4M_y}{L} \tag{5.6}$$

Equation 5.6 is derived from $M = 0.5Fx$ where in this case $x = 0.5L$. Knowing the applied force, the corresponding deflection at the center of the beam can be calculated using equation 5.7.

$$d_{elastic} = \frac{1}{48}\frac{F_y L^3}{EI} \tag{5.7}$$

The energy that is absorbed by the elastic deformation of the bumper beam can then be calculated using equation 5.8.

$$E = \frac{1}{2}F_y d_{elastic} \tag{5.8}$$

During the elastic deformation of the bumper beam it is highly likely that the foam layer on the bumper barrier is being compressed. The RCAR guidelines specify a force-deflection corridor based on a certain impactor that can be used to model the behaviour of the foam during an actual impact. The shape of the force-deflection corridor is like this because it resembles the behaviour of a foam under compression. This means that first the force increases, then stays constant at a certain level while compressing, and then increasing again. In order to eliminate the uncertainty of the foam behaviour within the corridor, and to more easily be able to include it in the analysis, a linearized force-deflection model is created. The force-deflection corridor can be seen in figure 5.11, together with the linearized model that is used here.

From figure 5.11 it can be seen that the linearized model falls nicely in between the force-deflection corridor specified by the RCAR guidelines. The amount of energy absorbed will therefore be estimated with reasonable accuracy and is even slightly conservative. The maximum amount of energy that can be absorbed by the foam layer on the barrier according to the linearized model is $0.5 * 10000 * 0.045 = 225\ J$. This value is reached as soon as the peak force in the rear low-speed crash structures has reached 10 kN. If the peak force is lower than 10 kN, the amount of energy absorbed by the barrier foam is $\left(\frac{F_{peak}}{10\ kN}\right) \times 225$ thanks to the linearized model for the barrier foam. The energy absorbed by the barrier foam is absorbed in a plastic manner, and can therefore not be restituted to the vehicle.

A curved bumper beam would lead to a higher F_Y as it can withstand more load before yielding, since part of the load transfer can be done through compression, compared to purely bending for a straight bumper beam. The difference in energy absorption because of this is negligible, and this F_Y will also never be the peak force of the combined bumper beam and crash boxes. Therefore it is acceptable to not include the curvature of the bumper beam in the calculation of the elastic phase of the bumper beam.

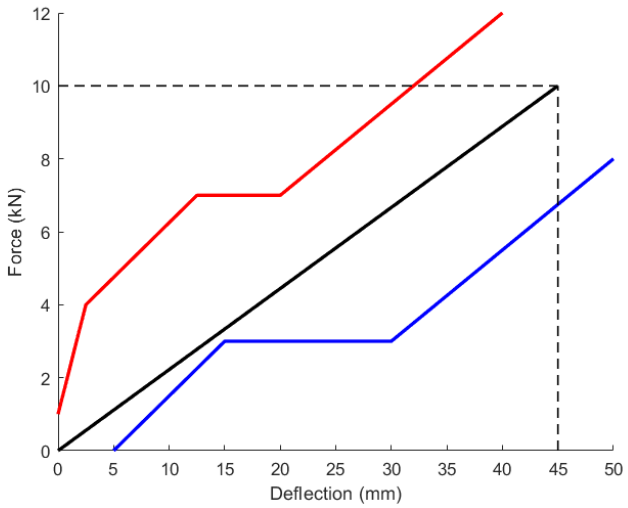

Figure 5.11: Force-deflection corridor specified by RCAR guidelines and linearized model

5.2.3. Elastoplastic deformation bumper beam - metals

Once the onset of yielding is reached in the beam, the previous analysis method is not valid anymore. Once this happens, the behaviour of the beam will be elastoplastic. Because the bumper beam material is ductile, yielding does not mean failure and the applied moment and equivalent force can still increase. During this elastoplastic phase significantly more energy will be absorbed than during the elastic phase. If the bumper beam is made from a brittle material, this part of the analysis should be skipped.

According to the plastic beam theory by Megson [48] the ratio of the plastic moment to its yield moment depends on the shape factor. Because only rectangular cross-sections will be evaluated for the bumper beam it is possible to take this shape factor as a constant. For rectangular cross-sections, the shape factor is 1.5, which means that the plastic collapse of the beam occurs at a bending moment 50% larger than the bending moment at the onset of yielding [48]. For this part of the analysis the assumption is made that the material is perfectly plastic, meaning no strain-hardening effects are taken into account. This will lead to an underestimation of the plastic moment and the energy absorption.

Due to the shape factor it is now possible to calculate the maximum plastic moment of the beam using equation 5.9.

$$M_p = \frac{3}{2} M_y \tag{5.9}$$

To account for strain-hardening effects of the material as well, instead of assuming a perfectly linear material, the ratio between the flow stress σ_0 and the yield stress σ_y is added to equation 5.9. This leads to equation 5.10.

$$M_p = \frac{3}{2} \frac{\sigma_0}{\sigma_y} M_y \tag{5.10}$$

In the elastic region the curvature of the beam relates to the applied bending moment in a linear manner, but as plastic effects are now in play this relation is no longer linear. Based on the shape factor for rectangular cross-sections the moment-curvature relation can be found in equation 5.11. This moment-curvature relation is visualized in figure 5.12.

$$M = \left[1 - \frac{1}{3} \left(\frac{k_y}{k} \right)^2 \right] M_p \tag{5.11}$$

Due to the shape of the bumper barrier, the maximum curvature that can be achieved is $k = 1/3400\ mm$, as this is the point where the barrier is touching the bumper beam along the entire width and the crash cans will

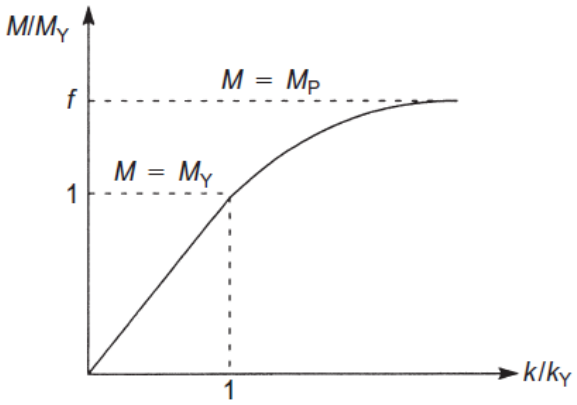

Figure 5.12: Moment-curvature relation for elastic and elastoplastic region, f is the shape factor [48]

start to be involved. The maximum effective curvature of the bumper beam is the barrier curvature plus the curvature the bumper beam already has before the impact. This is shown in equation 5.12.

$$k = \frac{1}{R_{bumperbeam}} + \frac{1}{R_{barrier}} \tag{5.12}$$

Now that the relation between applied moment and curvature is known, it is necessary to understand the relation between curvature and deflection as well. Normally this is done by integrating the moment distribution twice, but in this elastoplastic analysis method the moment distribution is not linear anymore. The shape of the distribution of the applied moment also changes due to the change in contact patch between the bumper beam and barrier. Therefore the assumption has been made that the curvature is equal along the entire beam, basically making the shape of the beam a part of the circumference of a circle with radius $R = 1/k$. This becomes more accurate when the bumper beam is deformed closer to the shape of the barrier, which will be the case at the end of the elastoplastic phase, which is when knowing the deflection is most important. Since only the energy absorption during this phase and the reaction force corresponding to M_p have to be known, this is expected to be a fair assumption. This means that the deflection can be found using equation 5.13.

$$d_{elastoplastic} = R - R\,cos\left[360\frac{L/2}{2\pi R}\right] \tag{5.13}$$

The applied force corresponding to the fully plastic bending moment can be calculated using equation 5.6. Now that both the applied force and the deflection are known, the amount of energy absorbed can be calculated using equation 5.14.

$$E_{elastoplastic} = F_p \times (d_{elastoplastic} - d_{elastic}) \tag{5.14}$$

From equation 5.14 it can be seen that the elastoplastic curve as seen in figure 5.12 is simplified to a horizontal relationship with the value of the fully plastic moment, and also written as force times deflection instead of moment-curvature or moment-rotation. This makes it easier to evaluate the two components (bumper beam curvature and barrier curvature) together. It was found that the applied moment very quickly approaches the fully plastic moment, meaning that the current approximation will be only a small overestimation. This is considered fair as for example no dynamic hardening effects or local energy absorption is taken into account, leading to the expectation that this analysis is still conservative.

At this point both the energy absorption by elastic deformation and elastoplastic deformation of the bumper beam are known. The impact force is from now on directly applied on the crash boxes, which will lead to crushing of the bumper beam section

5.2.4. Crushing of bumper beam section - metals

Estimating the energy absorption due to the crushing of the bumper beam section is difficult, due to the complex deformations and other highly nonlinear phenomena. In order to still get an estimation of the amount

of energy that is absorbed when the section is crushed, a method is used that could be called a 'minimum energy' approach. In figure 5.13 the assumed deformation can be seen, where all the plasticity is concentrated in six plastic hinges, which would be the most energy-efficient method of crushing the bumper beam section. Two different types of plastic hinges can be distinguished, α for the hinges that rotate approximately 90 degrees, and β for the hinges that rotate approximately 180 degrees.

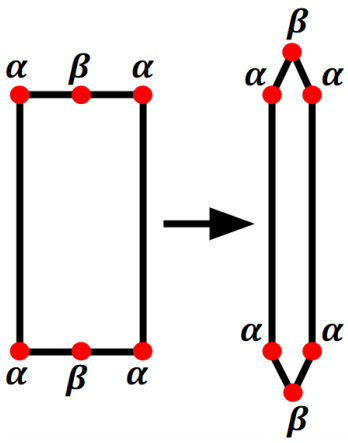

Figure 5.13: Location of plastic hinges in bumper beam cross-section

When looking at the deformed situation in 3D instead of only the 2D section, the situation is simplified with the assumption that there are only two states of the bumper beam section, namely fully crushed or not crushed at all. Extending from this, the width of the crushed section is assumed to be equal to the width of the crash boxes, plus two times the depth of the bumper beam. The applied moment to achieve onset of yielding in the plastic hinges can be found in equation 5.2. The area moment of inertia of the wall can be calculated using equation 5.15.

$$I = \frac{bt^3}{12} \tag{5.15}$$

In which b is the estimated width of the hinge line, and is assumed to be equal to the width of the crash box plus two times the depth of the bumper beam. The fully plastic moment corresponding to the formed hinges can be calculated using equation 5.10. Now that the fully plastic moment of the hinge line is determined, the amount of energy that is absorbed by rotation of each hinge line respectively can be calculated using equation 5.16.

$$EA = M_p\theta \tag{5.16}$$

In which θ is the rotation of the hinge in radians. When the energy absorption contributions of all 6 plastic hinge lines are added together and recognizing that 180 deg = π rad and 90 deg = $\frac{1}{2}\pi$ rad, equation 5.17 is found.

$$EA_{total} = 2 \times \left[2M_p\pi + 4M_p\frac{1}{2}\pi\right] = 8M_p\pi \tag{5.17}$$

Where the factor 2 comes from the fact that there is a crushed section both on the left and on the right of the bumper beam. Now that the energy absorption of the bumper beam due to crushing of the section is known, it is desired to also know the corresponding intrusion distance. This intrusion distance is based on the geometrical reduction of the depth of the bumper beam when both the front and rear face are pushed against each other. It can therefore be calculated using equation 5.18.

$$d_{bb,crush} = d_{bb} - 2t_{bb} \tag{5.18}$$

5.2.5. Deformation of crash boxes - metals

If the bumper beam has absorbed the maximum amount of energy, but there is still kinetic energy left in the impact, the crash boxes will start to deform. The energy absorption of the crash boxes can be split in both an elastic portion and a plastic portion, the elastic portion already being covered with the use of the coefficient of restitution. It should be noted that it is assumed that the behaviour of the two crash boxes found in the vehicle are identical. If the crash boxes are made from a ductile metal, this analysis method for progressive folding shall be used.

In section 2.6 several equations have been established based on progressive folding that can be used to analyze the structural behaviour of the crash boxes analytically. To analyze the metal crash boxes that are made from square extrusions, equation 2.8 can be used to find the static mean crush force and equation 2.9 to calculate the static peak force per crash box.

If the square extrusion is not filled with foam, the stroke efficiency is 0.64 for steel alloys and 0.76 for aluminium alloys. However, if the crash boxes are filled with aluminium foam equations 2.13, 2.14, 2.15 and 2.16 should be used to calculate the stroke efficiency.

When the metal crash boxes are made using the metal folding process equation 2.17 should be used to calculate the mean static mean crush force instead. It is assumed that the peak force can still be calculated using equation 2.9 and that the stroke efficiency is equal to the square metal extrusions without foam-filling.

Dynamic amplification factor

As explained in section 2.6.3 the inertia effects of the dynamic impact can be included to increase the accuracy of the prediction of the mean force and peak force of the metal crash boxes. The dynamic mean force can be calculated using equation 5.19, with $v_0 = 2.9167 m/s$. For most candidate designs this increases the mean force by a few percent, depending on geometry, material, and relative deformation. How to use this equation and how to find the value of C_{ine} is explained in section 2.6.3.

$$F_{avg}^{D} = F_{avg}^{S}\left[1 + C_{ine}\left(\frac{b_m}{t}\frac{\rho_0}{\sigma_0}v_0^2\right)^{1/2}\right] \tag{5.19}$$

Effective incidence angle

Due to the curvature of the RCAR bumper barrier the impactor locally has an incidence angle with respect to the crash boxes. Due to the elastoplastic deformation of the bumper beam, there is no contribution of the bumper beam to decrease this incidence angle. The incidence angle between the RCAR bumper barrier and the crash boxes at the location where they impact each other depends on the radius of the barrier and the lateral distance between the crash boxes, called $L_{unsupported}$, and can be calculated using equation 5.20.

$$\phi = R_{barrier} - \sqrt{R_{barrier}^2 - (L_{unsupported}/2)^2} \tag{5.20}$$

Since the radius of curvature of the RCAR bumper barrier is known to be 3400 mm, it is found that $\phi = 3.38$ degrees when $L_{unsupported} = 800 mm$. Using equation 2.6 to calculate the effect on the peak- and mean force, a reduction of 15.5% is found for this assumed value of $L_{unsupported}$.

In the analysis model it is calculated for each candidate design what the corresponding peak force and the dynamic mean force are. Then it is checked if the available crushing length, the total length multiplied by the stroke efficiency, is enough to fully absorb the remaining amount of energy that needs to be absorbed. If the necessary deformation of the crash boxes turns out to be larger than the allowed maximum deformation, then that means that this candidate design fails the RCAR full width load case as parts that are connected in a permanent manner will get damaged.

5.2.6. Deformation of crash boxes - composites

If the crash boxes are made from a brittle composite, the analysis method for progressive crushing shall be used. Foam-filled composite crash boxes are not considered as the literature study has shown that this is not advantageous. It is again assumed that both crash boxes show identical behaviour as the load case is symmetrical.

SEA is the Specific Energy Absorption showing how much energy can be absorbed per kg of material when using a proper detailed design. This value is found to be different for CFRP and GFRP. The Crush Load Efficiency is denoted as CLE, and shows the relation between F_{mean} and F_{peak}. The crush length efficiency is written as η_L and shows what percentage of the length of the crash boxes can be crushed, or what the maximum deformation is. The values that are used for both CFRP and GFRP can be found in section 4.1.

Now that these parameters are established, the mean sustained load F_m per crash box can be calculated backwards from the literature value for SEA using equation 5.21.

$$F_m = \frac{SEA \times \rho \times A}{\eta_L} \tag{5.21}$$

The peak force per crash box can also be calculated using equation 5.22.

$$F_{peak} = CLE \times F_m \tag{5.22}$$

The effective incidence angle as explained for the metal crash boxes is also applicable to the composite crash boxes. This means that a reduction in mean force is also applied here. The maximum amount of energy absorbed by crushing one crash box can then be calculated using equation 5.23.

$$E_{absorbed} = F_m \times L \times \eta_L \tag{5.23}$$

During the optimization it will be known how much energy there is still left in the system, making it more useful to turn equation 5.23 around in order to calculate the deformation needed. This can be seen in equation 5.24.

$$d = \frac{E_{absorbed}}{F_m} \tag{5.24}$$

The value of d can now be checked with $d_{max} = L \times \eta_L$. If the deformation necessary to absorb all the remaining energy in the system is larger than the allowed deformation, it means that this candidate design for the low-speed crash structures is unable to absorb the necessary amount of impact energy. This results in damage to permanently fixed components of the vehicle, and means the load case is not passed successfully.

If the value of d that was found is smaller than d_{max} it means that the load case is passed successfully.

5.2.7. Output parameters

If the deformation is possible for the current design of the rear low-speed crash structures, this means that the load case is succesfully passed. At this point all the deformations should be added in order to find the intrusion distance. This is shown in equation 5.25.

$$\delta = d_{bb,\,elastic} + d_{bb,\,elastoplastic} + d_{cb} \tag{5.25}$$

It is also desired to know the highest force that will act on the system during the impact to make sure the crash rails do not get damaged during this low-speed load case. This can be found by comparing F_{peak} of the crash boxes to $F_{plastic}$ of the bumper beam. The highest of these two (normally the crash box peak force) is the peak force of the entire system during the impact.

5.3. Analytical analysis: RCAR structural test

The RCAR structural test seems to be the most critical load case, due to the high impact speed and the offset of the impact, resulting in the energy absorption being concentrated in only one of the two crash boxes. Also the incidence angle has an influence on the structural behaviour. As can be seen in figure 5.14 first the amount of impact energy to be absorbed is calculated, through the determination of the coefficient of restitution and conservation of momentum. Then the energy absorption due to crushing of the bumper beam section is evaluated for metal bumper beams. If the bumper beam is made from a composite material this step is skipped. Finally the crash boxes are engaged and absorb the remainder of the impact energy through either progressive folding for metal crash boxes, or progressive crushing for composite crash boxes. A flowchart of these steps is shown in figure 5.15. The method to calculate the amount of impact energy that should be absorbed is shown in section 5.3.1. The behaviour and contribution of the bumper beam is shown in section 5.3.2 and the behaviour and contribution of the crash boxes is shown in section 5.3.3.

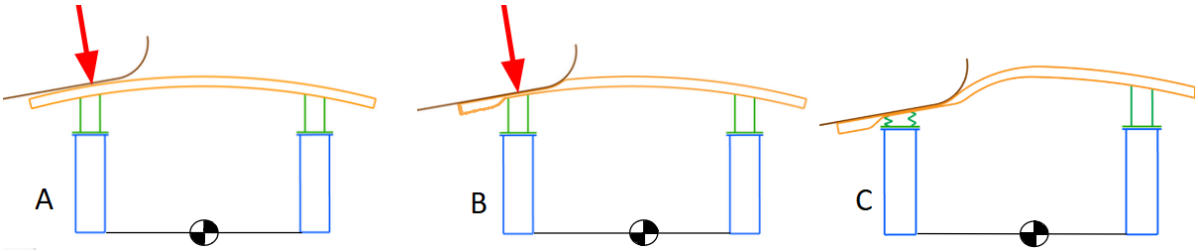

Figure 5.14: Different moments during the deformation: a) just before impact, b) when the bumper beam section is fully crushed , and c) fully deformed, all impact energy is absorbed

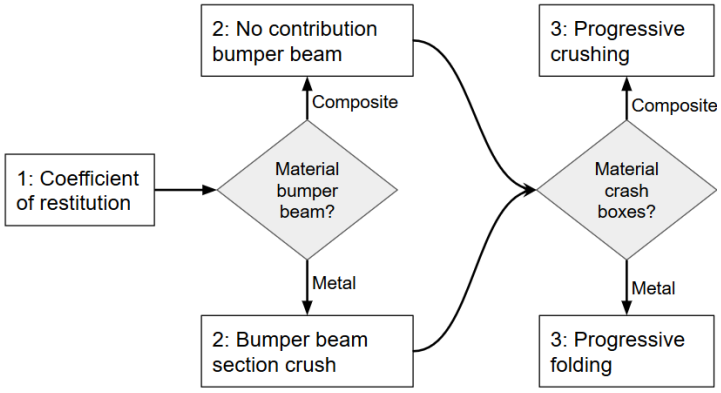

Figure 5.15: Flowchart of different steps in analysis method for RCAR structural test

5.3.1. Absorption of impact energy

From the definition of the load case in section 5.1 it is not directly clear how much energy needs to be absorbed by the rear low-speed crash structures. This depends not only on the elastic energy that is stored in the vehicle during the collision, but also on the velocity of both the vehicle and the barrier after the collision has occured and they are no longer in contact.

The coefficient of restitution is estimated using the trendline developed by Antonetti [7] and is found to depend only on the impact speed. This means the coefficient of restitution, ϵ, is constant for all vehicles and all candidate designs for the analysis performed during this thesis, and can be found in equation 5.26. In reality this is not true, so later in this section the sensitivity of the amount of energy to be absorbed to the coefficient of restitution is analyzed.

$$\epsilon = \frac{v'_{vehicle} - v'_{barrier}}{v_{barrier} - v_{vehicle}} = 0.5992^{\left(-0.2508 v_1 + 0.01934 v_1^2 - 0.001279 v_1^3\right)} = 0.2574 \tag{5.26}$$

In equation 5.26 $v_{barrier} = \frac{km/h}{3.6} = 4.4444\ m/s$ and $v_{vehicle} = 0\ m/s$, as this is given by the load case definition.

To find the actual velocities of both the vehicle and the barrier after the impact, an additional equation is needed. This can be found in the conservation of momentum, as shown in equation 5.27.

$$v_{vehicle} * m_{vehicle} + v_{barrier} * m_{barrier} = v'_{vehicle} * m_{vehicle} + v'_{barrier} * m_{barrier} \tag{5.27}$$

When solving equations 5.26 and 5.27 simultaneously it becomes possible to find the velocity of the vehicle and the barrier after the impact. The exact velocities depend on the mass of the vehicle, which is influenced by the candidate design for the low-speed crash structures. However, since the computational expense of solving this is relatively large and the influence of a small change in vehicle mass is very small it has been decided to only calculate the amount of impact energy that needs to be absorbed by the low-speed rear crash structures for the baseline vehicle weight. Calculating the amount of impact energy that needs to be absorbed is done using equation 5.28, which substracts the total kinetic energy in the system after the impact from the total kinetic energy before the impact.

$$E_{absorbed} = \frac{m_{barrier}}{2} v^2_{barrier} - \left[\frac{m_{vehicle}}{2} v'^2_{vehicle} + \frac{m_{barrier}}{2} v'^2_{barrier} \right] \tag{5.28}$$

A sensitivity analysis has been performed to find out what the influence is of variations in either the coefficient of restitution or the vehicle mass on the amount of energy that needs to be absorbed. A graphical representation can be found in figure 5.16. The vertical dashed line shows the coefficient of restitution that is based on the trendline by Antonetti (1999) and is used for this load case. The coefficient of restitution is varied between 0.2 and 0.35, as this is roughly the range of values found during the experimental testing performed by Antonetti, as can be seen in figure 2.12 in chapter 2.

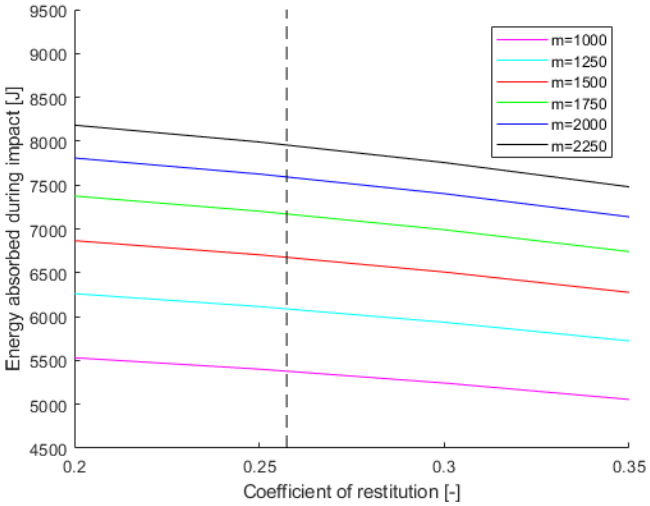

Figure 5.16: Sensitivity analysis of energy absorption to coefficient of restitution, for different values of vehicle mass

Interestingly, it has been found that the relative error of the amount of energy absorbed introduced by an inaccuracy in the coefficient of restitution is independent on the mass of the vehicle. The difference in absorbed energy between $\epsilon = 0.2$ ans $\epsilon = 0.35$ is found to be 9.4%, regardless of vehicle mass. When calculating the error around the assumed solution, it was found that the absorbed energy could be underestimated by a maximum of 2.4% and overestimated by a maximum of 6.8%. Based on this it has been concluded that the use of this trendline is acceptable, as the error diminishes in later steps.

The sensitivity of the amount of energy absorbed to the vehicle mass is shown in table 5.2. It can be seen that weight variations in lightweight vehicles have a larger effect on the amount of energy that is absorbed during the impact than for heavy vehicles, even when both the weight variation and the difference in absorbed energy are taken as relative to the baseline. This effect also seems to be visible in figure 5.16. However, the effect of the weight variation on the absorbed energy is in general small enough to yield accurate results without recalculating for each candidate design, drastically reducing computational expense of the analytical analysis of the RCAR structural test.

Table 5.2: Sensitivity of absorbed energy to weight variations

Baseline $m_{vehicle}$	**Weight variation[kg]**	**Weight variation [%]**	**Difference in $E_{absorbed}$ [%]**	**Difference in $E_{absorbed}$ [J]**
1000	10	1	0.59	31.4
1500	15	1	0.49	32.2
2000	20	1	0.41	31.1

5.3.2. Contribution of bumper beam

During the RCAR structural test the contribution of the bumper beam is assumed to consist only of the crushing of the section if the bumper beam is made from a ductile metal. If the bumper beam is made from a brittle composite, it is assumed that there is no contribution from the bumper beam during the RCAR structural test. The energy absorption of the crushing of the bumper beam section is calculated using the same method as shown in section 5.2.4. The combined equation for the energy absorption is slightly different though, as during this load case the section is being crushed on only one side of the bumper beam. The updated equation for the energy absorption during the RCAR structural test is shown in equation 5.29.

$$EA_{total} = 2M_p\pi + 4M_p\frac{1}{2}\pi = 4M_p\pi \tag{5.29}$$

Where M_p is the fully plastic moment as calculated in section 5.2.4. The intrusion distance is calculated in the same way, and is equal to $d_{bb} - 2t_{bb}$.

5.3.3. Contribution of crash boxes

The moving barrier has a 10 degree incidence angle with respect to the vehicle. This means that the loading on the crash box will not be axial, as during the RCAR full width test, but also under the same 10 degree incidence angle. In section 2.5 it has been investigated what the effect is on the structural behaviour of the crash boxes. A trendline for the relationship of the l/b ratio and the critical load angle where the bending behaviour starts dominating has been found.

If the critical load angle is too low and bending behaviour starts to dominate, up to 60% of the mean force (and therefore also energy absorption) is lost. A design for which this happens can never be the preferred design, and therefore it has been decided to automatically fail all candidate designs if they do not comply with the maximum l/b ratio as calculated later.

To be on the safe side, it has been decided to choose the maximum allowed l/b ratio such that the critical load angle is a minimum of 12 degrees. Based on equation 2.5 and the defined minimum value for the critical load angle of 12 degrees, a maximum l/b ratio of 4.8 was found. This means that the candidate designs will be checked, and if their l/b ratio is larger than 4.8 they will be removed.

The presence of the bumper beam influences the effective incidence angle between the RCAR mobile barrier and the crash box, as it is physically in between the two. To estimate this effect, the effective incidence angle that is used to calculate the reduction in mean force is taken as the angle between the RCAR mobile barrier and the bumper beam at the point where the crash box is attached. This angle is calculated using equation 5.30.

$$\phi = 10 - \arctan\left(\frac{R_{bb}/2 - \sqrt{(R_{bb}/2)^2 - \left(L_{unsupported}/2\right)^2}}{L_{unsupported}/2}\right) \tag{5.30}$$

The reduction in force can be calculated using equation 2.6 in section 2.5, using the incidence angle ϕ as calculated using equation 5.30. To give examples, it has been found that the mean force is decreased by 25.36% if the bumper beam is straight, but only by 11.7% if the bumper beam has a radius of curvature of 3000 mm (with an effective incidence angle of 2.27 degrees). During the structural analysis this reduction in force is taken into account for both the mean force and peak force.

Metal crash boxes

The structural behaviour of the metal crash boxes during the RCAR structural test is calculated using almost the same method as during the RCAR full width test, as documented in section 5.2.5. The difference is that

instead of both crash boxes only a single crash box is used to absorb the energy, and that the mean force and peak force are reduced by a different amount due to the incidence angle of the impact.

The dynamic amplification factor, as found in equation 5.19 and explained in section 2.6.3, is also applicable here. With the mean force being known, it is checked whether it is possible to absorb the amount of impact energy that is necessary within the maximum deformation length. If it is not, the candidate design is discarded as this would lead to permanent damage to the crash rails. If it is possible, the peak force and the intrusion distance are saved to later be used to calculate the crash rails weight penalty (if applicable) and for the performance evaluation.

Composite crash boxes

The structural behaviour of the composite crash boxes during the RCAR structural test is calculated using almost the same method as during the RCAR full width test, as documented in section 5.2.6. The differences are that instead of both crash boxes only a single crash box is used to absorb the energy, and that the literature value for the SEA is reduced by a certain amount due to the incidence angle of the impact. This reduction influences the mean force and peak force.

With the mean force being known, it is checked whether it is possible to absorb the amount of impact energy that is necessary within the maximum deformation length. If it is not, the candidate design is discarded as this would lead to permanent damage to the crash rails. If it is possible, the peak force and the intrusion distance are saved to later be used to calculate the crash rails weight penalty (if applicable) and for the performance evaluation.

5.4. Analytical analysis: RCAR corner test

The RCAR corner test has been created to ensure that the vehicle's bumper beam can also protect the corners of the vehicle during collisions with a small overlap. The difficulty in passing this test lies in creating enough overlap between the bumper beam and the barrier to get a stable impact without the vehicle moving sideways and the barrier passing past the bumper beam, damaging the corner of the vehicle. Even though the impact speed is only 5.5 km/h, the crash boxes can not be used for absorption of the impact energy as the impact location has too much lateral distance from them, and the bumper beam is not made to transfer this shear force.

For this analysis the situation is modelled as a cantilever beam, where only the part of the bumper beam extending laterally from the crash boxes is considered. The connection between the bumper beam and crash box is considered to be clamped as the crash box should be stiff enough that it will resist rotation and displacements. The load is applied at the center point of the contact patch between the bumper beam and the barrier. Schematic representations of the RCAR corner test and the cantilever beam model can be seen in figures 5.17 and 5.18 respectively.

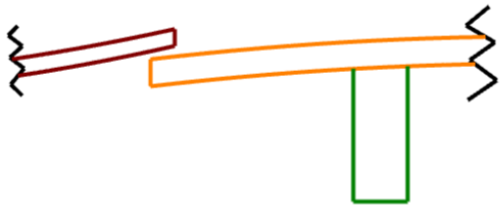

Figure 5.17: Schematic representation of RCAR corner test

Figure 5.18: Cantilever beam model of RCAR corner test

The method to calculate the amount of energy that should be absorbed is shown in section 5.4.1. The structural behaviour during the elastic portion is discussed in section 5.4.2, and during the elastoplastic portion due to the development of a plastic hinge (only for metal bumper beams) in section 5.4.3. A flowchart of the process for both material types is shown in figure 5.19.

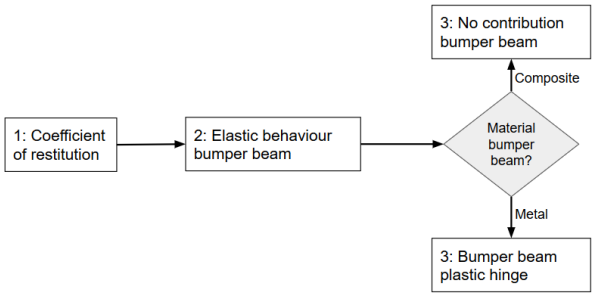

Figure 5.19: Flowchart of different steps for RCAR corner test

5.4.1. Absorption of energy

Due to the elastic energy stored in the vehicle not the full amount of kinetic energy has to be absorbed during the RCAR corner test. The estimation of the coefficient of restitution and therefore amount of energy that should be absorbed is done using the same method as the RCAR full width bumper test. The coefficient of restitution is calculated using the trendline from Antonetti [7] and is found to be $\epsilon = 0.4254$. This means that the amount of energy absorbed is only dependent on the vehicle mass and can be calculated using equation 5.31.

$$E_{absorbed} = \frac{m_{vehicle}}{2} 1.53^2 - \frac{m_{vehicle}}{2} 0.65^2 = 0.96 m_{vehicle} \tag{5.31}$$

5.4.2. Structural behaviour during elastic phase

Modelling the situation as a cantilever beam makes it easy to analyze the structural behaviour during the elastic phase as these equations are well-established. The maximum bending moment is found at the support, and the bending moment corresponding to the onset of yield can be calculated using equation 5.2. For composite bumper beams equation 5.32 should be used to find the bending moment corresponding to failure.

$$M_u = \frac{\sigma_u I}{0.5d} \tag{5.32}$$

Where d is the depth of the bumper beam section. The corresponding applied force is calculated using equation 5.33.

$$F = ML_{free} \tag{5.33}$$

Where L is the free length of the bumper beam between the support and the location where the load is applied. To find the free length it is first necessary to estimate the width of the overlap between the bumper beam and the barrier, which is done using equation 5.34.

$$w_{overlap} = 0.15 w_{vehicle} - \frac{w_{vehicle} - L_{bb}}{2} - 25.4mm \tag{5.34}$$

Where L_{bb} is the length of the bumper beam, and the substraction of 25.4 mm is done to allow for proper contact between the barrier and bumper beam, where this 25.4 mm is the dimension of the radius on the edge of the barrier as defined in section 5.1. Now the free length can be calculated using equation 5.35.

$$L_{free} = \frac{L_{total}}{2} - \frac{L_{unsupported}}{2} - w_{cb} - \frac{w_{overlap}}{2} \tag{5.35}$$

Where $L_{unsupported}$ is the lateral distance between the crash boxes (an input from the vehicle parameters) and w_{cb} is the width of the crash boxes. Now that the free length is known, the longitudinal deflection at the point of impact can be calculated using equation 5.36.

$$d = \frac{FL_{free}^3}{3EI} \tag{5.36}$$

The corresponding energy absorption is calculated using equation 5.37.

$$E = \frac{1}{2} Fd \tag{5.37}$$

Contribution of barrier foam

Since the barrier used for this test is the same as during the RCAR full width bumper test, there is a layer of energy absorbing foam present on the barrier, whose properties are defined in section 5.2. The data provided by the test procedure is based on a 100x160 mm contact patch, which is considered to be the standard contact patch for the RCAR full width bumper test. For the RCAR corner test the size of the contact patch is dependent on the geometry, especially the length, of the bumper beam. As the width of the contact patch has been determined earlier using equation 5.34 and the height of the barrier is known to be 100 mm, the area of the contact patch can be calculated using equation 5.38.

$$A_{contact} = 100 w_{overlap} \tag{5.38}$$

With the area of the contact patch known, the corresponding force and energy absorption of the barrier foam can be calculated as a ratio of the values from the RCAR full width bumper test, as shown in equation 5.39 and 5.40 respectively.

$$F_{foam} = \frac{A_{contact}}{16000} F_{full} \tag{5.39}$$

$$E_{foam} = \frac{A_{contact}}{16000} E_{full} \tag{5.40}$$

Where F_{full} and E_{full} are the force and energy as calculated for the RCAR full width bumper test. Also during this load case it is checked if the impact force is high enough to fully compress the foam, and if it is not only the relevant portion of the energy absorption is taken into account. Because of the small deformations until yielding for metal bumper beams or failure for composite bumper beams is reached, only a very small amount of energy can be absorbed during the elastic phase.

5.4.3. Structural behaviour during elastoplastic phase

If the bumper beam is made from a metal, after the onset of yielding the elastoplastic behaviour will also be able to absorb a part of the impact energy. If the bumper beam is made from a brittle composite material, this part of the analysis should be skipped. The elastoplastic behaviour is modelled using a plastic hinge that forms at the connection of the bumper beam to the crash box, allowing the free end of the beam to rotate.

The fully plastic moment of the bumper beam is, equal to what was found in section 5.2, found to be $M_p = \frac{3}{2} M_y$. This fully plastic moment is reached when the curvature is around 5 times the curvature at the point of yielding, which will happen at a small deformation already, since the deformation during the elastic phase is so small. Therefore it is assumed that the fully plastic moment can be used for the entire elastoplastic phase.

It is necessary to define when the rotation of the free end of the beam becomes too large, as theoretically the rotation could be up to 90 degrees if the alloy's elongation before break is large enough. For this, two criteria have been established:

1. Minimum width of overlap, $w_{min} = 0$ mm
2. Maximum rotation, θ_{max}=20 deg

The first criterion is the minimum width of the overlap between the bumper beam and the barrier. When the free end rotates, the lateral length becomes shorter. If the overlap becomes too small, there is a high risk of the barrier slipping next to the bumper beam. This would lead to unnecessary damage and is therefore unacceptable. The angle of rotation at which this happens can be calculated using equation 5.41.

$$\theta = cos^{-1}\left(\frac{L_{free} - w_{min}}{L_{free}}\right) \tag{5.41}$$

The second criterion is the maximum rotation that is allowed of the free end. When this rotation becomes large, a lateral component of the impact force develops, potentially causing the barrier and bumper beam to slip with respect to each other, again leading to unnecessary damage. In the analytical model these two criteria are taken into account by calculating the rotation corresponding to the minimum width of the overlap. The rotation angle is then set to the smaller of the two. The amount of energy absorbed during the elastoplastic phase can then be calculated using equation 5.16, and the corresponding longitudinal deformation using equation 5.42.

$$\delta_{elastoplastic} = tan(\theta)\, L_{free} \tag{5.42}$$

5.5. Additional notes on the structural analysis

In this section two additional notes are provided on the structural analysis. These do not fit in the analyzed load cases, but they are necessary to provide the full picture for the structural performance. Section 5.5.1 shows the adjustments that are made in order to make the intrusion distances during the three different load cases correspond correctly. In section 5.5.2 it is shown how the weight penalty of the crash rails is calculated in case that the peak force on the low-speed crash structures becomes too high for the crash rails to handle. This is done to increase the accuracy of the weight estimation by including the effect of the candidate design on the crash rails. In section 5.5.3 an upper limit is enforced on the peak force of the low-speed crash structures, to ensure that the accelerations during high-speed impact do not become dangerously high.

5.5.1. Congruency of intrusion distance

It was found that, based purely on geometrical reasoning, the three values for intrusion distance that are calculated do not have an equal influence on the extent to which the vehicle is damaged, or the dimensions of the trunk (and in the case of an SEV the solar array). The main reason of this is that the intrusion distance is calculated from the point of impact of the barrier, in the longitudinal direction. When the bumper beam is curved, this means for example that the intrusion of the RCAR corner test starts further towards the front of the vehicle than during the RCAR full width test.

It has been decided to define the intrusion distance of the low-speed rear crash structures as the intrusion distance during the RCAR structural test. This load case is critical for the length of the crash boxes, and therefore determines the location of the attachment to the crash rails. The RCAR structural test has the highest impact speed, and therefore also the highest amount of impact energy that needs to be absorbed. If a different load case would be considered as defining for the intrusion distance, that means that less than the full length of the crash boxes would be utilized, leading to a non-optimal design. Based on this it is decided to automatically fail candidate designs for which the (adjusted) intrusion distance of either the RCAR full width test of the RCAR corner test is larger than the intrusion distance for the RCAR structural test.

To show graphically what this intrusion distance means for the part of the vehicle where damage will occur during low-speed impact, figure 5.20 is presented here. The candidate design is plotted, together with the intrusion distance during all three loadcases that are considered. The black dashed line is the limit of the damaged area, as defined by the intrusion distance during the RCAR structural test.

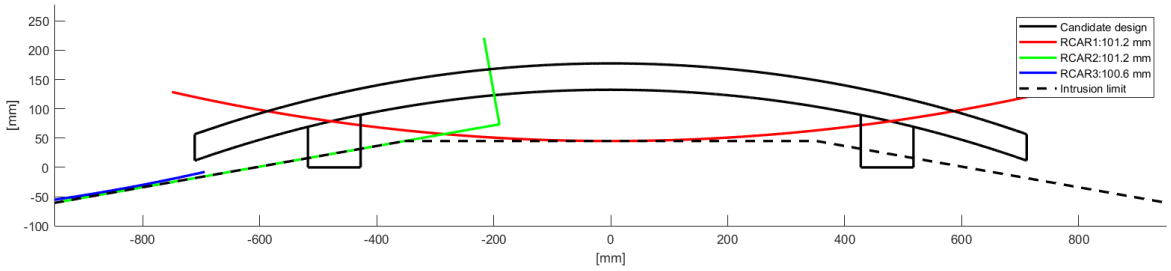

Figure 5.20: Example of intrusion distance combination shown on candidate design

It can be seen that the limit of the damaged area is a horizontal line in between the crash boxes, and slopes towards the front of the vehicle with a 10 degree angle (equal to the incidence angle of the RCAR structural barrier) further outside of the crash boxes. The adjustments to the intrusion distance of the RCAR full width test and the RCAR corner test are necessary to make sure that an equal intrusion distance for all three load cases means that all three different barriers that are shown in the figure are touching the dotted line, which will be called the intrusion limit.

Adjustment for RCAR full width test

To let the intrusion distance of the RCAR full width test correspond properly with the intrusion distance during the RCAR structural test, an adjustment needs to be made. The approach that is used here is to first calculate at what intrusion distance the RCAR barrier will exactly reach the intrusion limit during the RCAR full width test. It is then calculated what the difference is between this maximum intrusion distance and the actual intrusion distance. Then, this difference is subtracted from the intrusion distance that was found for

the RCAR structural test. The maximum intrusion distance for the RCAR full width test can be calculated using equation 5.43.

$$\Delta_{max} = L_{cb} + \left[R_{bb} - \sqrt{R_{bb}^2 - \left(\frac{L_{unsupported} + w_{cb}}{2} \right)^2} \right] \tag{5.43}$$

Where the term within square brackets calculates the difference in longitudinal location between the points of impact during the RCAR full width test and the RCAR structural test. The difference between the actual intrusion and the maximum intrusion distance can then be calculated using equation 5.44.

$$\Delta L = \Delta_{max} - \delta_{intrusion,fullwidth} \tag{5.44}$$

The updated intrusion distance for the RCAR full width test can then be calculated using equation 5.45.

$$\delta`_{intrusion,fullwidth} = \delta_{intrusion,structural} - \Delta L \tag{5.45}$$

Adjustment for RCAR corner test

To let the intrusion distance of the RCAR full width test correspond properly with the intrusion distance during the RCAR structural test, an adjustment needs to be made. This adjustment is again based on the difference between the actual intrusion of the design and the maximum intrusion before the intrusion limit is reached. The maximum intrusion distance can be calculated using equation 5.46.

$$\Delta_{max} = L_{cb} + d_{bb} + \left[R_{bb} - \sqrt{R_{bb}^2 - \left(\frac{L_{unsupported} + w_{cb}}{2} \right)^2} \right] - \left[R_{bb} - \sqrt{R_{bb}^2 - \left(\frac{L_{bb}}{2} \right)^2} \right] + (\tan(10) \times L_{extra}) - (L_{cb} + d_{bb} - \delta_{intrusion,structural}) \tag{5.46}$$

In which the part up to (and including) the second part in square brackets calculates the longitudinal distance between the impact point during the RCAR corner test and the attachment of the crash boxes to the crash rails. The term in round brackets at the end calculates the length of the crash box plus bumper beam when fully compressed, as this determines the point through which the sloped part of the intrusion limit passes through. The final term calculates the longitudinal distance between the location of the fully compressed crash box plus bumper beam and the intrusion limit at the lateral location of the impact point during the RCAR corner test. L_{extra} is calculated using equation 5.47.

$$L_{extra} = 0.5 L_{bb} - \left(\frac{L_{unsupported} + w_{cb}}{2} \right) \tag{5.47}$$

The difference between the maximum intrusion distance and the actual intrusion distance can then be calculated using equation 5.48.

$$\Delta L = \Delta_{max} - \delta_{intrusion,corner} \tag{5.48}$$

The updated intrusion distance for the RCAR corner test can then be calculated using equation 5.49.

$$\delta`_{intrusion,corner} = \delta_{intrusion,structural} - \Delta L \tag{5.49}$$

5.5.2. Weight penalty crash rails

The design of the low-speed crash structures has a direct influence on the design of the crash rails due to two main reasons. The first one is that there is a limited amount of longitudinal space available in the vehicle for the combination of the crash rails and the low-speed crash structures. The second one is that the crash rails should not get damaged when the low-speed crash structures are absorbing the impact energy of low-speed impacts. In order to take this interaction effect into account during the optimization of the low-speed rear crash structures a simplified crash rail geometry is also calculated. The main parameter of interest is the weight, but to calculate this the simplified geometry and material needs to be known.

For all candidate designs it is assumed that the crash rails are made out of the AL6061-T6 alloy, which has a density of 2710 kg/m3, and a flow stress of 287 MPa. For the geometry a square thin-walled cross-section is

assumed, with a section width of 150 mm but with an unknown wall thickness allowing to tweak the desired sustained load and therefore energy absorption levels. The length of the crash rails is calculated from the total length that is available, minus the longitudinal length of the low-speed crash structures. This is calculated using equation 5.50 if the bumper beam is straight, or equation 5.51 if the bumper beam is curved.

$$L_{cr} = L_{total} - (L_{cb} + d_{bb}) \tag{5.50}$$

$$L_{cr} = L_{total} - \left[L_{cb} + d_{bb} + \left(R_{bb} - \sqrt{R_{bb}^2 - (0.5L_{unsupported})^2}\right)\right] \tag{5.51}$$

Where d_{bb} is the depth of the bumper beam, R_{bb} is the radius of curvature of the bumper beam and $L_{unsupported}$ is the lateral distance between the crash rails.

The amount of energy that should be absorbed by the crash rails is determined by the highest speed rear impact load case, being FMVSS 301 [7] with a 1367.6 kg barrier hiting the rear of the vehicle at 79.3 ± 0.8 km/h, minus the amount of energy that can be absorbed by the low-speed crash structures during this load case. The maximum energy absorption of the low-speed rear crash structures is estimated as two times the impact energy during the RCAR structural test, as this is the most critical low-speed test and the energy is absorbed using only one of the two crash boxes and one half of the bumper beam. The energy absorption of the low-speed crash structures during the FMVSS 301 load case is underestimated by a few percent in certain cases, as the dynamic amplification factor (if applicable) will be higher here because of the higher impact speed. To calculate the amount of energy that should be absorbed during the FMVSS 301 load case the corresponding coefficient of restitution, $\epsilon = 0.0000257$, is used. Using the same method as how the energy to be absorbed is calculated for the RCAR structural test in section 5.3, the equations for the coefficient of restitution and conservation of momentum are solved simultaneously for the baseline weight of the vehicle. The amount of energy that should be absorbed by the crash rails during the FMVSS 301 load case can then be calculated using equation 5.52.

$$E_{CR} = E_{FMVSS301} - 2 \times E_{RCAR,structural} \tag{5.52}$$

During the FMVSS 301 test a mobile deformable barrier is used, on top of which an energy absorbing honeycomb is attached. This means that part of the impact energy does not have to be absorbed by the crash rails of the vehicle, but is instead absorbed by the honeycomb. For the estimation of the energy absorption of the honeycomb a stroke efficiency of 0.7 is assumed [8]. It is assumed that the honeycomb is fully compressed over the full overlap width between the bumper beam of the vehicle and the mobile deformable barrier. This overlap width is estimated as 55% of the vehicle width. This results from an estimated bumper beam length of 70% of the vehicle width, and a 70% overlap between the mobile deformable barrier and the vehicle. Based on these assumptions, it is found that a total of 73.1 kJ of impact energy is absorbed by the honeycomb on the mobile deformable barrier. This means equation 5.52 should be updated to equation 5.53.

$$E_{CR} = E_{FMVSS301} - 73.1\ \text{kJ} - 2 \times E_{RCAR,structural} \tag{5.53}$$

The desired mean sustained crash force per crash rail can then be calculated using equation 5.54.

$$F_{mean} = \frac{E_{rails}}{2L_{cr}\eta_L} \tag{5.54}$$

Where $\eta_L = 0.76$, the crush length efficiency for aluminium square thin-walled columns. The peak force per crash rail can be calculated using equation 5.56. Now it is possible to use a rewritten version of equation 2.7 to calculate the necessary wall thickness, as shown in equation 5.55.

$$t = \left[\frac{F_{mean}}{13.06\,\sigma_0\,b_m^{1/3}}\right]^{3/5} \tag{5.55}$$

With the wall thickness being known, the desired simplified geometry of the crash rails to absorb just enough energy is known and the weight of the crash rails can be calculated. However, it should be checked if the peak force on the low-speed crash structures does not exceed the peak force of the crash rails. A safety factor of

[7] `https://www.nhtsa.gov/sites/nhtsa.dot.gov/files/tp-301r-02.pdf`, accessed on 18/12/2019
[8] HexWeb Honeycomb Energy Absorption Systems - Design Data

1.2 is added due to the importance of the crash rails not being damaged during low-speed impact. The value of this safety factor is rather low, based on the results found during validation of the structural performance, where the peak force was shown to be between 1.6% and 5.2% lower than predicted by the analytical model. The peak force of the crash rails can be calculated using equation 5.56, where CLE = 0.48, the crush load efficiency for aluminium square thin-walled columns.

$$F_{peak} = \frac{F_{mean}}{CLE} \tag{5.56}$$

If the peak force on the low-speed crash structures is too high, the crash rails wall thickness will be chosen such that the crash rails peak force is exactly 1.2 times the low-speed crash structures peak force. This will lead to an increased weight, and more energy than necessary can be absorbed during high-speed rear impact. In certain cases this can be worth it for the reduction of the intrusion distance. The weight of the crash rails is saved for each candidate design, and taken into account later during the performance evaluation of the candidate designs.

5.5.3. Maximum allowed force on crash boxes

Due to the method that is used to generate the candidate designs, it is possible that the forces on the crash box become so high that the acceleration on the vehicle during the high-speed load cases reaches a level that it is no longer safe for the occupants. The maximum allowed acceleration in the high-speed load case is decided to be 25 g, as this is the standard design crash pulse for frontal high-speed impact. It was also found that the tolerance of the human body to +Gx ('eyes-out', frontal impact) is 28g for a time period of less than 1 second, while for -Gx ('eyes-in', rear impact) the tolerance is 35g for a time period of less than 1 second [9]. This corresponds to the mean sustained crush force on both crash rails together, through the mass of the vehicle. The acceleration corresponding to the peak force on the crash rails is allowed to be higher, as this acceleration will only happen during a very short time and this peak acceleration is not directly on the occupants. It is important to realize that, when the accelerations on the vehicle during rear high-speed impact become very high, what this could mean to the 'perceived safety' of the vehicle.

The maximum allowed acceleration of the vehicle can be related to the maximum allowed peak force on the crash boxes using a similar methodology as for the crash rails weight penalty in section 5.5.2. To be in agreement with the methodology for the crash rails weight penalty, a safety factor of 1.2 between the peak force of the crash rails and the crash boxes is used. The maximum peak force on a single crash rail can be calculated using equation 5.57.

$$F_{rail_{max}} = \frac{\frac{1}{2} \times m_{vehicle} \times 25\ g}{0.48} \tag{5.57}$$

Where the factor $\frac{1}{2}$ is used to go from both crash rails to a single one, $g = 9.81 m/s^2$ and the kerb weight of the vehicle is used as this is how the ECE-R32 load case is defined. The corresponding maximum allowed peak force on a single crash box can then be calculated using equation 5.58.

$$F_{cb_{max}} = \frac{F_{rail_{max}}}{1.2} \tag{5.58}$$

Where 1.2 is the safety factor as mentioned before. All the candidate designs are checked whether the peak force on the crash boxes does not exceed the maximum that is allowed. If this maximum is exceeded, the candidate design is considered invalid.

[9] `https://www.wired.com/2011/04/crashing-into-wall/`, accessed on 09/12/2019

6

Manufacturing cost model

In this chapter the simplified cost model that has been developed is explained. It should be emphasized that this cost model is not the focus of this thesis, but it is necessary to have an estimation of the manufacturing cost of the candidate design to properly evaluate the candidate design. Most of the values that are used in this chapter are based on personal experience or estimations, unless a different source is explicitly stated.

The manufacturing cost of a candidate design consists of two distinct parts. The first part consists of the recurring costs in section 6.1, which are the costs associated with the manufacturing of one additional part. The second part consists of the non-recurring costs in section 6.2. These non-recurring costs can be seen as up-front investments that can be spread over all the parts that are manufactured. The non-recurring cost that is incorporated in this cost model is the tooling cost, as shown in section 6.2. In section 6.3 it is shown how all these separate cost components are brought together to represent the manufacturing cost of the candidate design.

6.1. Recurring costs

Recurring costs are the costs that are associated with the manufacturing of one additional part. The recurring costs that are incorporated in this model are the material cost in section 6.1.1, equipment cost in section 6.1.2, labour cost in section 6.1.3, and additional operations that need to be performed in section 6.1.4. It should be noted that the learning curve effect and the cost of assembling the crash boxes and bumper beam together are not taken into account.

6.1.1. Material cost

The first recurring cost parameter is the base material cost. This is the cost in euro per kg to buy the base material that will be used during the manufacturing process. The values used for all the materials that are considered in the model can be seen in table 6.1. Here it becomes immediately clear that there are large differences in price between mainly the different material groups, but also within the groups the difference can be large. The base material cost for the steel alloys and composites is taken from CES EduPack 2019, but the base material cost for aluminium alloys is based on a personal estimation as data for material cost with heat treatment included has not been found.

Table 6.1: Material base cost for the considered materials (CES EduPack 2019)

Steel alloys		**Aluminium alloys**		**Composites**	
Name	**Cost [€/kg]**	**Name**	**Cost** [1] **[€/kg]**	**Name**	**Cost [€/kg]**
AISI 1020	0.65	AL6061 T6	2.5	Carbon/epoxy	33.63
DP800	0.7	AL2024 T4	3.5	Glass/epoxy	25.0
YS800	1.25	Advanz 6CM-s300 T4	2.0		
		Advanz 6CM-s300 T61	3.0		

[1] Personal estimation

In certain candidate designs the crash boxes are filled with an aluminium foam. The price of this foam is considered to consist only of the base material cost, and is therefore only dependent on the mass of the foam used in the crash box and the price per kg. The price per kg can be found in table 6.2.

Table 6.2: Cost of aluminium foams with varying density, values based on CES EduPack 2019

Foam density [kg/m3]	**Cost [€/kg]**
170	12.89
340	10.33
510	8.01

Scrap rate

During most manufacturing processes a percentage of the base material does not end up in the final product, but is wasted. For most metal manufacturing processes the scrap rate is quite low, but for composite processes the base cost of the scrapped material can become a significant part of the total manufacturing cost. An overview of the scrap rates used in the model can be seen in table 6.3. It should be noted that these values are rough estimations.

Table 6.3: Estimated scrap rates for metal and composite manufacturing processes

Metals		**Composites**	
Process	**Scrap rate [%]**	**Process**	**Scrap rate [%]**
Extrusion	10	Braiding	5
Folding	10	Prepreg	15
		Vacuum-infusion	15

6.1.2. Equipment cost

In this section the parameters needed to calculate the cost of the equipment used during the manufacturing are presented. An overview of these parameters is shown in table 6.4. These values are again estimated based on personal experience.

Table 6.4: Parameters used to calculate the cost of the equipment used during manufacturing

Process	**Equipment cost [€/hour]**	**Parts per hour**	**Equipment cost per part [€]**
Extrusion	300	100	3
Folding	50	60	0.83
Braiding	300	30	10
Prepreg	50	0.5 x number of tools	100/number of dies
Vacuum-infusion	50	0.5 x number of tools	100/number of dies

For the extrusion process it can be seen that the equipment cost is high as the direct hot extrusion process is used, which means a lot of energy is needed for the heating system. It is estimated that per hour 100 parts can be made

For the metal folding process the equipment cost is very low, as it is assumed to consist mainly of manual brake presses. Due to the simplicity of the considered geometries a high amount of parts per hour, 60, is assumed.

The equipment cost of the fiber braiding process is high, as a large, highly complex and automated machine is needed for the process. Due to the high fiber deposition rate that can be achieved with this process it is assumed that per hour 30 parts can be manufactured.

For both the prepreg and the vacuum-infusion process the equipment cost per is relatively low as this consists of only the autoclave. However, the amount of parts that can be manufactured per hour is low, as the cure cycle is estimated to take two hours. The amount of parts per hour is dependent on the number of tools that

is used simultaneously, as multiple parts would fit in the autoclave at the same time. It is likely that multiple tools are used at the same time as the amount of parts per tool per unit of time is very low and the tooling cost is low as well.

6.1.3. Labour cost

In this section it is explained how the labour cost portion of the manufacturing cost is calculated. The parameters that are used to calculate the labour cost are shown in table 6.5. These parameter values are based on personal experience, and are for now assumed to be independent of the size of the part.

Table 6.5: Parameters used to calculate the labour cost

Process	**Labour cost [€/hour]**	**Parts per hour**	**Labour cost per part [€]**
Extrusion	40	100	0.4
Folding	40	20	2
Braiding	40	30	1.33
Prepreg	40	0.5	80
Vacuum-infusion	40	1	40

From the combination of tables 6.4 and 6.5 it can be seen that for the extrusion process only one employee is used during the process for monitoring of the equipment. During the folding process three employees are working continuously, one operating the brake press and the other two performing the assembly steps. The braiding process uses only one employee. For prepreg and vacuum-infusion the amount of parts that can be manufactured per employee per hour is very low, 0.5 and 1 respectively. This leads to a very high labour cost per part.

6.1.4. Additional operations

Some parts of the manufacturing cost do not strictly fit under the model parameters as mentioned before, but can be seen as additional costs arising from the choice of a certain manufacturing process. The following additional costs have been identified and included in the model:

- Extrusion: cost of cutting to length. The extrusion process creates a part with a theoretically unlimited length. To create parts with the desired length, it is necessary to perform a cutting operation. This cutting operation is estimated to add €0.2 per part.
- Folding: cost of assembly of shells. Due to the inherent need of assembling the two shells into a closed-cross-section, an additional €1 per part is added for the mechanical fixings and/or adhesive that is used for this.
- Metal crash boxes: adding the trigger mechanism. The trigger mechanism often consists of one or more circular holes drilled into the finished part or stamped into the base sheet. To include this an additional €0.5 per metal crash box is added.
- Curved metal bumper beams: cost of the roll bending process to create curved geometry from a straight extrusion. With the roll bending no part specific tooling is necessary, so it is assumed that there are no non-recurring (tooling) costs. An additional €3 per curved metal bumper beam is added to include this in the model.
- Composite crash boxes: adding the trigger mechanism. With composites the trigger mechanism most often consists of a tapered edge on one of the sides, made by machining the part after it is finished. To include this in the model, an extra €2 per composite crash box is added.

6.2. Non-recurring costs

In this section it is shown how the non-recurring costs are taken into account during the calculation of the manufacturing cost of the candidate designs. The only non-recurring cost that is incorporated here is the tooling cost. In order to translate the tooling investment to the cost per part produced, it is necessary to know the total production volume. The determined tooling cost can then be divided over the total amount of parts produced. This also means that when a large amount of vehicles is manufactured, a higher investment can be accepted. It is interesting to note that the design of the crash boxes is identical, so the amount of crash

boxes produced is two times the amount of vehicles produced. For the bumper beam the amount of parts produced is equal to the amount of vehicles produced.

Tooling cost

The cost of tooling depends on the process that is used, but also on the material, dimensions and complexity of the part that needs to be manufactured. The complexity for all the parts are taken as equal during this optimization, which removes the need to include that parameter. The calculations of the tooling cost are based on personal experience and are not verified or validated in any way. When the metal folding process is used, the tooling cost is zero as no tooling is needed. The different punches and dies that are needed for this process are considered to to be part of the equipment cost, as these tools are not specific for the part that will be manufactured.

When extrusion is used as the manufacturing process, the tooling cost in € will be estimated using equation 6.1. This equation includes the part's material, the minimum diameter of the circle in which the cross-section fits and a factor to scale towards the desired tooling cost in €.

$$C_{tool,extrusion} = a \times \left(\frac{D}{2}\right)^2 \times 3 \tag{6.1}$$

Where a is a dimensionless parameter that is used to differentiate between tooling for aluminium or steel parts, as $a = 1$ for aluminium and $a = 5$ for steel. This distinction is made because it is much more difficult to extrude steel alloys, and the extrusion die needs to be made from stronger and more high-temperature resistant material. The minimum diameter $D = \sqrt{2} \times w_{cb}$ (in mm) for the square crash box cross-section and $D = \sqrt{h^2 + d^2}$ (in mm) for the rectangular bumper beam cross-section, as this is the diameter of the smallest circle that fits around the cross-section. This diameter is divided by two to get the radius, and is then squared to represent its influence on the size of the extrusion die.

For the braiding process a mandrel is needed to be the base geometry the fibers are braided around. This mandrel is a simple tool, especially since the cross-sections of both the composite crash boxes and the bumper beam are constant. The cost of the tool is dependent mainly on the size of the part, and therefore the volume of the tool itself. The type of fiber does not influence the cost of the tool. The tooling cost in € can be estimated using equation 6.2.

$$C_{tool,braiding} = 0.002 \times A \times L \tag{6.2}$$

Where A is the area of the solid cross-section in mm^2 corresponding to the part, and L is the length of the part to be manufactured in mm.

When either prepreg or vacuum-infusion is chosen as the manufacturing method the necessary tooling is simple. The tooling cost is again dependent mainly on the volume of the part, and not influenced by the fiber type. The tooling cost in € is estimated according to equation 6.3.

$$C_{tool,prepreg} = 0.001 \times A \times L \tag{6.3}$$

Where A is the area of the solid cross-section in mm^2 corresponding to the part, and L is again the length of the part in mm.

Tooling has a limited lifetime, defined as the maximum amount of parts that can be manufactured on them. The values for maximum parts per tool can be found in table 6.6. It can be seen that the automated processes have a much longer lifetime than the manual processes. This can be explained by the increased chance of damaging the tools when the process involves more manual labour. The lifetime can be heavily influenced by changing for example the temper of the tool's material, but this is considered out of scope for now. In the cost model this maximum amount of parts per tool is incorporated by dividing the production volume in parts with the maximum amount of parts per tool and rounding up to the nearest integer, as shown in equation 6.6.

Based on the data in the previous sections, it is found that the maximum annual production volume per tool is 180,000 for extrusion, 10,800 for braiding, 1800 for vacuum-infusion and 900 for prepreg. This is based on

Table 6.6: Maximum amount of parts per tool for different manufacturing processes

Process	Parts per tool
Extrusion	100,000
Braiding	10,000
Prepreg	500
Vacuum-infusion	500

the assumption of 45 work weeks of 40 hours per year, which yields 1800 yearly work hours. Especially for the prepreg and vacuum-infusion process it could be possible that the yearly volume exceeds this number. If this is the case the multiple tools should be used simultaneously. However, since the maximum number of parts per tool is lower than the maximum yearly volume per tool this annual volume does not have to be included in the model as it is already covered automatically by needed a new tool because the maximum number of parts per tool is exceeded.

In reality the production speed would increase with increasing production volume, due to the learning curve. This effect would be especially pronounced for processes with a high amount of manual labour. On the other hand, manufacturing processes that are highly automated would need additional set-up costs at the start of the production run. Both these effects are neglected at this point, as this would increase the complexity of the cost model.

6.3. Calculation of candidate design manufacturing cost

The total manufacturing cost of a candidate design is equal to the manufacturing cost of the bumper beam, plus two times the manufacturing cost of a crash box. The manufacturing cost of a part is a combination of the material cost, equipment cost, tooling cost, labour cost and additional cost. This is shown in equation 6.4.

$$C_{manufacturing} = C_{material} + C_{equipment} + C_{tooling} + C_{labour} + C_{additional} \tag{6.4}$$

The material cost per part is calculated from the base material cost as well as the scrap rate, as shown in equation 6.5.

$$C_{material} = m_{part} \times \text{base material cost} \times (1 + r_{scrap}) \tag{6.5}$$

The tooling cost per part is calculated based on the cost of the tool itself, the production volume and the amount of parts that can be manufactured per tool. This can be seen in equation 6.6.

$$C_{tooling} = ceiling\left(\frac{\text{Production volume}}{\text{Parts per tool}}\right) \times \left(\frac{\text{Cost of tooling}}{\text{Production volume}}\right) \tag{6.6}$$

The labour cost and equipment cost per part can be found in table 6.5 and 6.4 respectively. The additional cost per part, if applicable, is found in the itemization in the section above.

7

Verification and Validation

In this chapter the verification and validation of the analytical model is discussed. The methods used for verification are shown in section 7.1. The method for validation of the structural response calculated by the analytical model using FEA in ANSYS is explained in section 7.2, and the validation results for the three different load cases are shown in sections 7.3, 7.4, and 7.5 respectively. The validation of the complete results from the model is done using benchmarking of existing vehicles, and its methodology is shown in section 7.6. The validation results for the BMW 730d are shown in section 7.7, and for the Ford Focus in section 7.8.

7.1. Verification

Since the optimization model is developed in MatLab, it is necessary to check if the calculations that are performed are implemented correctly. This is done as a form of quality control, and to add credibility to the results of the optimization model. Verification is performed using multiple methods, being unit tests, system tests, and checking for unexpected behaviour using the parameter sensitivity analysis.

The optimization model consists of many different sub-routines that calculate for example the structural response during a certain phase of a load case, or the manufacturing cost of the candidate design. All of these sub-routines are cross-checked using hand calculations for all different types of candidate designs that it is applicable to. It is checked whether the output of the sub-routine corresponds exactly to results from the hand calculation if the input parameters are the same. This process is called unit testing, and shows that the sub-routines are working as desired.

When many of these sub-routines are combined the behaviour of the optimization model becomes too complex to check the behaviour using hand calculations. This means that different methods are necessary to check if the model behaves as intended and calculates the correct things. Initially the sub-routines are grouped into small systems, for example all the phases of a single load case together. This system is then run for multiple variations of each type of candidate design, and it is checked whether the effect of these variations is as expected based on the equations that are used and the physical phenomena they represent. Additionally, certain parameters such as SEA are checked to see if they stay in the expected range and if the variations have the expected influence. This is called system testing, and shows that the sub-routines are working together in the correct way.

As a final step to check whether the optimization model actually calculates what is intended to be calculated, the parameter sensitivity analysis as shown in appendix B is used. Here the results from the full model, as well as from large separate parts, are used to show the influence of variations in the most important parameters on the final results. These parameter sensitivities are then used to analyze whether this corresponds to the physical behaviour, the equations used, and common sense. The results of this can be found in appendix B. All of these steps have been implemented and all unexpected behaviours have been fixed. This means that the optimization model can be considered verified.

7.2. Validation of structural response

To gain confidence in the structural response predicted by the analytical model a validation study is carried out using the commercial FEA software ANSYS 2019 R2, more precisely the Explicit Dynamics workbench. This method is used to calculate dynamic responses of a structure due to stress wave propagation or impact, and can be used for the modelling of highly non-linear phenomena. The maximum timestep that is allowed is determined by the shortest time it will take for the stress wave to propagate through any of the elements (this travel time depends on dimensions of the element and stiffness of the material). For this reason Explicit Dynamics works best when the event only takes a short time, less than 1 second, which makes it a good fit for the crash analysis performed here.

In order to trust the results from the FEA, it is necessary to compare the model with known experimental tests from literature. These comparisons with experimental test data can be found in appendix A. The separate bumper beam and crash box models used to compare with experimental test data are then combined into a candidate design for the low-speed rear crash structures. On this model three different FEA's will be performed, the RCAR full width test in section 7.3, the RCAR structural test in section 7.4, and the RCAR corner test in section 7.5. These load cases are chosen to provide as much data as possible on the actual behaviour of the structures during the load cases, making it possible to compare as many parts of the analytical analysis as possible. No composite candidate designs are used during these simulations due to the increased difficulty in using them in the simulations, and the analytical model showing that with the current limit on geometries there are no composite bumper beam candidate designs that can pass all three load cases.

The predictions of the structural response by the analytical model developed during this thesis will then be checked on key metrics, such as peak force, mean force, energy absorption and intrusion distance, with the predictions of the finite element models. It is important to realize at this point that a perfect agreement (a difference of less than 1% on all key parameters for example) between the analytical and numerical models is not expected due to the complexity of capturing the highly non-linear impact behaviour in analytical equations. The aim of the structural response prediction is to use it for the conceptual design phase, and to compare different concepts with each other. The target on the maximum difference for the key parameters is set to 10%.

7.2.1. Material data

Two different materials are used during the simulations, namely the AL6060-T4 alloy for the candidate design and 'barrier foam' that is located on top of the rigid barrier during the RCAR full width and corner tests. The definition of the barrier foam model is elaborated on in appendix A.3 and not repeated here due to its limited influence on the final results.

The material model for the AL6060-T4 alloy consists of multilinear isotropic hardening, combined with the bulk modulus equation of state, the shear modulus and plastic strain failure. The values are based on experimental coupon test data from Hanssen [28], as this is the same material that is used for the validation of the bumper beam and crash box models themselves. The relation between the plastic strain and the corresponding stress level in the material used to define the multilinear isotropic hardening can be seen in figure 7.1. The other engineering data used to define the material model can be found in table 7.1. In the erosion controls, the option 'on material failure' is set to yes, and inertia of the eroded material is retained.

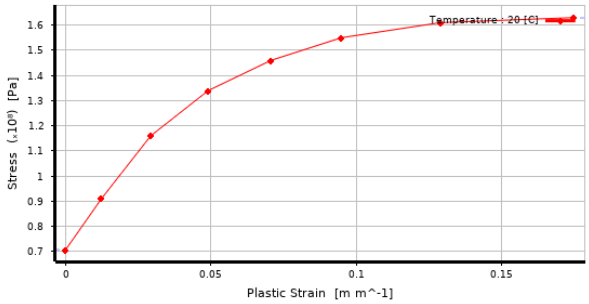

Figure 7.1: Definition of multilinear isotropic hardening of AL6060-T4 alloy

Table 7.1: Engineering data for the AL6060-T4 material model

Material property	Value
Density [kg/m3]	2703
Bulk modulus [GPa]	71.25
Shear modulus [GPa]	27.6
Plastic strain failure [-]	0.175

7.2.2. Geometry definition of candidate design

The candidate design that is used for these simulations is determined by running the analytical model with only the AL6060-T4 material available, and finding a promising design that would just pass the load cases. Unfortunately it was not possible to find a realistic geometry for the bumper beam using this alloy that would pass the RCAR corner test, as the wall thickness needs to be so large due to the low material properties that the beam is almost solid instead of thin-walled. This means that only the RCAR full width test and RCAR structural test are passed with this candidate design. The parameters that define the geometry can be found in table 7.2.

Table 7.2: Geometry defining parameters of candidate design used during finite element simulations

	Bumper beam		Crash box
L_{bb}	1590.8 mm	L_{cb}	226 mm
h_{bb}	100 mm	w_{cb}	50 mm
d_{bb}	40 mm	t_{cb}	3.1 mm
t_{bb}	2.8 mm		
R_{bb}	3000 mm		

An additional part, the 'closing plate', is included in the candidate design during the simulations. A part fulfilling the same function as this closing plate is normally also present in actual vehicles, and this simplified version is used here to stabilize the behaviour of the crash boxes (as it also would in reality) without having to impose any unrealistic boundary conditions. When the results are generated it will be checked if the energy absorption of this closing plate is low enough to not influence the results. A point mass of 1325 kg is attached remotely to the eight edges of the crash boxes where they are connected to the closing plate. This point mass is positioned 2000 mm in the x-direction, representing an estimate of the center of gravity of the vehicle. The results should not be sensitive to the exact location of this point mass, as the lateral and vertical movement of the closing plate is restricted (explained in more detail later). The surface model of the candidate design is created in Catia V6 and then imported into ANSYS. All edges are kept sharp instead of using fillets, as it was found during the replication of experimental tests (shown in appendix A) that this improves both the speed and accuracy of the simulation. A graphical representation of the candidate design used during the simulations is shown in figure 7.2.

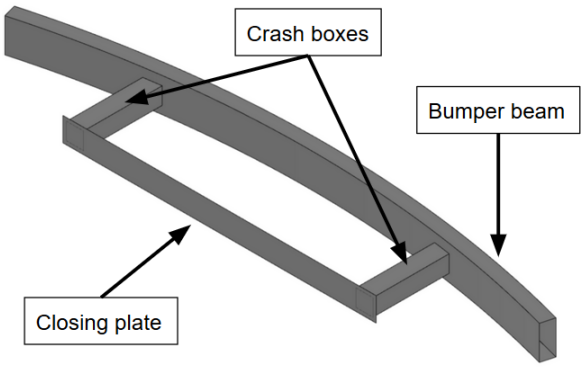

Figure 7.2: Graphical representation of candidate design surface model in Catia

The bumper beam, crash boxes and closing plate are imported as separate parts. To achieve the desired behaviour in a simplified manner, unbreakable bonded connections are specified both from the crash boxes to the bumper beam and the crash boxes to the closing plate.

7.3. FEA1: RCAR full width test

The first FEA that is performed is the RCAR full width test, to validate the analytical structural response of the bumper beam and crash boxes. First, the setup of the model is discussed, and secondly the simulation results are compared to the analytical predictions.

7.3.1. Model setup

In this simulation the vehicle (modelled as the candidate design plus a 1325 kg point mass located at the vehicle's estimated center of gravity) impacts the RCAR barrier with a velocity of 10.5 km/h. This leads to an impact energy of 5.64 kJ. The impact energy will be absorbed by the bumper beam, both crash boxes and the foam that is part of the RCAR barrier, but also partly as elastic energy that is restituted as kinetic energy of the vehicle bouncing back after the impact. The barrier is modelled according to the geometry definitions from the RCAR guidelines, as detailed in section 5.1. The rigid part of the barrier is modelled as a rigid surface with a thickness of 1 mm and the same material as the candidate design. The foam part of the barrier is modelled as a solid using the material properties as described in appendix A.3.

Connections

As mentioned before, unbreakable bonded connections are defined between the crash boxes and the bumper beam, as well as between the crash boxes and the closing plate. An additional frictional contact is defined between the impacting face of the bumper beam and the foam, where a static friction coefficient of 0.3 is chosen. Shell thickness is taken into account, and so is body and element self contact.

Mesh

After a few iterations with different mesh sizes, it was found that an element size of 5.0 mm is the optimum when considering how quickly the simulation is solved and whether the physical behaviour can be properly modelled. This holds for the candidate design, the barrier foam and the rigid part of the barrier. This also corresponds to the findings in appendix A. The candidate design and the rigid part of the barrier are meshed using linear shell elements, and the foam using linear hex8 elements. This results to a total of 58,948 nodes and 48,816 elements.

Boundary conditions

To properly constrain the barrier, a fixed support is added to the rigid part of the barrier. This makes sure that there is no movement or deformation, which corresponds to the definition of the load case. An additional boundary condition is applied to the closing plate, where only movement in the x-direction is allowed. During a physical test the tires of the vehicle would prevent sideways movement due to their friction with the ground, and vertical movement is prevented on the one hand by the floor itself, and on the other hand by the inertia of the vehicle.

Initial conditions

At the start of the simulation, when t=0, an initial velocity of 2916.7 mm/s (corresponding to 10.5 km/h) is applied to the candidate design in the direction towards the barrier. All parts of the candidate design, plus the point mass attached to it, have this initial velocity.

Analysis settings

The analysis settings are set up in accordance to the ANSYS Explicit Dynamics manual [6], and to represent the physical behaviour as well as possible. The analysis will run up to the end time of 0.1 seconds, with a maximum of $1e^7$ cycles, as this captured the full impact event. The initial, minimum and maximum time step are program controlled. Automatic mass scaling is set to 'no', as it did not increase the speed of the analysis. Erosion of elements will happen only due to material failure, and the inertia of the eroded material is retained. For the damping, a linear artifical viscosity of 0.2 and a quadratic artificial viscosity of 1.0 are used. Hourglass damping is set to AUTODYN standard, the viscous coefficient to 0.1 and static damping to 0. These are the standard settings within the ANSYS workbench.

7.3.2. Results and comparison with analytical model

The results that are requested as outputs, using a Butterworth filter with a cut frequency of 1000 Hz in accordance with SAE J211 for component analysis, are the following:

- Total Deformation
- Equivalent Plastic Strain
- Force Reaction on rigid part of barrier
- Position in x-direction of a node on the closing plate
- Internal Energy of the barrier foam
- Internal Energy of the bumper beam
- Internal Energy of the crash boxes

With these results it is possible to determine the key metrics, such as peak force and intrusion distance, but also gain information on the behaviour of the individual parts and see if they correspond well with the assumptions that have been made for the analytical model.

The result files from ANSYS are exported to a MatLab script that performs some operations to show the data with respect to the intrusion distance instead of the elapsed time. The relation between reaction force on the barrier and the intrusion distance can be seen in figure 7.3. The distribution of internal energy between the different energy absorbing parts is shown in figure 7.4.

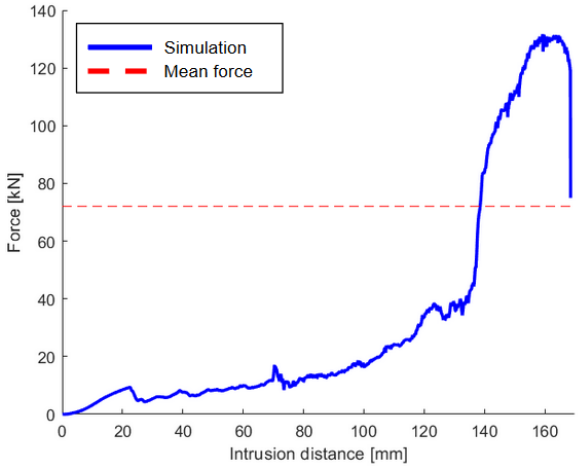

Figure 7.3: Force versus intrusion distance graph for RCAR full width test

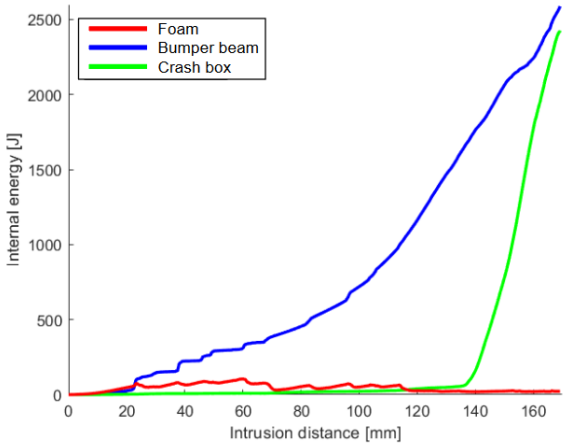

Figure 7.4: Graph of internal energy of different parts versus intrusion distance for RCAR full width test

When looking at figure 7.3 it can be seen that the force slowly increases during the first 100 mm of intrusion distance. During this period the foam is compacted, absorbing energy, and the bumper beam starts yielding and deforming until its curvature is equal to the rigid barrier. The bumper beam section close to the attachment to the crash boxes is crushed between 100 mm and 140 mm of intrusion distance, and it can be seen that the force increases more quickly here. When the bumper beam section is crushed, the force quickly rises. This corresponds to the peak load of the crash boxes, and after this peak force is reached the force drops quickly again. These different phases are confirmed by looking at the distribution of internal energy in figure 7.4. At an intrusion distance of 169.2 mm all impact energy is absorbed and the simulation is stopped. In figure 7.5 the locations and intensity of the plastic strain at the end of the simulation can be seen.

From the plastic strain distribution and intensity in figure 7.5 it can be seen at which locations most of the impact energy is absorbed. The first main locations are the bumper beam close to the attachment of the crash boxes, as the section is crushed. The second main locations are the crash boxes, due to the small amount of progressive folding that occurs. It can also be seen that the crash boxes are pushed sideways by the deformation of the bumper beam. The mean force is calculated by dividing the internal energy of the crash boxes

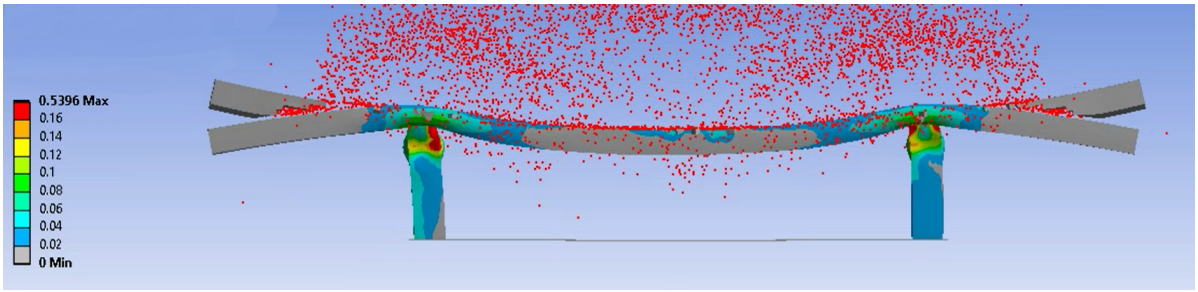

Figure 7.5: Distribution and intensity of plastic strain at t=0.1 s. The red dots are eroded (foam) elements

at the maximum intrusion distance by the contribution of the crash boxes to the intrusion distance, to make sure the contribution of the bumper beam is removed. At this point the results from the simulations are clear, and they can be compared with the predictions from the analytical model. An overview of the comparison on key metrics as well as secondary parameters can be found in table 7.3.

Table 7.3: Comparison between analytical predictions and simulation results for RCAR full width test

	Analytical model	**Simulation**	**Difference**
F_{peak}	131.2 kN	129.2 kN	+1.6%
$F_{mean,cb}$	67.8 kN	72.1 kN	-6.0%
$\delta_{intrusion,total}$	137.3 mm	119.2 mm	+15.2 %
EA_{total}	5.02 kJ	5.03 kJ	-0.2 %
$EA_{bumperbeam}$	1.68 kJ	2.59 kJ	-18.1% [1]
$EA_{crashboxes}$	3.34 kJ	2.41 kJ	+18.5% [1]
EA_{foam}	225 J	110 J	+2.5% [1]
$\delta_{intrusion,bb}$	84.5 mm	84.7 mm	-0.17% [2]
$\delta_{intrusion,cb}$	52.8 mm	34.5 mm	+15.4% [2]

[1] Calculated with respect to EA_{total}
[2] Calculated with respect to $\delta_{intrusion,total}$

When looking at table 7.3 it should be noted that the difference of the secondary parameters between the analytical model and the simulation is calculated with respect to either the total energy absorption or the total intrusion distance. This shows the influence of these differences in predictions on the results of the key metrics. It can be seen that the most important difference is found in the total intrusion distance, with a difference 15.2%. This discrepancy comes from a combination of the bumper beam absorbing more energy than expected, with a difference of 18.1%, while the contribution to the intrusion distance is almost identical to the prediction, and the mean force of the crash boxes being 6.0% higher than predicted. This means that the contribution of the crash boxes to the intrusion distance is 15.4% smaller than expected. The energy absorption of the bumper beam is higher than predicted by the analytical model because the deformed shape is different than assumed, a graphical representation of this during the RCAR structural test load case (it is very similar for the RCAR full width test) can be seen in figure 7.9. This is due to the crash boxes not covering the entire height of the bumper beam, while the analytical model needs to work for all sizes of crash boxes. The underestimation of the mean crash box force can be explained by two phenomena. The first one is the interaction effect between the bumper beam and the crash boxes, leading to the peak force having a much wider peak if plotted versus the intrusion distance, and therefore increasing the energy absorption (from which the mean force is derived). The second one is that only a small part of the complete crash boxes is used to absorb the energy and that no full folds are created yet. It can be seen in figure 7.5 that there is only a peak in the part where the crash boxes are active, and no valleys that would reduce the mean force. The peak force is predicted quite well, although it is overestimated by 1.6%. This is probably due to the crash boxes being pushed outwards by the deformation of the bumper beam before the crash boxes become active, increasing the effective incidence angle and therefore reducing the peak force slightly. It can be seen in figure 7.5 that the crash boxes are indeed being pushed outwards. The total amount of energy that is absorbed is predicted very well, with a difference of only 0.2%.

When looking at the secondary parameters, it can be seen that only the bumper beam's contribution to the intrusion distance is predicted well with a difference of only 0.17%, as this is more of a geometrical prediction than based on structural analysis. The energy absorption of the bumper beam is underestimated by 18.1%, which seems to be explained by a much larger zone of plasticity than assumed in the analytical model, when looking at figure 7.5. The energy absorption of the crash boxes is overestimated by 18.5%, mainly because there is less impact energy left to be absorbed due to the higher bumper beam contribution. The energy absorption of the foam is overestimated 115 J, which corresponds to 2.5% of the total energy absorption.

7.4. FEA2: RCAR structural test

The second FEA that is performed is the RCAR structural test, to validate the analytical structural response of the bumper beam and crash boxes. The setup of the finite element model is discussed first, and afterwards the simulation results are compared with the analytical predictions.

7.4.1. Model setup

The candidate design is impacted by a moving rigid barrier of 1400 kg, with a velocity of 16 km/h during this load case. The impact energy will be absorbed by the bumper beam and one of the crash boxes. The barrier is modelled according to the geometry definitions as explained in section 5.1, and as a rigid surface with a thickness of 1 mm made from the same material as the candidate design. A point mass of 1400 kg is attached to this surface, at a distance of 2000 mm in the opposite direction of its velocity vector. This remote attachment is used to provide directional stability of the impactor, balanced by the impactor's own inertia.

Connections

The internal bonded connections of the candidate design are identical to the situation in the model for the RCAR full width test that has been elaborated on earlier. In addition to this, a frictional connection is defined between the front face of the bumper beam and the impactor geometry. A friction coefficient of 0.3 is used. Shell thickness is taken into account, and so is body and element self contact.

Mesh

The candidate design is meshed in exactly the same way as for the analysis of the RCAR full width test, with an element size of 5.0 mm, using linear shell elements. The rigid barrier surface is also meshed with linear shell elements, of the same dimensions as the candidate design. This leads to a total of 29,168 nodes and 28,152 elements.

Boundary conditions

The only boundary condition that is used during the simulation of the RCAR structural test is imposed on the closing plate. Movement in the x-direction is free, but movement in the y- or z-direction is not allowed. This resembles the effect of the tires of the vehicle during the physical test, preventing sideways movement due to their friction with the ground and vertical movement being prevented by the support of the ground itself, as well as the inertia of the vehicle.

Initial conditions

At the start of the simulation, when t=0, an initial velocity vector with an x-component of 4376.5 mm/s and a y-component of 771.7 mm's is applied to the barrier surface and the attached point mass. This corresponds to an impact velocity of 16 km/h with an incidence angle of 10 degrees.

Analysis settings

The analysis settings are set up in accordance to the ANSYS Explicit Dynamics manual [6], and to represent the physical behaviour as well as possible. The analysis will run up to the end time of 0.08 seconds, with a maximum of $1e^7$ cycles, capturing the full impact event. The initial, minimum and maximum time step are program controlled. Automatic mass scaling is set to 'no', as including it showed only a marginal increase in the speed of the analysis. Erosion of elements will happen only due to material failure, and the inertia of the eroded material is retained. For the damping, a linear artificial viscosity of 0.2 and a quadratic artificial viscosity of 1.0 are used. Hourglass damping is set to AUTODYN standard, the viscous coefficient to 0.1 and static damping to 0. These are the standard values within the ANSYS workbench.

7.4.2. Results and comparison with analytical model

The results that are requested as outputs, using a Butterworth filter with a cut frequency of 1000 Hz in accordance with SAE J211 for component analysis, are the following:

- Total Deformation
- Equivalent Stress
- Equivalent Plastic Strain
- Force Reaction on barrier
- Position in x-direction of a node on the closing plate
- Position in x-direction of a node on the barrier, close the the crash box attachment
- Internal Energy of the bumper beam
- Internal Energy of the left crash box
- Internal Energy of the right crash box
- Internal Energy of the closing plate

With these results it is possible to determine the key metrics, such as peak force and intrusion distance, but also gain information on the behaviour of the individual parts and see if they correspond well with the assumptions that have been made for the analytical model.

The result files from ANSYS are exported to a MatLab script that performs some operations to show the data with respect to intrusion distance instead of the elapsed time. The crash box mean force is calculated by dividing the internal energy of the crash box over the crash box' contribution to the intrusion distance. Also the intrusion distance needs to be calculated from the difference between the x-position of the closing plate and the barrier. The mean force is calculated by dividing the internal energy of the crash boxes at the maximum intrusion distance by the contribution of the crash boxes to the intrusion distance, to make sure the contribution of the bumper beam is removed. The relation between reaction force on the barrier and the intrusion distance can be seen in figure 7.6. The distribution of internal energy between the different parts is shown in figure 7.7.

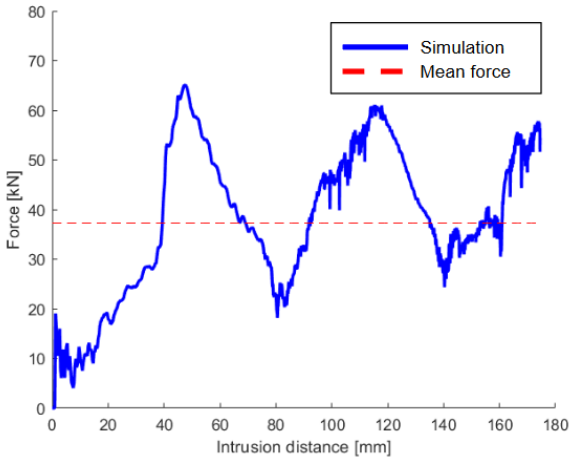

Figure 7.6: Force versus intrusion distance graph for RCAR structural test

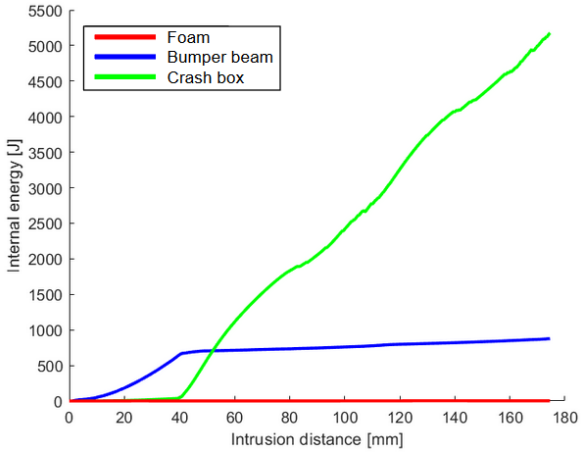

Figure 7.7: Graph of internal energy of different parts versus intrusion distance for RCAR structural test

When looking at figure 7.6 it can be seen that the load first has a small peak, then drops quickly. This is the initial collapse of the bumper beam section. After this the force slowly increases until an intrusion distance of 40 mm is reached, which is the crushing of the bumper beam section. When the bumper beam section is fully crushed, the force increases quickly to reach the peak force of the single crash box. When the peak force is reached the progressive crushing of the crash box is started. These observations are supported by the distribution of internal energies, where it can be seen that the bumper beam absorbs energy mainly in the first 40 mm of intrusion distance, after which the crash box quickly starts to absorb the energy. It can also

be seen that the energy absorption of the second crash box is negligible. In figure 7.8 the deformation of the parts and plastic strain intensity at full intrusion distance can be seen. Here it becomes clear that the energy absorption of the bumper beam is indeed due to collapse of the section around the location where the crash box is attached, and that the progressive folding behaviour absorbs a large amount of impact energy.

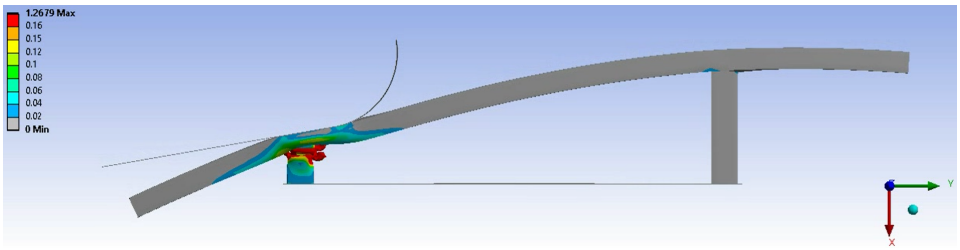

Figure 7.8: Deformation and plastic strain intensity at full intrusion distance

Table 7.4: Comparison between analytical predictions and simulation results for RCAR structural test

	Analytical model	**Simulation**	**Difference**
F_{peak}	68.5 kN	65.1 kN	+5.2%
F_{mean}	35.6 kN	37.3 kN	-4.6%
$\delta_{intrusion,total}$	200.1 mm	174.6 mm	+14.6 %
EA_{total}	6.28 kJ	6.1 kJ	+2.9 %
$EA_{bumperbeam}$	0.38 kJ	0.88 kJ	-8.2% [3]
$EA_{crashbox}$	5.9 kJ	5.2 kJ	+11.5% [3]
$\delta_{intrusion,bb}$	34.4 mm	35.7 mm	-0.74% [4]
$\delta_{intrusion,cb}$	165.7 mm	140.2	+14.6% [4]

[3] Calculated with respect to EA_{total}
[4] Calculated with resepect to $\delta_{intrusion,total}$

In table 7.4 the comparison between the analytical predictions and simulation results is shown. The first four parameters have a high importance, as they are directly used the evaluate the candidate design. The second set of four parameters shown is mainly to be able to reflect on the accuracy of the different sub-parts of the model and find where the room for improvement is. Most notably is the difference in intrusion distance, where the analytical model overestimates it compared to the simulation by 14.6%. This can be explained by two things. The first one is that the bumper beam absorbs more of the impact energy than expected, with a difference of 8.2% on the total energy absorption. This means that there is less energy left for the crash box to absorb. The second is the underestimation of the crash box mean force by 4.6%, which results in a higher crash box deformation that is necessary to absorb the same amount of impact energy. The difference of 8.2% for the energy absorption capabilities of the bumper beam seem to be because the assumptions of the plastic hinge lines heavily underestimate the much more complex deformation patterns that actually occur, especially because the crash boxes do not cover the entire height of the bumper beam. The deformed shape of the bumper beam section and the plastic strain intensities can be seen in figure 7.9. The bumper beam also keeps on absorbing energy (around 3.5% of the total energy absorption) after the section is collapsed completely and the crash box is starting to absorb energy. This is not taken into account in the analytical model. From figure 7.10 it can also clearly be seen that when all the impact energy is absorbed there is still additional crushable length left in the crash box, which corresponds to the lower amount of impact energy absorption by the crash box than expected. It can also be seen that the first 20 to 30 mm of the crash box on the side of the bumper beam attachment is not crushed, as it is closed in by the deformed bumper beam section. This reduces the effective length of the crash box and therefore also the maximum energy absorption of the crash box. From this it can be concluded that using crash boxes with a height smaller than the height of the bumper beam section, even though it seems to be beneficial for achieving both a lower weight and lower manufacturing cost, is actually not a good idea as it increases the necessary length of the crash box in reality. This would in turn again increase the weight and manufacturing cost, and make the available space for the crash rails smaller.

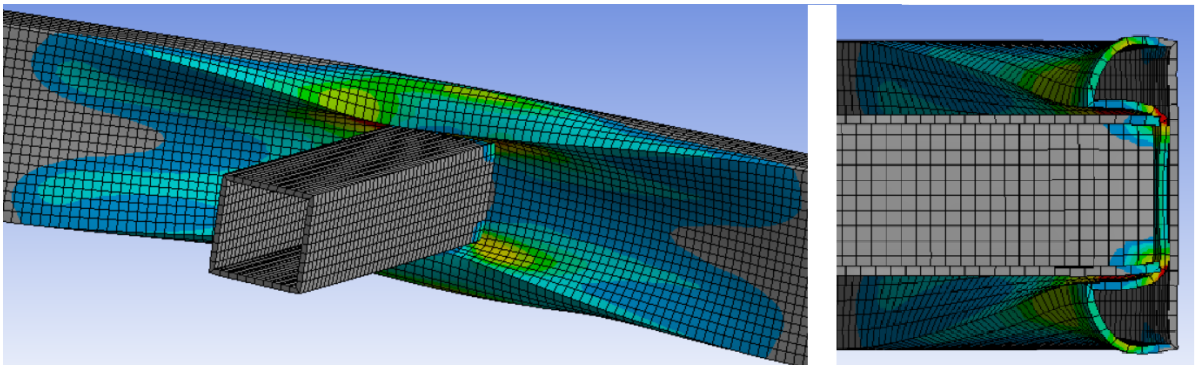

Figure 7.9: Deformation and plastic strain intensity of crushed bumper beam section (before crash box becomes active). Left: 3D view. Right: section view

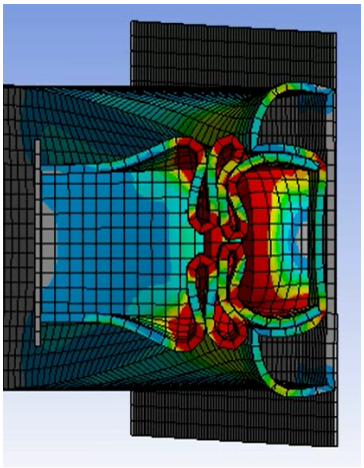

Figure 7.10: Deformation and plastic strain intensity of crash box and bumper beam section when all impact energy is absorbed

7.5. FEA3: RCAR corner test

The third FEA that is performed is the RCAR corner test, to validate the analytical structural response of the bumper beam during this load case. The setup of the finite element model is discussed first, and afterwards the simulation results are compared to the analytical predictions.

7.5.1. Model setup

In this simulation the candidate design impacts the RCAR barrier with a velocity of 5.5 km/h. This leads to an impact energy of 1.55 kJ. The impact energy will be absorbed by the bumper beam, due to the formation of a plastic hinge at the connection with the crash box, and partly as elastic energy which will be restituted as kinetic energy of the vehicle bouncing back on the barrier (if the load case is passed, which is not the case for this candidate design). The barrier is modelled in the same way as for the RCAR full width test, but only the half on which the candidate design is impacted, to save computational time. The barrier is positioned with respect to the candidate design in such a way that there is a 15% overlap if the vehicle width is 2000 mm.

Connections

Unbreakable bonded connections are defined between the crash boxes and the bumper beam, as well as between the crash boxes and the closing plate. An additional frictional contact is defined between the impacting face of the bumper beam and the barrier foam, where a friction coefficient of 0.3 is chosen. Shell thickness is taken into account, and so is body and element self contact.

Mesh

The candidate design is meshed in exactly the same way as for the analysis of the RCAR full width test, with an element size of 5.0 mm, using linear shell elements. The rigid part of the barrier is meshed using linear shell elements, and the barrier foam using linear hex8 elements. This results in a total of 45,440 nodes and 39,576 elements.

Boundary conditions

A fixed support is added to the rigid part of the barrier to properly constrain it. This makes sure there is no movement or deformation, corresponding to the definition of the load case. An additional boundary condition is applied on the closing plate, where only movement in the x-direction is allowed. This is done to include the effect of the vehicle's tires and the support of the ground.

Initial conditions

At the start of the simulation, when t=0, an initial velocity of 1527.8 mm/s (corresponding to 5.5 km/h) applied to the candidate design in the direction towards the barrier. All parts of the candidate design, including the point mass attached to it, have this initial velocity.

Analysis settings

The analysis settings are set up in accordance to the ANSYS Explicit Dynamics manual [6], and to represent the physical behaviour as well as possible. The analysis will run up to the end time of 0.2 seconds, with a maximum of $1e^7$ cycles. This longer run time is necessary to capture the full impact event, as the impact speed is lower and therefore happens more slowly. The initial, minimum and maximum timestep are program controlled. Automatic mass scaling is set to 'no', as it did not increase the speed of the analysis significantly. Erosion of elements will happen only due to material failure, and the inertia of the eroded material is retained. For the damping, a linear artificial viscosity of 0.2 and a quadratic artificial viscosity of 1.0 are used. Hourglass damping is set to AUTODYN standard, the viscous coefficient to 0.1 and static damping to 0. These are the standard settings within the ANSYS workbench.

7.5.2. Results and comparison with analytical model

The results that are requested as outputs, using a Butterworth filter with a cut frequency of 1000 Hz in accordance with SAE J211 for component analysis, are the following:

- Total Deformation
- Equivalent Stress
- Equivalent Plastic Strain

- Force Reaction of rigid part of the barrier
- Internal Energy of the barrier foam
- Internal Energy of the bumper beam
- Internal Energy of the crash box on the impacted side
- X-position of a node on the closing plate

With these results it is possible to determine the key metrics, such as peak force and intrusion distance, but also gain information on the behaviour of the bumper beam and see if it corresponds to the assumptions that have been made for the analytical model.

The result files from ANSYS are exported to a MatLab script that performs some operations to show the data with respect to the intrusion distance instead of the elapsed time. The relation between reaction force on the barrier and the intrusion distance can be seen in figure 7.11. The distribution of internal energy between the different energy absorbing parts is shown in figure 7.12.

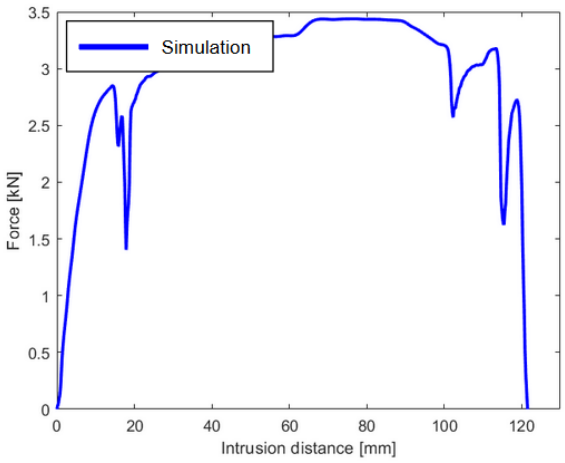

Figure 7.11: Force versus intrusion distance graph for RCAR corner test

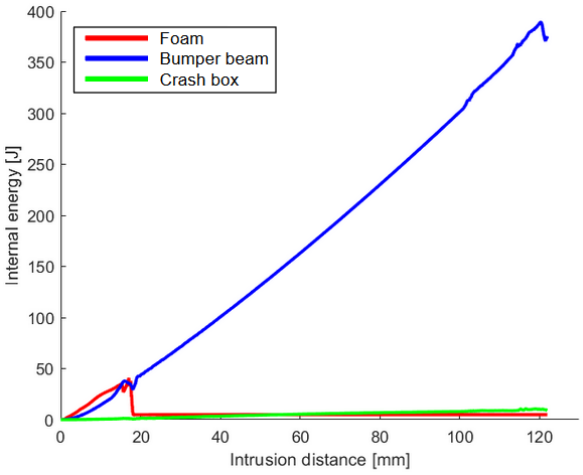

Figure 7.12: Graph of internal energy of different parts versus intrusion distance for RCAR corner test

When looking at figure 7.11 it can be seen that at first the force increases linearly, compressing the foam and increasing the stress in the bumper beam section at the connection to the crash box until the yield stress is reached. The steep valley can be explained by the erosion of the foam elements due to material failure. The load then slowly increases until the maximum plastic moment is reached in the plastic hinge that is formed in the crash box. The valleys and peaks after the intrusion distance reaches 100 mm are explained by the discretization of the corner radius of the barrier into linear elements. In figure 7.12 it can be seen that the internal energy of the bumper beam increases almost linearly until the contact between the barrier and the bumper beam is lost. The foam absorbs a small amount of energy in the first 20 mm of intrusion distance only. As expected, the energy absorption of the crash box is negligible. In figure 7.13 the deformation and plastic strain intensity at the moment just before contact between the bumper beam and barrier is lost. The formation of the plastic hinge can be identified easily, as well as the erosion of the foam elements.

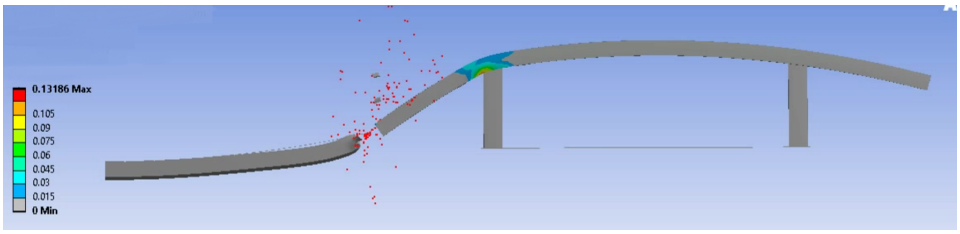

Figure 7.13: Deformation and plastic strain intensity at moment of maximum deformation

In table 7.5 the comparison between the predictions of the analytical model that is developed in this thesis is compared with the results from this simulation. For the energy absorption components (the secondary parameters) the difference is calculated with respect to the total energy absorption. This shows their effect on the results for the key parameter, in this case the total energy absorption. It can be seen that the prediction of the peak force is accurately predicted with a difference of only 2.6%. The total energy absorption shows a difference of 6.4% and the energy absorption of the bumper beam of 4.8%. The intrusion distance is predicted very accurately with a difference of only 1.1%. It can also be seen that the energy absorption of the crash box is only 2.4% of the total amount of energy absorbed, making it a fair assumption to neglect this in the analytical model. The largest difference is found in the energy absorption of the barrier foam, but this is in itself only 2.9% of the total energy absorption. It can therefore be concluded that the predictions of the analytical model are valuable. It is recommended to also validate the analytical model with a candidate design that does pass this load case in the future.

Table 7.5: Comparison between analytical predictions and simulation results for RCAR corner test

	Analytical model	**Simulation**	**Difference**
F_P	3.53 kN	3.44 kN	2.6 %
EA_{total}	469.0 J	440.9 J	6.4 %
$\delta_{intrusion}$	123.3 mm	122.0 mm	1.1 %
EA_{foam}	28.1 J	40.8 J	2.9 % [5]
$EA_{bumperbeam}$	410.5 J	389.5 J	4.8% [5]
$EA_{crashbox}$	0 J	10.6 J	2.4% [5]

[5] Calculated with respect to EA_{total}

7.6. Validation of complete results

In this section the validation method of the complete results is explained. This part of the validation is performed by using benchmarking of cars that are currently on the road, to see if the optimization model that is created during this thesis can predict the design if the low-speed crash structures of existing cars. This prediction is a combination of the performance evaluation parameters, the types of candidate designs that are generated, the structural performance as well as the cost model. For this, it is of course necessary to provide the model with the correct starting parameters and weight factors.

The cars that are considered for this benchmarking validation are the BMW 730d 2018 in section 7.7, and the Ford Focus 2018 1.5 EcoBoost in section 7.8. These two vehicles are chosen based on the availability of the necessary data, such as the exact geometry of the low-speed rear crash structures. As is normal in the automotive industry, multiply varieties of these cars are being produced. For both of these cars, one of the base models is chosen. This means specifically the BMW 730d from 2015 and the Ford Focus 1.5 EcoBoost from 2018. The input parameters corresponding to these benchmarked cars can be found in table 7.6. The total production volume is however estimated based on all different variants of the vehicle combined from the same generation, as production volumes for these specific variants could not be found, and it is highly probable that the design of the low-speed rear crash structures is shared between many of the different variants. This is not expected to have a significant influence on the results from the optimization model, as the total production volume will in any way still be large enough to not change the preferred manufacturing process, or influence the manufacturing cost as the recurring cost will be dominating this.

Table 7.6: Input parameters for benchmarked cars

Vehicle parameters	BMW 730d 2018 [6]	Ford Focus 1.5 EcoBoost 2018 [7]
Total production volume [-]	240,000 [8]	4,000,000 [8]
MSRP [€]	74,566 [9]	16,106 [9]
Kerb weight [kg]	1940	1325
Length [mm]	5072	4360
Width [mm]	1902	1830
$L_{available}$ [mm]	695 [10]	580 [10]
$L_{unsupported}$ [mm]	855 [10]	875 [10]
w_{cb} [mm]	89.5 [10]	91 [10]
R_{bb} [mm]	2150 [10]	2407 [10]

7.7. BMW 730d 2018

In this section the optimization model that is developed during this thesis is used to compare the results with the actual design of the rear low-speed crash structures of the BMW 730d. The actual design of the rear low-speed crash structures is shown in section 7.7.1, and the results from the model as well as the comparison to the actual design is presented in section 7.7.2.

To give the optimization model the correct starting point, the vehicle parameters as shown in table 7.6 are used. Next to these vehicle parameters it is also necessary to provide the optimization model with the desired values for the weight factors. The values that are chosen for this are shown in table 7.7. The values are chosen such that they are expected to match as well as possible with the design philosophy of the OEM. For the BMW 730d this means that cost-wise the focus is on purchase price instead of TCO. The value of lightweighting is set to 10 €/kg as this corresponds to the value for luxury vehicles (as shown in section 3.1), which the BMW 730d definitely is. Value of efficiency due to its influence on battery size is not taken into account, as the BMW 730d is not a BEV. Annual solar kilometers are also not taken into account, as it is not an SEV. The value of longitudinal trunk space is set to 0.8192 €/mm corresponding with a MSRP of €74,566, as outlined in section 3.6. Environmental impact is also not taken into account, as it is expected that this was also not done during the design of this vehicle.

Table 7.7: Weight factors used to run model for BMW 730d

Weight factor	Value	Explanation
w_1	1 [-]	Fully focussed on purchase price
w_2	0 [-]	No focus on TCO
w_3	10 [€/kg]	Value of lightweighting of luxury vehicle
w_4	0 [-]	No value due to influence energy efficiency on battery
w_5	0 [€/skm]	No value for SKM
w_6	0.8192 [€/mm]	Value of trunk for MSRP=€74566
w_7	0 [-]	Environmental impact not considered

7.7.1. Actual design of rear low-speed crash structures

In this section the actual design of the rear low-speed crash structures of the BMW 730d 2018 are shown. This data is based on a combination of a body-in-white 3D CAD model, a picture from 7ZAP.com as shown in figure 7.14, and a 2D bumper beam section from A2Mac1 as shown in figure 7.15. The values for the most important geometry-defining parameters are shown in table 7.8.

When looking at the bumper beam, it can be seen that the cross-section is close to constant along the entire length, with only some cutouts and details present. The cross-section itself consists of a two-cell closed sec-

[6] `https://www.ultimatespecs.com/car-specs/BMW/13440/BMW-F01-7-Series-730d.html`, accessed on 17/12/2019
[7] `https://www.car.info/en-se/ford/focus/focus-5-door-hatchback-15-ecoboost-7325134`, accessed on 17/12/2019
[8] Estimation
[9] `cars.usnews.com`, accessed on 27/12/2019
[10] Measured from CAD data

tion, with a vertical lip on the bottom. This leads to the conclusion that it is manufactured using the extrusion method. This two-cell closed section is a weight-effective method to increase the bending resistance and energy absorption compared to a single-cell closed section. The wall thickness is almost, but not completely, constant, and varies between 1.95 and 2.00 mm. The partitioning face is pre-buckled to promote a controlled collapse. The lip is present to increase the height of the bumper beam to close to 100 mm, but this method would not pass the RCAR requirements as the lip has a wall thickness of less than 5 mm. The depth of the section is 50.30 mm and the height of the main part of the section is 65 mm. The bumper beam radius of curvature has been measured in the CAD model and is found to be 2150 mm. Based on the alloy composition as shown in figure 7.15 it can be concluded that the alloy is part of the aluminium 6xxx family. An additional part, called the rear bumper lower reinforcement, is located between the bumper beam and the fascia, is made from polypropylene reinforced with 20% (by weight) long glass fibers. This part will also absorb a part of the impact energy.

The length of the bumper beam is 1160 mm, and the bumper beam barely extends past the crash boxes. This means the length of the bumper beam is not large enough to pass the RCAR requirements of at least 70% of vehicle width. A more complex method is used to absorb the impact during the RCAR corner test and ECE-R42 corner pendulum test, as this is done by energy-absorbing brackets that provide stiffness to the corner of the bumper fascia, as well as attachments to the rear closing panel and the light housing. This method can lead to weight savings, but is also much more complex to analyze during this initial design phase.

When looking at the crash boxes, it can be seen that the the cross-section is constant along the length, with some post-operations to ensure that the crash boxes and bumper beam fit well together. The cross-section is close to square, having a width of 89.5 mm and a maximum height of 91 mm. Some additional geometry is present on the top of the crash box, where the height is reduced to 82.5 mm. This adds additional corners to section, leading to an increased SEA, or looking at it differently, a higher mean sustained crushing force for the same wall thickness. It also seems to make it easier to position the bolt that connects the low-speed crash structures to the crash rails. The wall thickness seems to be a constant 2.0 mm all along the section. The crash boxes are manufactured using extrusions. The crash box length is 62 mm, measured at the centerline of the crash box itself. The material is unknown, but it is expected to be an Al6xxx alloy, as this is the same as the bumper beam and a very good fit for the extrusion process.

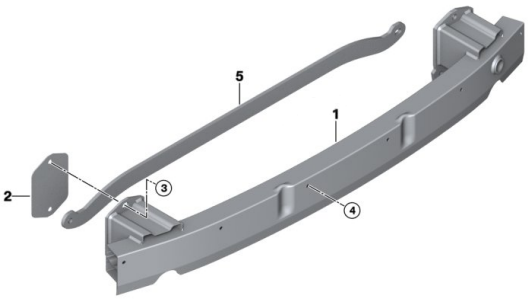

Figure 7.14: BMW 730d 2018 bumper beam (from 7ZAP.com)

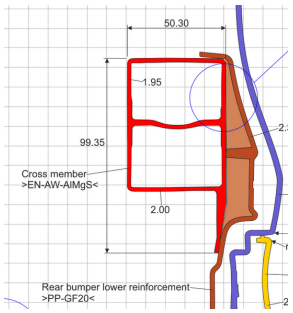

Figure 7.15: BMW 730d 2018 bumper beam section (from A2Mac1.com)

When looking at the actual design of the BMW 730d's low-speed rear crash structures some discrepancies with the results from the optimisation model can already be expected. The bumper beam will be less wide than predicted, due to the different method for managing the corner impact. The bumper beam itself will absorb more energy than expected, as well as have a lower wall thickness, due to the two-cell closed section. The height of the bumper beam will also not be predicted correctly as the minimum height to pass the RCAR requirements is 100mm. The crash boxes are also expected to have a lower wall thickness due to the added geometry on the top face. These features can not be predicted by the optimization model, as they are not included in the candidate design generation. It is also not known exactly what the yield stress and ultimate stress of the used materials are, which will add an additional possible factor of difference.

7.7.2. Model results and comparison

When the model is run with the input parameters from table 7.6 and the weight factors from table 7.7, two distinct options that are close in total cost are found. Option one is the best result using the same approach

as the actual design (without foam in the crash boxes) and is also the optimal solution. Option two has foam-filled crash boxes, and is shown here as well as the difference in total cost is only €2.3. Both these options are shown next to the actual design for comparison in table 7.8.

Table 7.8: Comparison of results generated with optimization model to benchmarked values

	BMW 730d	**Option 1**	**Option 2**
Material CB [-]	Al6xxx	Al6061-T6	Al6061-T6
L_{cb} [mm]	62	66	69
t_{cb} [mm]	~2.0	3.1	2.8
w_{cb} [mm]	89.5	89.5	89.5
ρ_f [kg/m3]	0	0	170
m_{cb} [kg]	~0.12	0.192	0.264
Material BB [-]	Al6xxx	Al6061-T6	Al6061-T6
L_{bb} [mm]	1160	1401.4	14014
t_{bb} [mm]	~2.0	3.6	3.6
h_{bb} [mm]	65.0	100	100
d_{bb} [mm]	50.3	44	47
R_{bb} [mm]	2150	2150	2150
m_{bb} [kg]	~2.0	4.072	4.162
m_{CR} [kg]	-	5.411	5.386
m_{total} [kg]	-	9.867	10.076
C_{manuf} [€]	-	28.8	35.6
C_{total} [€]	-	116.8	119.1
$\delta_{intrusion}$ [mm]	~89.4	87.0	79.0

Comparison option 1

When looking at the differences between option 1 and the actual design, as shown in table 7.8, it can be seen that there are some differences in both the design of the crash boxes and the bumper beam. The optimization model predicts that the crash boxes are 4 mm longer than in reality, and the wall thickness to be 1.1 mm larger. The bumper beam is predicted to have a length that is 241.4 mm larger (as shown before, due to a different method for handling the corner impact), a wall thickness that is 1.6 mm larger, and a section depth that is 6.3 mm smaller. For both parts, the predicted material and manufacturing method is predicted correctly. The predicted intrusion distance only has a difference of 2.4 mm compared to the estimation of the actual intrusion distance.

It can be seen that while the difference in the length of the crash boxes is small, there is a rather large difference in the crash box wall thickness. An explanation for this are that the design using crash boxes with additional corners would lead to a higher mean sustained crush force at an equal wall thickness. It is also possible that the bumper beam absorbs more energy than expected during the RCAR structural test due to the multi-cell cross-section, which is amplified by the small part of the crash boxes extending on top of the bumper beam.

The difference in cross-sectional shape for the bumper beam can also explain the discrepancy in wall thickness between the actual design and option 1. The additional middle wall increases the resistance to bending, and therefore decreases the wall thickness needed to have a similar yield strength as well as fully plastic strength. Next to this, additional plastic hinges can be formed for the absorption of impact energy, such that a similar bumper beam energy absorption can be reached with a lower wall thickness. This still holds, even though the actual effective bumper beam height is only 65 mm compared to the predicted 100 mm (necessary to pass the RCAR requirements), as this middle wall is much more effective in increasing the bending resistance and energy absorption than increasing the section height.

The suspected reason for the larger section depth of the actual design's bumper beam is that this two-cell section is more efficient at absorbing the impact energy through crushing of the section, limiting the intrusion distance during the RCAR structural test. During the RCAR full width test part of the impact energy is absorbed through crushing of the section, but another part through the elastoplastic deformation of the

bumper beam. When it is desired to limit the intrusion distance during RCAR full width test as well, an effective method to do this is to increase the bumper beam section depth, which in turn increases the elastoplastic energy absorption. This is shown in the parameter sensitivity analysis in Appendix B in figure B.15. Limiting the intrusion distance during the RCAR full width test compared to the RCAR structural test has the benefits of allowing for a curved closing panel, which makes the limit of the trunk space follow the outer curvature of the vehicle providing more trunk space locally.

It is interesting to note that the AL6061-T6 alloy that is found optimal for the candidate design has a lower yield-, flow-, and ultimate stress than the AL2024-T4 alloy. The weight savings due to the higher strength of the 2024 alloy is however not worth the additional material cost under these weight factors.

Comparison option 2

When looking at option two, with the foam-filled crash boxes, it can be seen that the main differences are that the crash boxes are filled with the lowest density foam, the crash boxes are 3 mm longer than for option 1, and the bumper beam has a section depth that is 3 mm larger. In this candidate design the intrusion distance is 8 mm smaller than for option 1, at the cost of an increase in manufacturing cost of €6.8. The total weight is 0.209 kg higher for the optimal solution using foam-filled crash boxes. The total cost is €2.3 higher, making option 2 slightly worse than option 1.

Due to the addition of the foam in the crash boxes, the peak force is reduced with respect to the mean sustained crush force, which in turn leads to both a shorter intrusion distance and a slightly lower crash rails weight. This limits the weight penalty that is incurred from the heavier crash boxes and the increase of bumper beam section depth. This increase in bumper beam section depth is necessary to make sure that the intrusion of the barrier during the RCAR corner test is not larger than during the RCAR structural test.

Discussion

When comparing the two options as shown in table 7.8 with the actual design of the BMW 730d's rear low-speed crash structures, it can be seen that there are definitely certain differences between the actual design and the best candidate designs. These differences can however be explained to a reasonable extent, and most of this should be characterized as optimization that is performed during later stages of the structural design, as well as the different method of managing the energy absorption during the RCAR corner test.

In figure 7.16 a graphical overview of the intrusion distance during the different load cases is shown for the candidate design that is option 1. It can be seen that there is a nice balance between the different intrusions, such that they all get close to the intrusion limit.

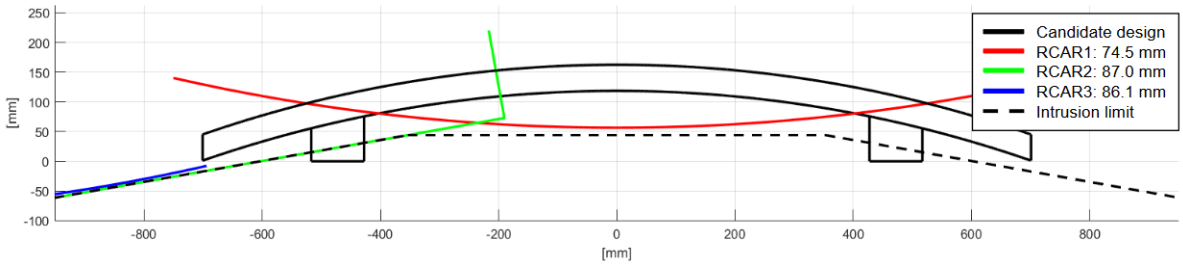

Figure 7.16: Graphical representation of different intrusion distances for the no-foam option for BMW 730d

7.8. Ford Focus 1.5 EcoBoost 2018

In this section the optimization model that is developed during this thesis is used to compare the results with the actual design of the rear low-speed crash structures of the Ford Focus 1.5 EcoBoost 2018. The actual design of the rear low-speed crash structures is shown in section 7.8.1, and the results from the model as well as the comparison to the actual design is presented in section 7.8.2.

To give the optimization model the correct starting point, the vehicle parameters as shown in table 7.6 are used. Next to these vehicle parameters it is also necessary to provide the optimization model with the desired

values for the weight factors. The values that are chosen for this are shown in table 7.9. These values are chosen such that they are expected to match as good as possible with the design philosophy of the OEM during the design of the vehicle. For the Ford Focus this means that cost-wise the focus is on purchase price instead of TCO. The value of lightweighting is set to 4 €/kg, as this vehicle should fall in a class slightly higher than the small car. This means the value of lightweighting should be a bit higher than the 3 €/kg for small vehicles. The value of efficiency due to its influence on battery size is not taken into account, as the Ford Focus is not a BEV. Annual solar kilometers are also not taken into account, as it is not an SEV. The value of longitudinal trunk space is set to 0.3807 €/mm, corresponding with a MSRP of €16,106, as outlined in section 3.6. Environmental impact is also not taken into account, as it is expected that this was also not done during the design of the vehicle.

Table 7.9: Weight factors used to run model for Ford Focus 1.5 EcoBoost

Weight factor	**Value**	**Explanation**
w_1	1 [-]	Fully focussed on purchase price
w_2	0 [-]	No focus on TCO
w_3	4 [€/kg]	Estimated value of lightweighting of medium vehicle
w_4	0 [-]	No value due to influence energy efficiency on battery
w_5	0 [€/skm]	No value for SKM
w_6	0.3807 [€/mm]	Value of trunk for MSRP=€16106
w_7	0 [-]	Environmental impact not considered

7.8.1. Actual design of rear low-speed crash structures

In this section the actual design of the rear low-speed crash structures of the Ford Focus 1.28 EcoBoost 2018 are shown. This data is based on a 3D CAD model of its body-in-white, of which a snapshot is shown in figure 7.17. The values for the most important geometry-defining parameters are shown in table 7.10.

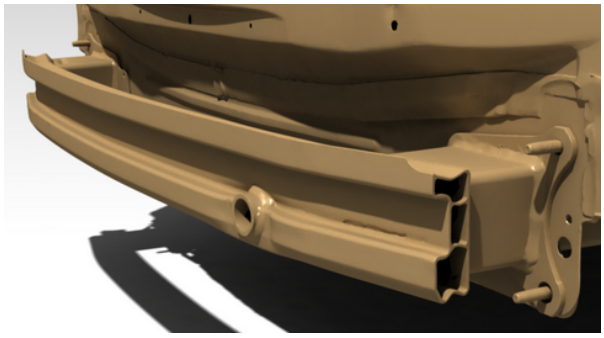

Figure 7.17: Ford Focus 2018 1.5 EcoBoost rear low-speed crash structures (from CAD model)

When looking at the bumper beam, it can be seen that the cross-section is almost constant along the entire length, with only some cutouts and small details present. The cross-section itself consists of a three-cell closed section, with pre-buckled horizontal faces. This leads to the conclusion that it is manufactured using the extrusion method. This three-cell closed section is a weight-effective method to increase the bending resistance and energy absorption with respect to a single-cell closed section. The wall thickness is close to constant, and is estimated to be 2.7 mm. The small lip on top is present to increase the height of the bumper beam section from 90 mm to 102 mm, probably to comply with the RCAR requirements of a minimum section height of 100m. This lip would not qualify though, as the flange thickness needs to be at least 5 mm. The depth of the section is 36.5 mm, and the bumper beam's radius of curvature is measured to be 2407 mm. The only knowledge about the bumper beam's material is that it is made from an aluminium alloy, but no specific alloy is known.

The length of the bumper beam is 1116 mm, and the bumper beam extends only minimally past the crash boxes. This means the length of the bumper beam is not sufficient to pass the RCAR requirements of at least 70% of vehicle width. Also for this vehicle a more complex method is used to absorb the corner impacts, as

this is done by energy-absorbing brackets that also provide stiffness to the corner of the bumper fascia, as well as possible attachments to the rear closing panel and the light housing. This method can lead to weight savings, but is also much more complex to analyze during this initial design phase.

When looking at the crash boxes, it can be seen that the cross-section is completely constant along the length, although some post-operations are necessary to properly make the crash boxes and bumper beam fit together. The cross-section is rectangular, with a height of 80 mm and a width of 102 mm. This would be equivalent to an 91 mm x 91 mm square crash box. The crash boxes are manufactured using extrusions. The crash box length is 80 mm, measured at the centerline of the crash box itself. The wall thickness is unfortunately unknown. The material that is used is unknown, but it is expected that it is an Al6xxx alloy.

Already at this point some discrepancies between the actual design of the Ford Focus rear low-speed crash structures and the model results can be expected. The bumper beam will be shorter than predicted, due to the different method for managing the corner impact. The bumper beam itself will absorb more energy than expected, as well as have a lower wall thickness, due to the three-cell closed section. The height of the bumper beam will also not be predicted correctly as the minimum height to pass the RCAR requirements is 100 mm. The resulting cross-sectional shape of the crash boxes will be square instead of rectangular. These features can not be predicted by the optimization model, as they are not included in the candidate design generation.

7.8.2. Model results and comparison

When the model is run with the input parameters from table 7.6 and the weight factors from table 7.9, one single optimal option is found. This candidate design is characterized by extruded Al6061-T6 crash boxes without foam-filling, as well as an extruded Al6061-T6 bumper beam.

Table 7.10: Comparison between the result generated by the optimization model and benchmarked values

	Ford Focus	Optimal result
Material CB	Al6xxx	Al6061-T6
L_{cb} [mm]	82	75
t_{cb} [mm]	-	2.7
w_{cb} [mm]	91	91
ρ_f [kg/m3]	0	0
m_{cb} [kg]	-	0.194
Material BB	Al6xxx	Al6061-T6
L_{bb} [mm]	1116	1351.0
t_{bb} [mm]	~2.7	2.6
h_{bb} [mm]	90	100
d_{bb} [mm]	36.5	37
R_{bb} [mm]	2407	2407
m_{bb} [kg]	~2.66	2.663
m_{CR} [kg]	-	4.165
m_{total} [kg]	-	7.215
$\delta_{intrusion}$ [mm]	~88.0	88.8

Comparison option 1

When looking at the differences between the actual design and the prediction by the optimization model, as shown in table 7.10, it can be seen that there a few small differences. The optimization model predicts that the crash boxes are 7 mm shorter than in reality, and the predicted length of the bumper beam is 235 mm larger. The section height of the bumper beam is also predicted to be 10 mm larger than the actual design. On the other hand, there is agreement for the materials that are used, as well as the manufacturing techniques. The section depth and wall thickness are predicted well, and so is the total intrusion distance during the RCAR structural test, with a difference of only 0.8 mm.

As mentioned during this comparison for the BMW 730d, the bumper beam will absorb a larger part of the impact energy due to its multi-cell closed section. This leads to the expectation that the actual bumper beam

wall thickness should be lower than in the prediction of the optimization model, but instead the difference between them is only 0.1 mm. The effect of this is that the intrusion distance during the RCAR full width test is probably much smaller than the intrusion distance during the RCAR structural test for this vehicle. This could possibly be beneficial for the packaging of the vehicle in this specific case, as it allows the trunk space to extend a bit further at the center of the vehicle. This could mean that this was done to fit a spare wheel in the trunk. Since the Ford Focus is quite a short vehicle, with not a lot of available length for the rear crash structures, this is a viable explanation. Another parameter that could explain part of this discrepancy is that a material with a lower yield stress and ultimate stress is used in the actual design. This would decrease the manufacturing cost (due to the cost per kg of the raw material), but at the price of an increase in weight.

The optimization model's prediction for the height of the bumper beam is 10 mm larger than the actual situation. The reasons for this are also mentioned during the comparison for the BMW 730d, but can be summarized by saying that this bumper beam of the Ford Focus should not pass the RCAR requirements. The same goes for the length of the bumper beam, as also for this vehicle the corner impact is managed by different physical parts than the bumper beam.

Discussion

When comparing the result from the optimization model with the actual design of the Ford Focus 1.5 EcoBoost's rear low-speed crash structures, it can be seen that there are some differences, especially in the cross-sectional shape and length of the bumper beam. However some main parameters, such as the total intrusion distance, materials, and not using foam-filling, are also predicted well. This shows that, while there are still some limitations on the capabilities of the optimization tool, a useful starting point for the initial design of the rear low-speed crash structures is provided.

In figure 7.18 a graphical overview of the intrusion distance during the different load cases is shown for the optimal result according to the optimization model. It can be seen that there is a good balance between the three different intrusion distances, where all three come very close to the intrusion limit.

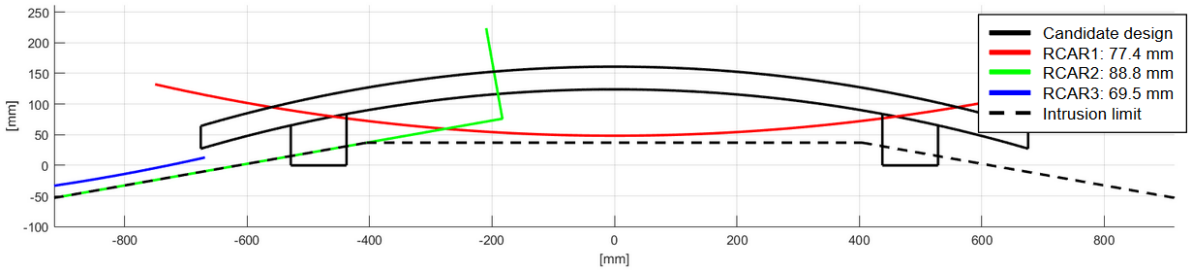

Figure 7.18: Graphical representation of different intrusion distances for result for Ford 1.5 Ecoboost

8

Design for Lightyear One

In this chapter the developed optimization tool is used to provide the conceptual design of the rear low-speed crash structures of the Lightyear One. This is not only useful for Lightyear as a company, but this result will also be used to show how the design of the rear low-speed crash structures should be different for an SEV when compared to other vehicles. To achieve a proper direct comparison, the optimization model is also used to generate a conceptual design for a vehicle with the same input parameters as the Lightyear One, but excluding everything that has to do with the SKM parameter. This means that, when both these results are generated, it will be possible to perform a direct comparison that will show the influence of the inclusion of SKM on the results. The reasons why differences are expected are a stronger incentive for a reduction of the intrusion distance as this increases SKM, as well as the vehicle having more length available for the rear crash structures due to the long and gradually sloping rear end.

The input parameters and weight factors that are used to run the optimization model are shown and explained in section 8.1. The conceptual design for the Lightyear One is presented in section 8.2. After this, the conceptual design for the Lightyear One when excluding SKM is shown and compared to the original design in section 8.3. Finally, it is investigated in section 8.4 if it is already possible to identify possible improvements of the conceptual design, based on certain limitations of the optimization model or design philosophies that are used by current OEM's as was discovered during the benchmarking for validation of the optimization model.

8.1. Input parameters and weight factors

In this section both the input parameters and the weight factors that are used to run the optimization model to generate the conceptual design for the Lightyear One are presented and explained. The input parameters can be found in table 8.1 and are based on both the current status of the CAD model of the vehicle, and the design targets that have been set by the company.

Table 8.1: Input parameters for design for Lightyear One

Parameter	**Value**
Manufacturer Suggested Retail Price	€50,000
SKM	8750
Kerb weight	1250 kg
Vehicle width	1950 mm
Lateral distance between crash boxes	840 mm
Available length for crash structures	860 mm
Bumper beam radius of curvature	2750 mm
Total production volume	100,000

The vehicle width is measured from the CAD model at the widest point of the rear wheel wells, in accordance with the RCAR guidelines. The lateral distance between the crash boxes is also measured from the CAD model. This value follows from how far outwards the crash rails are mounted, which in turn is dependent

on the suspension pick-up points. These suspension pick-up points are positioned relatively far inwards for the Lightyear One, due to the in-wheel motors and relatively large suspension travel that is desired to provide all-road capabilities. This means that the lateral distance between the crash boxes is smaller than for similar cars. The next parameter is the available length, which is also measured from the CAD model. This dimension measures the longitudinal distance between the start of the collapsible part of the crash rails and the most aft position the bumper beam can be positioned at the centerline of the vehicle. The available length for the crash structures is significantly longer for the Lightyear One than most other vehicles, due to the gradually sloping roofline and long rear end of the vehicle. The available length is 860 mm for the Lightyear One compared to 695 mm for the BMW 730d, a car of similar length. This is an increase of 23.7%. The bumper beam radius of curvature is determined by checking which value would allow the bumper beam to fit best inside the bumper fascia along the entire width.

The weight factors that are used to run the optimization model for the design for the Lightyear One can be found in table 8.2. Further information on how these weight factors are used, and how their values are calculated, can be found in chapter 3.

Table 8.2: Weight factors for design for LY01

Weight factor	Value	Explanation
w_1	0	Not focussed on initial purchase price
w_2	1	Fully focussed on TCO
w_3	10 [€/kg]	Value of weight saving for a luxury vehicle
w_4	1	Value due to influence of energy efficiency on battery size is considered
w_5	5.71 [€/SKM]	Value of SKM corresponding to MSRP of €50,000 and 8750 SKM
w_6	0.671 [€/mm]	Value of trunk space for MSRP of €50,000
w_7	1	Environmental impact is taken into account

From table 8.2 it can be seen that during the design of the Lightyear One the focus lies on minimizing the TCO instead of keeping the initial purchase price as low as possible, which is in line with the company's vision. The value of weight saving is set to 10 €/kg, as this corresponds to the value for a luxury ICE vehicle as well as the low end of the values for a luxury BEV value. It is shown in chapter 9 that an increase of this value only has a small effect on the final results for an SEV, and a decrease of this value has no influence on the results at all. Since the Lightyear One is an electric vehicle with a large battery to provide the energy during driving, the value due to the influence of energy efficiency on the size of the battery is also taken into account. The value of 1 SKM is set to €5.71 in accordance with the calculation methodology described in section 3.5. The value of trunk space is set to €0.671 per longitudinal mm, as this corresponds to the MSRP of €50,000 using the methodology outlined in section 3.6. Finally, since Lightyear's mission is to provide clean mobility for everyone, environmental impact is also taken into account.

8.2. Presentation of optimal result

In this section the conceptual design for the Lightyear One is presented. This is considered to be the optimal result by the optimization model based on the provided input parameters and weight factors. An overview of the parameters that define the geometry of the crash boxes and the bumper beam, as well as the general parameters that show how this conceptual design performs is presented in table 8.3. It is important to note that it was decided to limit the bumper beam's wall thickness to a maximum of 4.0 mm, as the additional value of SKM has the tendency to increase the bumper beam's wall thickness to increase the bumper beam energy absorption in order to limit the intrusion distance. However, when the wall thickness becomes larger than roughly 10% of either the bumper beam section depth or section height, the cross-section can not be considered to be thin-walled anymore. This leads to the undesired risk that the assumptions made during the development of the structural analysis methods are not valid anymore. One example of this would be that the bumper beam section actually does not crush anymore before the peak force on the crash boxes is reached.

The main takeaway from table 8.3 is that the optimal design of the rear low-speed crash structures for the Lightyear One consists of an extruded AL2024-T4 bumper beam with a high wall thickness and short, foam-filled extruded AL2024-T4 crash boxes. This leads to a high bumper beam energy absorption, effectively reducing the necessary length of the crash boxes, as this is worth the additional weight. This also leads to a

Table 8.3: Optimal result for Lightyear One

General parameters		**Crash boxes**		**Bumper beam**	
m_{total}	9.721 kg	Material	AL2024-T4	Material	AL2024-T4
m_{CR}	4.914 kg	L_{cb}	54 mm	L_{bb}	1428 mm
C_{manuf}	€41.2	t_{cb}	1.8 mm	t_{bb}	4.0 mm
Intrusion full width test	55.7 mm	w_{cb}	100 mm	d_{bb}	38 mm
Intrusion structural test	62.3 mm	ρ_{foam}	170 kg/m3	h_{bb}	100 mm
Intrusion corner test	62.2 mm	η_L	0.60	R_{bb}	2750 mm
Peak force	117.4 kN	m_{cb}	0.191 kg	m_{bb}	4.426 kg
Mean force	76.3 kN	c_{cb}	€11.0	c_{bb}	€19.1

decreased crash box peak force in order to reduce the crash rails weight penalty, since the available length for the rear crash structures is so large, as this is worth the additional manufacturing cost. This bumper beam length provides an overlap of 6.1 mm between the bumper beam and the RCAR barrier during the RCAR corner test. The more expensive aluminium alloy AL2024-T4 with improved structural properties should be used, as the increased flow stress leads to a higher energy absorption of the bumper beam as well as a lower weight, and this is worth the small amount of extra manufacturing cost that is incurred. A graphical overview of the intrusion distance during the three different low-speed load cases that are considered in the optimization model is overlaid on a top view of the conceptual design and shown in figure 8.1.

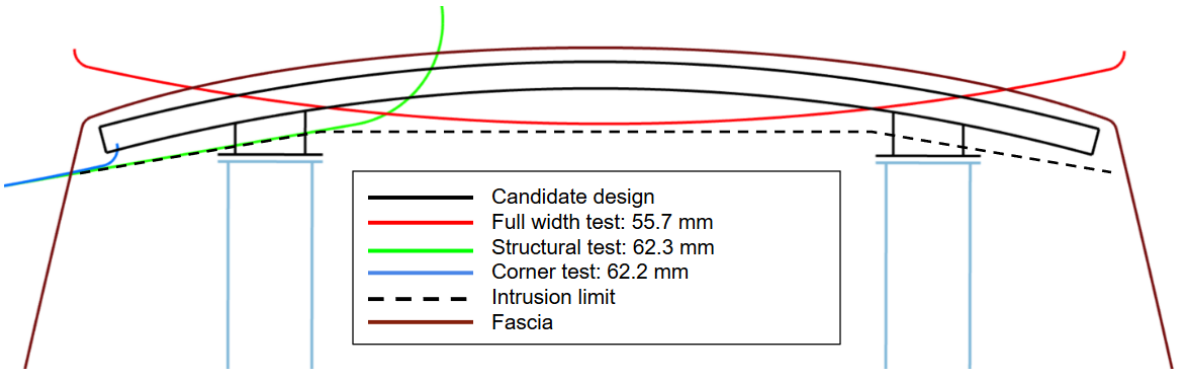

Figure 8.1: Graphical overview of intrusion distance for optimal result

It is interesting to check what the differences are in total performance between the optimal solutions for different types of candidate designs. This will show the performance of the conceptual design that is presented in table 8.3 compared to two designs using different approaches (AL2024-T4 crash boxes without foam-filling and CFRP braided crash boxes, the bumper beam is an AL2024-T4 extrusion in all cases), and therefore show how much improvement there is compared to these other options. The comparison on purely the direct parameters intrusion distance, total weight, and manufacturing cost is shown in table 8.4.

Table 8.4: Comparison of direct parameters between different types of candidate designs

	Foam-filled crash box	**Empty crash box**	**CFRP braided crash box**
$\delta_{intrusion}$ [mm]	62.3	68.0	67.5
m_{total} [kg]	9.721	9.990	9.251
C_{manuf} [€]	41.2	34.2	56.6

In table 8.5 the comparison between the different types of designs is shown regarding the differences in cost of the individual performance evaluation parameters as well as the total cost. The optimal result for the Lightyear One, as presented in table 8.3 is taken as the baseline, from which the cost differences are calculated.

When comparing the full-aluminium design without foam-filled crash boxes to the optimal conceptual de-

Table 8.5: Comparison of performance evaluation parameters and total cost between different types of candidate designs

	Foam-filled crash box	**Emty crash box**	**CFRP braided crash box**
Cost of Δ weight [€]	-	+2.7	-4.7
Cost of Δ TCO [€]	-	-1.0	+2.8
Cost of Δ energy efficiency [€]	-	+1.1	-2.2
Cost of Δ SKM [€]	-	+65.6	+59.9
Cost of Δ trunk space [€]	-	+3.8	+3.5
ΔC_{total} [€]	-	+72.0	+59.3

sign for the Lightyear One, the intrusion distance is increased by 5.7 mm (which yields a reduction of 11.49 SKM, which is a reduction in value of €65.6). The total weight of the rear crash structures shows a decrease of 0.269 kg (yielding an additional value of €2.7), as well as a reduction in manufacturing cost of €7.0. This reduction in manufacturing cost results in an improvement in TCO of only €1.0, as this is largely offset by the increased SKM leading to lower charging costs. There is an increase of €1.1 in the cost of energy efficiency, as the increased total weight means that the energy efficiency goes down and a slightly larger battery capacity is needed to keep the same range. Due to the increased intrusion distance the cost of trunk space is increased by €3.8. Combined this leads to a total increase in cost of €72.0, which is large enough to warrant the additional engineering effort necessary to design the foam-filled crash boxes successfully.

When comparing the best performing design consisting of an AL2024-T4 bumper beam and braided CFRP crash boxes to the optimal conceptual design for the Lightyear One, an increase in the intrusion distance of 5.2 mm (which yields a reduction of 10.48 SKM, reducing the value by €59.9). The total weight of the rear crash structures shows a decrease of 0.470 kg (increasing the total value by €4.7), but this is at the cost of an increase in manufacturing cost of €15.4. This translates to an increased cost of TCO of only €2.8, as it is partly offset by the lower fuel cost. Due to the decreased total weight a reduction of €2.2 in the cost of energy efficiency is realized, as the energy efficiency goes up and a slightly smaller battery capacity is needed for equal range. Due to the increased intrusion distance the cost of trunk space is increased by €3.5. Moving from the optimal conceptual design for the Lightyear One to a variant with CFRP braided crash boxes will therefore result in an increase in total cost of €59.3. This would make it a better option than the all-aluminium design without foam-filling the crash boxes, but still much worse than the full-aluminium design with foam-filled crash boxes.

Based on this comparison it can be concluded that the design with the foam-filled crash boxes is indeed the preferred solution, even when including externalities like the additional engineering effort to design and test the foam-filled crash boxes.

8.3. Comparison result with non-SEV situation

To provide the most direct information on how the design of the rear low-speed crash structures should be different for an SEV, the optimization tool is also used to generate the optimal results for the Lightyear One in the case that the SKM parameter is left out. This result will then be compared to the optimal result for the Lightyear One when including the SKM parameter, as presented in table 8.3. To be explicit in how the optimization model is set up, the weight factors for this run are shown in table 8.6, in which the only difference is that here the parameter w_5 is set to zero. The remaining parameters are identical to the ones shown in table 8.1.

An overview of the parameters that define the geometry of the crash boxes and the bumper beam, as well as the general parameters that show how well the conceptual design performs is presented in table 8.7.

From table 8.7 it can be seen that the optimal conceptual design still uses foam-filled crash boxes when the parameter SKM is left out. When compared to the result presented in table 8.3, significant changes can however be seen in the length of the crash boxes (42.6% longer), as well as the bumper beam wall thickness (decreased by 30.0%) and section depth (increased by 15.8%). This results in an increase in the intrusion distance of 22.1 mm, which is 35.5%, as well as a decrease in the total crash structures weight of 1.159 kg, which is a reduction of 11.9%. Based on these differences, it can be concluded that the addition of the SKM parameter

Table 8.6: Weight factors for design for LY01 when excluding SKM

Weight factor	Value	Explanation
w_1	0	Not focussed on initial purchase price
w_2	1	Fully focussed on TCO
w_3	10 [€/kg]	Value of lightweighting of luxury vehicle
w_4	1	Value due to influence of energy efficiency on battery size is considered
w_5	0 [€/SKM]	Value of SKM is excluded
w_6	0.671 [€/mm]	Value of trunk space for MSRP of €50,000
w_7	1	Environmental impact is taken into account

has a significant influence on the optimal design of the rear low-speed crash structures. The influence of the vehicle being an SEV would be even larger if the large available length for the crash structures is also taken into account. This would reduce the need for foam-filled crash boxes due to the crash rails weight penalty inherently being smaller.

Table 8.7: Optimal result for Lightyear One when excluding SKM

Overall parameters		Crash boxes		Bumper beam	
m_{total}	8.562 kg	Material	AL2024-T4	Material	AL2024-T4
m_{CR}	4.720 kg	L_{cb}	77 mm	L_{bb}	1428 mm
C_{manuf}	€38.4	t_{cb}	1.8 mm	t_{bb}	2.8 mm
Intrusion full width test	63.3 mm	w_{cb}	100 mm	d_{bb}	44 mm
Intrusion structural test	84.4 mm	ρ_{foam}	170 kg/m3	h_{bb}	100 mm
Intrusion corner test	63.2 mm	η_L	0.60	R_{bb}	2750 mm
Peak force	117.4 kN	m_{cb}	0.272 kg	m_{bb}	3.298 kg
Mean force	76.3 kN	c_{cb}	€11.8	c_{bb}	€14.8

The comparison in total performance of the winning candidate design is again compared here to the optimal solution in the case that crash boxes are not filled with foam, as well as the optimal solution when using composite crash boxes. This comparison is shown for the direct parameters (intrusion distance, total weight, manufacturing cost) in table 8.8 for both crash boxes without foam and CFRP braided crash boxes, both having an AL2024-T4 bumper beam.

Table 8.8: Comparison of direct parameters between different types of candidate designs

	Foam-filled crash box	Empty crash box	CFRP braided crash box
$\delta_{intrusion}$ [mm]	84.4	80.1	101.7
m_{total} [kg]	8.562	9.272	7.821
C_{manuf} [€]	38.4	33.6	53.3

Table 8.9 shows the comparison between the different types of designs regarding the diferences in cost of the individual performance evaluation parameters as well as the total cost. The optimal result for the Lightyear One (when excluding SKM), as presented in table 8.7 is taken as the baseline, from which the cost differences are calculated.

Table 8.9: Comparison of performance evaluation parameters and total cost between different types of candidate designs

	Foam-filled crash box	Empty crash box	CFRP braided crash box
Cost of Δ weight [€]	-	+7.1	-7.4
Cost of Δ TCO [€]	-	-3.6	+11.5
Cost of Δ energy efficiency [€]	-	+3.2	-2.9
Cost of Δ trunk space [€]	-	-2.9	+11.6
ΔC_{total}	-	+4.6	+12.8

When comparing the best full-aluminium design without foam-filled crash boxes with the optimal design (when the parameter SKM is excluded), the intrusion distance is decreased by 4.3 mm (which increases the

value of trunk space by €2.9). The total weight of the rear crash structures is increased by 0.710 kg (which reduces the total value by €7.1). However, the manufacturing cost is €4.8 lower. This is reflected in the decreased TCO, which is €3.6 lower. This decrease is slightly smaller than the difference in manufacturing cost as the fuel cost will be higher due to the increased total weight. This increase in total weight also has an effect on the cost of energy efficiency, increasing it by €3.2, as a slightly larger battery capacity is needed for an equal range. Due to the decreased intrusion distance the cost of trunk space is decreased by €2.9. Combined this leads to an increase in total cost of €4.6, which is possibly not large enough to warrant the additional engineering effort necessary to design the foam-filled crash boxes. The design of foam-filled crash boxes increases the amount of simulations and physical testing that is necessary, as their behaviour is not as well-known as empty metal crash boxes. The amount of total value that foam-filling the crash boxes should bring before it is worth the additional engineering efforts is dependent on the total production volume, as it can be seen as an investment that is spread out over all vehicles produced.

When comparing the best performing design consisting of an AL2024-T4 bumper beam and braided CFRP crash boxes to the optimal design (when SKM is excluded), the intrusion distance is increased by 17.4 mm (which reduces the value of trunk space by €11.6). However, the total weight is 0.740 kg lower for the design using composite crash boxes (which is a difference in value of weight saving of €7.4), but the increase in manufacturing cost if €14.9. This results in an increase of €11.5 of TCO. The cost of energy efficiency is reduced by €2.9 as the total weight is lower and therefore the energy efficiency is improved. Since the intrusion distance is increased by 17.3 mm the cost of trunk space is also increased by €11.6. This leads to an increase in total cost of €12.8 when the design using braided CFRP crash boxes is chosen. From this it can be concluded that the composite crash boxes are not a great option in this situation, as this would also lead to additional engineering complexity to design the connection between the crash boxes and the bumper beam.

Effect of large available length for rear crash structures

An additional comparison that can be made is to decrease the length available for the rear crash structures to 695 mm, equal to this dimension for the BMW 730d (which has a very similar vehicle length compared to the Lightyear One) that has been used for validation of the complete results using benchmarking, as can be found in section 7.6. A large value for $L_{available}$ is not necessarily something that happens automatically for every SEV that is designed, but for the Lightyear One this came naturally based on the elongated aerodynamic rear end which pushes the occupants forwards during the packaging of the vehicle. This comparison will show the influence of this increase in available length for the rear crash structures, and the optimal design for $L_{available}$ = 695 mm is shown in table 8.10.

Table 8.10: Optimal result for Lightyear One when excluding SKM and $L_{available}$ = 695 mm

Overall parameters		**Crash boxes**		**Bumper beam**	
m_{total}	7.630 kg	Material	AL2024-T4	Material	AL2024-T4
m_{CR}	4.338 kg	L_{cb}	71 mm	L_{bb}	1428 mm
C_{manuf}	€29.2	t_{cb}	2.4 mm	t_{bb}	2.4 mm
Intrusion full width test	95.4 mm	w_{cb}	100 mm	d_{bb}	48 mm
Intrusion structural test	97.2 mm	ρ_{foam}	0 kg/m3	h_{bb}	100 mm
Intrusion corner test	70.2 mm	η_L	0.76	R_{bb}	2750 mm
Peak force	158.6 kN	m_{cb}	0.184 kg	m_{bb}	2.925 kg
Mean force	82.2 kN	c_{cb}	€7.9	c_{bb}	€13.4

It can be seen from table 8.7 that the optimal result has both an AL2024-T4 bumper beam and crash boxes, and no foam-filling is used. When compared to the result for the original $L_{available}$ the bumper beam depth is increased by 9.1% and the bumper beam wall thickness is decreased by 14.3%. This leads to a reduction in the bumper beam weight of 11.3%. The length of the crash boxes is decreased by 6 mm, but since no foam-filling is used (increasing the effective length) the contribution of the crash box to the intrusion distance during the RCAR structural test is actually 8 mm larger. When combined, this leads to an increase in the intrusion distance of 12.8 mm, which is 15.2%. The total weight of the crash structures is however reduced by 0.932 kg, corresponding to a reduction of 10.9%. This shows that a reduction of the available space for the crash structures brings the optimal design even further away from the optimized conceptual design for the Lightyear One, as the difference in intrusion distance becomes larger, the energy absorption of the

bumper beam becomes much smaller, and at this point foam-filling should definitely not be used anymore. Additionally, the corner test is not limiting anymore for the intrusion distance, while this was the case for the conceptual design for the Lightyear One as shown in section 8.2.

8.4. Possible improvements

In this section it is investigated if there are possible improvements to the conceptual design of the rear low-speed crash structures for the Lightyear One that can already be identified, but are out of the scope of the optimization model. These possible improvements are based on both the results from the benchmarking in sections 7.6 to 7.8, and the results from the parameter sensitivity analysis based on the Lightyear One input parameters as shown in section 9.1.

Decrease of bumper beam length

During the benchmarking of the BMW 730d and the Ford Focus, it was found that their bumper beams do not fully comply with the RCAR requirements as their bumper beam length is less than 70% of the vehicle width. Instead of absorbing the impact energy during the RCAR corner test using their bumper beam, it was found that they use a different method, namely including energy absorbing brackets inside the bumper fascia. Since it was found that the intrusion distance during the RCAR corner test is critical for the current design, it is investigated here how the optimal result would change in case the RCAR corner test is excluded from the optimization model. The length of the bumper beam is then decreased such that it sticks out 50 mm on both sides of the crash boxes. This value of 50 mm is chosen, as this length of the free end was found to be 63 mm for the BMW 730d and 30 mm for the Ford Focus, which means that 50 mm falls nicely within this range. The new length of the bumper beam is calculated in equation 8.1.

$$L_{bb} = L_{unsupported} + 2 * w_{cb} + 2 * 50\text{mm} = 840 + 200 + 100 = 1140\text{mm} \tag{8.1}$$

The optimal result that is generated by the optimization model is shown in 8.11. The input parameters and weight factors used here are identical to the ones found in table 8.1 and 8.2.

Table 8.11: Result when excluding RCAR corner test from the optimization model

Overall parameters		**Crash boxes**		**Bumper beam**	
m_{total}	10.657 kg	Material	AL2024-T4	Material	AL2024-T4
m_{CR}	7.295 kg	L_{cb}	37 mm	L_{bb}	1140 mm
C_{manuf}	€34.9	t_{cb}	2.7 mm	t_{bb}	4.0 mm
Intrusion full width test	36.0 mm	w_{cb}	100 mm	d_{bb}	25 mm
Intrusion structural test	38.5 mm	ρ_{foam}	170 kg/m3	h_{bb}	100 mm
Intrusion corner test	-	η_L	0.58	R_{bb}	2750 mm
Peak force	214.4 kN	m_{cb}	0.164 kg	m_{bb}	3.035 kg
Mean force	130.1 kN	c_{cb}	€10.6	c_{cb}	€13.8

When looking at table 8.11 and comparing to the result presented in table 8.3 it can be seen that the intrusion distance can be decreased significantly, from 62.3 mm when the RCAR corner test is included to 38.5 mm when it is excluded. This is due to the inefficient energy absorption mechanism when the impact energy is absorbed by rotation of the plastic hinge that develops in the bumper beam. The total weight of the crash structures also increases significantly, from 9.721 kg to 10.657 kg, which is mainly due to the increased crash rails weight penalty since the peak force on the crash forces is so high (even though foam-filling is used to reduce it). The weight of the bumper beam is actually 1.391 kg lower, as the length is reduced, but also a smaller section depth is needed since it does not to absorb the impact energy during the RCAR corner test anymore. It should be noted that at this point the efforts to reduce the intrusion distance become so large that this leads to an unrealistic design, due to the bumper beam section not being thin-walled anymore, and the contribution of the crash boxes to the intrusion distance being only very small. The peak force on the crash box also becomes so high that the expected average acceleration of the vehicle during the rear high-speed load case (in accordance with section 5.5.2) is around $20.1g$. While this is still lower than the absolute maximum that is allowed, it is less favourable than the expected average acceleration of the vehicle for the design as shown in table 8.3, being $11.0g$. It is important to realize that an additional increase in the weight will happen due to the weight of the energy absorbing brackets inside the bumper fascia. A graphical overview of the geometry

and intrusion distances is shown in figure 8.2.

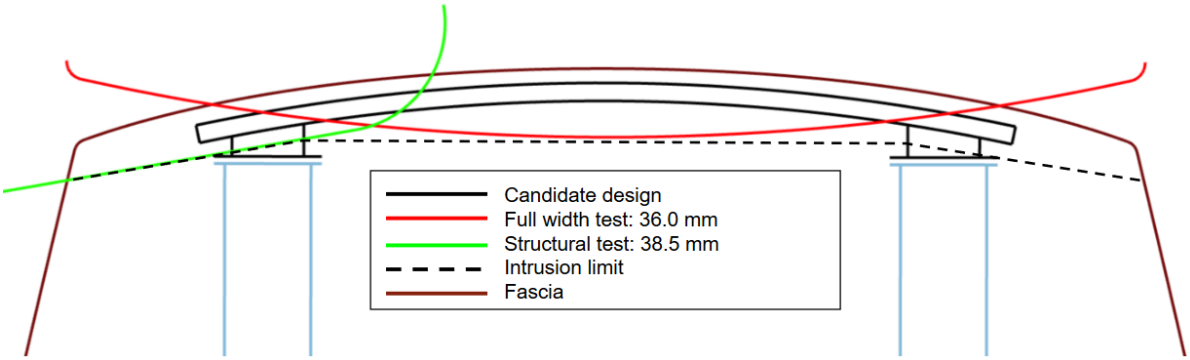

Figure 8.2: Overview geometry and intrusion distances when RCAR corner test is excluded

However, an interesting takeaway from this is that it is possible to reduce the intrusion distance further when the RCAR corner test is managed without using the bumper beam. Apparently it is possible to pass the RCAR requirements when it can be demonstrated that the new approach that is used will also work properly. Especially the reduction in bumper beam section depth seems like a good method to both decrease the intrusion distance and save some weight on the design of the bumper beam.

Multi-cell extruded bumper beam

The second thing that was noticed during the benchmarking of the BMW 730d and the Ford Focus, was that they both use extruded bumper beams that consist of multiple closed cells. In the case of the BMW 730d it is a relatively simple two-cell section, while for the Ford Focus a more complicated three-cell section is used. This does not add a lot of complexity or cost during the manufacturing, as it is possible to incorporate these multi-cell sections in the extrusion dies. The advantage of using a multi-cell extruded bumper beam is that there is an increased amount of horizontal flanges that can be compressed for bumper beam energy absorption.

From the resulting conceptual design for the Lightyear One it can be seen that there is a strong emphasis on the energy absorption of the bumper beam during the RCAR structural test, as this reduces the amount of energy that needs to be absorbed by the crash boxes. This in turn results in shorter crash boxes and a lower peak force, in order to limit the crash rails weight penalty as well. The structural model that is developed during this thesis to analyze the energy absorption of the bumper beam is not able to analyse the performance of multi-cell extruded bumper beams, and neither is it accurate enough to reach this level of detail in the optimization of the bumper beam cross-section. This means that this should be looked at during later stages of the structural design, and analysed using FEA.

Another improvement that should be looked at during the optimization of the bumper beam section is using a varying wall thickness. The wall thickness of the horizontal flanges is useful for the energy absorption due to crushing of the section, but the wall thickness of the vertical flanges is more effective at increasing the bending resistance of the bumper beam, which is beneficial during the RCAR corner test and for the elastoplastic energy absorption of the bumper beam during the RCAR full width test. The proper balance between these needs to be found for the specific design, using FEA, in later stages of the structural design.

Increase of lateral distance between crash boxes

The final possible improvement that will be suggested here is to increase the lateral distance between the crash boxes, and is based on the results from the sensitivity analysis in chapter 9. This will only be effective in improving the rear low-speed crash structures if the bumper beam is used for absorption of the impact energy during the RCAR corner test, as the goal of increasing the lateral distance between the crash boxes is to reduce the length of the free end of the bumper beam and therefore decreasing the intrusion distance during the RCAR corner test. It will actually have a negative effect on the intrusion distance during the RCAR full width test, as geometrically the RCAR barrier will intrude further before the crash boxes are engaged, since it

has a fixed radius of 3400 mm, automatically increasing the longitudinal distance when the lateral distance is increased.

Increasing the lateral distance between the crash boxes will not be easy for the Lightyear One, as the lateral location of the crash rails is already determined by the pick-up points from the rear suspension. It is also important to reasonably align the crash boxes with the crash rails, as a misalignment would lead to an increased risk of a global bending mode being exhibited, which is detrimental for the energy absorption. This possible improvement should therefore be seen more as something to keep in mind during the later stages of the design project, rather than something that should be actively pursued.

Another method that was found (during the parameter sensitivity analysis) to be very effective in reducing the intrusion distance during the RCAR corner test is decreasing the vehicle width. Unfortunately, this will also negatively influence the packaging of the vehicle, width of the solar array, as well as the overall design. It will also push the crash rails further inside, reducing the lateral distance between the crash boxes. Based on this, reducing the vehicle width is not advised.

9

Parameter sensitivity analysis

In this chapter the robustness of the solution generated by the optimization model is investigated. This is done to provide knowledge of which input parameters have a large influence on the solution that is found, and which input parameters have less importance. This will help in understanding for which parameters it is of high importance to determine their specific values, and for which a best-guess approach can possibly be enough.

Due to the generality of the optimization model, it is necessary to limit the range of input parameters that is used. For this reason, the input parameters that are used for the design of the Lightyear One are used as a starting point. It was found that the additional value of SKM has a large influence on the optimal result, and trumps the effect of variations on certain other parameters, like the value of weight saving and trunk space. To also assess the influence of whether the considered vehicle is an SEV, an adapted set of weight factors corresponding to the Lightyear One if it would be a normal BEV is also used. These input parameters and weight factors can be found in tables 8.1, 8.2 (when including SKM), and 8.6 (when excluding SKM).

Based on these two sets of input parameters, it is investigated what the influence is of a variation of 10% of these values on the most important ouput parameters that summarize the design. For some parameters this variation of 10% has no influence on the final results, in which case a larger variation is chosen. The output parameters considered here are the following:

- m_{total}, the weight of the combination of bumper beam, crash boxes, and crash rails
- C_{manuf}, the estimated manufacturing cost of the low-speed rear crash structures
- $\delta_{intrusion}$, the intrusion distance during the RCAR structural test

The results and discussion of the sensitivity analysis when including SKM is shown in section 9.1, and when excluding SKM in section 9.2. A positive percentage means that an increase of the input parameter leads to an increase of the output parameter, while a negative percentage means that the value of the output parameter decreases if the input parameter is increased.

9.1. Including SKM

In this section the influence of variations of the main input parameters on the optimal result are analysed based on the same input parameters as during the design for the Lightyear One.

Kerb weight

For the sensitivity analysis of the input parameter kerb weight, its value is varied by 10%. In table 9.1 it can be seen that the kerb weight of the vehicle has a reduced effect on the weight of the low-speed rear crash structures plus the crash rails. This is due to the bumper beam having the maximum wall thickness in all three results to increase the bumper beam energy absorption and therefore limit the intrusion distance. The main difference is in the weight of the crash rails, as the peak force of the crash boxes changes if either more or less energy needs to be absorbed. The amount of energy that needs to be absorbed is also not linearly related

to the vehicle weight for the RCAR structural test, from which follows that the difference in energy absorbed between a kerb weight of 1125 kg and 1250 kg is larger than between 1250 kg and 1375 kg. This effect is also shown in figure 5.16. A smaller sensitivity is found for the manufacturing cost of the rear low-speed crash structures, as the material and production techniques do not change, and the weight of the parts changes only slightly, leading to a small change in material cost. The sensitivity of the intrusion distance is found to be between 2.3% and 2.6%. This can also be explained by all results having the same bumper beam wall thickness, and therefore a very similar energy absorption of the bumper beam during the RCAR structural test. In the case where the kerb weight is increased, more impact energy needs to be absorbed by the crash boxes which will increase the length of the crash boxes that is necessary to limit the peak force, and vice versa.

Table 9.1: Sensitivity of result to $m_{vehicle}$

$m_{vehicle}$ [kg]	**Difference**	**1125 kg**	**1250 kg**	**1375 kg**	**Difference**
m_{total} [kg]	6.2%	9.175	9.721	9.964	2.5%
C_{manuf} [€]	0.7%	40.9	41.2	41.5	0.7%
$\delta_{intrusion}$ [mm]	2.3%	60.9	62.3	63.9	2.6%

Vehicle width

The input parameter vehicle width is varied by 10% to investigate the sensivity of the final result. It can be seen from table 9.2 that the total weight has a sensitivity of between 1.5% and 3.9% to the width of the vehicle. This can be considered a small sensitivity as the vehicle width is well-known and this 10% variation has a large effect on parameters like the length of the free end of the bumper beam. For all three results the bumper beam already has the maximum wall thickness in order to limit the intrusion distance, but the difference comes partly from the change in length of the bumper beam that is necessary to keep the optimal overlap width between the bumper beam and the RCAR barrier. This is however countered by a change in peak force on the crash boxes, which influences the weight of the crash rails, as will be explained later. Around 70% of the change in vehicle width is translated into the change in bumper beam length. The intrusion distance during the RCAR corner test depends only on the length of the free end of the bumper beam, when the bumper beam cross-section and vehicle kerb weight are identical. Since in this analysis the distance between the crash boxes stays equal, the change in bumper beam length directly relates to the length of the free end in an absolute sense. This means that a shorter bumper beam (and therefore shorter free end) leads to a much smaller intrusion distance during the RCAR corner test, while a longer bumper beam leads to a much larger intrusion. This is confirmed by the results in table 9.2, showing a large sensitivity of between 17.1% and 24.6%. From this it also follows that the peak force on the crash boxes changes, as it either needs to increase to correspond to the smaller intrusion distance, or decrease as it has no use to have a smaller intrusion during the RCAR structural test than during the RCAR corner test. The estimated manufacturing cost decreases by around 7% when the vehicle width is decreased by 10%, due to mainly the change in weight for the bumper beam. However, when the vehicle width is increased by 10%, a large change of -10.9% is found in the manufacturing cost. Due to the increased intrusion distance, foam-filling of the crash boxes is no longer the preferred solution, which leads to a sharp decrease in the manufacturing cost of the crash boxes.

Table 9.2: Sensitivity of result to $w_{vehicle}$

$w_{vehicle}$ [mm]	**Difference**	**1800 mm**	**2000 mm**	**2200 mm**	**Difference**
m_{total} [kg]	1.5%	9.577	9.712	10.096	3.9%
C_{manuf} [€]	7.0%	38.5	41.2	36.7	-10.9%
$\delta_{intrusion}$ [mm]	17.1%	53.2	62.3	77.6	24.6%

Lateral distance between crash boxes

For the sensitivity analysis of the input parameter $L_{unsupported}$, its value is varied by 10%. From table 9.3 it can be that a decrease of $L_{unsupported}$ leads to an increase of all output parameters considered here, and vice versa. The main effect of changing the lateral distance between the crash boxes is that the length of the free end of the bumper beam changes, similar to changing the width of the vehicle. However, this effect is significantly smaller here, as the difference in absolute length of the free end is smaller (70 mm vs 42 mm).

This means that sensitivity to this input parameter is also lower. Additionally, changing the lateral distance between the crash boxes also changes the contribution of the bumper beam to the intrusion distance during the RCAR full width test based purely on geometry. A larger $L_{unsupported}$ leads to a larger bumper beam contribution to the intrusion distance, which is confirmed by the changes of between -6.0% and -6.9% in the intrusion distance.

Table 9.3: Sensitivity of result to $L_{unsupported}$

$L_{unsupported}$ [mm]	**Difference**	**756 mm**	**840 mm**	**924 mm**	**Difference**
m_{total} [kg]	0.6%	9.665	9.712	9.513	-2.1%
C_{manuf} [€]	-1.0%	41.6	41.2	40.7	-1.2%
$\delta_{intrusion}$ [mm]	-6.0%	66.3	62.3	58.0	-6.9%

Available length for crash structures

The input parameter $L_{available}$ is varied by 10% to investigate the sensivity of the final result. From table 9.4 it can be seen that the total weight changes by between 2.6% and5.5%. This can be explained by the crash rails weight penalty. If more length is available for the crash rails, a lower crash rails mean force (and therefore also crash rails peak force) is needed to absorb the impact energy during the FMVSS 301 high-speed load case. However, the peak force on the crash boxes stays almost the same which means that the wall thickness of the crash rails needs to increase to ensure that they are not damaged before the crash boxes are fully utilized, which leads to a higher total weight. The design of the low-speed rear crash structures changes only minimally, which is reflected in the small sensitivities for the manufacturing cost and intrusion distance.

Table 9.4: Sensitivity of result to $L_{available}$

$L_{available}$ [mm]	**Difference**	**774 mm**	**860 mm**	**946 mm**	**Difference**
m_{total} [kg]	5.5%	9.215	9.712	9.973	2.6%
C_{manuf} [€]	0.7%	40.9	41.2	41.2	0%
$\delta_{intrusion}$ [mm]	-0.6%	62.7	62.3	62.9	1.0%

Total production volume

To analyse the sensitivity of the output parameters to the total production volume a slightly different approach is taken, as a 10% variation produced only very small differences, and it is more interesting to see these differences over a larger range of production volumes. For this reason, it is decided to check the results for total production volumes of 10,000 and 50,000, compared to the actual total production volume of 100,000 units. From the results in table 9.5 it can be seen that the total weight of the crash structures and the intrusion distance are not influenced by these changes in production volume. This means that an identical design for the low-speed rear crash structures is optimal in all three situations. As expected, there is a difference in the estimated manufacturing cost, of 6.6% for a production volume of 10,000 units, and 0.7% for 50,000 units. This is due to the non-recurring cost being spread over a smaller amount of vehicles. It can be seen that the manufacturing costs are the highest for the lowest total production volume.

Table 9.5: Sensitivity of result to total production volume

Production volume [-]	**Difference**	**10,000** [-]	**100,000** [-]	**50,000** [-]	**Difference**
m_{total} [kg]	0%	9.712	9.712	9.712	0%
C_{manuf} [€]	6.6%	44.1	41.2	41.5	0.7%
$\delta_{intrusion}$ [mm]	0%	62.3	62.3	62.3	0%

Value of weight saving

In order to analyse the sensitivity of the output results to the value of weight saving, a much larger variation is taken, as the standard 10% variation did not show any difference in the output results. This means that the sensitivity of the output results to the value of weight savings is low, which can be explained by the solution being dominated by the value of SKM and trunk space. It is checked what the differences in the output parameters are for w_3=0 €/kg (the lowest value that is possible) and w_3=20 €/kg (the value that just shows a

difference in the results). Both these values are unrealistic, but this method is necessary because the solution is dominated by the value of SKM. It can be seen in table 9.6 that there is no difference in the optimum candidate design if the value of weight saving is completely eliminated, which shows that the solution is dominated by the value of trunk space and SKM. When the value of weight saving is set to 20 €/kg a decrease of 2.0% is found for the total weight of the rear crash structures. The intrusion distance increases by 0.8%, as a longer crash box is used in order to reduce the crash rails weight penalty. The estimated manufacturing cost however stays the same, as the difference in the design itself is so small. Interestingly, even with the very high value of weight saving of 20€/kg the composite crash boxes still do not become the optimal solution. The total weight does reduce in a design with CFRP crash boxes, but the intrusion distance also increases, which leads to a worse design overall.

Table 9.6: Sensitivity of result to value of weight saving

w_3 [€/kg]	**Difference**	**0 [€/kg]**	**10 [€/kg]**	**20 [€/kg]**	**Difference**
m_{total} [kg]	0%	9.712	9.712	9.531	-2.0%
C_{manuf} [€]	0%	41.2	41.2	41.2	0%
$\delta_{intrusion}$ [mm]	0%	62.3	62.3	62.8	0.8%

Value of SKM

To analyse the influence of the value of SKM on the output results, this value is varied from 0.1 times the original value, and 10 times the original value. Looking at table 9.7 it can be seen that when the value of SKM is €0.57 the total weight is reduced by 2.7% and the intrusion distance is increased by 2.2%. This also leads to a reduction in the estimated manufacturing cost of 1.7%. The optimal material and manufacturing techniques stay the same. When the value of SKM is increased to €57.1 the optimal result does not change at all. From this it can be seen that the final design is not sensitive at all to the exact value of SKM. This can be explained by the bumper beam already having reached the maximum allowed wall thickness, which is the limit of how far the intrusion distance can be reduced.

Table 9.7: Sensitivity of result to value of SKM

w_5 [€/SKM]	**Difference**	**0.57 [€/SKM]**	**5.71 [€/SKM]**	**57.1[€/SKM]**	**Difference**
m_{total} [kg]	2.7%	9.463	9.712	9.712	0%
C_{manuf} [€]	1.7%	40.5	41.2	41.2	0%
$\delta_{intrusion}$ [mm]	-2.2%	63.7	62.3	62.3	0%

Value of trunk space

To analyse the influence of the value of trunk space on the output results, a variation of half the actual value and double this value is chosen. It can be seen from table 9.8 that this does not have any influence on the output parameters, as the same candidate design is found to be optimal. This is due to the value of SKM being significantly more important, as under these weight factors reducing the intrusion distance by 1 mm is worth €3.07 due to the increase in SKM. It was also found that the sensitivity around the design point is very low for the value of SKM input parameter.

Table 9.8: Sensitivity of result to value of trunk space

w_6 [€/mm]	**Difference**	**0.34 [€/mm]**	**0.67 [€/mm]**	**1.34 [€/mm]**	**Difference**
m_{total} [kg]	2.0%	9.531	9.712	9.712	0%
C_{manuf} [€]	0%	41.2	41.2	41.2	0%
$\delta_{intrusion}$ [mm]	-1.0%	62.9	62.3	62.3	0%

Discussion

From the sensitivity analysis performed here based on the Lightyear One input parameters and weight factors, including SKM, it is found that the parameters that influence the final result the most are the vehicle width and $L_{unsupported}$ due to their influence on the length of the free end of the bumper beam and therefore

intrusion distance during the RCAR corner test. In the case of the vehicle width, the value of this parameter is normally known with a high accuracy during the conceptual design of the rear low-speed crash structures, as this the vehicle width is already determined during the packaging of the vehicle. Decreasing the vehicle width is also expected to move the crash rails further inwards, largely eliminating this effect. In the case of $L_{unsupported}$ this value is largely determined based on the location of the suspension pick-up points, but the accuracy of this location is lower than for the vehicle width. The changes in this value that can reasonably be expected should also be smaller than the 10% variation that is investigated here.

It was also found that a variation of the vehicle kerb weight has a diminishing effect on the total weight of the crash structures, as the amount of impact energy to be absorbed during the RCAR structural test does not scale linearly with this kerb weight. In the case of the Lightyear One it was found that it actually has almost no effect on the conceptual design of the rear low-speed crash structures themselves, but that the main difference is found in the weight of the crash rails. When the dimension $L_{available}$ is changed, this also has almost no influence on the conceptual design of the rear low-speed crash structures, the main difference again being found in the weight of the crash rails.

An unexpectedly small influence of changes in the value of weight saving, SKM, and trunk space was also found. This shows that the conceptual design presented for the Lightyear One is robust, in the sense that it does not change by much if the values for the input parameters or weight factors are changed within reasonable bounds). This shows that the additional incentive to reduce the intrusion distance, being a potential increase in SKM, provides a clear direction the design should take.

9.2. Excluding SKM

In this section the influence of variations of the main input parameters on the optimal result are analysed based on the same input parameters as during the design for the Lightyear One, but with the difference of not taking the parameter SKM into account

Kerb weight

For the sensitivity analysis of the input parameter kerb weight, its value is varied by 10%. In table 9.9 it can be seen that the kerb weight of the vehicle has an influence of between 4.9% and 6.9% on the total weight of the crash structures. This is partly because the amount of impact energy that needs to be absorbed changes, but the higher value for the 1375 kg kerb weight is explained by the need for an increased bumper beam wall thickness. This also leads to a smaller intrusion distance. The effect on the manufacturing cost of the rear low-speed crash structures is relatively small, between 1.6% for the lower curb weight (where the outer dimensions of the cross-sections do not change), and 3.6% for the increased kerb weight (where both the bumper beam wall thickness and section depth increases). The intrusion distance is reduced by 1.6% for the kerb weight of 1125 kg, but also decreases by 5.2% for the increased kerb weight. This large decrease is explained by the need for a higher bumper beam wall thickness and section depth, which leads to a reduced intrusion distance.

Table 9.9: Sensitivity of result to $m_{vehicle}$

$m_{vehicle}$ [kg]	**Difference**	**1125 kg**	**1250 kg**	**1375 kg**	**Difference**
m_{total} [kg]	4.9%	8.163	8.562	9.154	6.9%
C_{manuf} [€]	1.6%	37.8	38.4	39.8	3.6%
$\delta_{intrusion}$ [mm]	1.6%	83.1	84.4	80.0	-5.2%

Vehicle width

To analyse the sensitivity of the results to the width of the vehicle, this parameter is varied by 10%. The main thing that can be seen from table 9.10 is the reduction of 24.1% in the intrusion distance when the vehicle width becomes 10 % smaller. Identically to the situation where SKM is included, the length of the free end of the bumper beam is influenced heavily by a change in vehicle width, as the lateral distance between the crash boxes stays the same. A shorter free end means that the intrusion distance during the RCAR corner test will be reduced for an equal bumper beam cross-section, from which follows that it becomes advantageous to use shorter crash boxes with a higher peak and mean force. This also leads to the increase in the total weight

of the crash structures, due to the crash rails weight penalty. This increase is only 1.3% since it is largely offset by a reduced bumper beam length. The manufacturing cost is reduced by 3.5% for the smaller vehicle width, as the weight of the rear low-speed crash structures is decreased.

When the vehicle width increases, this also increases the length of the bumper beam and the length of the free end of the bumper beam. This leads to an increase of 3.6% in total weight, but also in an increase of 5.1% in the intrusion distance. The section depth and wall thickness of the bumper beam are increased to limit the increase of the intrusion distance. Since the intrusion distance has become larger, longer crash boxes with a lower peak and mean force can be used, which leads to a smaller crash rails weight penalty. The estimated manufacturing cost is increased by 6.0% as more raw material is used for the increased weight of the low-speed crash structures.

Table 9.10: Sensitivity of result to $w_{vehicle}$

$w_{vehicle}$ [mm]	**Difference**	**1800 mm**	**2000 mm**	**2200 mm**	**Difference**
m_{total} [kg]	-1.3%	8.678	8.562	8.875	3.6%
C_{manuf} [€]	3.5%	37.1	38.4	40.7	6.0%
$\delta_{intrusion}$ [mm]	24.1%	68.0	84.4	88.7	5.1%

Lateral distance between crash boxes

The sensivity of the optimal result to the lateral distance between the crash boxes is analysed through a variation of 10% in its value. Changing the lateral distance between the crash boxes while the length of the bumper beam stays the same leads to a change in the length of the bumper beam's free end, similar to changing the vehicle width. However, the effect on the length of the free end is much smaller here. It can be seen that when $L_{unsupported}$ is decreased, the length of the free end is increased, which leads to an increase in the intrusion distance of 3.0%. An increased bumper beam depth is used to limit this additional intrusion distance, which in turn leads to an increase of the total weight of 1.1% and an increase in manufacturing cost of 0.5%. When $L_{unsupported}$ is increased, the length of the free end becomes smaller, allowing for the intrusion distance to be reduced. A smaller crash box length as well as a decreased bumper beam section depth are used, which leads to a reduction in the intrusion distance of 6.5%, a reduction in total weight of 0.3% (the shorter crash boxes have a higher peak and mean force, which leads to a small crash rails weight penalty), and an increase in the manufacturing cost of 0.3%.

Table 9.11: Sensitivity of result to $L_{unsupported}$

$L_{unsupported}$ [mm]	**Difference**	**756 mm**	**840 mm**	**924 mm**	**Difference**
m_{total} [kg]	-1.1%	8.654	8.562	8.540	-0.3%
C_{manuf} [€]	-0.5%	38.6	38.4	38.5	0.3%
$\delta_{intrusion}$ [mm]	-3.0%	87.0	84.4	78.9	-6.5%

Available length for crash structures

To analyse the sensitivity of the results to the available length for the crash structures, this parameter is varied by 10%. From table 9.12 it can be seen that if the available length is reduced to 774 mm the total weight of the crash structures decreases by 1.8%, the manufacturing cost decreases by 1.3%, and the intrusion distance decreases by 7.2%. This happens because shorter crash boxes can be used without incurring a significant crash rails weight penalty, as the peak and mean force of the crash rails need to be higher anyways as they are shorter. The cross-sectional properties of the bumper beam stay roughly the same. When the available length is increased to 946 mm, the total weight increases by 4.7%, the manufacturing cost increases by 1.3%, and the intrusion distance increases by 1.1%. This can be explained by the crash rails being longer, which leads to a larger contribution to the total weight of the crash rails.

Total production volume

To analyse the sensitivity of the output parameters to the total production volume a slightly different approach is taken, as a 10% variation produced only very small differences, and it is more interesting to see these differences over a larger range of production volumes. For this reason, it is decided to check the results for total production volumes of 10,000 and 50,000, compared to the actual total production volume of

Table 9.12: Sensitivity of result to $L_{available}$

$L_{available}$ [mm]	**Difference**	**774 mm**	**860 mm**	**946 mm**	**Difference**
m_{total} [kg]	1.8%	8.408	8.562	8.968	4.7%
C_{manuf} [€]	1.3%	37.9	38.4	38.9	1.3%
$\delta_{intrusion}$ [mm]	7.2%	78.7	84.4	85.3	1.1%

100,000 units. From table 9.13 it can be seen that the optimal design of the rear low-speed crash structures stays exactly the same for all three production volumes. This means that no changes in total weight or intrusion distance are found. For the manufacturing cost an increase of 7.0% is found when the total production volume is reduced to 10,000 units, while the cost increase is only 1.0% for a total production volume of 50,000. This differences comes from the non-recurring costs being spread out over a lower amount of units, therefore increasing the manufacturing cost per unit.

Table 9.13: Sensitivity of result to total production volume

Production volume	**Difference**	**10,000 [-]**	**100,000 [-]**	**50,000 [-]**	**Difference**
m_{total} [kg]	0%	8.562	8.562	8.562	0%
C_{manuf} [€]	-7.0%	41.3	38.4	38.8	-1.0%
$\delta_{intrusion}$ [mm]	0%	84.4	84.4	84.4	0%

Value of weight saving

To analyse the sensitivity of the results to the value of weight savings, a halving and doubling of the original value is chosen, as a 10% variations showed no differences. This means that the value of weight saving is varied from 5 €/kg to 20 €/kg. It can be seen from table 9.14 that if the value of weight saving is increased to 20 €/kg, the optimal result stays exactly the same. This means that a lighter solution can not be found without increasing the intrusion distance by more than it is worth. However, if the value of weight saving is reduced to 5 €/kg, some large differences are found. The intrusion distance is reduced by 24.1%, as the value of trunk space increases compared to the value of weight saving. This means that shorter crash boxes are used, as well as a higher bumper beam wall thickness and section depth to decrease the intrusion distance. This also leads to a mass increase of 7.8%, due to an increased weight of the rear low-speed crash structures as well as an increased crash rails weight penalty. The difference in manufacturing cost is found to be 4.5%.

Table 9.14: Sensitivity of result to value of weight saving

w_3 [€/kg]	**Difference**	**5 [€/kg]**	**10 [€/kg]**	**20 [€/kg]**	**Difference**
m_{total} [kg]	-7.8%	9.283	8.562	8.562	0%
C_{manuf} [€]	-4.5%	40.2	38.4	38.4	0%
$\delta_{intrusion}$ [mm]	24.1%	68.0	84.4	84.4	0%

Value of trunk space

To analyse the sensitivity of the results to the value of weight savings, a halving and doubling of the original value is chosen, as a 10% variations showed only very minimal differences. This means that the value of trunk space is varied from 0.34 €/mm to 1.34 €/mm. It can be seen from table 9.15 that this has an especially large influence on the intrusion distance. When the value of trunk space is halved, it can be seen that the intrusion distance is increased by 18.7%, while the total weight of the crash structures shows a difference of only 0.2%. Since minimizing the intrusion distance has less value in this situation, a longer crash box length without foam-filling is found optimal. This means that the manufacturing cost is decreased by 29.3%, but the total weight is barely reduced. This is because the peak force is higher compared to the mean force for crash boxes without foam-filling.

When the value of trunk space is doubled, it can be seen that a reduction of 19.4% is found for the intrusion distance. This is due to a shorter crash box length (with foam-filling), as well as an increased bumper beam wall thickness and section depth to limit the intrusion distance. This results in a higher total weight of 8.4%, and an increase in manufacturing cost of 4.7%.

Table 9.15: Sensitivity of result to value of trunk space

w_6 [€/mm]	**Difference**	**0.34 [€/mm]**	**0.67 [€/mm]**	**1.34 [€/mm]**	**Difference**
m_{total} [kg]	0.2%	8.547	8.562	9.283	8.4%
C_{manuf} [€]	29.3%	29.7	38.4	40.2	4.7%
$\delta_{intrusion}$ [mm]	-18.7%	103.8	84.4	68.0	-19.4%

Discussion

From the sensitivity analysis performed here based on the Lightyear One input parameters and weight factors, when excluding SKM, it is found that the parameters that influence the final result the most are the value of weight saving and trunk space. This is different than the situation where SKM is included, as expected because the addition of the SKM parameter heavily influences what the optimization tool considers important.

An increase of the value of weight saving does not lead to changes in the design of the low-speed crash structures or the output parameters considered here. However, when this value is halved, the trade-off between intrusion distance and total weight becomes different, as the value of trunk space stays the same. The intrusion distance is reduced much more percentage wise than the relative increase of total weight of the crash structures. This same phenomenon happens for a halving or doubling of the value of trunk space. Also here the difference is the largest for the intrusion distance, and much smaller relatively for the total weight. This shows that it is important to have the ratio between the value of weight saving and trunk space correct. This ratio depends on the vehicle that is considered. The higher the value of trunk space, the larger the chance that foam-filling of the crash boxes should be used. It should be noted here that this analysis is performed for the vehicle parameters of the Lightyear One, which includes a very large available length for the rear crash structures compared to other cars. This also increases the favorability of using foam-filled crash boxes to reduce the crash rails weight penalty.

It can also be seen that a variation in the kerb weight leads to a relatively smaller difference total weight of the crash structures, similar to when SKM is included. The effect of variations in the vehicle width and the lateral distance between the crash boxes are also similar to the situation when including SKM.

10

Conclusion

The goal of this thesis was to develop insight in how the design of the rear low-speed crash structures should be different for an SEV compared to a conventional vehicle. This was done by the creation of an optimization model in MatLab that both calculates the structural performance of a set of candidate designs, and determines how well these designs perform based on certain attributes. These attributes are its weight, its manufacturing cost and the intrusion distance during the rear low-speed load cases. To allow this optimization model to also work for SEVs, the performance evaluation parameter SKM is added.

The accuracy of the predicted structural performance was validated using FEA in ANSYS for all three load cases, and was found to be useful for the conceptual design of the rear low-speed crash structures. Compared to the results from the FEA it was found that the prediction of the intrusion distance is between 1.1% and 15.2% too high, and the predictions for the peak force of the crash boxes between 1.6% and 5.2% too high. For the mean force of the crash boxes the prediction is between 4.6% and 6.0% too low, and the total energy absorption is predicted with an accuracy between 0.2% and 6.4%. The optimization model is also used to predict the actual situation for two benchmarked vehicles, the BMW 730d and the Ford Focus, with good results. The materials and manufacturing techniques are predicted correctly, as well as most of the geometry defining parameters (within the limitations of the optimization model) and the intrusion distance. This has demonstrated that the results from the optimization model are useful for the structural design of the rear low-speed crash structures, and that it works for passenger vehicles in different segments and with different types of powertrains.

When the parameter SKM was added to the optimization model an additional motivator to decrease the intrusion distance was provided. It was found that it becomes favorable to increase the energy absorption of the bumper beam through an increased wall thickness, in order to allow the impact energy to be absorbed in a shorter distance while keeping the peak and mean force of the crash boxes reasonable. Foam-filing the crash boxes also is found to be a good strategy to limit the peak force of the crash boxes, decreasing the weight of the crash rails.

In order to determine how the addition of the SKM parameter influences the optimal design of the rear low-speed crash structures for the Lightyear One, designs were generated using the optimization model for both with and without considering the influence on SKM. It is found that when including SKM the total intrusion distance is reduced by 26.2% while the total weight of the crash structures is increased by 13.5%. The manufacturing cost is increased by 7.3%. This provides an additional 44.5 SKM, which corresponds to a value of €254.4. Corresponding to the previous paragraph, the optimal design for the Lightyear One consists of foam-filled crash boxes and a bumper beam with a high wall thickness to increase its energy absorption. Due to the Lightyear One's long available length for the crash structures, foam-filling the crash boxes would also be beneficial when excluding the SKM parameter, although the difference in the total cost of the design is only €4.6 when compared to the crash boxes without foam-filling. When including the SKM parameter this difference in total cost due to the foam-filling of the crash boxes is €72.0.

Using the optimization tool developed during this thesis is therefore shown to improve the conceptual design

of the rear low-speed crash structures of the Lightyear One. Next to this, it can also be used for the conceptual design of different conventional passenger vehicles in order to speed up the design process. The calculation of the structural performance that is done within the optimization tool will reduce the amount of FE simulations needed, as it provides a better starting point.

11

Discussion and recommendations

This chapter will conclude the report by discussing the final thoughts on the work performed during this thesis, as well as providing recommendations for improvement of the optimization tool and future work. The discussion, consisting of a reflection of the goals of this thesis and to what extent they are met, as well as how iterations were used to improve the accuracy and results, is shown in section 11.1. The recommendations for future work are presented in section 11.2.

11.1. Discussion

In this section there will be a look-back on the initial objectives of the thesis, and it is evaluated to what extent these objectives are met. A short discussion on the iterations that have been performed is also included, as this will show how the accuracy of the optimization tool has improved over time.

11.1.1. Reflection on goals

The main objective of this thesis was to create insight in how the design of the rear low-speed crash structures should be different for an SEV compared to a conventional vehicle, and to extend this to how trade-offs in structural engineering in general are different for an SEV. This has been done by creating a general optimization tool for the rear low-speed crash structures that can be used for a wide range of vehicles, and using this to provide a conceptual design for the Lightyear One.

Clear differences have been found in the optimal design of the rear low-speed crash structures for the Lightyear One, compared to the cases where the parameter SKM is not taken into account, and when the available length of the rear crash structures is reduced. It also shows that the preferred design changes when a systems engineering approach is taken. This means that the influence of the design of a subsystem on the performance of the total system is investigated and taken into account in the decisions framework for the subsystem itself. Taking into account the crash rails weight penalty is one of the efforts to use this systems thinking, having an influence on the final results as this is what makes foam-filling the crash boxes useful. It was found that for an SEV a relatively small increase in weight can lead to a large additional value in SKM and trunk space. An improved design of the rear low-speed crash structures is presented during this thesis, along with a strong argumentation why this provides an improved situation. Based on these points, it can definitely be said that the goals and objectives of this thesis have been met.

On the other hand, there were also two smaller things that were tried to include in the optimization tool but did not work out in the end because either the approach taken was not correct or the amount of time available was limited and prioritization lead to this not being included. It was attempted to also include composite (CFRP and GFRP) bumper beams in the optimization tool, but the geometries considered for these composite bumper beams were only thin-walled rectangular beams. This turned out to be problematic during the RCAR corner test as it was impossible for a composite bumper beam with this geometry to absorb enough impact energy during this load case. An analysis method for the energy absorption of composite bumper beams during the RCAR structural test and RCAR full width test was also not developed successfully, which resulted in composite bumper beams never being a viable solution according to the optimization tool, even when the

RCAR corner test is managed using different physical parts than the bumper beam. In reality it is possible to use a composite bumper beam on a vehicle, as is shown by for example the 2020 Chevrolet Corvette Stingray.

To fully cover the most common combinations of material and manufacturing technique for the rear low-speed crash structures that are currently used, the metal stamping process also needs to be included, especially for steel alloys. This would be a viable option for vehicles with a very high total production volume with the main focus on keeping the cost low, and having only a small value of weight saving. This means that the omission of this manufacturing process does not influence the results found for SEVs or the design for the Lightyear One, as this would not be a viable technique for these specific cases.

11.1.2. Iterations

During the development of a complex analysis method it is always important to check if the performance and accuracy of the analyis method are satisfactory, or if certain elements need improvement. Next to many small iterations, one major iteration has been performed during this thesis.

When the initial analysis method for the structural performance during all three load cases considered was ready, it was investigated using FEA if the predictions of the structural performance corresponded with the results from the FEA. This was set up in such a way that the comparison could be made not only on the main output parameters, but also showed whether certain physical behaviours were predicted correctly. During these initial validation efforts it was found that there was a large underestimation of the bumper beam energy absorption during both the RCAR structural test and the RCAR full width test, as at this point the assumption was made that the energy absorption due to collapse of the section would be negligible compared to the energy absorption capabilities of the crash boxes. It was also found that the mean force of the crash boxes was underestimated consistently. These two sources of error lead to a discrepancy of up to 30% between the developed structural analysis method and the results from the FEA, and this was deemed unsatisfactory.

To improve the accuracy of the structural analysis method from this point, the method was extended to also include the dynamic amplification factor for the crash boxes and an estimation of the energy absorption of the bumper beam due to collapse of the section. After these two parts were included in the optimization tool, new predictions of the structural performance were generated and checked with the FEA models that were used before. It was found that the discrepancy between the two decreased by a lot. The energy absorption capabilities of the bumper beam are still underestimated, but the difference is much smaller than before. The discrepancy in the mean force of the crash boxes also improved, going to an underestimation of between 4.6% and 6.0%. This lead to the largest difference that was found (for the intrusion distance) to be reduced from around 30% to 15.2%. Further improvements are possible, but this iteration made sure that the predictions made using the structural analysis method are actually useful for the conceptual design of the rear low-speed crash structures.

11.2. Recommendations for future work

In this section possible improvents of the optimization tool that are already identified, and can be already implemented based on existing knowledge, are shown. Next to this, recommendations for future research are presented.

The generality of the optimization tool can be improved, making it useful for vehicles with very high production volumes and a focus on cost rather than weight saving as well. This should be done by adding the metal stamping manufacturing technique, especially for steel alloys. The structural analysis methods are already present, as they should be identical to the analysis methods for crash boxes and bumper beams manufactured using the metal folding process. This means that only the cost model needs to be expanded.

It was found that many vehicles use multi-section extruded bumper beams to improve the energy absorption of the bumper beam and also lower its weight. For SEVs, where decreasing the intrusion distance becomes more important, this will be especially useful. New analysis methods need to be developed for this, in order to estimate the energy absorption of the bumper beam due to both the collapse of the section and the elasto-plastic deformation.

Currently the validity of composite bumper beams can not be evaluated using the optimization tool. These can be a good choice for small series vehicles with very aggressive weight saving requirements such as sports cars. To properly include this in the optimization tool, additional types of bumper beam geometries need to be considered. Next to this, a method to estimate the energy absorption due to crushing of the section should be added.

It was found that the peak force on the crash boxes is one of the drivers of the design. More knowledge needs to be available on this topic to have more confidence in the results. Questions that need to be answered are how the peak force of the crash boxes is influenced by connecting them to the bumper beam, and how this peak force is influenced by dynamic impact. Additional methods to improve the crush load efficiency (other than foam-filling or changing the material) should also be investigated.

The influence of the design of the rear low-speed crash structures on the performance of the complete crash structures during high-speed impact also needs to be analysed. This influence is not expected to be large, as the crash boxes plus bumper beam combination takes up only a small portion of the available length, especially for SEVs. However, the performance during the high-speed impact load cases is critical for the safety of the occupants and therefore this influence should be known.

In the current version of the optimization tool only the sustainability during the use phase is taken into account. It would be a more fair and complete approach to also include the manufacturing phase and end-of-life phase so that the entire lifecycle is covered. This is expected to mainly decrease the favorability of composites (especially CFRP) due to the large amount of energy necessary to produce the fibers as well as being more difficult to recycle.

Finally, this optimization tool can be extended to also be useful for the front of the vehicle. There are some small changes in the definition of the low-speed load cases, and pedestrian impact needs to be added. There is also a change in the critical high-speed load case for the crash rails. Knowing the desired length of the low-speed crash structures and which areas will be damaged during low-speed frontal impact in an early stage of the development will help with deciding on the packaging of under-the-hood components.

A

Validation of FEA models using experimental test data

To gain confidence in the structural response predicted by the analytical model a validation study is carried out using the commercial FEA software ANSYS 2019 R2, more precisely the Explicit Dynamics workbench. This method is used to calculate dynamic responses of a structure due to stress wave propagation or impact, and can be used for the modelling of highly non-linear phenomena. Explicit Dynamics works best when the event only takes a short time, less than 1 second, which makes it a good fit for the crash analysis performed here. In order to trust the results from the FEA, it is necessary to compare the model with some known experimental tests from literature. This is done for the bumper beam model in section A.1, for the crash box model in section A.2, and for the foam model in section A.3 .

A.1. Validation using experimental bumper beam test

The experimental test results with which the bumper beam FEA model is validated come from the research of Hanssen [28] in which square aluminium extrusions are tested quasi-statically on a three-point bending test machine. The material properties and geometry definition are specified with a high level of detail, making it easy to recreate the experimental test using an FEA model.

The material is modelled based on the experimental coupon testing of the aluminium 6060-T4 alloy that is shown in Hanssen [28], using multilinear isotropic hardening, the bulk modulus equation of state and material failure based on the maximum equivalent plastic strain of 15%. The cross-section consists of a square 80x80 mm section with a wall thickness of 1.90 mm. The distance between the supports is 800 mm, and they are modelled as lines where only displacement in the vertical direction is constrained.

The model is meshed using 4890 linear shell elements with a size of 10x10 mm. An applied displacement of 30 mm in the negative z-direction is imposed on the impactor, to replicate the quasi-static impactor used during the experimental test. With an analysis end time of 0.1 s, this means that the impactor has a velocity of 300 mm/s. The quasi-static impactor using during the experimental test used a loading rate of 40 mm/min, which is 0.67 mm/s. This means that there is a large difference between the impact speeds, which can lead to some inaccuracy due to inertial effects (no strain rate effects are present in the chosen aluminium alloy). Slowing down the impactor in the FEA model is not feasible, as this would increase the computational time prohibitively, due to the nature of performing an explicit analysis.

In figure A.1 three snapshots of deformation plots while running the FEA model are shown. The expected sidewall buckling next to the impactor, reducing the bending moment the beam can resist, can also be seen. A comparison between the force-rotation behaviour of the experimental test and the FEA model is shown in figure A.2. Here it can be seen that the trends are predicted correctly, but the prediction of the peak force is 5.2% too high. The predicted strength of the beam after the buckling of the sidewalls starts seems quite accurate, but less constant than the experimental test data. As mentioned before, this is due to trying to replicate a quasi-static test in a dynamic manner using an explicit FEA. The reason that the FEA model reaches

a smaller rotation is because the runtime of the model needed to be limited, it does not mean that the beam failed at this point. Considering the large difference in impact speed, it can be concluded that the FEA bumper beam model still provides an accurate prediction.

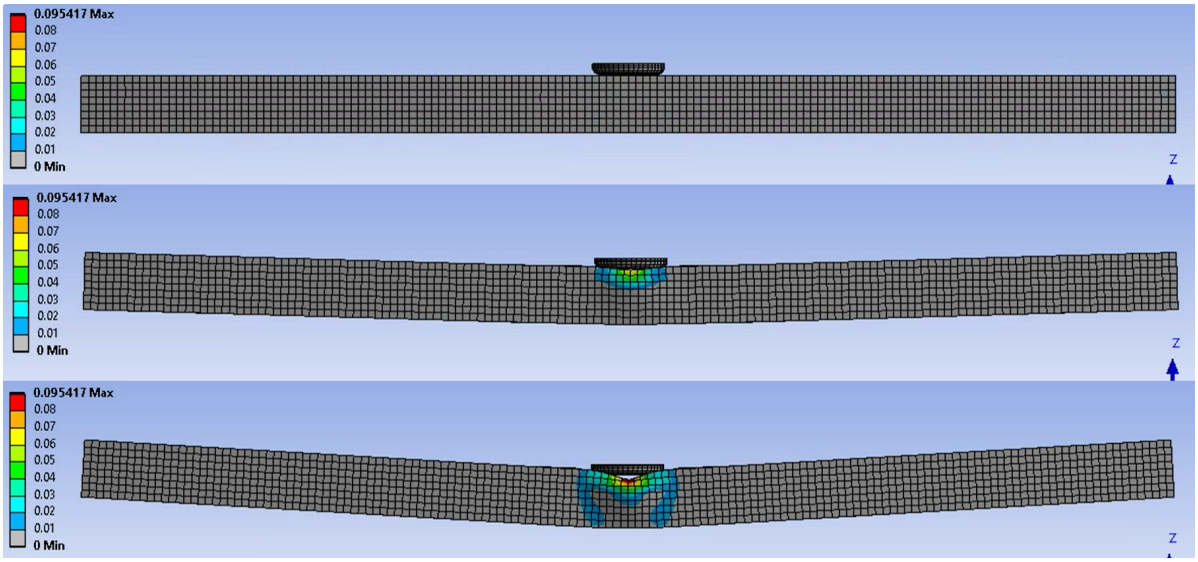

Figure A.1: Deformation plots of FEA model at t=0 (top), t=0.05 s (middle) and t=0.1 s (bottom)

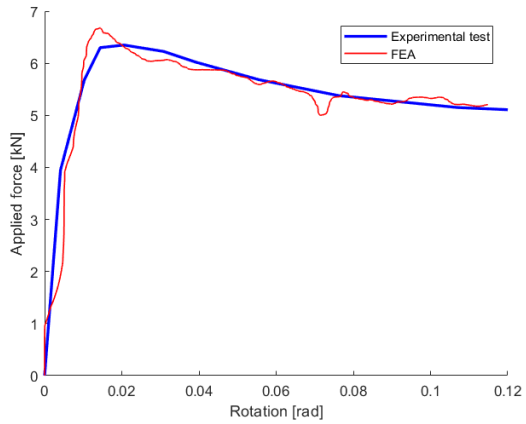

Figure A.2: Force-rotation plot comparing results from the FEA with an experimental test by Hanssen [28]

A.2. Validation using experimental crash box test

The experimentel test results with which the crash box FEA model is validated come from a different research by Hanssen [30]. Here square aluminium extrusions are experimentally tested in a quasi-static and dynamic manner in axial compression. The dynamic test of a square column made from the AL6060-T4 alloy is used to compare the FEA model with. The material properties are equal to the ones used for the bumper beam validation case.

The geometry consists of a square column with a cross-sectional width of 80 mm, a length of 295 mm and a wall thickness of 2.45 mm. The corner radius is not specified, but square corners are used in the FEA model as it was found that using fillets in the corners led to undesired behaviour during the simulation and larger errors when comparing with the experimental test data. The bottom 50 mm of the column is clamped during the experimental test and in the FEA model this is represented with a fixed support on the bottom 50 mm.

The model is meshed using 8960 linear shell elements with a size of 5x5 mm. The impactor consists of a 56 kg rigid block, with a flat horizontal surface. The impactor is constrained in such a way that it can only move in the z-direction. The impact velocity $v_0 = 14.6\ m/s$. With this impact velocity, an analysis end time of 0.03 seconds is used to completely capture the energy absorption phase.

In figure A.3 three deformation plots of the FEA crash box model during the impact are shown. It can be seen that progressive folding takes place, and the lobes are forming nicely. The full amount of impact energy is absorbed without using the entire length of the crash box. Figure A.4 shows the comparison of the force-displacement curve between the experimental test data and the FEA results. It can be seen that the peak force is predicted nicely, but that the locations and amplitudes of the peaks seem to be shifted to the left. There are also some additional smaller peaks and valleys between the deflection of 20 mm and 50 mm. This is not problematic, as the key metrics of interest are predicted well as shown in table A.1.

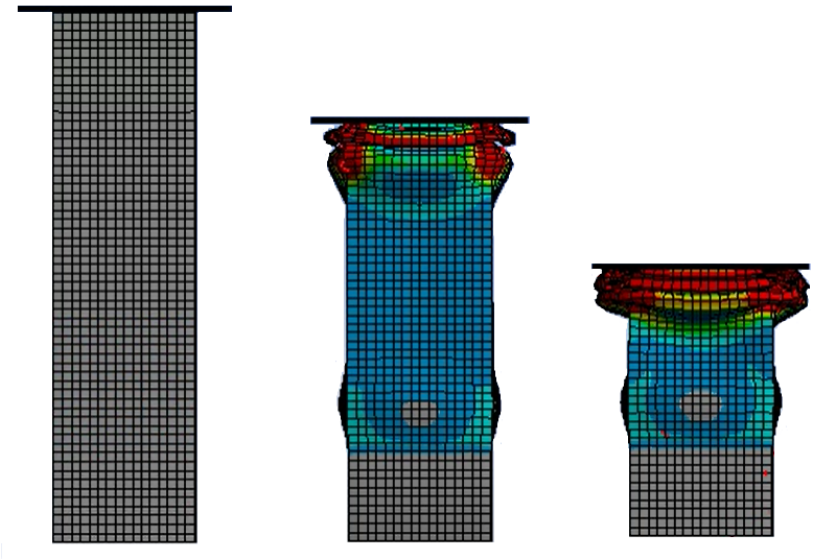

Figure A.3: Deformation plots of FEA model at t=0 (left), t=0.0075 s (middle) and t=0.0225 s (right)

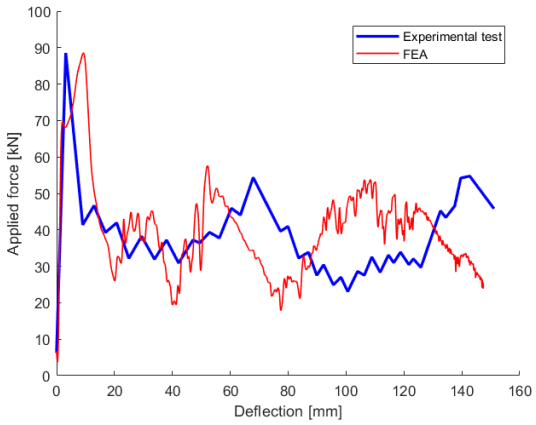

Figure A.4: Force-displacement plot comparing results from the FEA with an experimental test by Hanssen [30]

From table A.1 it can be seen that all parameters are predicted with a good accuracy. Especially the prediction for the peak force is very accurate. The small difference in energy absorption is logical, as the amount of impact energy that can be absorbed is defined by the mass and velocity of the impactor, and all impact energy is absorbed in both cases. The differences in the predictions for the mean force and displacement are 3.14% and 2.5% respectively. This is considered accurate enough to validate the setup of the FEA model.

Table A.1: Comparison on key metrics between literature experimental test and FEA model

	Literature	FEA	Difference
Peak force	88.5 kN	88.5 kN	0.003%
Mean force	39.3 kN	40.5 kN	3.14%
Energy absorption	5.93 kJ	5.98 kJ	0.79%
Displacement	151.1 mm	147.4 mm	2.5%

A.3. Validation of foam material model using RCAR test procedure

In the RCAR bumper test procedure[1] an experimental test is described using which the behaviour of the foam on the bumper barrier can be checked. This test consists of quasi-statically impacting the barrier with an 100x160 mm steel impactor with a speed of 450 ± 50 mm/min. A force-deflection corridor is provided that shows the upper and lower bounds between which the force response of the foam should fall. To gain confidence in how the foam is modelled during the FEAs this experimental test is replicated using ANSYS.

The foam layer is modelled as a solid, and meshed using linear hex8 elements with dimensions of around 10x10x10 mm. The material properties are modelled using the 'Crushable Foam' material model, with the maximum tensile stress as 0.2 MPa and the relationship between maximum principal stress vs volumetric strain as shown in figure A.5.

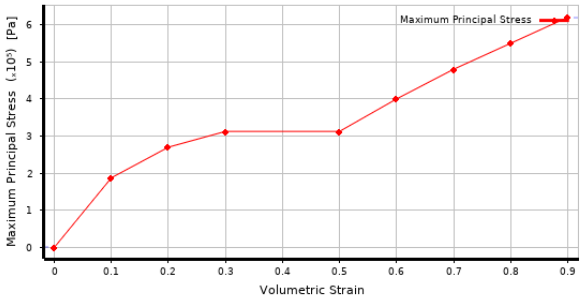

Figure A.5: Relationship between maximum principal stress vs volumetric strain of foam model

In the analysis settings the end time is set to 0.1 seconds, and erosion due to material failure is set to 'yes'. The impactor is modelled as a 100x160 mm rigid plate, with an applied displacement of 45 mm in 0.1 seconds. The force reaction is measured on the impactor, and the results are shown in figure A.6.

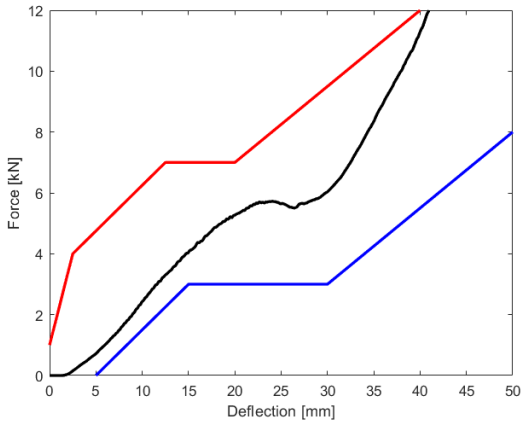

Figure A.6: Comparison of foam behaviour with force-deflection corridor in RCAR test procedure

From figure A.6 it can be seen that the behaviour of the foam model falls within the force-deflection corridor

[1] http://www.rcar.org/Papers/Procedures/BumperTestProcedure.pdf

as specified in the RCAR bumper test procedure. This means that the material model can be seen as validated. If more time was available it would have been possible to optimize the material properties of the foam to achieve a foam behaviour that falls more perfectly within the bounds, especially at the higher deflection. However, due to the relatively small contribution of the foam to the energy absorption during the three load cases that are considered in the FEA it is decided to spend the time available on running more iterations of the full model FEAs that are used to validate the structural response of the analytical model.

B

Parameter sensitivity analysis for verification

As a part of the verification efforts for the optimization model, in this appendix a parameter sensitivity analysis is carried out. The influence of many different parameters on the structural performance are analysed. This is done to check whether the response predicted by the optimization model corresponds to the physical behaviour, the equations used, as well as common sense. This is done for the parameters that define the design of the crash boxes in section B.1, and for the bumper beam in section B.2.

B.1. Crash box design

To fairly compare crash boxes, the optimization model is run using a vehicle weight of 1250 kg and all having the same design of the bumper beam, the design parameters of which are shown in table B.1. It is then determined what is the lowest weight crash box design to pass the RCAR structural load case, while $L_{cb} = 100$ mm. This is done to eliminate the contribution of the bumper beam to the impact energy absorption. From the total 6.28 kJ of impact energy that needs to be absorbed, between 0.92 and 1.27 kJ will be absorbed by the bumper beam depending on the crash box width only. Three different crash box widths are used, 50 mm, 75 mm, and 100 mm. This is done to show the sensitivity to the crash box width.

Table B.1: Design parameters bumper beam

Parameter	**Value**
Material	Al6061-T6
L_{bb}	1441 mm
h_{bb}	100 mm
d_{bb}	40 mm
t_{bb}	2.8 mm
R_{bb}	3000 mm

B.1.1. Material choice

The lowest weight crash box to pass the RCAR structural test under the aforementioned circumstances is calculated by the optimization model for all three steel alloys that are considered, the two aluminium alloys that are used for extruded crash boxes, as well as the composite materials for all three of their considered manufacturing processes. The results can be seen in figure B.1. The steel alloy AISI 1020 is left out of the graph, as its weight is so much higher than the others that it strongly reduces the readability of the graph.

When looking at figure B.1 it can be seen that the crash boxes made from CFRP result in the lowest weight for the same amount of energy absorption, with the braided crash boxes having the absolute lowest weight. At small crash box widths the aluminium alloys are only slightly heavier, but this difference increases quickly

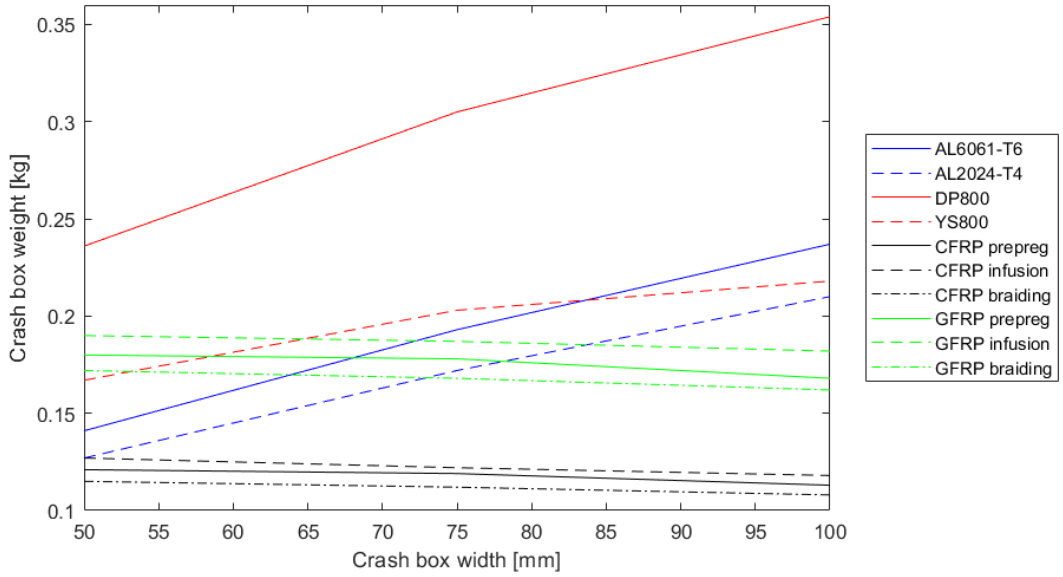

Figure B.1: Crash box weight/diameter vs width, for steel alloys, aluminium alloys, CFRP, and GFRP

with increasing crash box width. GFRP crash boxes are heavier than aluminium ones at $w_{cb} = 50$ mm, roughly equal at $w_{cb} = 75$ mm and lighter at $w_{cb} = 100$mm. Using steel alloys results in the heaviest crash boxes, although the steel alloy YS800 comes very close in weight to the AL6061-T6 alloy, and can even be lighter if the crash box width is large. This can be explained by the $\frac{\sigma_0}{\rho}$ that is higher than for AL6061-T6. Aluminium alloys perform better for the lightweight energy absorption of the crash boxes, since the lower density leads to higher wall thicnkesses for the same weight. The sustained mean crush force scales with the wall thickness to the power $\frac{5}{3}$, while it scales linearly with σ_0.

It can also be seen in figure B.1 that the weight of metal the crash boxes increases if the width of the section increases. This effect is explained by the decreased wall thickness that is necessary when the width is larger, and the sustained mean crush force scales with section width to the power $\frac{1}{3}$, while it scales with wall thickness to the power $\frac{5}{3}$. This effect is therefore not present for the composite crash boxes, as for these materials the mean sustained crush force is calculated based on an assumed literature value for the SEA, based on only the cross-sectional area and not the specific geometry.

The reason that the composite crash boxes reach a slightly lower weight if the diameter is larger is that the energy absorption of the bumper beam is dependent on the crash box width/diameter. This means this effect is also present for the metal crash boxes, but it is not visible due to the trend of increasing weight with increasing width due to the effect of the wall thickness.

B.1.2. Manufacturing techniques

In this section the different manufacturing techniques for the crash boxes are compared with respect to manufacturing cost as well as weight. This is done for the metal crash boxes and the composite crash boxes separately, as they are made using very different processes. The estimated manufacturing cost for the crash boxes is calculated for total production volumes of 1, 10, 100, 1000, 10000, and 100000. However, since the manufacturing cost of the folded metal crash boxes is not dependent on the production volume, this one is logically only calculated for one single amount of crash boxes manufactured.

Folding vs. extrusion

In the optimization model two different manufacturing process are used for metal crash boxes. In this section it is investigated what the advantages and the drawbacks are in terms of part weight and manufacturing cost.

Based on the output from the model, the comparison in manufacturing cost between extruded and folded

crash boxes is shown in figure B.2 for the steel AISI 1020 alloy (the other two steel alloys show very similar behaviour). For the aluminium crash boxes this comparison is more complicated, as a different alloy (and therefore different material properties and material cost) is used for the metal folding process than for the extrusion process. To minimize this effect, the two alloys that are the closest to each other in material properties are used, being AL6061-T6 and 6CM300sT61. The results for aluminium alloys can be seen in figure B.3. It should be noted that in both figures the manufacturing cost of the folded crash box is only plotted for the 75 mm crash box width. The manufacturing cost of the smaller and larger crash boxes are so close (maximum difference of €0.2) that these lines would overlap in the figures.

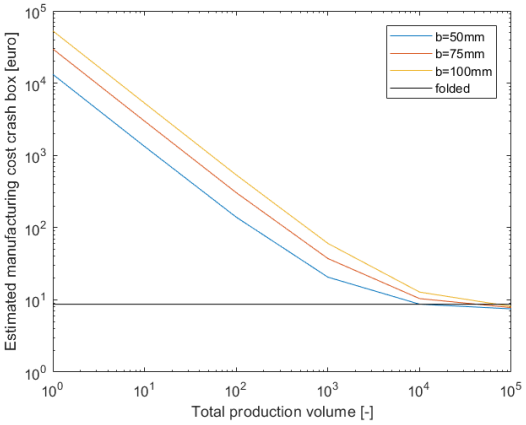

Figure B.2: Manufacturing cost comparison for AISI 1020 alloy

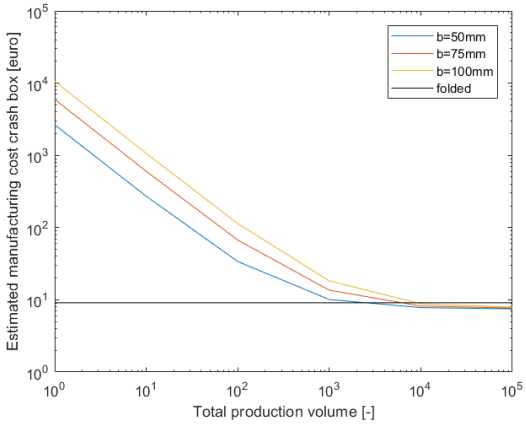

Figure B.3: Manufacturing cost comparison for AL6061-T6 and 6CM300sT61 alloys

Since it is difficult to determine the cross-over points from figures B.2 and B.3, the production volumes at which the estimated manufacturing cost is equal for both processes are summarized in table B.2.

Table B.2: Cross-over point between extrusion and metal folding for different crash box widths

Crash box width	**AISI 1020**	**AL6061-T6 vs 6CM300s-T61**
50 mm	10,000	2,532
75 mm	41,727	6,225
100 mm	69,796	8,999

From the combination of table B.2 and figures B.2 and B.3 two main trends can be seen. The first one is that the cross-over production volume is much lower for the aluminium alloys than for the steel alloys. This is due to large difference in tooling cost for the extrusion process, where extrusion dies for steel alloys are much more expensive. This means that this investment needs to be spread over more produced parts to achieve a manufacturing cost that is lower than for the metal folding process. The second trend is that smaller diameter crash boxes are cheaper to manufacture using the extrusion process, especially when the total production volume is not very large. This is explained by the dependence of the extrusion tooling cost on the minimum size of the circumscribing circle that fits around the design's cross-section.

Now that the influence of the manufacturing process on the estimated manufacturing costs is known, it is time to investigate the influence of the two processes on the weight of the crash boxes. The crash box designs that are considered are found in the same way as for the manufacturing cost comparison. In figure B.4 the weight of the folded crash box designs is shown for the three steel alloys and the aluminium alloy comparision. The weights are normalized to the weight of the extruded crash box made from the same alloy.

In figure B.4 it can be seen that the main trend is very similar for all the materials that are considered. When the crash box width is small, this leads to a high weight penalty when using the metal folding process. This is explained by the higher wall thickness, as well as the set flange size leading to being a larger percentage of the cross-sectional area if the cross-section is small. This also explains why the weight penalty is higher for

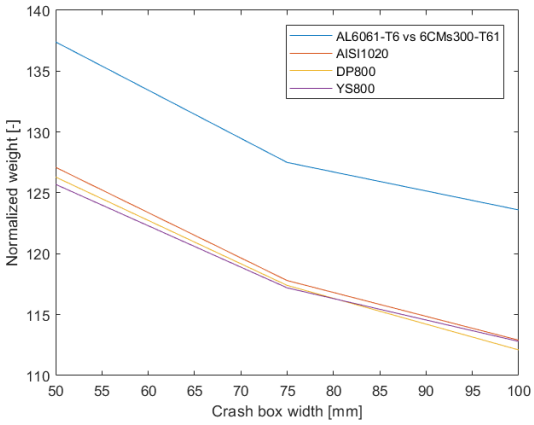

Figure B.4

the aluminium alloys, as the aluminium crash boxes have an inherent larger wall thickness due to the lower density of the material.

Braiding vs. prepreg vs. vacuum-infusion

Three different manufacturing methods are considered in this optimization model for composite crash boxes, being pre-preg, vacuum-infusion, and braiding. In this section it is investigated what the advantages and drawbacks are in terms of part weight and manufacturing cost.

Based on the output from the model, when run in the method as described earlier, the comparison in manufacturing cost between the three production methods are shown for both CFRP and GFRP in figure B.5. The graphs for CFRP are shown in a thin solid line, while the values for GFRP are plotted using a thick dashed line. The values that are shown correspond to a crash box diameter of 75 mm, as it was found that the trend is independent of the diameter and showing the data for all diameters would lead to a cluttered and unclear graph.

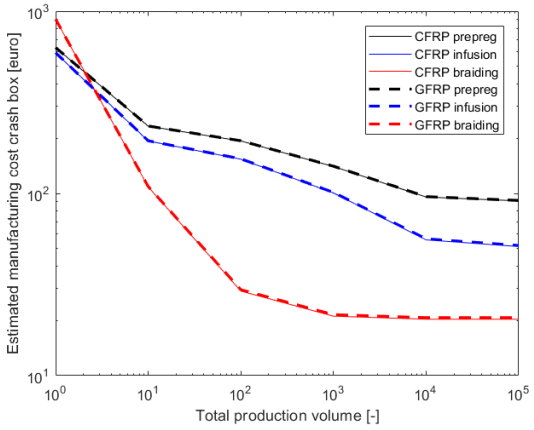

Figure B.5: Estimated manufacturing cost vs total production volume for composite crash boxes with $w_{cb} = 90$ mm

When looking at figure B.5 it can be seen that the cross-over point already happens at very low total production volumes, at 2.08 units for pre-preg and at 2.65 units for vacuum-infusion. It is also interesting to see that the data is very similar for both CFRP and GFRP, as it turns out that the difference in material cost per kg is negated because more material is needed for the GFRP crash boxes to absorb the same amount of impact energy. From this it can be concluded that GFRP crash boxes will never be the optimal solution, as the manufacturing cost will be almost exactly equal while they do exhibit a higher part weight (as can be seen in figure B.1).

Another interesting aspect of figure B.5 is that the graphs do not show a smooth behaviour of decreasing cost with increasing production volume for the pre-preg and vacuum-infusion manufacturing methods. This can be explained by the need for additional tooling if the total production volume increases, as only 500 parts can be made for both processes using a single mould. This also influences the equipment cost, as the amount of parts that can be put inside the autoclave for curing is equal to the amount of moulds that is used. For the braiding process 10,000 parts can be made using a single tool, reducing the effect of the decreasing equipment cost by a lot.

The different manufacturing methods also lead to a different part weight, but this is purely based on the assumption made in section 4.1 that the SEA of braided parts if 5% higher than for pre-preg parts, and the SEA of vacuum-infused parts is 5% lower than for pre-preg parts.

B.1.3. Effect of foam-filling

In the generation of the candidate designs the foam-filling of the crash boxes is also considered. According to the literature study this can reduce the weight of the crash boxes under certain circumstances. It is investigated in this section if this is also the case for the considered materials and geometries during this optimization model, as well as the other effects it has on the structural performance of the low-speed rear crash structures.

The results that were generated showed no weight savings due to the foam-filling of the crash boxes, except for the AISI 1020 steel alloy as its structural material properties are low enough that it can be improved by foam-filling. It was found that weight-savings should not be the main reason to include foam in the crash boxes, as it is simply more cost-effective to use a material with better structural material properties. The more important effect of foam-filling was determined to be the reduction in peak force with respect to the mean force, or in other words, an improvement in CLE. This allows for a shorter intrusion distance without a large crash rails weight penalty. To show this effect, results are generated using the optimization model based on a maximum allowed peak force on a single crash box of 150 kN. The length of the crash boxes was allowed to vary between 50 and 150 mm, and the wall thickness between 1 and 4 mm. The model was run three times, each time with a different value for the crash box width of either 50, 75 or 100 mm. It was then evaluated which candidate design exhibited the lowest weight at each foam density. Data on the intrusion distance, weight of the crash boxes, effective length ratio and CLE are generated. For AL6061-T6 the results for crash box weight and intrusion distance are shown in figure B.6, and the results for the steel alloy AISI 1020 are shown in figure B.7.

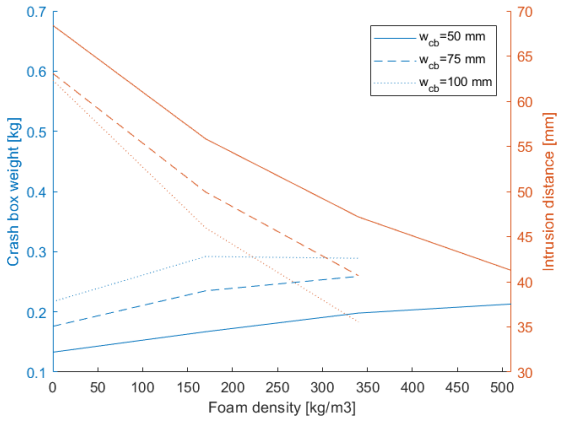

Figure B.6: Effect of foam-filling on crash box weight and intrusion distance for AL6061-T6

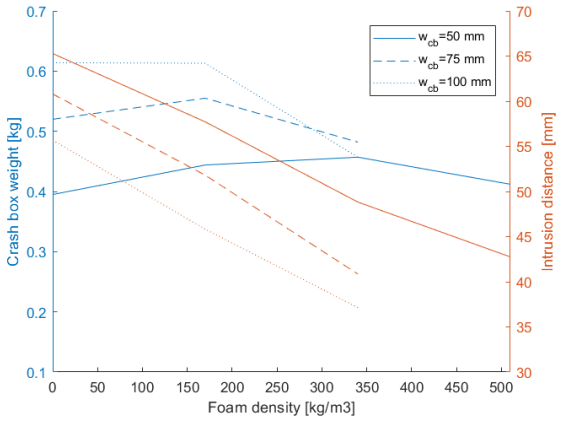

Figure B.7: Effect of foam-filling on crash box weight and intrusion distance for AISI 1020

From figure B.6 it can be seen that if the AL6061-T6 alloy is used, that the foam-filling results in an increased crash box weight for every crash box width. This weight increases however becomes smaller if the crash box width is larger. This happens because an empty crash box with a smaller width is more weight-effective at absorbing energy than one with a large width, while the efficiency of the foam does not depend on this. It can also be seen that the crash box contribution to the intrusion distance decreases by up to 43%. This contribu-

tion to the intrusion distance can be the smallest in the absolute sense if a larger crash box width is used, as this means that the behaviour is dominated more by the foam instead of the extrusion walls. This shows that for certain vehicles, where limiting the intrusion distance is very important, it is very well possible that the increase of crash box weight and manufacturing cost is worth it to decrease the intrusion distance by this much.

In figure B.9 a similar trend can be seen for the intrusion distance, but the effect of foam-filling on the weight of the crash boxes is different. For small crash box widths the most light-weight solution is still the one without foam-filling, but as the crash box width increases it becomes more beneficial to use the foam-filling for weight-saving reasons. This is most effective for higher foam densities.

The effect of foam-filling on the effective length and the CLE has also been investigated, and the results can be found in figure B.8 for AL6061-T6 and in figure B.9 for AISI 1020.

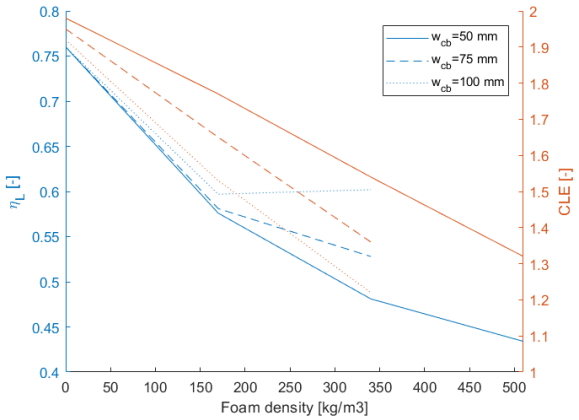

Figure B.8: AL6061-T6

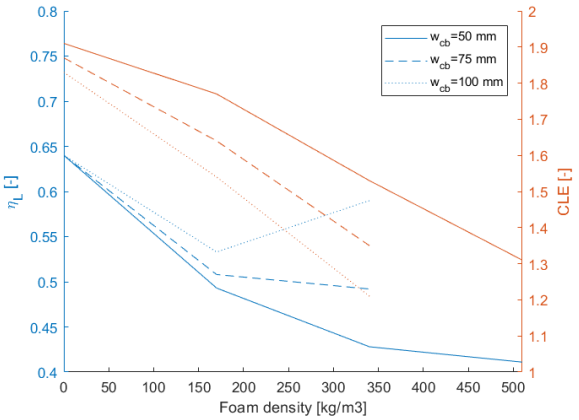

Figure B.9: AISI 1020

It can be seen in figures B.8 and B.9 that for both materials the dimensionless value for the CLE reduces rapidly with increasing foam density. This effect is stronger when the crash box width is larger, as the structural behaviour of the foam starts to dominate instead of the behaviour of the extrusion's metal walls. A reduction in CLE is very beneficial, as this allows for a smaller intrusion distance without incurring a significant weight penalty of the crash rails, and the accelerations becomes dangerously large. The effect of foam-filling on the effective length is also very similar between the two materials. It can be seen that η_L reduces quickly between no foam-filling and the lowest density foam, but this effect becomes weaker when increasing the foam density. For large crash box widths, η_L actually increases again.

B.2. Bumper beam design

In this section it is investigated what the influence is of changing certain parameters of the bumper beam design on the structural performance and manufacturing cost. To eliminate the influence of the crash boxes to a large extent, the same crash box design is used for all the candidate designs that are considered in this section. The design parameters of this standard crash box design can be found in table B.3.

Table B.3: Design parameters crash box

Parameter	**Value**
Material	Al6061-T6
L_{cb}	100 mm
w_{cb}	100 mm
t_{cb}	3.0 mm

The most important part of the structural performance that is influenced by the design of the bumper beam is the intrusion distance during the RCAR corner test, as during this load case the impact energy is absorbed by only the bumper beam. The energy absorption of the bumper beam during the RCAR structural test and full widt test are also important, but during these load cases the impact energy can also be absorbed in a more

weight-efficient manner using the crash boxes. It is however necessary that the bumper beam absorbs a certain amount of the impact energy during these load cases for a good balance between the different intrusion distances. For these reasons, the influence of the different bumper beam design parameters on the following terms will be evaluated, althought the focus will mainly be on the first two:

- $\delta_{intrusion}$ in RCAR corner test
- m_{bb}
- EA_{bb} in RCAR structural test
- EA_{bb} in RCAR full width test

B.2.1. Material choice

During the candidate design generation three distinct types of materials are used, being steel alloys, aluminium alloys, and composite materials. The first important thing that was found is that none of the composite bumper beams are able to pass the RCAR corner test, as the composite beams are unable to absorb the impact energy due to their brittle nature. Catastrophic failure will happen at the connection between the crash box to the bumper beam at a very small deformation, which leads to a low energy absorption. This does not mean that a composite bumper beam is not possible at all, but that it is not possible under the limitations of this optimization model. A composite bumper beam with a different type of geometry, specifically designed to be able to absorb energy during the RCAR corner test, or absorbing the impact energy using different parts than the bumper beam (e.g. using energy absorbing brackets inside the bumper fascia, as explained in section 7.7), would be possible. For this reason, composite bumper beams are not considered any further in this section.

To analyze the influence of the material choice for metal bumper beams, it is calculated using the optimization model what the minimum m_{bb} is to reach an intrusion distance of less than 75 mm during the RCAR corner test when h_{bb} = 100 mm, d_{bb} = 100 mm, L_{bb} = 1490.8 mm (this leads to an overlap of 20 mm with the RCAR corner test barrier), and R_{bb} = 3000 mm. This intrusion distance is not adjusted to correspond correctly to the intrusion distance during the RCAR structural test (as is shown in section 5.5.1), but measured from the point of contact between the bumper beam and the RCAR barrier. Since a curved bumper beam is used, the manufacturing process is extrusion. It is also shown how much of the impact energy is absorbed by the bumper beam during the RCAR structural test and the RCAR full width test. This gives a good idea of the influence of the material properties on the performance of the bumper beam. The results are shown in table B.4.

Table B.4: Bumper beam weight and energy absorption

BB material	m_{bb} **[kg]**	EA_{bb} **structural test [J]**	EA_{bb} **full width test [J]**
AL6061-T6	2.787	966.2	2994.0
AL2024-T4	2.523	911.5	2973.0
AISI 1020	6.885	835.9	2810.3
DP 800	3.678	446.8	2108.9
YS 800	3.379	534.4	2636.8

From table B.4 it can be seen that the aluminium alloys yield the lowest weight bumper beam if the goal is to limit the intrusion during the RCAR corner test. A bumper beam made from the steel alloy YS 800 could however limit the intrusion during the RCAR corner test to 75 mm with a wall thickness of 0.72 mm and a weight of 2.442 kg which would be the most lightweight solution. This option is however not valid due to the imposed minimum wall thickness due to manufacturing reasons. From this it can be seen that the material parameter that is leading here is $\frac{\sigma_y}{\rho}$, as is expected based on the developed analysis method.

It is also interesting to see that the aluminium alloys as well as the AISI 1020 steel alloy show a high energy absorption during the RCAR structural test. The energy absorption of the bumper beam during this load case is based only on the crushing of the section, which is based on the rotation of plastic hinges. The moment that is needed to rotate these plastic hinges depends on both the flow stress σ_0 (linearly) and the wall thickness (to the power three), which makes it logical that the aluminium alloys perform well due to their lower density

and therefore higher wall thickness. The AISI 1020 alloy has a low flow stress, but because of this a higher wall thickness is needed and this is beneficial for the energy absorption during this load case.

The difference in energy absorption between the different materials is much smaller during the full width test, as here only a part (between 40.5% for the YS 800 alloy and 64.5% for the AL6061-T6 alloy) is absorbed by the crushing of the bumper beam section. The remaining part of the energy is absorbed by the elastoplastic deformation of changing the bumper beam's curvature until it reaches the same curvature as the RCAR bumper barrier. This portion of the energy absorption is dependent linearly on both the flow stress σ_0 and the wall thickness, which explains why the DP 800 and YS 800 alloys absorb a relatively larger amount of impact energy using this mechanism.

To complete the comparision between the different materials that can be used for the design of the bumper beam, a cost analysis is performed as well. The geometrical design parameters of the bumper beam are the same as mentioned earlier in this section, and the results are shown in figure B.10.

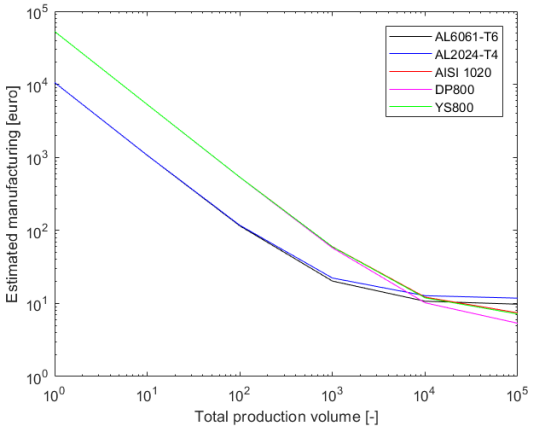

Figure B.10: Comparison of estimated manufacturing cost for curved bumper beams made from different materials

It can be seen in figure B.10 that at low total production volumes the estimated manufacturing cost is much higher for the steel alloys, due to the much higher tooling cost compared to the tooling for aluminium alloys. At high total production volumes, above 10,000 units, the estimated manufacturing cost of the steel bumper beams becomes lower than the aluminium versions, as the cost of raw material is lower for the steel alloys and the recurring costs start dominating the manufacturing costs. Comparing the AL2024-T4 bumper beam with the YS 800 bumper beam at a total production volume of 100,000, a weight difference of 1.126 kg and a cost difference of €4.65 is found, which would correspond to €4.13 per kg of weight saved.

B.2.2. Manufacturing techniques

Since in the candidate design generation the assumption is made that curved bumper beams can not be manufactured using the metal folding technique, the bumper beam designs that are considered in this section will be straight. Using the same method as in the previous section, it is again calculated using the optimization model what the minimum m_{bb} is to reach an intrusion distance of less than 75 mm during the RCAR corner test when h_{bb} = 100 mm, d_{bb} = 100 mm, and L_{bb} = 1490.8 mm. The corresponding manufacturing cost of the bumper beam is also calculated. When aluminium allloys are considered, the specific alloy is different for the extrusion and metal folding process. To minimize the effect of this, only the two alloys that are closest to each other in terms of material properties are considered. This is the AL6061-T6 alloy for extrusion and the 6CM-s300 T61 alloy for folding.

In figure B.11 it the comparison in manufacturing cost for a range of different production volumes is shown for the aluminium alloys. It can be seen that at low production volumes the metal folding process leads to a lower estimated manufacturing cost, as no tooling investment is needed that needs to be written off over a certain amount of parts. However, once the cross-over point is reached at 2,664 units, the manufacturing cost of the extruded bumper beam becomes lower.

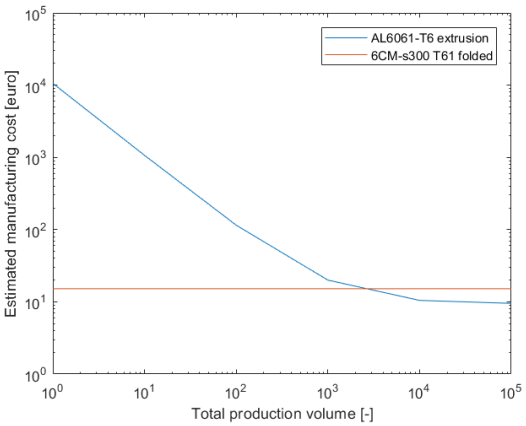

Figure B.11: Comparison of estimated manufacturing cost for extruded and folded aluminium alloy bumper beam

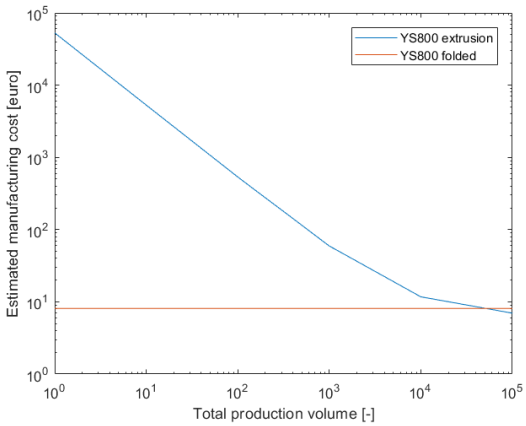

Figure B.12: Comparison of estimated manufacturing cost for extruded and folded steel alloy bumper beam

The same comparison is made for the steel alloy YS800 in figure B.12. The same trend can be seen where the manufacturing cost is lower for the folded bumper beam at lower production volumes, but the extruded bumper beams become cheaper to manufacture after a certain point. This cross-over point is at 51,446 units, a much higher number than for the aluminium alloys. This can be explained by the much higher tooling cost for the steel extrusions as steel is more difficult to extrude.

Not only the manufacturing cost is important while considering which manufacturing technique to use, but also the weight of the part. When the metal folding process is used flanges are present to connect the two shells, leading to increased weight but barely contributing to the structural performance. This means that a weight penalty is incurred if this process is chosen. The mass of the different bumper beams as well as the weight penalty is shown in table B.5.

Table B.5: Weight comparison of extruded and folded metal bumper beams

	m_{bb} extrusion [kg]	m_{bb} folded [kg]	Weight penalty [%]
AL6061-T6 vs. 6CM-s300 T61	2.696	3.803	41.1
AISI 1020	6.644	8.209	23.6
DP800	3.580	4.411	23.2
YS800	3.230	3.979	23.2

From table B.5 it can be seen that the weight penalty is around 23.5% for the steel alloys, and 41.1% for the aluminium alloys that are compared. This difference is explained by the set size of the flange, dictated by the joining of the parts. However, the aluminium bumper beams automatically have a larger wall thickness due to their lower density, which leads to relatively heavier flanges in comparison to the steel bumper beams.

B.2.3. Cross-section

In this section the parameter sensitivity is analyzed of the parameters that define the cross-section of the bumper beam. Since the effects will be the same for the all different metal alloys, although with some slightly different values, only the AL6061-T6 alloy is considered here. The approach is to vary a single parameter at a time, while keeping the others constant. The base geometry that is used is defined as follows:

- t_{bb}=2 mm
- d_{bb}=40 mm
- h_{bb}=100 mm
- R_{bb}=3000 mm
- L_{bb}=1440.8 mm

Wall thickness

To evaluate the effect of the wall thickness on the most important parameters of the structural performance of the bumper beam, the wall thickness is varied from 20 mm to 60 mm, while keeping the other parameters constant. It is then calculated what the corresponding values are for the energy absorption during the RCAR full width test, the energy absorption during the RCAR structural test, and the intrusion distance during the RCAR corner test. The weight of the bumper beam scales linearly with this wall thickness. These results are shown in figures B.13 and B.14.

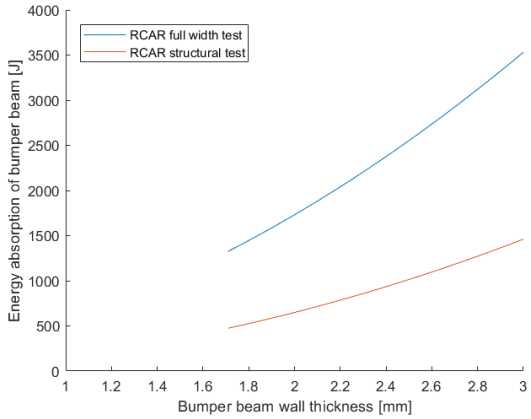

Figure B.13: Sensitivity of bumper beam energy absorption to wall thickness

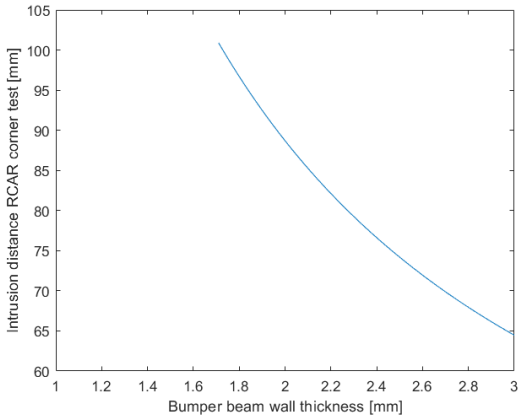

Figure B.14: Sensitivity of intrusion distance during RCAR corner test to wall thickness

In both figures it can be seen that the bumper beam is unable to pass the RCAR corner test if the wall thickness is lower than 1.71 mm. This means that the plastic moment that is developed is not large enough to absorb all of the impact energy, and the candidate design is failed. From figure B.13 it can be seen that the energy aborption of the bumper beam during the RCAR full width test (both crushing of the bumper beam section and elastoplastic deformation) increases rapidly with increasing wall thickness. It is calculated that if the wall thickness doubles, the energy absorption increases by a factor 2.9382. This means that it scales with the power of 1.555. The energy absorption during the RCAR structural test (only crushing of the bumper beam section) also increases rapidly with an increasing wall thickness. If the wall thickness doubles, this energy absorption increases by a factor by a factor 4, which means that it scales quadratically. This means that increasing the wall thickness is a weight-effective method to increase the energy absorption of the bumper beam in both load cases. This can help in finding the desired balance between the different intrusion distances during all of the low-speed load cases.

In figure B.14 it can be seen that the intrusion distance during the RCAR corner test has a high dependency on the wall thickness. It was found that if the wall thickness doubles, the intrusion distance reduces by a factor 1.694. This means that it scales with the power of 0.761. From this it can be included that while increasing the wall thickness does reduce the intrusion distance, other parameters are more effective at this.

Section depth

The influence of the section depth on the structural parameters of importance is analysed by varying it from 20 mm to 60 mm, while keeping the other parameters constant. It is the calculated what the influence is on the energy absorption of the bumper beam during the RCAR full width test and RCAR structural test, as well as the intrusion distance during the RCAR corner test. The results can be seen in figures B.15 and B.16. It can be seen that if the section depth is smaller than 36 mm, the bumper beam can not fully absorb the energy during the RCAR corner test and therefore the candidate is failed. The effect of the section depth on the weight of the bumper beam is not linear, as only part of the cross-section is increased. In this specific case it means that doubling the section depth from 30 mm to 60 mm leads to a weight increase of only 23.8%.
In figure B.15 it can be seen that the energy absorption of the bumper beam increases for both the RCAR full width test and the RCAR structural test if the section depth increases. The influence of an increased section depth is however not very large, especially for the RCAR structural test. This can be explained by the energy absorption due to crushing of the bumper beam section, as the plastic moments that are generated in the

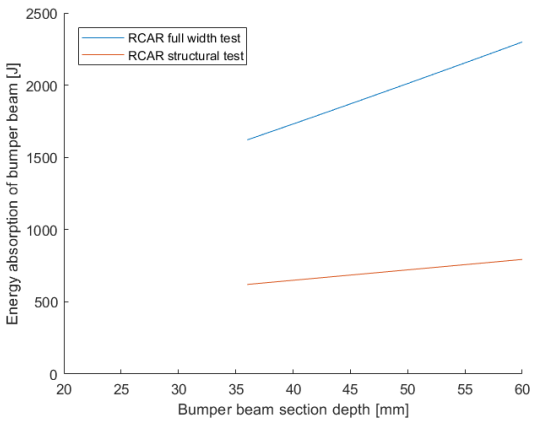

Figure B.15: Sensitivity of bumper beam energy absorption to section depth

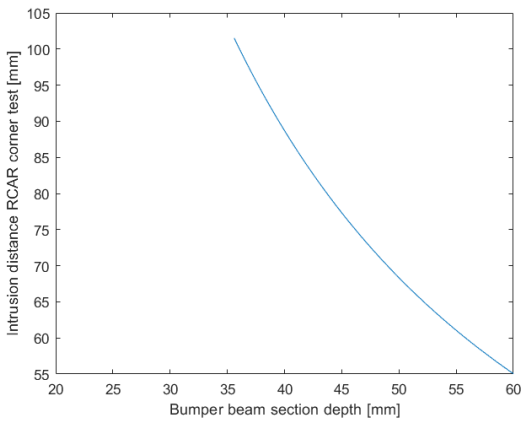

Figure B.16: Sensitivity of intrusion distance during RCAR corner test to section depth

plastic hinges are not dependent on the section depth. An increased section depth however does increase the plastic moment necessary to push to bumper beam into the shape of the RCAR bumper barrier, which explains the larger effect on the energy absorption during the RCAR full width test.

From figure B.16 it can be seen that the intrusion distance during the RCAR corner test decreases rapidly with an increasing section depth. This happens because an increased section depth pushes the vertical walls of the bumper beam further away from the neutral axis, and therefore increasing the plastic moment that is generated by rotating the free end of the bumper beam. From this it can be seen that increasing the section depth is a very weight-effective method to decrease the intrusion distance during the RCAR corner test. It should however be noted that an increased section depth also influences the intrusion distance during the other two load cases, as it increases the contribution of the bumper beam to the intrusion distance by an equal amount.

Section height

To investigate the influence on the section height of the bumper beam, this value is varied between 100 mm and 120 mm. It is then calculated what the effect is on the energy absorption of the bumper beam during the RCAR full width test and the RCAR structural test, as well as the intrusion during the RCAR corner test. The results can be seen in figures B.17 and B.18 respectively. The weight of the bumper beam does not depend linearly on the section height, as only part of the cross-section is increased. This means that the increase of 20% in the section height results in a weight increase of 14.7% under these specific parameters.

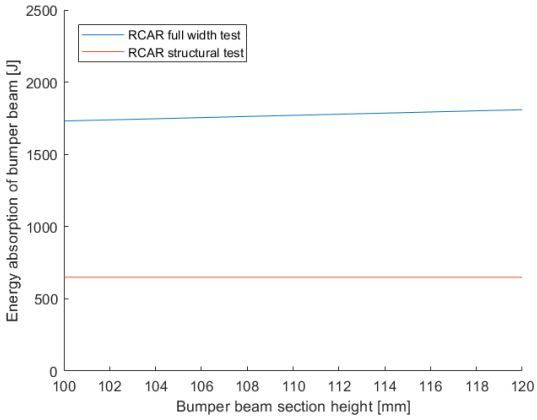

Figure B.17: Sensitivity of bumper beam energy absorption to section height

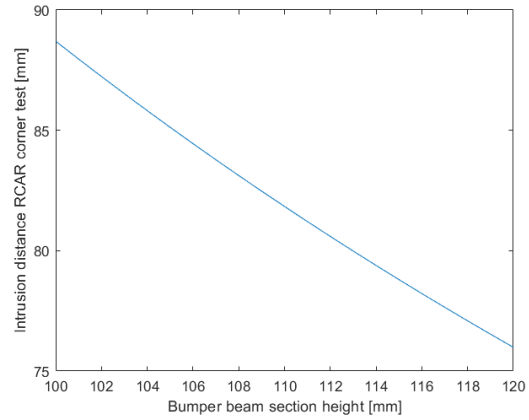

Figure B.18: Sensitivity of intrusion distance during RCAR corner test to section height

From figure B.17 it can be seen that all three load cases are passed for each of the considered section heights. It is also interesting to notice that the energy absorption of the bumper beam during the RCAR strucutral test does not increase if the section height increases. This is exactly as is expected, because the section height does not influence the formation of the plastic hinges during the crushing of the bumper beam section. The energy absorption of the bumper beam during the RCAR full width test does increase, as the plastic moment developed during the elastoplastic phase increases slightly with an increasing section height. However, this increase is only 7.43% for a 20% increase in section height, which leads to a 14.7% weight increase. From this it can be concluded that increasing the section height is not an weight-effective method to increase the energy absorption of the bumper beam. Next to this, an increased section height could also lead to a more difficult packaging situation, making it even more undesirable.
In figure B.18 it can be seen that an increased section height leads to a lower intrusion distance during the RCAR corner test. A reduction of 14.33% in the intrusion distance can be realised for a weight penalty of 14.7%. Based on this, it can be concluded that increasing the section depth is more weight-effective at reducing the intrusion distance during the RCAR corner test. Increasing the section height is however more weight-effective at reducing the intrusion distance than increasing the wall thickness.

B.2.4. Bumper beam length

Here the influence of the length of the bumper beam on the structural performance is investigated. This only has an effect during the RCAR corner test, as the extremities of the bumper beam are not involved in the other two load cases. The length of the bumper beam influences the width of the overlap between the bumper beam and the RCAR barrier. The results can be seen in figure B.19. An increase of bumper beam length of course leads to an increase of the weight of the bumper beam.

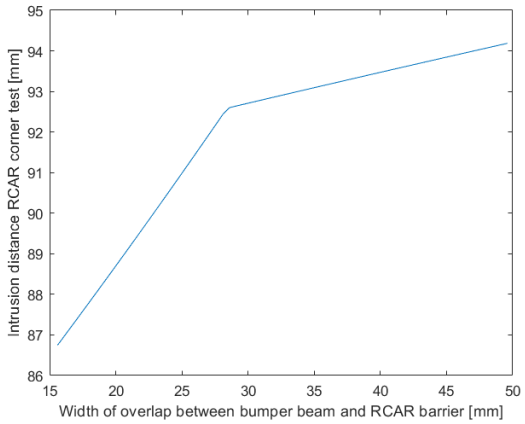

Figure B.19: Influence of overlap width on intrusion distance during RCAR corner test

From figure B.19 it can be seen that if the overlap is less than 16 mm, the candidate design does not pass the load case. This minimimum overlap width is necessary because the free end of the bumper beam exhibits shortening in the lateral direction when there is a rotation at the plastic hinge, and a certain rotation angle is necessary to absorb all of the impact energy.

It can also be seen that when the width of the overlap becomes larger, the intrusion distance actually increases. If the free end is longer, this does not increase the plastic moment in the hinge, or decrease the rotation that is necessary for the energy absorption. A longer free end does however increase the intrusion distance at the same value of the rotation angle.

At a certain overlap width, in this case at 27 mm, a knee-point can be identified in the relation between overlap width and intrusion distance. This knee-point corresponds with the failure mode changing from the limit on the lateral shortening of the free end, to the maximum rotation angle being reached. The force vector changes direction with an equal angle, which means that at a certain point a significant lateral force is developed which increases the unwanted risk of the bumper beam slipping past the RCAR barrier, which would lead to damage of the vehicle structure and failing the load case.

B.2.5. Bumper beam radius of curvature

In this section the influence of the bumper beam radius of curvature on the structural performance and the bumper beam weight is investigated. The results for the weight of the bumper beam can be seen in figure B.20.

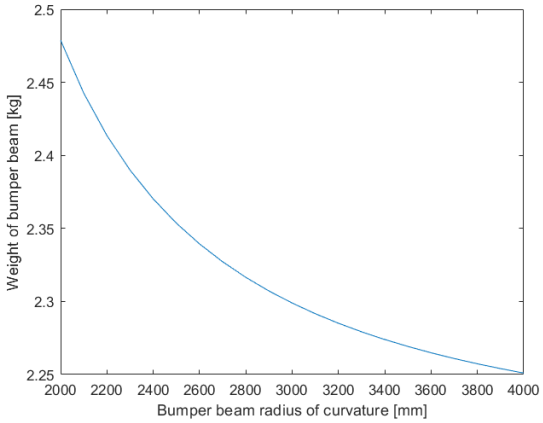

Figure B.20: Influence of radius of curvature on weight of bumper beam

In figure B.20 it can be seen that a more curved bumper, which means having a smaller radius of curvature, leads to a higher weight of the bumper beam. This can be explained by the curvilinear length of the bumper beam incresaing, while the lateral length stays equal. Decreasing the radius of curvature from 4000 mm to 2000 mm leads to a weight increase of 10.2%.

The influence of the bumper beam radius of curvature is not taken into account for all parameters on which it can have an influence, to limit the complexity of the analysis and increase the availability of analysis methods that are suitable for use in such an optimization model. However, the two main structural performance parameters that are influenced by it are the energy absorption of the bumper beam during the RCAR full width test and the peak- and mean force during the RCAR structural test. These results can be seen in figures B.21 and B.22 respectively.

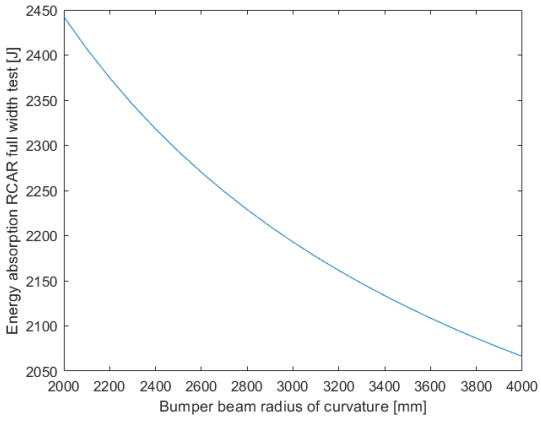

Figure B.21: Sensitivity of bumper beam energy absorption during RCAR full width test to radius of curvature

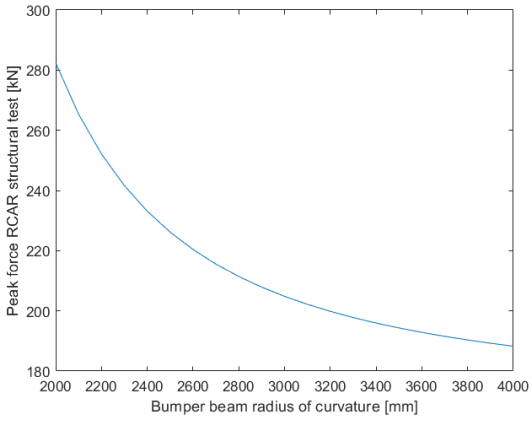

Figure B.22: Sensitivity of peak force during RCAR structural test to radius of curvature

From figure B.21 it can be seen that the energy absorption of the bumper beam during the RCAR full width test is higher if the bumper beam is more curved. This can be explained by the bumper beam being pushed into the same shape as the RCAR barrier during this load case. This consists of two phases, first pushing the curved bumper beam to a straight geometry, and then pushing it further until the same radius of curvature of the RCAR barrier of 3400 mm is reached. This first phase becomes larger if the bumper beam is more curved initially. Decreasing the radius of curvature from 4000 mm to 2000 mm leads to an increase in the energy

absorption of 17.9%.

In figure B.22 it can be seen that the peak force during the RCAR structural test increases if the bumper beam is more curved. This effect is exactly the same for the mean force, which means the CLE does not improve because of this. This effect on the peak and mean force of the crash boxes is due to the incidence angle of the load case, which reduces these forces. Since the bumper beam is in between the barrier and the crash box, it has a sort of cushioning effect where it decreases the influence of the incidence angle. However, under almost all conditions the weight increase of the bumper beam due to the radius of curvature will be larger than the weight decrease of the crash boxes due to the smaller influence of the incidence angle.

From the explanations above it can be seen that although the radius of curvature can have some positive effects, it is not a great method from a weight perspective. The curvature of the bumper beam should mainly be dictated by packaging reasons, to increase the space available for the crash structures and reduce the intrusion distance due to the gap between the bumper fascia and the bumper beam. This part of the intrusion distance is not included in this optimization model, as it is a matter of packaging.

Bibliography

[1] W. Abramowicz and N. Jones. Dynamic axial crushing of square tubes. *International Journal of Impact Engineering*, 2(2):179–208, 1984. doi: 10.1016/0734-743X(84)90005-8.

[2] A. Ahmadi and M. Asgari. Efficient crushable corrugated conical tubes for energy absorption considering axial and oblique loading. *Journal of Mechanical Engineering Science*, 2018. doi: 10.1177/0954406218806006.

[3] E. Ahmed. *Advanced composite materials for automotive applications: structural integrity and crash worthiness*. John Wiley & Sons, Ltd., Hoboken, New Jersey, 2013.

[4] M. Akhshik, J. Tjong, and M. Sain. The effect of lightweighting on greenhouse gas emissions and life cycle energy for automotive composite parts. *Clean Technologies and Environmental Policy*, 21(3):625–636, 2019. doi: 10.1007/s10098-018-01662-0.

[5] M. Altin, M.A. Gueler, and S.K. Mert. The effect of percent foam fill ratio on the energy absorption capacity of axially compressed thin-walled multi-cell square and circular tubes. *International Journal of Mechanical Sciences*, 131:368–379, 2017. doi: 10.1016/j.ijmecsci.2017.07.003.

[6] Inc. ANSYS. *ANSYS Explicit Dynamics Analysis Guide*. ANSYS, Inc., Canonsburg, Pennsylvania, 2019.

[7] V.W. Antonetti. Estimating the coefficient of restitution of vehicle-to-vehicle bumper impacts. *Society of Automotive Engineers*, 1998.

[8] G. Belingardi, A.T. Beyene, E.G. Koricho, and B. Martorana. Alternative lightweight materials and component manufacturing technologies for vehicle front bumper beam. *Composite Structures*, 120:483–495, 2015. doi: 10.1016/j.compstruct.2014.10.007.

[9] C. Bisagni. Experimental investigation of the collapse modes and energy absorption characteristics of composite tubes. *International Journal of Crashworthiness*, 14(4):365–378, 2009.

[10] L. Björnsson and S. Karsson. The potential for brake energy regeneration under swedish conditions. *Applied Energy*, 168:75–84, 2016. doi: 10.1016/j.apenergy.2016.01.051.

[11] R.M. Brach. Modeling of low-speed, front-to-rear vehicle impacts. *Society of Automotive Engineers*, 2003.

[12] S. Bubeck, J. Tomaschek, and U. Fahl. Perspectives of electric mobility: Total cost of ownership of electric vehicles in germany. *Transport Policy*, 50:63–77, 2016. doi: 10.1016/j.tranpol.2016.05.012.

[13] W. Chen and T. Wierzbicki. Relative merits of single-cell, multi-cell and foam-filled thin-walled structures in energy absorption. *Thin-walled structures*, 39(4):287–306, 2001. doi: 10.1016/S0263-8231(01)00006-4.

[14] B.A. Constantin, D. Iozsa, and G. Fratila. Studies about the behavior of the crash boxes of a car body. *Material Science and Engineering*, 161, 2016. doi: 10.1088/1757-899x/161/1/012010.

[15] C. Davila, P. Camanho, and C. Rose. Failure criteria for frp laminates. *Journal of Composite Materials*, 39(4):323–345, 2005. doi: 10.1177/0021998305046452.

[16] M.M. Davoodi, S.M. Sapuan, A. Aidy, N.A. Abu Osman, A.A. Oshkour, and W.A.B. Wan Abas. Developement process of new bumper beam for passenger car: A review. *Materials and Design*, 40:304–313, 2012. doi: 10.1016/j.matdes.2012.03.060.

[17] Q. De Clerck, T. Van Lier, P. Lebeau, M. Messagie, Vanhaverbeke L., C. Macharis, and J. Van Mierlo. How total is a total cost of ownership? *World Electric Vehicle Journal*, 8(4):736–747, 2016. doi: 10.3390/wevj8040742.

[18] Q. De Clerck, T. Van Lier, M. Messagie, C. Macharis, J. Van Mierlo, and L. Vanhaverbeke. Total cost for society: A persona-based analysis of electric and conventional vehicles. *Transportation Research*, 64: 90–110, 2018. doi: 10.1016/j.trd.2018.02.017.

[19] Q. Estrada, D. Szwedowicz, E. Gutierrez-Wing, J. Silva-Aceves, A. Rodriguez-Mendez, M. Elisa-Espinosa, J. Vergara-Vazques, and J. Bedolla-Hermandez. Energy absorption of single and multi-cell profiles under bending load considering damage evolution. *Journal of Automobiles Engineering*, 223(8):2120–2138, 2019. doi: 10.1177/0954407018773020.

[20] L. Farkas, L. Ciubotaru, C. Canadas, J. Kang, S. Donders, J. Tielens, and D. Schildermans. Optimization study of a parameteric vehicle bumper subsystem under multiple crashworthiness and safety load cases. *Optimization and Applications Engineering*, 2009. doi: 10.1007/978-3-642-12598-0.

[21] G.L. Farley. Energy absorption of composite materials. *Journal of Composite Materials*, 17(3), 1983. doi: 10.1177/002199838301700307.

[22] G.L. Farley and R.M Jones. Analogy for the effect of material and geometrical variables on energy-absorption capability of composite tubes. *Journal of Composite Materials*, 26(1):78–89, 1992. doi: 10.1016/0010-4361(92)90339-V.

[23] G.L. Farley and R.M. Jones. Crushing characteristics of continuous fiber-reinforced composite tubes. *Journal of Composite Materials*, 26(1):37–50, 1992. doi: 1c0.1177/002199839202600103.

[24] J. Funk, E. Bonugli, H. Guzman, and M. Freund. Comparison of quasistatic bumper testing and dynamic full vehicle testing for reconstructing low speed collisions. *Society of Automotive Engineers*, 7(3):1036–1086, 2014. doi: 10.4271/2014-01-0481.

[25] H. Hamada, S. Ramakrishna, and H. Satoh. Crushing mechanism of carbon fibre/peek composite tubes. *Journal of Composite Materials*, 29:749–755, 1995. doi: 10.1016/0010-4361(95)98195-Q.

[26] A. Hambali, S.M. Sapuan, N. Ismail, and Y.J. Nukman. Application of analytical hierarchy process in the design concept selection of autmotive composite bumper beam during the conceptual design stage. *Scientific Research and Essays*, 4(4):198–211, 2009.

[27] D.C. Han and S.H. Park. Collapse behavior of square thin-walled columns subjected to oblique loads. *Thin-Walled Structures*, 35(3):167–184, 1999. doi: 10.1016/S0263-8231(99)00022-1.

[28] A.G. Hanssen, O.S. Hopperstad, and M. Langseth. Bending of square aluminium extrusions with aluminium foam filler. *Acta Mechanica*, 142(1-4):13–31, 2000. doi: 10.1007/BF01190010.

[29] A.G. Hanssen, M. Langseth, and O.S. Hopperstad. Static and dynamic crushing of circular aluminium extrusions with aluminium foam filler. *International Journal of Impact Engineering*, 24(5):475–507, 2000. doi: 10.1016/S0734-743X(99)00170-0.

[30] A.G. Hanssen, M. Langseth, and O.S. Hopperstad. Static and dynamic crushing of square aluminium extrusions with aluminium foam filler. *International Journal of Impact Engineering*, 24(4):347–383, 2000. doi: 10.1016/S0734-743X(99)00169-4.

[31] A.G. Hanssen, L. Lorenzi, K.K. Berger, O.S. Hopperstad, and M. Langseth. A demonstrator bumper system based on aluminium foam filled crash boxes. *International Journal of Crashworthiness*, 5(4):381–392, 2000.

[32] R. Hosseinzadeh, S.M. Mahmood, and L.B. Lessard. Parametric study of automotive composite bumper beams subjected to low-velocity impacts. *Composite Structures*, 68(4):419–427, 2000. doi: 10.1016/j.compstruct.2004.04.008.

[33] R.B. Howard, J. Bomar, and C. Bare. Vehicle resitution response in low velocity collisions. *Society of Automotive Engineers*, 1993.

[34] D. Hu, Y. Wang, L. Dang, and Q. Pan. Energy absorption characteristics of composite tubes with different fibers and matrix under axial quasi-static and impact crushing conditions. *Journal of Mechanical Science and Technology*, 32(6):2587–2599, 2018. doi: 10.1007/s12206-018-0516-y.

[35] D. Hull. A unified approach to progressive crushing of fibre-reinforced composite tubes. *Composite Science and Technology*, 40(4):377–421, 1991. doi: 10.1016/0266-3538(91)90031-J.

[36] S. Kang. Bumper stay design for rcar front low speed impact test. *Korean Society of Automotive Engineers*, 24:191–197, 2016. doi: 10.7467/KSAE.2016.24.2.191.

[37] D. Kecman. Bending collapse of rectangular and square section tubes. *International Journal of Mechanical Sciences*, 25(9):623–636, 1983. doi: 10.1016/0020-7403(83)90072-3.

[38] B. Kim and W. Lee. Analysis of crarsh impact of composites stay-shaped bumper using fem method. *International Journal of Computing, Communications & Instrumentation Engineering*, 4(2), 2017.

[39] H. Kim. New extruded multi-cell aluminium profile for maximum crash energy absorption and weight efficiency. *Thin-Walled Structures*, 40(4):311–327, 2002. doi: 10.1016/S0263-8231(01)00069-6.

[40] T.H. Kim and S.R. Reid. Bending collapse of thin-walled rectangular columns. *Computers and Structures*, 79(20):1897–1911, 2001. doi: 10.1016/S0045-7949(01)00089-X.

[41] F. Leimbach and H. Kiebach. *Reparability and insurance ratings in the development of cars*. John Wiley & Sons, Ltd., Hoboken, New Jersey, 2014.

[42] Z. Li, R. Chen, and F. Lu. Comparative analysis of crashworthiness of empty and foam-filled thin-walled tubes. *Thin-walled Structures*, 124:343–349, 2018. doi: 10.1016/j.tws.2017.12.017.

[43] Y.J. Liu, L. Ding, and C.H.N. Zhuhai. Influence of the cross section shape on energy absorbing component of bumper subjected to low speed crash. *Applied Mechanics and Materials*, 477:3–6, 2014. doi: 10.4028/www.scientific.net/AMM.477-478.3.

[44] G. Lu and T.X. Yu. *Energy absorption of structures and materials*. Woodhead Publishing, Sawston, Cambridge, 2003.

[45] A. Mamalis, D.E. Manolakos, G. Demosthenous, and M.B. Ioannidis. *Crashworthiness of composite thin-walled structural components*. Taylor & Francis Group, Milton Park, Abingdon-on-Thames, 1998.

[46] A.G. Mamalis, M. Robinson, D.E. Manolakos, G.A. Demosthenous, M.B. Ioannidis, and J. Carruthers. Crashworty capability of composite material structures. *Composite Structures*, 37(2):109–134, 1997. doi: 10.1016/S0263-8223(97)80005-0.

[47] J. Marzbanrad, M. Alijanpour, and M.S. Kiasat. Design and analysis of an automotive bumper beam in low-speed frontal crashes. *Thin-Walled Structures*, 47(8):902–911, 2009. doi: 10.1016/j.tws.2009.02.007.

[48] T.H.G. Megson. *Structural and stress analysis*. Butterworth-Heineman, Jordan Hill, Oxford, 2005.

[49] J. Meredith, E. Bilson, R. Powe, E. Collings, and K. Kirwan. A performance versus cost analysis of prepreg carbon fibre epoxy energy absorption structures. *Composite Structures*, 124:206–213, 2015. doi: 10.1016/j.compstruct.2015.01.0227.

[50] B.S. Min and J. Cho. Impact characteristics according to the structure of crash box at the vehicle. *Society of Automotive Engineers*, 62, 2017. doi: 10.1515/amm-2017-0151.

[51] L.K. Mitropoulos, P.D. Prevedouros, and P. Kopelias. Total cost of ownership and externalities of conventional, hybrid and electric vehicle. *Transportation research procedia*, 24:267–274, 2017. doi: 10.1016/j.trpro.2017.05.117.

[52] H. Mozafari, S. Lin, G.C.P. Tsui, and L. Gu. Controllable energy absorption of double sided corrugated tubes under axial crushing. *Composites*, 134(Part B):9–17, 2018. doi: 10.1016/j.compositesb.2017.09.042.

[53] M. Nasiruddin, A. Hambali, J. Rosidah, S.W. Wahyono, and A. Modh. A review of energy absorption of automotive bumper beam. *International Journal of Applied Engineering Research*, 12(2):238–245, 2017.

[54] N. Onsalung and C. Thinvongpituk. The influence of foam density on specific energy absorption of rectangular steel tubes. *Energy Research Journal*, 1(2):135–140, 2010. doi: 10.3844/erjsp.2010.135.140.

[55] A. Pandarkar, M.D. Goel, and M.S. Hora. Axial crushing of hollow and foam filled tubes: An overview. *Sadhana*, 41(8):909–921, 2016. doi: 10.1007/s12046-016-0525-4.

[56] W. Pawlus, N.J. Einvind, H.R. Karimi, and J. Robbersmyr. Mathematical modeling and analysis of a vehicle crash. *Proceedings of the 4th conference on European Computing*, pages 194–199, 2010. doi: 10.5555/1844367.1844401.

[57] S. Potkamp. Lightweight design of low-speed crash structures: A review. 2019.

[58] S.A. Pradeep, R.K. Iyer, H. Kazan, and S. Pilla. *Automotive applications of plastics: Past, present and future - chapter 30*. Elsevier Inc., Amsterdam, The Netherlands, 2017.

[59] S. Ramakrishna and H. Hamada. Energy absorption characteristics of crash worthy structural composite materials. *Key Engineering Materials*, 141(2):585–622, 1998.

[60] M.J. Rezvani and A. Jahan. Effect of initiator, design, and material on crashworthiness performance of thin-walled cylindrical tubes: A primary multi-criteria analysis in lightweight design. *Thin-Walled Structures*, 96:169–182, 2015. doi: 10.1016/j.tws.2015.07.026.

[61] A. Rusich and R. Danielis. Total cost of ownership, social lifecycle cost and energy consumption of various automotive technologies in italy. *Research in Transportation Economics*, 50:3–16, 2015. doi: 10.1016/j.retrec.2015.06.002.

[62] B. Stok and M. Halilovic. Analytical solutions in elasto-plastic bending of beams with rectangular cross-section. *Applied Mathematical Modelling*, 33(3):1749–1760, 2009. doi: 10.1016/j.apm.2008.03.011.

[63] M.N. Sudin, S. Sapuan, N. Ismail, M. Maleque, and E.S. Zainudin. Total design of polymer composite automotive bumper fascia. *Suranaree Journal for Science & Technology*, 12(1):39–45, 2004.

[64] M.N. Sudin, A.T. Din, M.F.B. Abdollah, and S. Shamsudin. Conceptual design of automotive bumper beam. *Conference on Design, Simulation, Product Development and Optimization*, 2007.

[65] M.N. Sudin, M. Ruzi Harun, and A. Tajudin Hamzah. A prototype of kbs for material selection in bumper beam design. *Suranaree Journal for Science & Technology*, 14(3):215–222, 2007.

[66] G. Sun, S. Li, Q. Liu, G. Li, and Q. Li. Experimental study on crash worthiness of empty/aluminium foam/honeycomb-filled cfrp tubes. *Composite Structures*, 152:969–993, 2010. doi: 10.1016/j.compstruct.2016.06.019.

[67] G. Sun, F. Xu, G. Li, and Q. Li. Crashing analysis and multiobjective optimization for thin-walled structures with functionally graded thickness. *International Journal of Impact Engineering*, 64:62–74, 2014. doi: 10.1016/j.ijimpeng.2013.10.004.

[68] Q. Tai and X.Y. Zhang. Research and application on automotive aluminium bumper based on topology optimization. *Applied Mechanics and Materials*, 189:495–500, 2012. doi: 10.4028/www.scientific.net/AMM.189.495.

[69] T. Tang, W. Zhang, H. Yin, and H. Wang. Crushing analysis of thin-walled beams with various section geometries under lateral impact. *Thin-Walled Structures*, 102:43–57, 2016. doi: 10.1016/j.tws.2016.01.017.

[70] N. Tanlak, F. Sonmez, and M. Senaltun. Shape optimization of bumper beams under high-velocity impact loads. *Engineering Structures*, 95:49–60, 2015. doi: 10.1016/j.engstruct.2015.03.046.

[71] V. Tarigopula, M. Langseth, O.S. Hopperstad, and A.H. Clausen. Axial crushing of thin-walled high-strength steel sections. *International Journal of Impact Engineering*, 32(5):847–882, 2006. doi: 10.1016/j.ijimpeng.2005.07.010.

[72] P.H. Thornton, J.J. Harwood, and P. Beardmore. Fiber-reinforced plastic composites for energy absorption purposes. *Composite Science and Technology*, 24(4):275–298, 1985. doi: 10.1016/0266-3538(85)90026-0.

[73] T. Wang and Y. Li. Design and analysis of automotive carbon fiber composite bumper beam based on finite element analysis. *Advances in Mechanical Engineering*, 7:1687–1840, 2015. doi: 10.1177/1687814015589561.

[74] M.D. White, N. Jones, and W. Abramowicz. A theoretical analysis for the quasi-static axial crushing of top-hat and double-hat thin-walled sections. *International Journal of Mechanical Sciences*, 41(2):209–233, 1999. doi: 10.1016/S0020-7403(98)00048-4.

[75] T. Wierzbicki and W. Abramowicz. On the crushing mechanics of thin-walled structures. *Journal of Applied Mechanics*, 50(4a):727, 1983. doi: 10.1115/1.3167137.

[76] R.L. Wooley. Crash pulse modeling of force limiting structures. *Society of Automotive Engineers*, 2008. doi: 10.4271/2008-01-0175.

[77] L. Ye, G. Lu, and J.L. Yang. An analytical model for axial crushing of a thin-walled cylindrical shell with a hollow foam core. *Thin-Walled Structures*, 49(11):1460–1467, 2011. doi: 10.1016/j.tws.2011.07.007.

[78] Y. Yoshida, X. Wan, M. Takahashi, and T. Hosokawa. Bending energy absorption of extruded aluminium beams. *Japanese Society of Automotive Engineers*, 18(4):385–392, 1997. doi: 10.1016/S0389-4304(97)00029-5.

[79] F. Zeng, H. Xie, Q. Liu, F. Li, and W. Tan. Design and optimization of a new composite bumper beam in high-speed frontal crashes. *Structural and Multidisciplinary Optimization*, 53(1):115–122, 2016. doi: 10.1007/s00158-015-1312-2.

[80] Z. Zhang, S. Liu, and Z. Tang. Design optimization of cross-sectional configuration of rib-reinforced thin-walled beam. *Thin-Walled Structures*, 47:868–878, 2009. doi: 10.1016/j.tws.2009.02.009.